Production and spectroscopy of ultracold YbRb* molecules

Inaugural-Dissertation

zur
Erlangung des Doktorgrades der
Mathematisch-Naturwissenschaftlichen Fakultät
der Heinrich-Heine-Universität Düsseldorf

vorgelegt von

Nils Nemitz

aus Wolfsburg

November 2008

Aus dem Institut für Experimentalphysik
der Heinrich-Heine-Universität Düsseldorf

Gedruckt mit der Genehmigung der
Mathematisch-Naturwissenschaftlichen Fakultät der
Heinrich-Heine-Universität Düsseldorf

Referent:	Prof. Dr. Axel Görlitz
Koreferent:	Dr. Bernhard Roth
Tag der mündlichen Prüfung:	18.12.2008

Contents

Chapter 1

Introduction

This chapter gives a motivation for the work presented here by outlining the history of atomic and molecular spectroscopy and placing the experiments described in the context of current developments. For a brief summary of the work presented, please see chapter 8, which also provides a German version.

1.1 History

Spectroscopy is one of the oldest fields in modern science. Over the years it has provided insight into the structure of atoms and molecules and has laid the foundations of quantum mechanics.

As early as 1802, W. H. Wollaston found dark lines in the solar spectrum observed through a prism. These were later rediscovered and investigated by J. Fraunhofer. In 1862 G. R. Kirchoff was awarded the Rumford medal for his work in describing the solar spectrum and explaining why the dark absorption lines found there show the same structure as the emission lines from hot gases.

In 1872 the same award was presented to A. J. Ångström, whose measurements of the hydrogen spectrum prompted J. J. Balmer's discovery of the underlying mathematical progression in 1885. This was developed into a more general formalism by J. Rydberg in 1888. Rydberg was also the first to discover the mathematical advantages of working with wavenumbers. This work led directly to N. Bohr's theory of the atomic structure with electrons at fixed energy levels and emission and absorption based on transitions between them, that was presented in 1913. Bohr was awarded the 1922 Nobel Prize in physics for his work.

This is not the only Nobel Prize awarded in this field: It was given to H. A. Lorentz and P. Zeeman in 1902 for the discovery of what is now known as the Zeeman effect, to A. A. Michelson in 1907 for the invention of the interferometer and its applications, and in 1911 to W. Wien for his work on thermal radiation. Between M. Planck (in 1918) and A. Einstein (in 1921) for their respective insights into the quantized nature of radiation, the prestigious prize went to J. Stark in 1919, for his discovery of the splitting of spectroscopic lines in an electric field - now known as the Stark effect. The year 1930 saw the Nobel Prize for C. V. Raman and his work on light scattering and in 1955 it was awarded to W.

E. Lamb for his investigations into the fine structure of the hydrogen spectrum.

By this time the physical principles behind atomic and molecular energy levels and the resulting spectra were well established. G. Herzberg's book on the "Spectra of Diatomic Molecules" was first published in 1939 and its later editions remain definitive in many respects even today. He, too, was awarded the Nobel Prize in 1971 for his work on the properties of molecules.

Later surges in activity were caused by new techniques and technologies: Based on the previous work on masers (Nobel Prize for Townes, Basov, and Prokhorov in 1964), the first laser was built in 1960 by T. H. Maiman. In 1969 the appearance of the dye laser with its tunable wavelength turned this into a mighty spectroscopic tool. The first continuous-wave laser diode was built in Z. Alferov's group in 1970 (Nobel Prize in 2000). Modern laser diodes have turned lasers into a manageable, compact technology for a wide range of wavelengths.

Besides the obvious advantage of providing a narrow probe for transitions, the high intensity in a narrow frequency range has led to the development of advanced spectroscopic methods, involving saturation of transitions, multi-photon processes and non-linear mixing.

While these methods opened up the field of sub-Doppler spectroscopy, S. Chu and his coworkers demonstrated in 1985 that it was also possible to use lasers to actually cool atoms down to temperatures in the micro-Kelvin range where the Doppler effect becomes small, as originally suggested by Wineland and others. For this and later extensions towards proper traps and advanced cooling methods the Nobel Prize was once again awarded in 1997.

A further Nobel Prize was given to E. A. Cornell, C. E. Wieman and W. Ketterle for the realization of the Bose-Einstein condensate, a new state of matter made accessible through the success of laser cooling and trapping. It has already provided many fascinating experiments in atomic quantum mechanics.

Recently, frequency combs (also awarded with the Nobel Prize for J. L. Hall and T. W. Hänsch in 2005) have reached a state of development where they provide a reliable means of comparing laser and radio frequencies with unprecedented precision throughout a wide wavelength range. As they approach technical maturity and spread from specialist labs to common usage, they are likely to cause new break-throughs in spectroscopy.

1.2 Ultracold Molecules

There is great interest in adapting the success of measurements on ultracold atoms to the field of molecules, which have a much greater variety of interactions.

Precision measurements of molecular transitions might provide new insight into electron-nucleon interactions (DeMille et al., 2008), time-reversal symmetry (Hinds, 1997) or possible changes of the fine structure constant (Hudson et al., 2006). Ultracold polar molecules in particular have potential for applications in quantum computing (DeMille, 2002) and as a toolbox for exploring condensed matter physics (Pupillo et al., 2008). Phase transitions in quantum degenerate or near degenerate states (Baranov et al., 2002) also promise interesting results.

However, all of these require an efficient method of creating ultracold molecules, preferably in the rovibrational ground state or a at least one of a low, known excitation. Doyle et al. (2004) give an overview of the different approaches to this problem.

A basic method relies on creating molecules in a strategically chosen excited state from where a useful fraction of molecules decay into interesting bound ground states (Sage et al., 2005; Deiglmayr et al., 2008). Improving on this, recent experiments have demonstrated coherent transfer through a two-photon process, with much higher efficiencies. Danzl et al. (2008) report two-photon transfer from a caesium Bose-Einstein-condensate to a defined, low vibrational molecular state with 80% efficiency.

The first experiment to reach the rovibrational ground state with similar transfer efficiency in a heteronuclear molecule is described in (Ni et al., 2008). Here, weakly bound potassium-rubidium molecules are initially formed using a Feshbach resonance and then transferred to the absolute ground state via a two-photon stimulated Raman adiabatic passage process.

1.3 This Thesis

The experiments presented in this thesis are the first steps towards the creation of rovibrational ground state ytterbium-rubidium molecules. At this time they represent the first system of ultracold molecules consisting of an alkali and a rare earth atom. This combination offers significantly different physical properties from the alkali-alkali combinations investigated in most current experiments. Possibly the most interesting of these is the ${}^2\Sigma_{1/2}$ ground state, which allows stable ground state YbRb molecules to be held in a magnetic trap. Additionally, the existence of an unpaired electron makes this molecule a candidate for the investigation of lattice spin models (Micheli et al., 2006).

Using photoassociation in clouds of ultracold atoms avoids the problems of laser-cooling molecules down to sub-millikelvin temperatures. The remaining difficulties lie in forming the molecules in a known rovibrational state and then transferring them down to a ground state which has no rotational or vibrational excitation. Designing and implementing an efficient method for this requires detailed knowledge of the molecular properties in general and of suitable intermediate states in particular.

Unfortunately, very little is known about the ytterbium-rubidium molecule. Theoretical work so far has mostly concentrated on the more common alkali-alkali pairs (Derevianko et al., 2001; Azizi et al., 2004; Aymar and Dulieu, 2007) and only recently the first ab-initio calculations of the molecular potentials have become available (Fleig, 2008).

The work presented here shows that it is possible to efficiently form loosely bound, excited state molecules from cold rubidium and ytterbium atoms using photoassociation. This provides a defined starting point for the controlled transfer of the molecules from the excited state to a selected ground state that will be developed in future work of the group.

This thesis begins with a review of the relevant atom and molecular physics (chapter 3), followed by a description of the experimental setup and procedures in chapter 4. Photoassociation spectra taken for the formation of YbRb* molecules with two different isotopes of ytterbium are presented and analyzed in chapter 6. Chapter 7 outlines a path to follow in the near future, discussing different transfer methods for reaching the rovibrational ground state. The summary in chapter 8, also provided in a German version, provides a review of the essential results.

Chapter 2

Atomic Species

The experiments make use of a mixture of rubidium and ytterbium atoms that was chosen to keep the technical requirements manageable, while still providing interesting physics beyond the more common alkali-alkali mixtures.

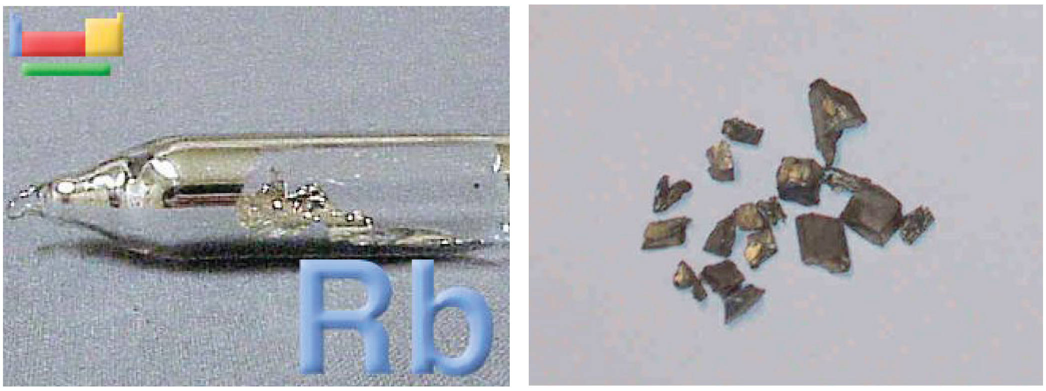

Figure 2.1: Rubidium (left, picture from *webelements.com*) and Ytterbium (right)

2.1 Rubidium

Rubidium (Rb) is the alkali metal with the atomic number 37. Its most common isotopes are ^{85}Rb at 71.2% natural abundance and ^{87}Rb at 27.8%. While ^{85}Rb is more abundant, its negative scattering length causes instability at ultracold temperatures. Since future experiments will rely on sympathetic cooling of ytterbium with rubidium down to the point of quantum degeneracy, working with ^{87}Rb is preferable as this isotope has a positive scattering length.

The lowest open shell in the ground state is 5s, occupied by one valence electron. The single unpaired electron makes the rubidium atom paramagnetic and therefore magnetically trappable. In a first stage of cooling, atoms are trapped in a magneto-optical trap (MOT) using the D2 transition. The required wavelength of 780.24 nm is easily supplied by diode lasers.

Rubidium has the distinction of being the first element Bose-Einstein-condensation was

Element:		^{87}Rb	
atomic mass	$[10^{-25}$ kg]	1.4432	
ground state C_6 coeff.	[a.u.]	4703 ± 9	
nuclear spin I		3/2	
s-wave scatt. length	$[a_0]$	98.98 ± 0.04	
transition		$^2S_{1/2} \rightarrow {}^2P_{1/2}$	$^2S_{1/2} \rightarrow {}^2P_{3/2}$
used for		MOT, slower	photoassoc.
wavelength	[nm]	780.24	794.77
wavenumber	[cm^{-1}]	12817	12579
linewidth ω	[MHz]	$2\pi \cdot 6.065$	$2\pi \cdot 5.746$
exc. state lifetime τ	[ns]	26.24	27.70
MOT: Doppler temp.	[μK]	146	–
MOT: saturation int.	[mW/cm^2]	1.669	–

Table 2.1: Relevant properties of Rubidium atoms. Sources: Steck (2003); Tassy (2007)

achieved in. It was selected for these experiments because it is still considered to be the easiest element to work with in the field of ultracold atoms, due to a fortunate combination of electronic, optical, magnetic and collisional properties.

The photoassociation experiments are performed with a laser operating near the D1 transition at 794.98 nm. This was chosen because it is the lowest electronic state and because this line has only two hyperfine components separated by 817MHz (or 0.0272cm^{-1}) which makes it easier to tell which features of the spectrum are caused by the hyperfine splitting. Most of the rubidium atoms start out in the lower $F = 1$ hyperfine level of the ground state. The energetic difference between this state ($^2S_{1/2}$,$F = 1$) and the excited $^2P_{1/2}$,$F' = 2$ state was chosen as the reference for the photoassociation experiments and in the following, the wavenumber $\widetilde{\nu}_{PA}$ and therefore the photon energy $E_{PA} = h\,c\,\widetilde{\nu}$ of the photoassociation laser will generally be described relative to this:

$$\Delta_{PA} = \widetilde{\nu}_{PA} - \widetilde{\nu}^0_{PA} = \widetilde{\nu}_{PA} - 12578.862\,\mathrm{cm}^{-1} \tag{2.1}$$

2.2 Ytterbium

Ytterbium (Yb) is the rare earth with the atomic number 70. It occurs in seven stable isotopes, the most common of which is ^{174}Yb at 31.8% natural abundance. All of the isotopes ^{171}Yb, ^{172}Yb, ^{173}Yb and ^{176}Yb have abundances between 12% and 22%. This makes ytterbium very flexible in an experiment on cold interactions, as the cooling will be specific to one particular isotope, but changing to another one can be done by simply changing the frequency of the trapping and slowing lasers. The presence of both bosonic (even-numbered) and fermionic (odd) isotopes makes it possible to explore both Bose-Bose and Bose-Fermi interactions without changing the experimental setup. Table 2.2 lists some properties of the isotopes ^{174}Yb and ^{176}Yb investigated here.

Ytterbium is also one of the elements besides the alkalis that can be trapped in a MOT. It actually has two cycling transitions that can be used. One is the broad $^1S_0 \rightarrow {}^1P_1$

Element:		^{174}Yb	^{176}Yb
atomic mass	[10^{-25} kg]	2.8883	2.9216
s-wave scattering length	[a_0]	105 ± 2	-24 ± 4
scatt. length with ^{87}Rb	[a_0]	$\pm(83^{+89}_{-25})$	$\pm(127^{+245}_{-45})$
ground state C_6 coeff.	[a.u.]	1932 ± 30	
est. YbRb C_6 coefficient	[a.u.]	3186	
nuclear spin I		0	

Transition:		^{1}S$_0$→^{3}P$_1$	^{1}S$_0$→^{1}P$_1$
used for		MOT	slower
wavelength	[nm]	555.80	398.91
wavenumber	[cm^{-1}]	17992	25068
linewidth ω	[MHz]	$2\pi \cdot 0.181$	$2\pi \cdot 28.01$
excited state lifetime τ	[ns]	877	5.68
MOT: Doppler temp.	[μK]	4.4	672
MOT: saturation int.	[mW/cm^2]	0.138	57.24

Table 2.2: Relevant properties of ytterbium atoms. Sources: Loftus (2001); Tassy (2007)

transition at 399 nm. In the experiments reported here, this is used for slowing the atoms. The forbidden nature of the intercombination ^{1}S$_0$→^{3}P$_1$ transition at 556 nm causes the linewidth to be considerably smaller. This transition is used for the ytterbium trap since it puts a lower Doppler limit on the temperatures that can be reached.

While its diamagnetic ground state makes ytterbium unsuited to magnetic trapping, both Bose-Einstein-Condensates (Takasu et al., 2003) and quantum degenerate Fermi gases (Fukuhara et al., 2007) have been created in optical traps.

Previous experiments have shown that sympathetic cooling of ytterbium with rubidium is possible (Tassy, 2007). Since the current focus is the creation of molecules at temperatures near or even below the onset of Bose-Einstein-Condensation, the experiments in this thesis all use the bosonic isotopes ^{174}Yb and ^{176}Yb where sympathetic cooling was found to be most efficient due to a large inter-species scattering cross-section.

2.3 Energy Levels and Wavenumbers

To provide an overview of the various transitions and how their photon energies relate to each other, figure 2.2 shows the lower energy levels. Throughout this thesis it will occasionally become relevant whether exciting a certain transition in one species will cause unintended excitations in the other. For this reason a list of energy levels given in wavenumbers is provided in table 2.3.

Even though they are not an SI unit, wavenumbers are still the most common unit in the field of spectroscopy and generally convenient in atomic and molecular physics as they provide a measure of both wavelengths and energy levels. Usually given in the unit of cm^{-1}, the wavenumber $\tilde{\nu}$ simply describes how many wavelengths fit into the length of one centimeter: $\tilde{\nu} = 1/\lambda$. This reciprocal definition has the advantage of being proportional to the photon energy $E = h\nu$ of the light, so that energy differences can simply be added or subtracted: The wavenumber for the light required to drive a transition between any two states is simply the difference between their energies expressed in wavenumbers.

Some of the more useful conversion formulas have been gathered here for reference:

$$E = h\,c\,\tilde{\nu} \qquad \Longrightarrow \qquad 1\,\mathrm{cm}^{-1} \;\widehat{=}\; 1.9865 \cdot 10^{-23}\,\mathrm{J} \tag{2.2}$$

$$\tilde{\nu} = \frac{E}{h\,c} \qquad \Longrightarrow \qquad 1\,\mathrm{J} \;\widehat{=}\; 0.5034 \cdot 10^{23}\,\mathrm{cm}^{-1} \tag{2.3}$$

$$\nu = c\,\tilde{\nu} \qquad \Longrightarrow \qquad 1\,\mathrm{cm}^{-1} \;\widehat{=}\; 29.978\,\mathrm{GHz} \tag{2.4}$$

$$\tilde{\nu} = \frac{\nu}{c} \qquad \Longrightarrow \qquad 1\,\mathrm{GHz} \;\widehat{=}\; 0.03336\,\mathrm{cm}^{-1} \tag{2.5}$$

When converting to and from wavenumbers, care must be taken not to mix up the units. When the wavenumber is given in units of cm^{-1}, the speed of light needs to be converted to $\mathrm{cm/s}$ as well. To keep conversions simple, all wavelengths in this thesis are given as they would be in vacuum. Only in this case is the definition $\tilde{\nu} = 1/\lambda$ actually correct.

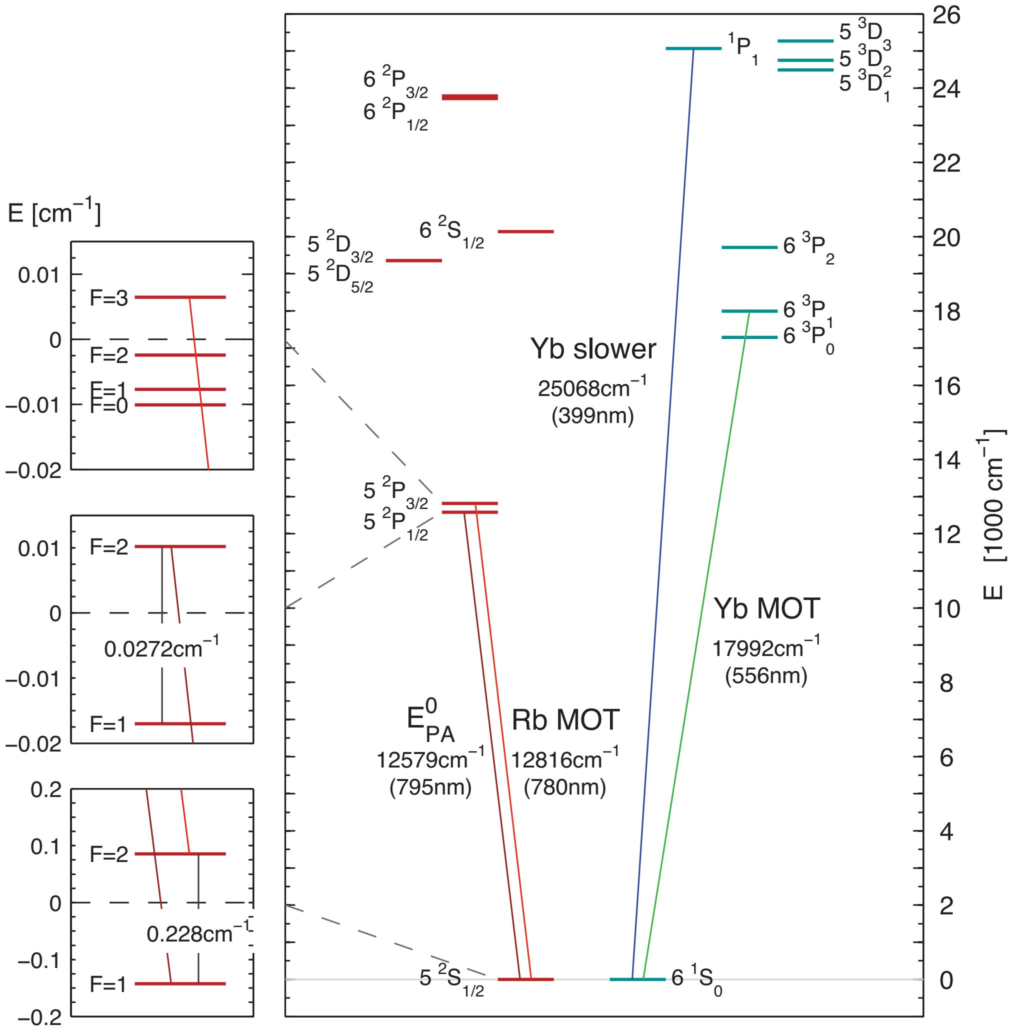

Figure 2.2: Lower energy levels and important transitions in rubidium (left) and ytterbium (right). The insets on the left show the hyperfine structure in rubidium. The bosonic ytterbium isotopes investigated do not have any nuclear spin and therefore no hyperfine structure. All energies are given in cm^{-1}.

rubidium

state	config.	E [cm^{-1}]
$5S_{1/2}$	$4p^6 5s$	0.0
$5P_{1/2}$	$4p^6 5p$	12579.0
$5P_{3/2}$	”	12816.5
$4D_{5/2}$	$4p^6 4d$	19355.2
$4D_{3/2}$	”	19356.6
$6S_{1/2}$	$4p^6 6s$	20132.5
$6P_{1/2}$	$4p^6 6p$	23715.0
$6P_{3/2}$	”	23792.6
$5D_{3/2}$	$4p^6 5d$	25700.5
$5D_{5/2}$	”	25703.5
$7S_{1/2}$	$4p^6 7s$	26311.4
$7P_{1/2}$	$4p^6 7p$	27835.0
$7P_{3/2}$	”	27870.1
$6D_{3/2}$	$4p^6 6d$	28687.1
$6D_{5/2}$	”	28689.4
$8S_{1/2}$	$4p^6 8s$	29046.8
$8P_{1/2}$	$4p^6 8p$	29834.9
$8P_{3/2}$	”	29853.8
$7D_{3/2}$	$4p^6 7d$	30280.1
$7D_{5/2}$	”	30281.6
$9S_{1/2}$	$4p^6 9s$	30499.0
$9P_{1/2}$	$4p^6 9p$	30958.9
$9P_{3/2}$	”	30970.2
$8D_{3/2}$	$4p^6 8d$	31221.4
$8D_{5/2}$	”	31222.4
$10S_{1/2}$	$4p^6 10s$	31362.3
$10P_{1/2}$	$4p^6 10p$	31653.9
$10P_{3/2}$	”	31661.2
$9D_{3/2}$	$4p^6 9d$	31821.9
$9D_{5/2}$	”	31822.6
...		...
ionization	$4p^6$	33690.8

ytterbium

state	config.	E [cm^{-1}]
$6S_0$	$4f^{14}6s^2$	0.0
$(6)^3P_0$	$4f^{14}6s6p$	17288.4
$(6)^3P_1$	”	17992.0
$(6)^3P_2$	”	19710.4
$(7/2,\ 3/2)_2$	$4f^{13}_{7/2}5d_{3/2}6s^2$	23188.5
$(7/2,\ 3/2)_5$	”	25859.7
$(7/2,\ 3/2)_3$	”	27445.6
$(7/2,\ 3/2)_4$	”	28184.5
$5D_1$	$4f^{14}5d6s$	24489.1
$5D_2$	”	24751.9
$5D_3$	”	25270.9
$(6)^1P_1$	$4f^{14}6s6p$	25068.2
$(5/2,\ 3/2)_6$	$4f^{13}_{7/2}5d_{5/2}6s^2$	27314.9
$(5/2,\ 3/2)_2$	”	28196.0
$(5/2,\ 3/2)_1$	”	28857.0
$(5/2,\ 3/2)_4$	”	29775.0
$(5/2,\ 3/2)_3$	”	30207.4
$(5/2,\ 3/2)_5$	”	30524.7
$5D_2$	$4f^{14}5d6s$	27677.7
$(7/2,1/2)_3$	$4f^{13}_{7/2}6s^26p_{1/2}$	32065.3
$(7/2,1/2)_4$	”	32273.6
$(7)^3S_1$	$4f^{14}6s7s$	32694.7
$(7)^1S_0$	$4f^{14}6s7s$	34350.7
...		...
ionization	$4f^{13}6s^2$	71859.7

laser wavelengths

laser	λ [nm]	$\widetilde{\nu}$ [cm^{-1}]
ODT1	532	18797
Yb MOT	556	17992
Rb MOT	780	12817
ODT2	1064	9398
CO_2	10000	1000

Table 2.3: Energy levels for single Rb and Yb atoms. Data from the NIST atomic spectra database at *http://physics.nist.gov/PhysRefData/ASD/*. Labeling of states follows the conventions for alkalis, with the number on the left indicating the principal quantum number of the last orbital occupied. For brevity, only levels that might actually be populated at a minimum wavelengths of 532 nm from either the ground state or the excited states used in photoassociation have been listed in Rb. Wavelengths of several lasers related to the optical trapping of molecules are given for comparison.

Chapter 3

Review of Molecular Physics

The following chapter gives an overview of molecular wavefunctions and how to separate them into more easily understood parts. It also discusses the approximations required to do so.

3.1 Wavefunctions

Molecular states, just like their atomic equivalents, are described by the Schrödinger equation. However, the presence of several nuclei and their interactions complicate matters considerably. Fortunately it is possible to separate the wavefunction into several more easily understood parts. The following will give an overview of this process and the approximations involved. It follows the somewhat simplified reasoning in Haken and Wolf (1998). For a more rigorous treatment, see Brown and Carrington (2003).

The full Schrödinger equation for a diatomic molecule with a single electron is

$$\begin{aligned} \Big\{ -\frac{\hbar^2}{2m_0}\triangle - \frac{\hbar^2}{2m_1}\triangle_1 - \frac{\hbar^2}{2m_2}\triangle_2 - \frac{e^2}{4\pi\epsilon_0|R-R_1|} \\ - \frac{e^2}{4\pi\epsilon_0|R-R_2|} + \frac{e^2}{4\pi\epsilon_0|R_1-R_2|} \Big\} \Psi(R,R_1,R_2) = E\,\Psi(R,R_1,R_2). \end{aligned} \tag{3.1}$$

The first three terms deal with the kinetic energies, with the first Laplace-operator $\triangle$ acting on the electronic coordinate R, while $\triangle_1$ and $\triangle_2$ act on the nuclear coordinates R_1 and R_2 respectively. m_0, m_1 and m_2 are the masses of the electron and the two nuclei respectively. The next three terms deal with the Coulomb interaction of the electron with nucleus 1, with nucleus 2 and finally that between the two nuclei.

The first separation is made possible by realizing that the electrons move much faster than the nuclei due to their smaller mass. On the time scale of the nuclear movement, the electronic part of the wavefunction can be assumed to adapt to the position of the nuclei instantaneously. This is known as the Born-Oppenheimer approximation.

The wavefunction can then be split into the product

$$\Psi(R,R_1,R_2) = \psi(R,R_1,R_2)\cdot\Phi(R_1,R_2) \tag{3.2}$$

where only the electronic part ψ depends explicitly on the electronic coordinate, while the effect of the electronic attraction/repulsion on the nuclear part Φ will take the form of an additional energy term that only depends on the nuclear coordinates R_1 and R_2. Inserting the new wavefunction into the Schrödinger equation yields

$$\begin{aligned}
&\Phi\Big\{-\frac{\hbar^2}{2m_0}\triangle-\frac{e^2}{4\pi\epsilon_0|R-R_1|}-\frac{e^2}{4\pi\epsilon_0|R-R_2|}\Big\}\psi\\
&+\psi\Big\{-\frac{\hbar^2}{2m_1}\triangle_1-\frac{\hbar^2}{2m_2}\triangle_2+\frac{e^2}{4\pi\epsilon_0|R_1-R_2|}\Big\}\Phi\\
&-\frac{\hbar^2}{m_1}(\nabla_1\psi)\nabla_1\Phi-\frac{\hbar^2}{m_2}(\nabla_2\psi)\nabla_2\Phi-\frac{\hbar^2}{2m_1}\Phi\triangle_1\psi-\frac{\hbar^2}{2m_2}\Phi\triangle_2\psi\\
&=E\,\psi\,\Phi \qquad . \qquad (3.3)
\end{aligned}$$

Here the operators in the first line are acting on the electronic wavefunction, the operators in the second line act on the nuclear wavefunction, while the third line contains the remaining mixed terms. These are found to be on the order of $m_0/m_{1,2}$ compared to the other terms and will be neglected in the following.

Holding the nuclei fixed at positions R_1 and R_2, the electronic wavefunction must fulfill the Schrödinger equation

$$\Big\{-\frac{\hbar^2}{2m_0}\triangle-\frac{e^2}{4\pi\epsilon_0|R-R_1|}-\frac{e^2}{4\pi\epsilon_0|R-R_2|}\Big\}\psi=W\psi \qquad . \qquad (3.4)$$

There will generally be many solutions with different energy eigenvalues, each of which can be characterized by a set of quantum numbers X. Due to the isotropy of space, the energy values depend only on the relative position $\Delta R=R_1-R_2$ of the nuclei. Therefore $W=W(X,\Delta R)$. The left part of the equation is identical to the main term on the first line of equation 3.3 and replacing it yields (neglecting the mixing terms)

$$\Phi\ W(X,\Delta R)\ \psi+\psi\Big\{-\frac{\hbar^2}{2m_1}\triangle_1-\frac{\hbar^2}{2m_2}\triangle_2+\frac{e^2}{4\pi\epsilon_0|R_1-R_2|}\Big\}\Phi=E\ \psi\ \Phi. \qquad (3.5)$$

The electronic wavefunction ψ now only appears in multiplication with scalar values and can be removed from the equation by division. This gives a new Schrödinger equation for the movement of the nuclei where the electronic energy term W simply adds to the potential:

$$\Big\{-\frac{\hbar^2}{2m_1}\triangle_1-\frac{\hbar^2}{2m_2}\triangle_2+\overbrace{\underbrace{\frac{e^2}{4\pi\epsilon_0|R_1-R_2|}}_{\text{Coulomb part}}+\underbrace{W(X,\Delta R)}_{\text{electronic part}}}^{\text{effective potential}}\Big\}\Phi=E\ \Phi. \qquad (3.6)$$

The sum of the Coulomb interaction and the distance-dependent electronic energy forms an effective potential. Since this potential is only valid if the changes of the nuclear coordinates are slow compared to the changes of the electronic wavefunction, it is called the adiabatic potential and has the form

$$V(X,\Delta R)=\frac{e^2}{4\pi\epsilon_0|R_1-R_2|}+W(X,\Delta R) \qquad . \qquad (3.7)$$

A discussion of the quantum numbers describing the various eigenfunctions follows in the next section.

Equation 3.6 can be further simplified by a transformation to a center of mass coordinate R_{cm} and the relative coordinate $\Delta R = R_1 - R_2$:

$$\left\{ -\frac{\hbar^2}{2m_{\mathrm{cm}}} \triangle_{\mathrm{cm}} - \frac{\hbar^2}{2\,\mu} \triangle_r + V(X, \Delta R) \right\} \tilde{\Phi} = E\ \tilde{\Phi} \tag{3.8}$$

$$\text{with the total mass} \qquad m_{\mathrm{cm}} = m_1 + m_2 \tag{3.9}$$

$$\text{and the reduced mass} \qquad \mu = \frac{m_1\ m_2}{m_1 + m_2} \quad . \tag{3.10}$$

Here $\triangle_{\mathrm{cm}}$ acts on the center-of-mass coordinate R_{cm} and $\triangle_r$ acts on ΔR. Now the wavefunction can be split into a part $\tilde{\Phi}$ describing the relative movement of the nuclei and a part for the movement of the center of mass. When the resulting form

$$\tilde{\Phi}(R_{\mathrm{cm}}, \Delta R) = e^{iKR_{\mathrm{cm}}} \chi(\Delta R) \tag{3.11}$$

is put into the Schrödinger equation, the energy eigenvalues take on the form

$$E = \tilde{E} + \frac{\hbar^2 K^2}{2\, m_{\mathrm{cm}}} \tag{3.12}$$

where $\tilde{E}$ is the energy from the relative motion of the nuclei. By switching to a system of coordinates centered on the molecule's center of mass, R_{cm} and the corresponding energy term become zero. The remaining energy term depends only on the absolute value of the internuclear distance $r = |\Delta R|$ and not on its direction. In close analogy to the well-known hydrogen problem, the wavefunction can be separated again into a radial part $f(r)$ and an angle-dependent part $F(\theta, \phi)$:

$$\chi(\Delta R) = f(r) \cdot F(\theta, \phi) \tag{3.13}$$

This gives us the new Schrödinger equation

$$\left\{ -\frac{\hbar^2}{2\,\mu} \frac{1}{r^2} \frac{\partial}{\partial r} \left(r^2 \frac{\partial}{\partial r} \right) + \frac{\mathbf{L}^2}{2\,\mu\, r^2} + V(X, r) \right\} fF = \tilde{E} fF \tag{3.14}$$

where $\mathbf{L}$ is the angular momentum operator. The eigenfunctions of this operator are described by the quantum numbers L (describing total angular momentum) and M (describing its projection onto a chosen direction) such that

$$\mathbf{L}^2\ F_{L,M} = \hbar^2\, L(L+1)\, F_{L,M} \tag{3.15}$$

$$\mathbf{L_p}\ F_{L,M} = \hbar\, M\, F_{L,M} \tag{3.16}$$

For a given rotational quantum number L=0,1,2,... the projection quantum number M can take any integer number from $-L$ to $+L$.

Using equation 3.15 to replace $\mathbf{L}$ in equation 3.14 leads to

$$\left\{ -\frac{\hbar^2}{2\,\mu} \frac{\partial^2}{\partial r^2} - \frac{\hbar^2}{\mu} \frac{1}{r} \frac{\partial}{\partial r} + \frac{\hbar^2 L(L+1)}{2\,\mu\, r^2} + V(X, r) \right\} f = \tilde{E} f. \tag{3.17}$$

The second term is small compared to the leading kinetic energy term. For low vibrational states this can be shown by approximating the potential as harmonic around the equilibrium position:

$$V(R) \approx V(R_e) + 0.5\,k\,(R - R_e)^2 \tag{3.18}$$

The eigenfunctions for a harmonic potential are the Hermite functions. The effect of the second term can then calculated directly. The kinetic energy term in equation 3.17 will be on the order of the total vibrational energy $E_{\text{vib}} = (\text{v} + \frac{1}{2})\,\hbar\omega = (\text{v} + \frac{1}{2})\,\hbar\sqrt{k/\mu}$ (v is the vibrational quantum number), which is considerably larger. This can be shown more rigorously by transforming to the Eckart frame of reference (Eckart, 1935), where rotation and vibration decouple completely as long as the internuclear distance stays close enough to the equilibrium distance. Without the second term the Schrödinger equation becomes

$$\Big\{ - \frac{\hbar^2}{2\,\mu}\frac{\partial^2}{\partial r^2} + \underbrace{\frac{\hbar^2 L(L+1)}{2\,\mu\,r^2} + V(X,r)}_{\text{combined potential U(r)}} \Big\} f = \tilde{E} f \tag{3.19}$$

and takes on the familiar form for a mass moving in a combined potential U(r), the shape of which depends on the electronic and rotational state. Although the final approximation is not necessarily valid for molecules created by photoassociation as they tend to be in highly excited vibrational states, this is a very useful result nevertheless as it nicely explains the features observed in molecular spectra. The following sections will explore this in more detail.

3.1.1 Electronically Mediated Potentials

When two atoms are brought close enough together, they will begin interacting. At large distances of 20 Bohr radii or more, the electronic structure of each atom will still be essentially unchanged. The interaction is limited to Van-der-Waals interactions and, more specifically, the induced dipole-dipole forces also known as London dispersion forces. These are created by a short-lived spontaneous electric dipole moment in one atom creating a matching dipole moment in the other, leading to an attractive force.

It can be shown that the resulting potential goes to zero as C_6/r^6 for large interatomic distances r. The coefficients describing behavior of the form C_n/r^n are collectively called dispersion coefficients. For specific electronic states, e.g. when both atoms are in an electronic P state, the potential can be slightly longer-ranged and the leading dispersion coefficient will be C_5 (Marinescu and Sadeghpour, 1999). If both atoms are identical and one of them starts in an excited state, then the quantum-mechanical superposition with the state where the other atom is in the excited state and the first is in the ground state causes a much longer-ranged potential that is described by a C_3 coefficient. This leads to considerable differences in behavior of homonuclear and heteronuclear molecules in photoassociation experiments.

At closer ranges the electronic wavefunctions will change in reaction to the presence of the second nucleus. This makes calculations of the resulting potential $V(X, r)$ more complicated, but with the rapid growth of available computing power solving these complicated problems has become possible by using self-consistent Hartree-Fock methods or their continuously refined successors (such as coupled cluster, configuration interaction, Dirac-Fock or multi-configurational self-consistent field methods). Calculating the the possible electronic configurations for different internuclear distances gradually creates potential curves for each configuration X. This is still not a simple task and very time consuming.

Thanks to the work of Fleig (2008), the first ab-initio potential curves are now available for the YbRb molecule. At this point they do not yet agree with the known limiting case of separated atoms. More precise calculations are in progress and the available potentials should already represent the shape and features of the real potentials quite nicely, especially at shorter internuclear distances. Figure 3.1 shows the latest available data.

3.1.2 Molecular Electronic States

One important change when moving from atoms to molecules is the breaking of the complete rotational symmetry by the presence of the second nucleus. In this case L and S (and their per-electron equivalents ℓ and s) are not strictly good quantum numbers any more.

However, a diatomic molecule still has a remaining symmetry for rotation around the the internuclear axis. This causes the projection of angular momentum to this axis to be conserved. The molecular equivalents of the atomic projection quantum numbers (like m_L, m_S and m_J) are Λ for the projection of the sum orbital momentum, Σ for the projection of the summed spin and Ω for the projection of the combination of the first two.

The total energy of the electrons moving in the electric field of the two nuclei, which are assumed to be fixed in space for now, does not depend on the direction of their rotation. Reversing the movement of all electrons turns each m_ℓ into $-m_\ell$ and the sum m_L into $-m_L$, but does not change the energy of the state. Because there is now no spectroscopical distinction between the two possibilities, m_L and $-m_L$ are both grouped into one state $\Lambda = |m_L|$. Depending on the value of Λ, the resulting molecular electronic state is then called Σ (for $\Lambda = 0$), Π (for Λ=1), Δ (for $\Lambda = 2$) and so on.

Rotation of the molecule can lift this degeneracy and the energy levels with $\Lambda > 0$ will split into their two components. This is called Λ-type doubling.

Depending on the strength of the couplings between the angular momenta, not all the quantum numbers mentioned above are useful at all times. The molecules formed in the experiments described here spent most of their time at large interatomic distances. Under these circumstances the second atom sometimes forms nothing but a minor disturbance, and although the atomic quantum numbers are no longer good quantum numbers, they still offer a good description of the molecular state.

3.1.3 Hund's Cases

To describe the molecules at closer ranges it is helpful to look at the different cases of angular moment coupling that were first assembled and compared by Hund (Hund, 1926). This section will only provide a short overview, for a more complete description see Herzberg (1950) or Brown and Carrington (2003).

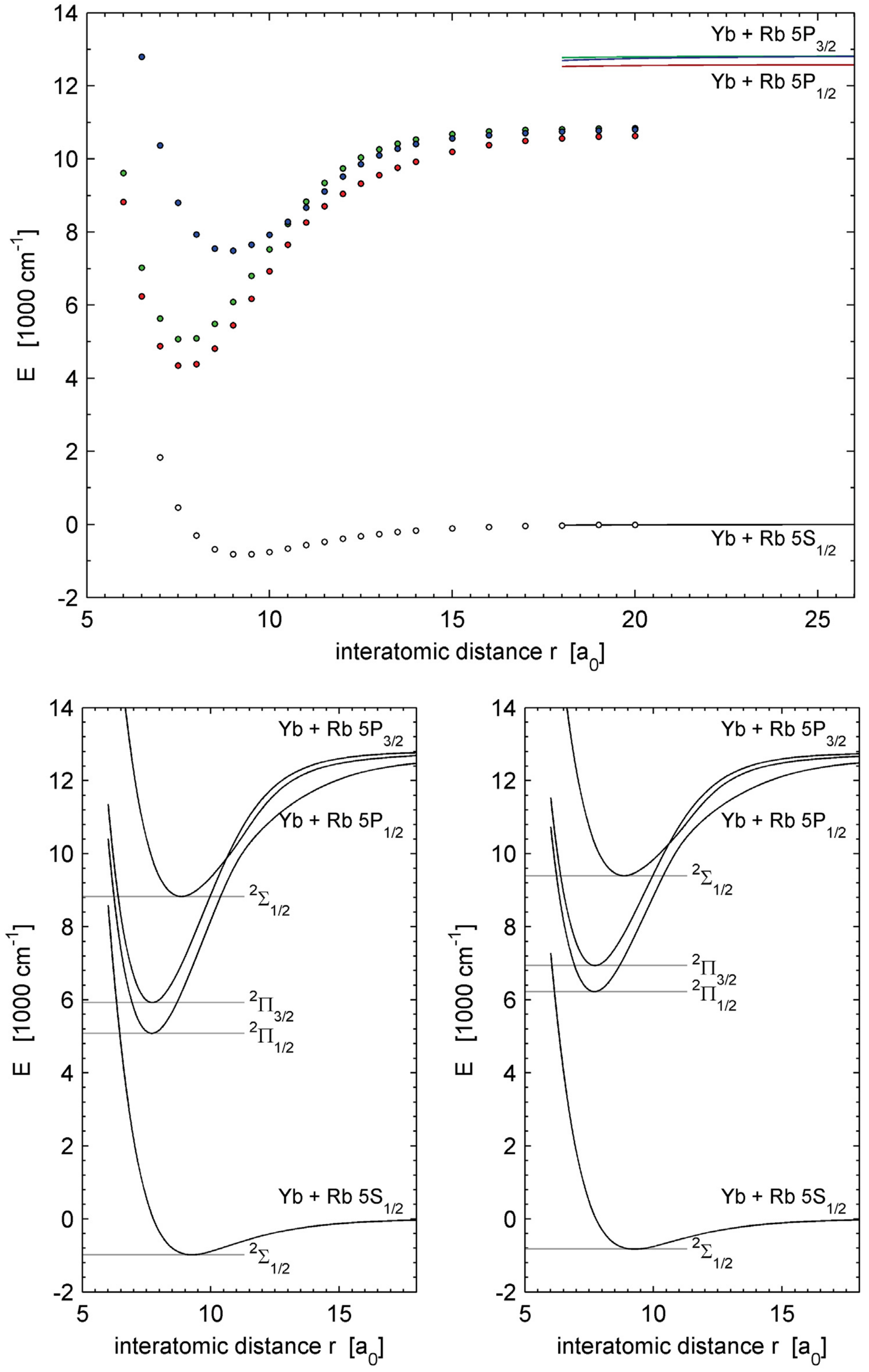

Figure 3.1: **(top)** Current state of the ab-initio potential curves for the YbRb molecule (Fleig, 2008). Energy is given in wavenumbers relative to the atomic ground states, interatomic distance in Bohr radii.
(bottom) Adaptation of the datapoints to match the single atom states by either scaling all energies (left) or shifting the upper potentials (right). States are labeled according to the convention described in chapter 3.1.3 and additionally with the states of the rubidium atom for large internuclear separation. All potential curves converge on the 6^1S_0 state for ytterbium.

coupling case (a)

If the coupling of the electronic orbital angular momentum $\overrightarrow{L}$ to the internuclear axis is very strong, the angular momentum vector will quickly precess around this axis. The spin vector $\overrightarrow{S}$ then couples to the effective field resulting from this, and therefore indirectly to the internuclear axis as well. The projections $\overrightarrow{\Lambda}$ and $\overrightarrow{\Sigma}$ add to form $\overrightarrow{\Omega}$ which couples to the molecular rotation vector $\overrightarrow{R}$, forming the total angular momentum vector $\overrightarrow{J}$. See figure 3.2 for a graphical representation. States are usually labeled $^{2S+1}$"Λ"$_{\Lambda+\Sigma}$, with the value for "Λ" written as Σ, Π, Δ and so on.
Condition: strong coupling of L to the internuclear axis.
Good quantum numbers: Λ, S, Σ, J, Ω

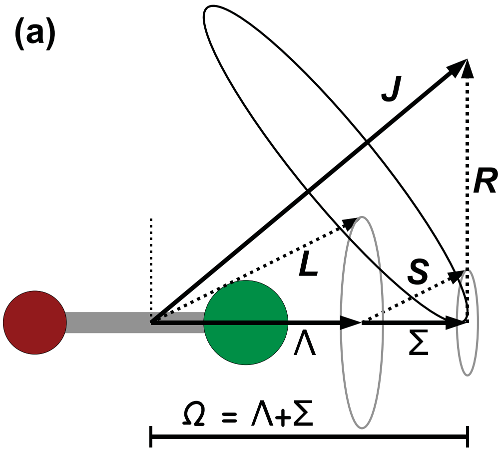

Figure 3.2: Hund's case (a). Electronic orbital and spin angular momentum are projected onto the internuclear axis to form Λ and Σ. Their sum Ω then couples to the molecular rotation. Solid arrows indicate momenta described by good quantum numbers.

coupling case (b)

If the spin-orbit coupling is weak, which can happen in light molecules, then $\overrightarrow{L}$ will couple to the internuclear axis as before, but the resulting $\overrightarrow{\Lambda}$ will couple to the molecular rotation $\overrightarrow{R}$ first and form a resulting angular momentum $\overrightarrow{N}$. Only in the last step does this couple with $\overrightarrow{S}$ to form the total angular momentum $\overrightarrow{J}$. See figure 3.3. Similar effects occur when $L = 0$.
Conditions weak spin-orbit coupling
Good quantum numbers: Λ, N, S, J

coupling case (c)

The opposite happens if the spin-orbit coupling is very strong, as sometimes found in heavy molecules. In this case $\overrightarrow{L}$ and $\overrightarrow{S}$ will couple to form a total electronic angular momentum $\overrightarrow{J_a}$ which then precesses rapidly around the internuclear axis. The resulting projection $\overrightarrow{\Omega}$ then couples to the molecular rotation $\overrightarrow{R}$, forming $\overrightarrow{J}$. See figure 3.3.

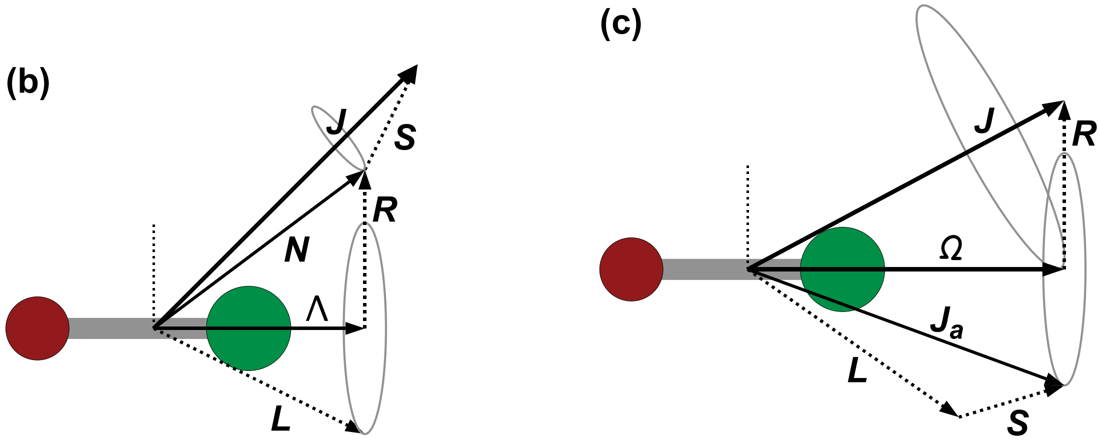

Figure 3.3: Hund's case (b) occurs when the spin-orbit coupling is weak compared to the other interactions and case (c) occurs when it is very strong.

Condition: strong spin-orbit coupling
Good quantum numbers: Ω, J

coupling case (d)

Effects like a polar moment on a rotating molecules can cause the electronic orbital angular momentum $\overrightarrow{L}$ to couple to the molecular rotation $\overrightarrow{R}$ instead of the internuclear axis. See figure 3.4.
Conditions: coupling mechanism between molecular rotation and electron orbit
Good quantum numbers: L, R, N, S, J

coupling case (e)

When a strong spin-orbit interaction couples $\overrightarrow{L}$ and $\overrightarrow{S}$ to form $\overrightarrow{J_a}$ before this couples to the molecular rotation, we have coupling case (e). See figure 3.4.
Conditions: coupling of molecular and electronic rotation, strong spin-orbit interaction
Good quantum numbers: J_a, R, J

3.1.4 Nuclear Spin

The nuclear spin has so far been neglected. Depending on the strength of the hyperfine coupling, it can take effect at various points in the coupling scheme, dividing Hund's cases onto subcases. An attempt to classify these subcases has been made in Dunn (1972). Since the hyperfine effects are fairly straightforward in the results presented later, they will be explored only where necessary and the subclasses will not be presented here.

3.1.5 Transitions between Cases and Effects on Spectra

It is important to note that Hund's cases only present an approximation and useful description of the actual molecular state. When looking at the case of two atoms at a large

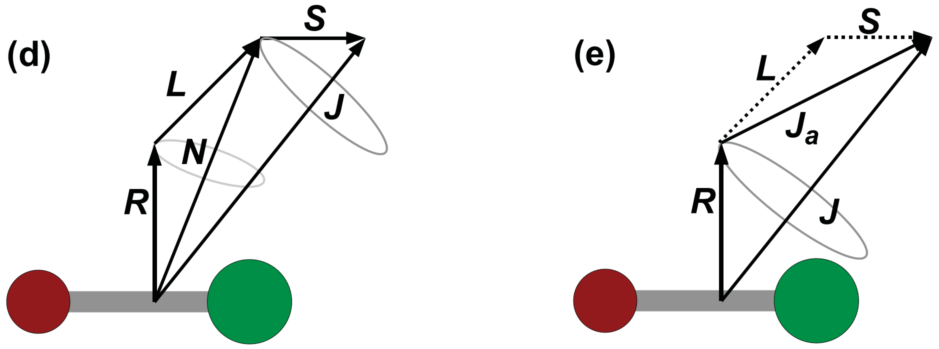

Figure 3.4: Hund's cases (d) and (e) occur when there is a coupling of electronic angular momentum to the rotational (instead of the internuclear) axis of the molecule. In case (d) the orbital angular momentum couples to the rotation more strongly than to the electronic spin, while in case (e) spin and orbital angular momentum form a resultant J_a first, which then couples to the rotation.

distance moving closer together, the presence of atom A will obviously have a growing effect on atom B. This will gradually change the strengths of the interactions between the various momenta, leading to a transition between different states that occurs just as gradually. Herzberg (1950, chapter V.2) goes into more detail on this.

Since the photoassociation experiments described in this thesis form molecules in states where the two nuclei are far apart most of the time, the coupling of electronic momentum to the internuclear axis is quite weak, especially since the ytterbium atom is in an $F = 0$ state that exerts very little force on the rubidium atom. Together with the strong spin-orbit coupling found in the excited rubidium atom this leads to an angular momentum coupling best described by case (e). Evidence for this is the splitting of the rotational lines into a number of subcomponents corresponding to the possible relative alignments of the molecular angular momentum vector to the resultant of all other angular momenta, as shown in the spectra in chapter 6.3. This can not happen in cases (a) to (c) where the time averaged values for $\overrightarrow{L}$ and $\overrightarrow{S}$ are always orthogonal to $\overrightarrow{R}$.

Looking at the calculated potentials for the excited states in figure 3.1, it is also clear that at interatomic distances $r \lesssim 11\,a_0$ the Π states have the lowest energies. This shows that the coupling to the internuclear axis is even stronger than the spin-orbit interaction, indicating coupling case (a).

It is likely that there is a region between the innermost and outermost part of the potential where the molecular state is best described by case (c) as the coupling to the internuclear axis becomes weaker than the spin-orbit interaction. (See also the next section.)

These transitions between coupling cases should be observable directly in the molecular spectra for more deeply bound molecules. For example, a rotational series with a progression of energies in the form $E_{\text{rot}} = B_{\text{rot}} X(X+1)$ will appear for all cases. This will be $E_{\text{rot}} = B_{\text{rot}} R(R+1)$ when R is a good quantum number, but this is not true for case (a) and (c), and in case (b) it would require $\Lambda = 0$. Otherwise the total angular momentum number J will take the place of R. Since its main constituents $\overrightarrow{\Lambda}$ and $\overrightarrow{R}$ are at right angles to each other, there is often no combination that will give $J = 0$ or other low numbers and the rotational series will then miss the first few lines. Similarly, the inclusion of $\overrightarrow{S}$ can lead to a series consisting of half-integer values. Both of these cases are obvious from the rotational progression, even if the rotational constant B_{rot} is initially unknown.

3.1.6 Avoided Crossings and Diabatic Potential Curves

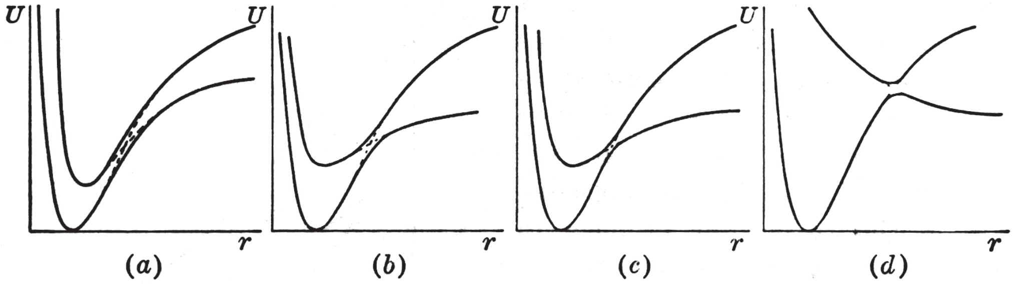

Figure 3.5: Avoided crossings of potentials can have dramatic effects if their shapes differ substantially. Figure taken from Herzberg (1950).

When two potential curves get close to each other, they often show what is known as an avoided crossing. Understanding the perturbations this adds to molecular spectra has always been a major challenge (Herzberg, 1950, chapter V.4).

We will assume that the progression of unperturbed eigenfunctions and energies is known for both of the crossing states. It is found that the proper eigenfunctions in the area where the energies are near-degenerate are mixtures of both unperturbed eigenfunctions. The reason is a breakdown of the Born-Oppenheimer approximation under these circumstances (Smith, 1969). This results in one state with an energy that is higher than both of the unperturbed values and one state with an energy that is lower, creating the appearance that the two curves repel each other. There is no crossing since one energy curve connects the higher states to the left and the right of the crossing, while another connects the lower ones. Potentials that take these crossings into account are called diabatic potentials to differentiate them from calculations that fully depend on the adiabatic Born-Oppenheimer approximation and yield incorrect curves that cross.

If a molecule crosses the range of interatomic distances where the avoided crossing occurs, it will generally follow either the lower curve or the higher curve changing from a state described by one series of unperturbed eigenfunctions to another. This can dramatically change the effective potential curves, particularly when the unperturbed curves converge on atomic states with notably different energies as illustrated in figure 3.5.

An avoided crossing is seen in the potential curves in figure 3.1 between the excited $\Sigma_{1/2}$ and $\Pi_{1/2}$ states at an internuclear distance of $r \approx 11\, a_0$. Since a physical mechanism is required to transfer the molecules from what would be one molecular state to another without violating conservation laws, only certain states are compatible and will show avoidance of crossings. The states where this happens are said to be "of the same species". For the coupling cases (a) and (b), which are the most common in normal molecular spectroscopy, this requires the states to have the same symmetry and the same value for Λ.

This is obviously not the case in the diagram, as the curves attributed to $\Sigma_{1/2}$ ($\Lambda = 0$) and $\Pi_{1/2}$ ($\Lambda = 1$) show an avoided crossing, while there is no perturbation when $\Sigma_{1/2}$ crosses $\Pi_{3/2}$. This is due to the fact that in this region of the potential the spin-orbit interaction is stronger than the coupling between orbital angular momentum and molecular axis as demonstrated by the energy difference between the $\Pi_{1/2}$ and the $\Pi_{3/2}$ curves. The best description of the coupling case is then Hund's case (c) where Λ is not a good quantum number and Ω becomes the quantum number to classify species.

3.2 Vibration

Each electronic configuration creates a different potential curve over the possible internuclear distances r. If the interaction is attractive, the potential can have bound states, generally many of them. The corresponding nuclear wavefunctions can be found by solving the Schrödinger equation of equation 3.19 numerically. Several model wavefunctions are shown in figure 3.6. While some scaling was done and the energies and vibrational levels are therefore not correct solutions, the general shape of the wavefunctions is accurate. It is clear to see that the lowest vibrational states resemble those of the harmonic oscillator, while for higher vibrational states the asymmetry of the potential leads to a wavefunction that is also asymmetric. Each wavefunction has a number of nodes corresponding to its vibrational quantum number v.

An effect that will become important later can be seen at the classical outer points. At these points the potential energy is equal to the total energy of the vibrational state and the curvature of the wavefunction is necessarily zero. Due to the gradual change of potential, the difference between potential curve and the total energy (and therefore the curvature) remains small nearby. This leads to the outer lobes being more pronounced than those in regions of stronger potential and corresponds to the higher likeliness of finding a classical harmonic oscillator near its turning points.

The potential changes more slowly at the outer turning point and for high vibrational levels near the last bound state, the wavefunction extends into a region where the potential is very nearly flat. This can cause a considerable fraction of the total probability amplitude to be concentrated in the last outer lobe.

The energies and eigenfunctions near the bottom of the potential well can be calculated quite accurately and traditionally harmonic approximations of the potential plus some correction terms have been used to great effect in the explanation of molecular spectra. However, Photoassociation spectroscopy accesses the range of highly excited vibrational states. This makes all calculations extremely sensitive to even small changes of the potential and it is nearly impossible to obtain accurate predictions for the energies of the last few levels relative to the dissociation energy.

Fortunately, the semi-analytical approximation presented in LeRoy and Bernstein (1970) predicts systematics that help in interpreting the observed vibrational lines in this range. More detail on this will be given in chapter 6.4.4 when dealing with the actual spectra.

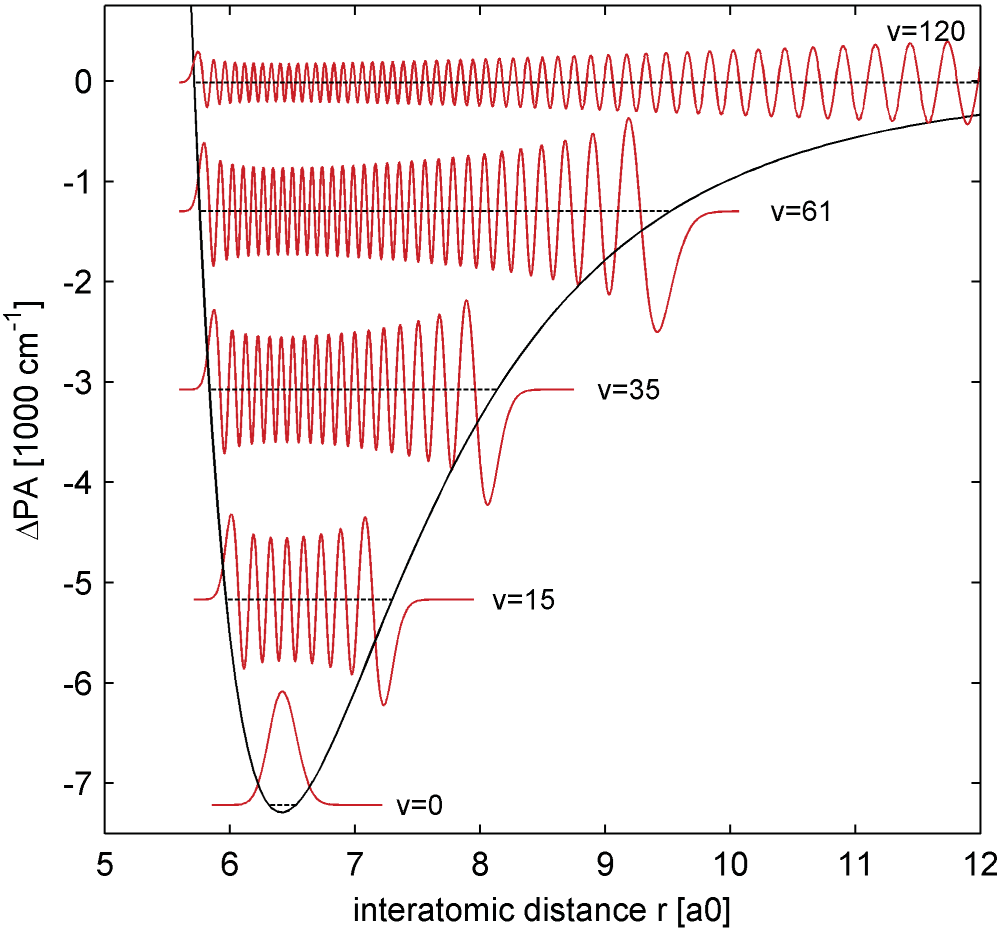

Figure 3.6: Nuclear wavefunctions in a model potential for a selection of vibrational levels. Exact energies and vibrational quantum numbers are not supposed to be accurate for the actual potential of the YbRb* molecule.

3.3 Rotation

3.3.1 Rotational Constant

The vibrational wavefunctions also have a strong effect on the rotational spectrum. Looking back to equation 3.19, this is created by the part

$$E_{\mathrm{rot}} = \frac{\hbar^2\, J(J+1)}{2\,\mu\, r^2} \qquad . \tag{3.20}$$

The constants are usually absorbed into a rotational constant B_{rot}

$$B_{\mathrm{rot}} = \frac{\hbar^2}{2\,\mu\, r^2} \qquad \text{such that} \qquad E_{\mathrm{rot}} = B_{\mathrm{rot}}\, J(J+1) \qquad . \tag{3.21}$$

In the rigid rotor approximation the wavefunction is assumed to be concentrated in a single point and this is simply the quantum mechanical version of the classical rotational energy

$$E_{\mathrm{cl}} = \frac{L^2}{2\Theta} = \frac{1}{2}\Theta\,\omega^2 \tag{3.22}$$

where $L = \Theta\,\omega$ is the angular momentum and $\Theta = \mu\, r^2$ is the moment of inertia of a rigid rotor with a reduced mass μ and a spacing between masses of r.

For low vibrational states it makes sense to assume that the internuclear distance does not deviate much from the equilibrium distance r_e that corresponds to the bottom of the potential well. The energy spacing of the rotational lines can then be used to measure r_e directly.

For higher vibrational states the nuclei become less localized and near the dissociation limit the wavefunction becomes spread out over a large range of distances. This can be dealt with by averaging over the internuclear distances, weighting each data point with the local probability amplitude to calculate the moment of intertia

$$\Theta = \mu\, r_{\mathrm{eff}}^2 = \mu \int_0^\infty f(r)^2 r^2 dr \qquad . \tag{3.23}$$

This defines an effective internuclear distance r_{eff}

$$r_{\mathrm{eff}} = \sqrt{\frac{\Theta}{\mu}} = \frac{\hbar}{\sqrt{2\mu\ B}} \qquad , \tag{3.24}$$

which is a good description of the system since the vibrational processes happens at much shorter time scales than the molecular rotation.

3.3.2 Rotation in Photoassociation Spectroscopy

Rotationally resolved spectroscopy usually measures the energy differences between two states, both with their own rotational energies. When the photon angular momentum can only interact with molecular rotations (e.g. in $\Sigma \rightarrow \Sigma$ transitions), selection rules only allow a change of angular momentum according to $\Delta J = \pm 1$, leading to two series of equally spaced lines in this case. This is explained in any book on molecular spectroscopy, such as Haken and Wolf (1998) or Herzberg (1950).

Photoassociation spectroscopy utilizes a free-bound transition. Although the initial state already carries angular momentum based on the motion of the separated atoms, the rotational energy is effectively zero as r is large. The total energy then remains unchanged as the atoms move closer together, with the increasing rotational energy supplied by the attractive potential. For this reason the spectra directly show the rotational energies of the molecular state, making them quite simple to identify due to the characteristic energy sequence proportional to $J'(J'+1)$, where J' is the excited state rotational quantum number. It is worth pointing out that higher rotational states are populated without violating conservation of angular momentum because photoassociation to a state with a specific J' is possible if the angular momentum of the unbound atoms J_{at} already is $J'-1$, J' or $J'+1$ and the photon provides a maximum of $\pm\hbar$ to the angular momentum. The process is therefore based on selection, not transfer: A molecular state with e.g. $J'=4$ can only be formed if an unbound atom pair with an angular momentum $J_{\mathrm{at}} \geq 3$ approaches closely enough while the photoassociation laser is active.

$\Delta J = 0$ transitions are allowed in the investigated case, as momentum conservation can be satisfied by the photons interacting with the electronic angular momentum. In fact, since this interaction is required for the creation of molecules at the investigated energies, any change of the angular momentum of the rotation of the whole molecule can only happen due to its coupling to the electronic angular momentum. Without this, an incident photon will leave the molecular rotation unchanged.

The assumption of weak coupling is appropriate for the experiments presented here, where the coupling is best described by Hund's case (e) and the coupling of the internal angular momentum F' to the R' is directly observed to be small compared to all other interactions, including the hyperfine structure. It is therefore expected that the majority of photoassociation events occur with $\Delta R = 0$.

3.4 Photoassociation

Photoassociation is the formation of molecules from unbound atoms by using light.

Under normal circumstances, two atoms in a conservative, attractive interatomic potential will simply pass each other and separate again. Entering a bound state will either require dissipation of some of the kinetic energies or an increase in the depth of the potential.

3.4.1 Switching Potentials

In photoassociation, the mechanism for this is provided by photons. The photonic momentum p_{ph} is too small to slow down the moving atoms considerably:

$$p_{\mathrm{at}} = \sqrt{3\, m_{\mathrm{at}} k_B T} \qquad \Longrightarrow \qquad 2.4 \cdot 10^{-26}\, \frac{\mathrm{kg\,m}}{\mathrm{s}} \qquad \text{is much larger than} \tag{3.25}$$

$$p_{\mathrm{ph}} = \frac{h}{\lambda} \qquad \Longrightarrow \qquad 8.3 \cdot 10^{-28}\, \frac{\mathrm{kg\ m}}{\mathrm{s}} \qquad . \tag{3.26}$$

The examples given are for ^{87}Rb at a temperature of 100μK and a photon with a wavelength of 795 nm.

However, the photon can provide the necessary energy and angular momentum to change the electronic state. This can lead to a situation where the two atoms move towards each other, gaining kinetic energy from the attractive potential. At some point inside the potential, an incident photon switches the electronic state to one that provides a deeper potential. This leaves the kinetic energy unchanged except for the small change caused by the photon, but the new, deeper potential well means that the atoms cannot escape again. A bound state is formed, the two atoms have been photo-associated. Figure 3.7 illustrates this process.

In this diagram the initial kinetic energy of the approaching atoms is exaggerated for clarity. For cold atoms, the average kinetic energy is very small compared to the depth of the potential:

$$E_{\mathrm{at}}^{\mathrm{kin}} = \frac{3}{2} k_B\, T \qquad \Longrightarrow \qquad 2.1 \cdot 10^{-27}\,\mathrm{J} \mathrel{\widehat{=}} 1.0 \cdot 10^{-4}\,\mathrm{cm}^{-1} \tag{3.27}$$

The example values are again given for atoms at a temperature $100\,\mu$K, a realistic value for laser-cooled atoms (Metcalf and van der Straten, 1999). This well-defined starting energy first led to the proposal of photoassociation as a useful spectroscopic method (Thorsheim et al., 1987).

3.4.2 Condon Points

A photon does not change the position of the nuclei when it is absorbed and, as explained above, its low momentum also leaves the kinetic energy of the nuclei effectively unchanged. Any momentum they might have had in the (bound or unbound) molecular ground state will carry over into the excited state. The kinetic contribution to the total energy at the point of the transition is indicated by the red bars in figure 3.7. The wavelength of the photon needs to match the difference in total energy between the two states for the current internuclear distance such that

$$E_e(r) - E_g(r) = h\,\nu = h\frac{c}{\lambda} \tag{3.28}$$

and the kinetic energy remains mostly unchanged. Therefore the energy difference between the potential curves also needs to match the photon energy. The internuclear separation r where this is the case is called the Condon point.

Together with the realization that a particle oscillating in a potential well will spend more time near the turning points, where its kinetic energy is very low, this forms the classical version of the Franck-Condon principle: Among the transitions between electronic states, those that have inner or outer turning points at the same internuclear distance are particularly favored (Condon, 1926).

Although this line of argument relies on a purely classical description of the molecule, it provides a first, intuitive access to the variation of transitions strengths. A quantum mechanical version of the Franck-Condon principle is presented in chapter 6.6.1.

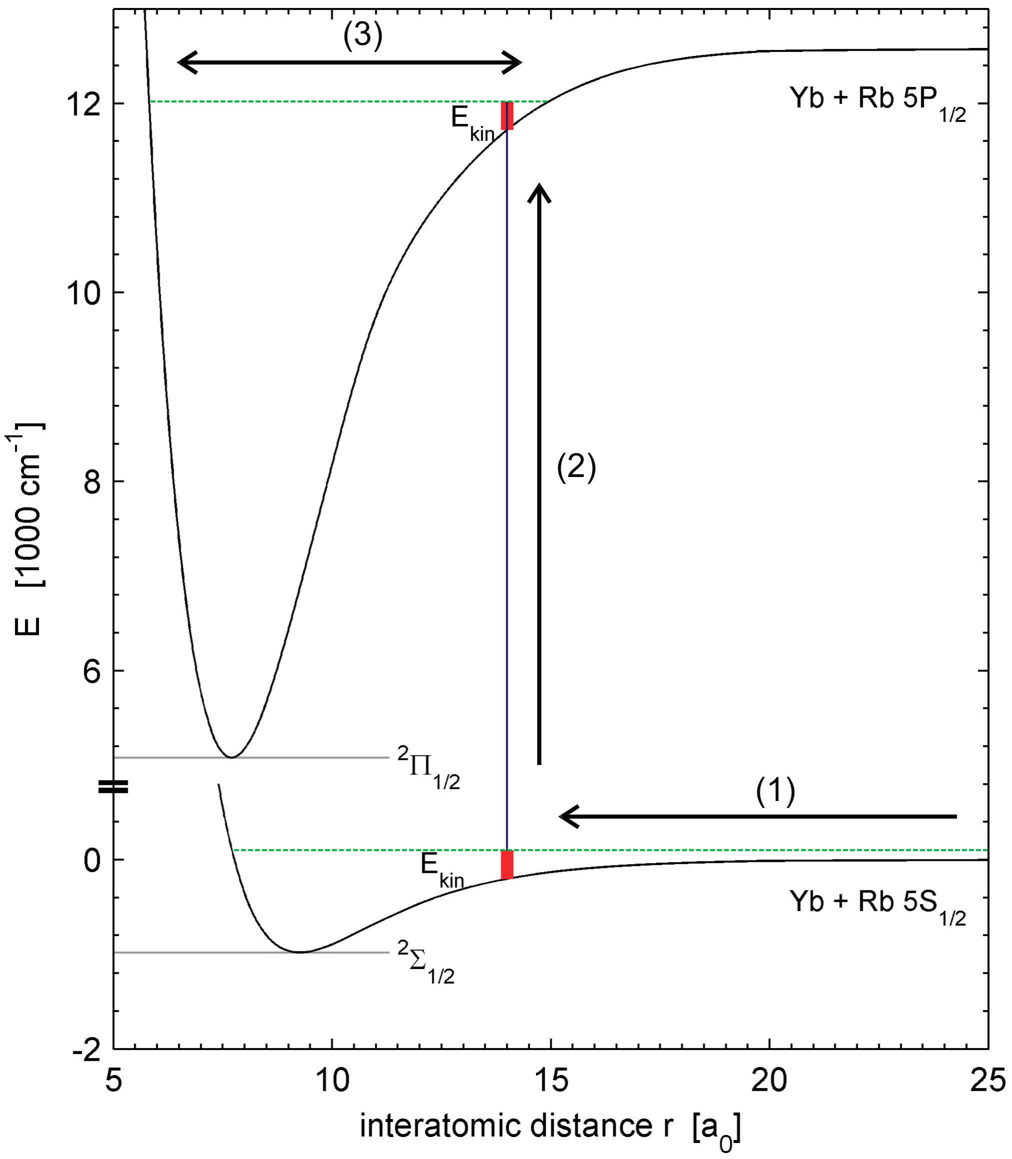

Figure 3.7: Schematic of the photoassociation process. The unbound atoms approach each other in the electronic ground state (1), gaining kinetic energy. A suitable photon then changes the electronic configuration to one with a deeper corresponding potential (2), leaving motion and position of the nuclei essentially unchanged. The result is a vibrating molecule in an excited electronic state (3).

3.4.3 Centrifugal Barriers

The rotational part of the effective potential $U(r)$ in equation 3.19

$$U(r) = U_{\text{rot}}(r) + V(X,r) = \frac{\hbar^2 J(J+1)}{2\,\mu\, r^2} + V(X,r) \tag{3.29}$$

can also be interpreted in a different way. Instead of assuming r to be fixed and simply treating the rotational term as an extra energy contribution, a full analysis also needs to account for the changed shape of the potential. Figure 3.8 illustrates the effects of this.

The additional potential is very weak compared to the electron-mediated attraction. Even for an ytterbium-rubidium molecule at an internuclear distance of $r = 6\,a_0$, less than the inner turning points of the potentials investigated here, U_{rot} is only $0.057\,\text{cm}^{-1}$ for $R = 1$. For significantly higher R, which do occur in thermal ensembles at higher temperatures, U_{rot} becomes strong enough to change the effective potential considerably. Besides changing the energies of the vibrational states, it also shifts the bottom of the nuclear potential well outwards. This affects the nuclear wavefunctions in a way that corresponds to the centrifugal stretching of the molecule expected in a classical theory.

For experiments with ultracold atoms, the rotational part of the potential has the additional effect of suppressing higher rotational states. While the attractive potential is described at long range by the dispersion coefficients and falls of as $1/r^6$ for YbRb* (this becomes $1/r^3$ in homonuclear molecules and certain special cases), the repulsive rotational term goes to zero as $1/r^2$. Thus for any state with $R > 0$ there is an internuclear distance where $|U_{\text{rot}}|$ becomes equal to $|V(X,r)|$. The effective potential then becomes repulsive and goes through a maximum before it starts falling off again. The region around this repulsive maximum is called the centrifugal barrier and in the case of an attractive potential that is described entirely by the C_6 coefficient at long range, its location r_c and height E_c for a given rotational quantum number R can be shown to be (Jones et al., 2006, p. 499)

$$r_c(R) = 2\left(\frac{3}{R(R+1)}\right)^{1/4} r_{\text{vdW}} \tag{3.30}$$

$$E_c(R) = \frac{1}{2}\left(\frac{R(R+1)}{3}\right)^{3/2} E_{\text{vdW}} \qquad . \tag{3.31}$$

r_{vdW} and E_{vdW} contain the specific properties of the atom pair and serve to generalize the results:

$$r_{\text{vdW}} = \frac{1}{2}\left(\frac{2\,\mu\, C_6}{\hbar}\right)^{1/4} \tag{3.32}$$

$$E_{\text{vdW}} = \frac{\hbar^2}{2\,\mu\, r_{\text{vdW}}^2} \tag{3.33}$$

The barrier is present in both the ground and the excited state, but the suppression effect is caused by that in the ground state potential: If the approaching unbound atoms do not have sufficient energy to cross the barrier, they will be repelled before they can reach the Condon point. In heteronuclear molecules only the vibrational states immediately

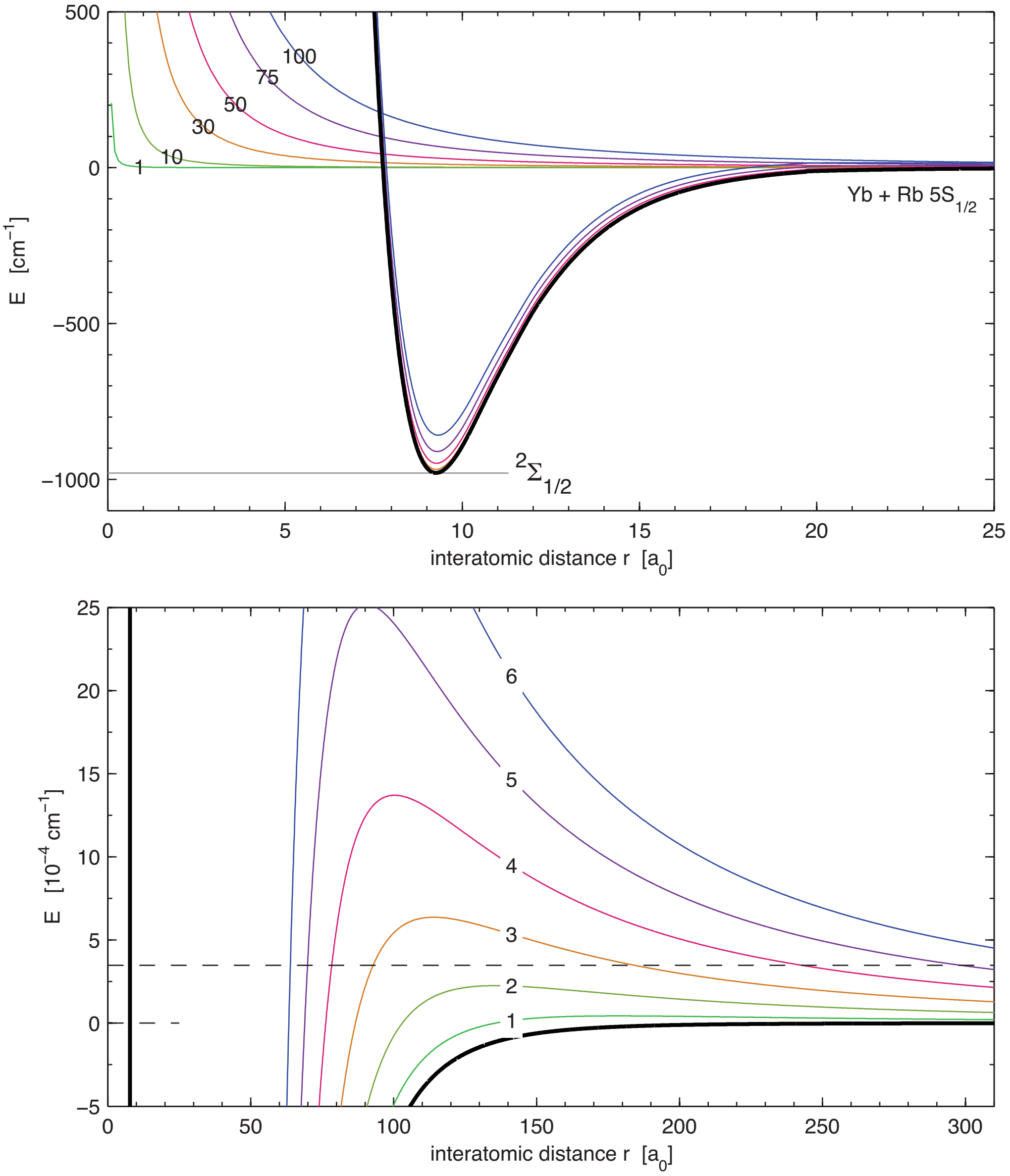

Figure 3.8: Effects of rotation on the nuclear potential.
top Due to the low strength of the rotational potential at normal internuclear distances, only states with very high rotational quantum numbers R (indicated by numbers on the colored curves) show a noticeable change near the bottom of the potential (lower curves). Same colors indicate identical rotational quantum numbers.
bottom Centrifugal barriers at larger internuclear distances. Note the difference in the scale of the energy axis. The dotted line indicates an energy $E = k_B T$ corresponding to a temperature of 500 μK.

R	^{87}Rb + ^{176}Yb r_c $[a_0]$	E_c $[10^{-3}cm^{-1}]$	T_c $[\mu K]$	^{87}Rb + ^{174}Yb r_c $[a_0]$	E_c $[10^{-3}cm^{-1}]$	T_c $[\mu K]$
0		no barrier			no barrier	
1	178.4	0.043	62.4	178.3	0.044	62.7
2	135.6	0.225	324.0	135.4	0.226	325.9
3	114.0	0.637	916.4	113.9	0.641	921.7
4	100.3	1.371	1971.9	100.2	1.378	1983.1
5	90.7	2.518	3622.5	90.6	2.532	3643.2

Table 3.1: Height and location of centrifugal barriers in collisions of Yb and Rb atoms with varying initial angular momentum. T_c is the equivalent temperature for the energy E_c given by $T_c = E_c/k_B$.

below the dissociation threshold are likely to have Condon points outside the centrifugal barriers.

Finding numerical values requires knowledge of the C_6 coefficient that describes the ground state of the YbRb molecule. The experiments presented probe only the excited state and the ab-initio potentials do not extend to long ranges yet, so neither of them provides this. Fortunately, an approach presented in Derevianko et al. (2001) can be used to find an estimate. This was already used for a previous thesis within our group on the topic of sympathetic cooling (Tassy, 2007):

$$C_6^{\text{Yb-Rb}} \approx \frac{1}{2}\sqrt{C_6^{\text{Yb}}\, C_6^{\text{Rb}}\, \frac{\Delta E_{\text{Yb}} + \Delta E_{\text{Rb}}}{\sqrt{\Delta E_{\text{Yb}}\, \Delta E_{\text{Rb}}}}} \approx 3186\,\text{a.u.} \tag{3.34}$$

$$\text{with } C_6^{\text{Yb}} = 1932\,\text{a.u.} \qquad \Delta E_{\text{Yb}} = \frac{h\,c}{399\,\text{nm}} \tag{3.35}$$

$$\text{and } C_6^{\text{Rb}} = 4703\,\text{a.u.} \qquad \Delta E_{\text{Rb}} = \frac{h\,c}{\frac{1}{2}(780\,\text{nm} + 795\,\text{nm})} \tag{3.36}$$

ΔE_{Yb} and ΔE_{Rb} are the energies corresponding to the main atomic transitions. The higher oscillator strength of the 780 nm transition might cause it to have a stronger effect than assumed here, leading to an estimate of the C_6 coefficient that is slightly too large.

Table 3.1 lists the resulting values for the centrifugal barriers of the lower rotational states in the ground state YbRb molecule. As the temperatures in a MOT are in the range of 100 μK to 1 mK, the highest rotational states expected to contribute significantly to the spectrum are those with $R = 2$. For higher R the fraction of atom pairs energetic enough to cross the barrier, as described by the Boltzmann distribution, becomes very small.

3.4.4 Shape Resonances

The centrifugal barrier can also hinder the dissociation of a molecule above the normal dissociation threshold. Even though the barrier will eventually be crossed by tunneling, a quasi-bound state like this can have a significant lifetime.

Atoms can also tunnel through the centrifugal barrier from the outside. If the energy of the unbound state is resonant with that of a quasi-bound state within the effective potential as shown in figure 3.9, a dramatically increased amplitude of the wavefunction inside the centrifugal barrier can be the result. This is called a shape resonance.

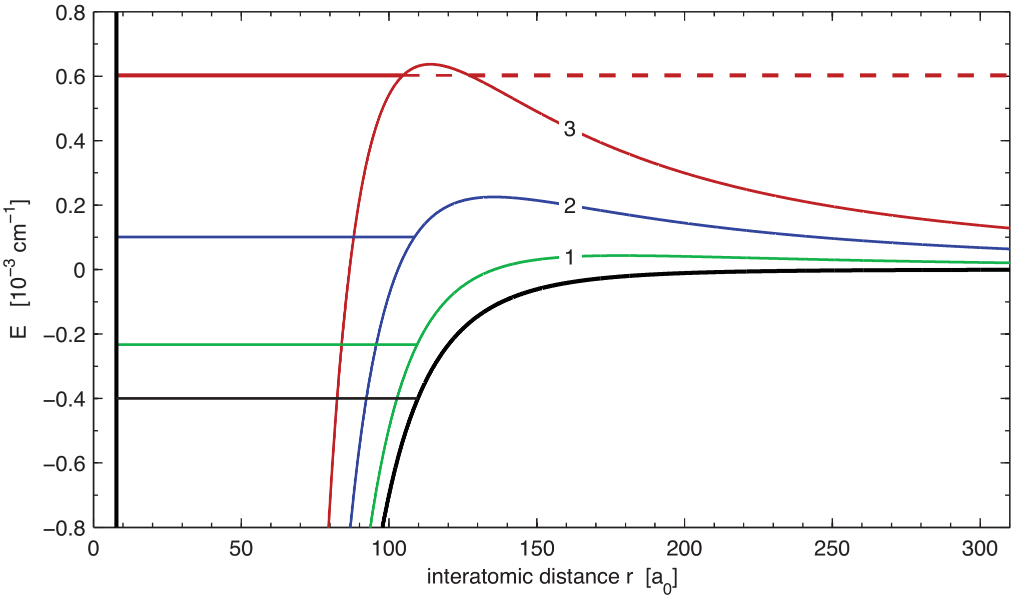

Figure 3.9: Shape resonance. The black solid lines show the nuclear potential without rotation and a bound level near the dissociation threshold. At higher rotational quantum numbers (indicated by numbers), both the shape of the potential curve and the energy of the bound level changes. The levels shown for $R = 2$ and $R = 3$ are quasi-bound. If a collision occurs at an identical energy (indicated by the dashed, thick red line) tunneling through the barrier (thin dashed line) can cause the atom pair to enter the quasi-bound state where it will be trapped for a considerable time.

The shape resonance itself happens between the kinetic energy of the separated atoms and a specific rovibrational state of the ground state molecule with matching angular momentum. But since it generally leads to a much higher probability to find the atoms near the Condon point, it directly affects the photoassociation spectrum. Molecules are much more likely to be formed starting from the resonant rovibrational state, and the excited states that can be reached from there will show a higher population than otherwise expected.

Due to the selection rule $\Delta R = [0, \pm 1]$, this will be directly reflected in the relative strength of the observed rotational lines. If there is a shape resonance for the ground state $R = 2$ state, the excited state $R' = 1$, $R' = 2$ and $R' = 3$ lines will be enhanced. The strength of this enhancement depends dramatically on the fraction of collisions with resonant energies and therefore on the temperature in the trap.

Chapter 4

Experimental Setup

This chapter aims to give an overview of the experimental setup to the point that is needed for the interpretation of results in the following chapter. For more details on the setup used in this and previous experiments, see Batär (2005); Tassy (2007). For specifics on the photoassociation laser system see Münchow (2008).

4.1 Overview

Rubidium and ytterbium atoms are held in a combined magneto-optical trap. Figure 4.1 shows a sketch of the general layout. The atoms are trapped inside a wheel-style steel vacuum chamber. The axial beams shown in the top view enter through small windows. Larger windows around the circumference allow access for all other beams, as shown in the side view. The main field coils are mounted around the axial windows, outside the vacuum.

4.2 Magneto-Optical Traps

A magneto-optical trap or MOT makes use of counter-propagating laser beams to both trap and cool neutral atoms (Raab et al., 1987). By choosing the wavelength of the lasers somewhat red-detuned from an atomic absorption line, atoms are more likely to absorb photons moving in the opposite direction. The momentum of the photon then slows down the atom. This alone is known as an optical molasses (Chu et al., 1985). By using circularly polarized laser light and applying a magnetic quadrupole field, it is possible to add a centering effect and obtain full trapping of the atoms. Since this works through selective excitation to specific Zeeman sub-levels, the ground state and the excited state need to have a different magnetic momentum that is of sufficient strength for trapping in at least one of them. For a detailed description, see Metcalf and van der Straten (1999).

The selective absorption of photons that creates the trapping forces can only continue to work if the atom returns to the initial state afterwards. For this reason a magneto-optical trap can only be used with atoms that have a so-called closed or cycling transition, where the atom will alternate between the ground state and a single excited state indefinitely,

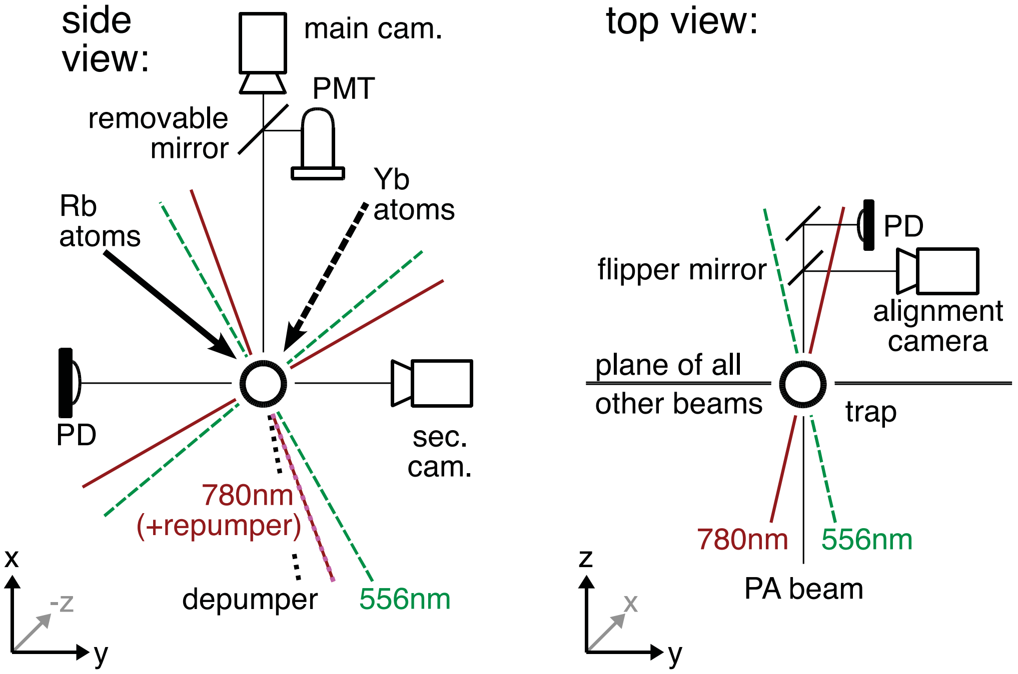

Figure 4.1: Experimental scheme as seen from the side (left figure) and from the top (right figure). Dashed green lines represent the trapping beams for Yb (556 nm), solid red lines the beams for Rb (780 nm). The bottom right 780 nm beam has the dark-spot repumper (pink dots) superimposed. The photoassociation beam enters the vacuum chamber through the axial windows.

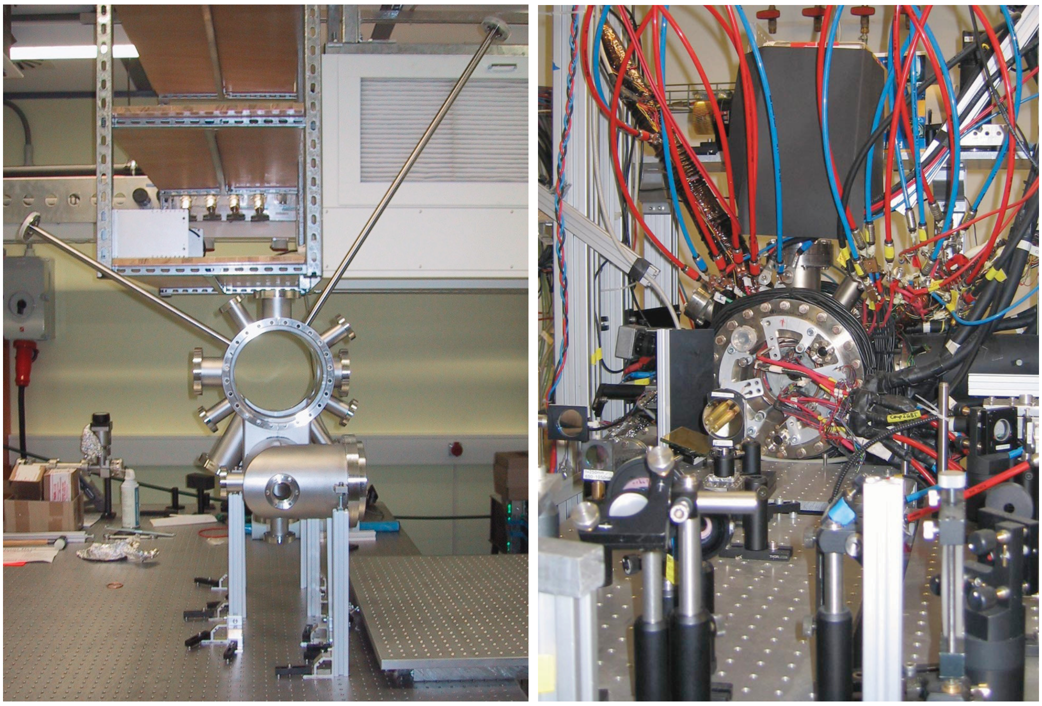

Figure 4.2: The experimental chamber after preliminary assembly (left) and as currently used in the experiment (right). The view corresponds to that in the left drawing of figure 4.1.

with a negligible chance of being lost to a different state. For rubidium and many other atoms this requires an additional repumping laser to return lost atoms to the cycle.

A dual-species MOT is possible when trapping light for each atomic species does not drive any transitions in the other species, neither from the ground nor from the excited state. This is usually the case. Additionally, both traps need to operate in the same magnetic field. Since the trapping forces depend on the interaction of many individual factors such as the transition linewidth and wavelength, the mass and magnetic momentum of the atoms, the optimum field for catching large atom numbers at low temperatures is specific for each species. A combined trap will generally require a compromise.

For these experiments a current of 60 A in the MOT coils provides an axial field gradient of 26 G/cm. The radial gradients are half of this value.

4.2.1 Ytterbium MOT

The ytterbium MOT uses the $^1\mathrm{S}_0$ to $^3\mathrm{P}_1$ intercombination transition at 555.8 nm, which has essentially no losses to other states and no repumper is required. Since it is a semi-forbidden transition that requires the electronic spin to change from a singlet to a triplet configuration, the line is quite narrow with $\gamma_{\mathrm{gr}} = 2\pi \cdot 181\,\mathrm{kHz}$.

The green light is produced by a TekhnoScan AMETIST-SF-07 linear dye laser using Rhodamin 110 as dye. This reliably produces around 20 mW of laser power. The dye in the recirculation system gradually decays over a useful lifetime of approximately six weeks,

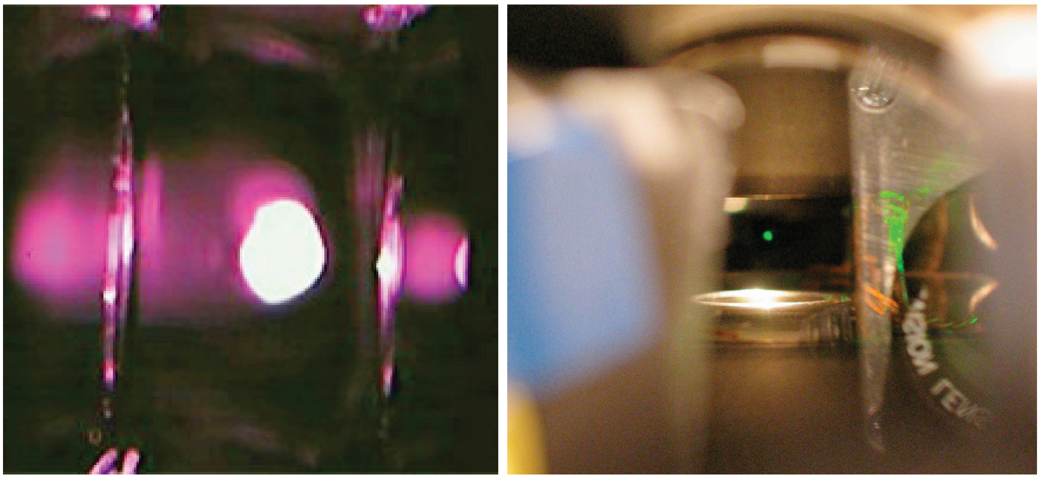

Figure 4.3: Pictures of the rubidium (left) and ytterbium (right) MOTs

with the required pumping power rising gradually from approximately 1 W to 3.5 W. A Coherent Verdi V-10 DPSS laser with a wavelength of 532 nm provides the pumping light.

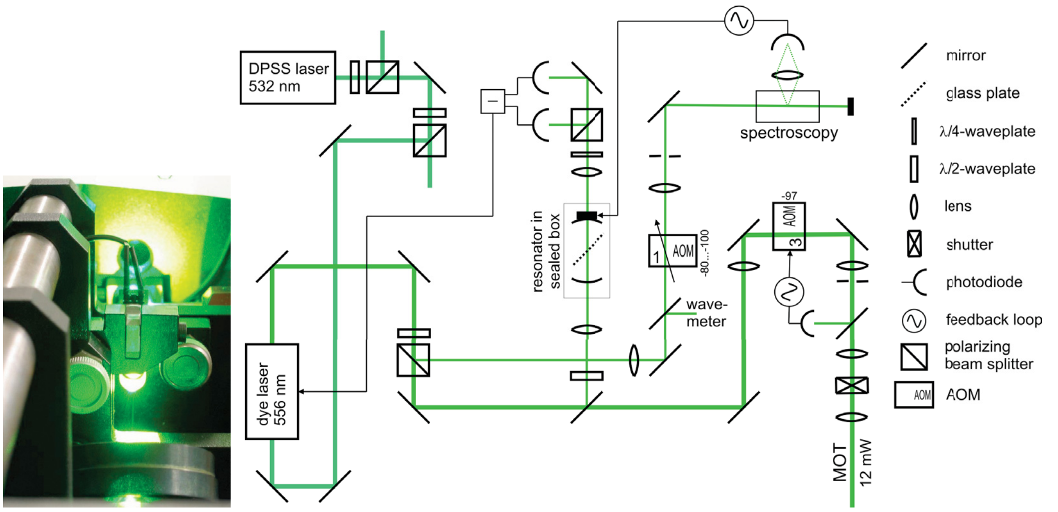

Figure 4.4: **(left)** Dye laser in operation at 555.8 nm.
(right) Laser system for the ytterbium MOT. Somewhat simplified from Münchow (2008).

Figure 4.4 shows an overview of the optical system. For short-term stability, the laser is first stabilized to a resonator using a transmission Hänsch-Couillaud-scheme (Hänsch and Couillaud, 1980). The FWHM linewidth after this step is approximately 1 MHz on a time scale of seconds. To reduce the impact of small but sudden changes in air pressure occasionally caused by the air-conditioning system, the resonator is mounted in a sealed metal box. This also provides better stability under temperature changes.

For long term stability, a piezo-electric element can adjust the exact length of the Hänsch-Couillaud resonator to stabilize the laser to a spectroscopy signal. This is obtained from a collimated ytterbium beam in a separate vacuum system. The branch of the laser beam that enters the spectroscopy cell is frequency-modulated by an AOM and the resulting ytterbium fluorescence is measured with a photomultiplier tube. Demodulating this signal with a lock-in amplifier directly provides a dispersion-shaped lock signal. Spatially filtering the transversal velocities in the ytterbium spectroscopy beam with a series of apertures reduces the Doppler broadening to acceptable values. The detuning of the trapping laser with respect to the resonance is controlled through the difference between the frequency of the MOT switching AOM (3) and the center frequency of the modulation AOM (1).

Different isotopes can be trapped by locking the dye laser to the corresponding spectroscopic line. The isotopes ^{171}Yb, ^{172}Yb, ^{174}Yb and ^{176}Yb have all been trapped in this way. The low relative abundance of ^{170}Yb and the complex structure of the ^{173}Yb line prevented reaching a sufficient signal-to-noise ratio for a stable laser lock with the current setup. A spectrum that identifies the isotopes is shown in figure 4.5.

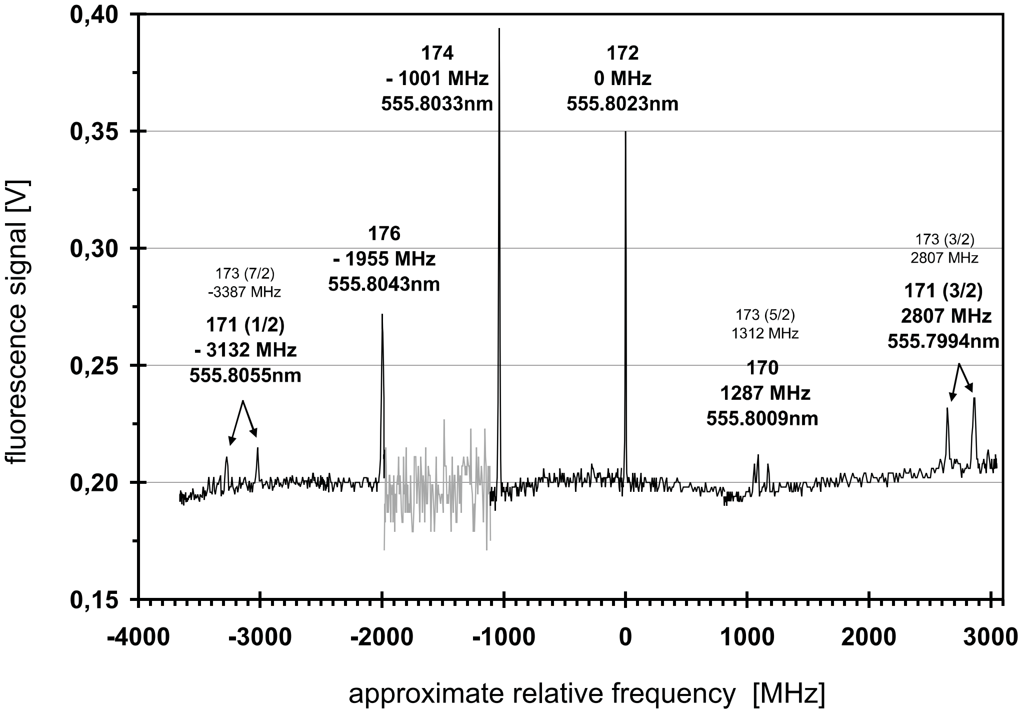

Figure 4.5: Ytterbium spectrum taken in the natural isotope mix in the spectroscopy beam.

Controlled by a feedback loop, AOM (3) in the path to the trap serves to suppress the fast intensity fluctuations caused by turbulence in the dye jet, thereby reducing the noise level of the trap fluorescence signal used in the photoassociation experiments. The same AOM also serves to quickly switch off the trap for time-of-flight temperature measurements. The disadvantage of using the same AOM for both functions is that when the beam is switched off, the feedback loop measures an intensity value of zero and gradually increases the control signal to maximum. When the beam is then switched back on, the feedback loop can take up to a millisecond to settle to the stabilized value again.

About 12 mW of stabilized power is consistently available for the MOT itself. To make the best use of this light, it is split into three arms which are then retro-reflected to complete the trap.

An estimate for the maximum atomic velocity that can be captured in a MOT is given in Batär (2005, p. 32) as

$$v_c = \sqrt{\frac{2r_c\,\hbar\,k\,\gamma}{M}} \quad , \tag{4.1}$$

where $k = 2\pi/\lambda$ is the wave vector of the trapping light and M is the atomic mass. The cutoff radius of the trap r_c is given either by the size of the beams or the point where the Zeeman shift becomes equal to the detuning. Assuming that the detuning has been chosen such that the cutoff radius matches the beam radius of approximately 4 mm, this gives a maximum capture velocity of $v_c = 6.1\,\mathrm{m/s}$ with a kinetic energy corresponding to $0.27\,\mathrm{cm}^{-1}$.

A flow of ytterbium atoms is provided by an oven heated to a temperature of $435°C$. These are then decelerated and cooled by a Zeeman slower designed for a final velocity of 5 m/s (Kroboth, 2002). It operates on the $^1\mathrm{S}_0$ to $^1\mathrm{P}_1$ transition at 399 nm. The broader linewidth of $\gamma = 2\pi\cdot 28\,\mathrm{MHz}$ allows for a much faster deceleration than the green transition, where a Zeeman slower would require an impractical length.

The slowing light comes from two blue laser diodes in a master-slave configuration. The master laser is an external cavity diode laser (ECDL) of similar construction as that described in Wieman and Hollberg (1991, section IV.C). Figure 4.6 shows an example of the type currently used. The master laser is directly locked to the ytterbium spectroscopy using a modulation method like in the green system. It then injects the slave laser which provides 12 mW of usable power at the Zeeman slower.

4.2.2 Rubidium MOT

Due to the presence of additional hyperfine structure, the rubidium MOT is somewhat more complicated. The MOT uses the $^2\mathrm{S}_{1/2}$,$F = 2$ to $^2\mathrm{P}_{3/2}$,$F' = 3$ transition. Due to the selection rule $\Delta F = [0, \pm 1]$ the only hyperfine level of the ground state that they can return to is $F = 2$.

Since the splitting between the excited $F' = 3$ and $F' = 2$ hyperfine levels of 267 MHz is not large enough to ignore the atomic linewidth of $\gamma_{\mathrm{Rb}} = 2\pi\cdot 6.1\,\mathrm{MHz}$ and the Doppler broadening entirely, a certain fraction of atoms gets excited to the $F' = 2$ state. Some of these atoms will then return to the $F = 1$ ground state and be lost from the cycle. Although the probability of this happening is low for every single excitation process, the excitation – spontaneous emission cycle happens only slightly below the saturated rate of $\gamma_{\mathrm{Rb}}/2$. The resulting loss rate is normally high enough that no trapped atoms are detectable this way.

In order to reclaim the atoms from the $F = 1$ ground state, a repumping laser is used. This is resonant with the $F = 1$ to $F' = 2$ transition and will keep re-exciting atoms until spontaneous emission takes them to the $F = 2$ ground state, where they reenter the MOT cycle. Figure 4.7 shows the atomic energy terms and transitions involved.

This complicates the required optical system as shown in figure 4.8. All light is provided by diode lasers near 780nm. Two ECDLs are stabilized to rubidium vapor cells two provide

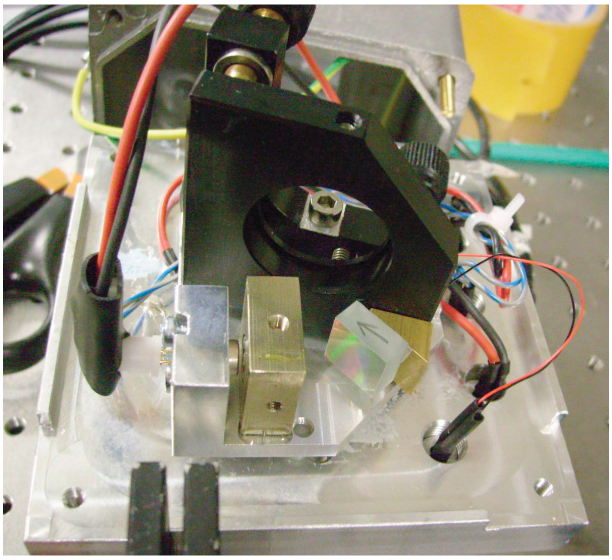

Figure 4.6: Current setup of the ECDL lasers used in the experiment. The grating is fixed to a mirror mount for easy adjustment. To increase the accessible wavelength range, the axis of rotation is positioned as closely as possible to the plane the laser diode is in. A piezoelectric element under the horizontal adjustment screw of the mirror holder controls the angle of the grating.

stable references that the wavelengths required for the MOT and repumper beams are then derived from through AOMs. A slave laser increases the available power at the trap position to approximately 40 mW. Because of this higher available power, the rubidium MOT does not need a retro-reflected setup and uses six individual beams of about 15 mm diameter.

Atoms are again loaded from a Zeeman slower operating on the same transition as the MOT. The wavelengths required are derived from the two spectroscopy-locked ECDLs described before using AOMs. A second slave laser amplifies the slowing light.

4.2.3 Forced Dark-spot MOT

It is possible to take advantage of the ground state splitting. In a so-called dark-spot MOT, an obstacle is introduced into the repumping beam, literally creating a dark spot. By carefully positioning this shadow-casting object between the two lenses of a telescope, an image can be created at the trap center without affecting the collimation of the repumper. This is illustrated in figure 4.9.

In the center region, atoms in the $F = 1$ ground state do not see any resonant light. The repumper will return them to the MOT cycle only when they drift out of the region again. This can help overcome density limitations (Ketterle et al., 1993) near the trap center, where a considerable fraction of the photons encountered by the atoms have been re-emitted by other atoms and create an effective repulsion between them. It also reduces the fraction of excited state atoms in the center region which is significant for two reasons:

- A collisions between a ground-state atoms and an excited atom can release part of the excitation energy as kinetic energy, leading to heating and atom loss.

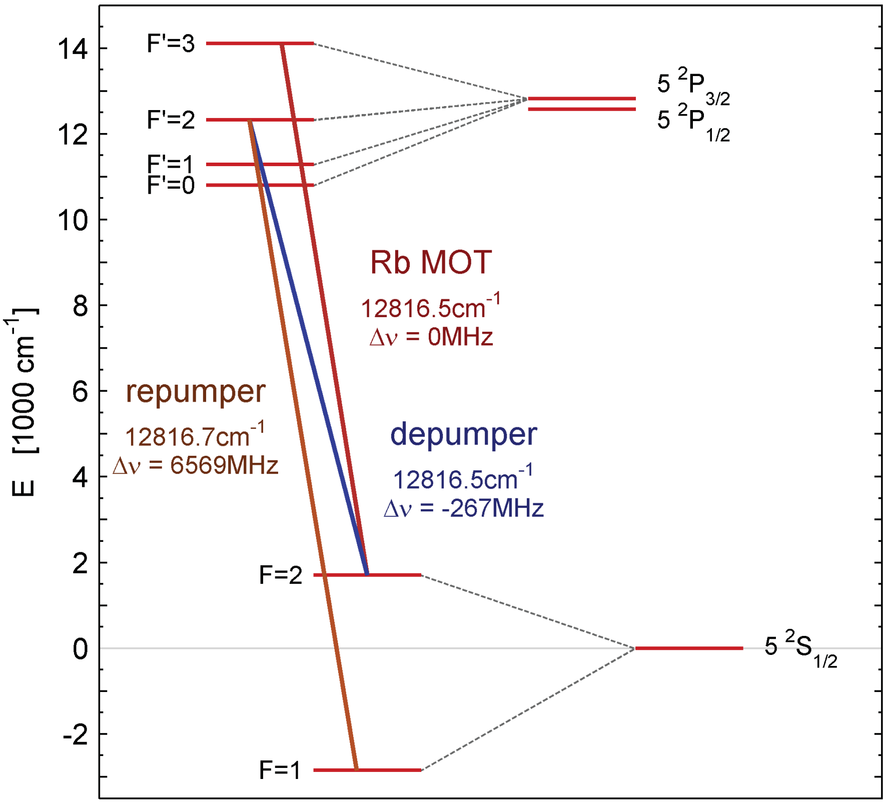

Figure 4.7: Relevant atomic states for the Rb MOT. Hyperfine splittings have been magnified by 20,000 in the ^{2}S$_{1/2}$ ground state and by 200,000 in the ^{2}P$_{3/2}$ excited state. Detunings $\Delta\nu$ are given relative to the main MOT transition.
The MOT operates between the $F = 2$ and $F' = 3$ state. Off-resonant excitation to the $F' = 2$ state can allow some atoms to go to the the ground $F = 1$ state, removing them from the cycle. The repumper returns these atoms to the $F = 2$ state through optical pumping so that they reenter the MOT cycle.
When the MOT is operated as a forced dark-spot MOT, the suppression of the central region of the repumping beam together with a depumping beam supports the transfer of atoms to the dark $F = 1$ state near the center of the trap.

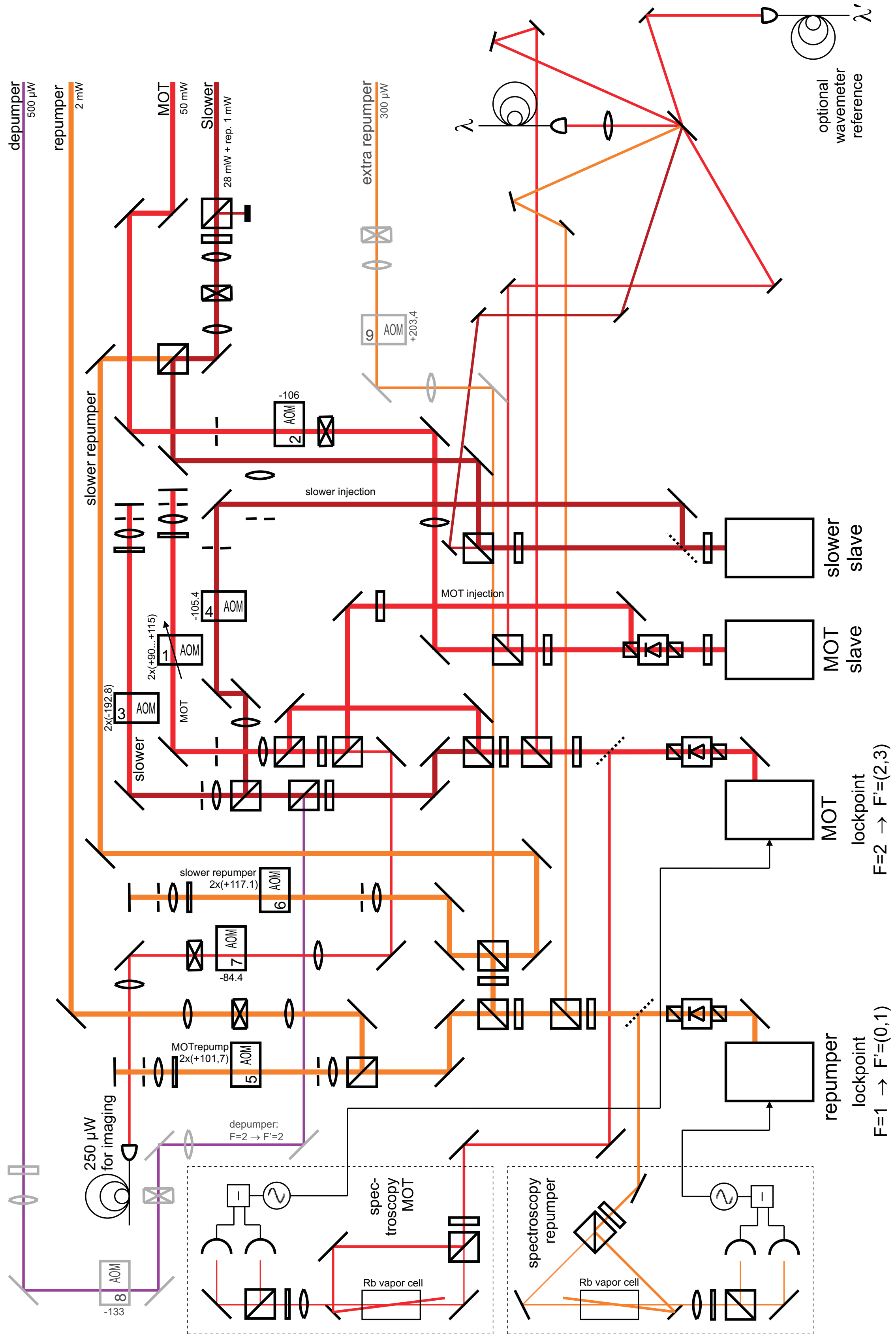

Figure 4.8: Laser system for rubidium. From Münchow (2008)

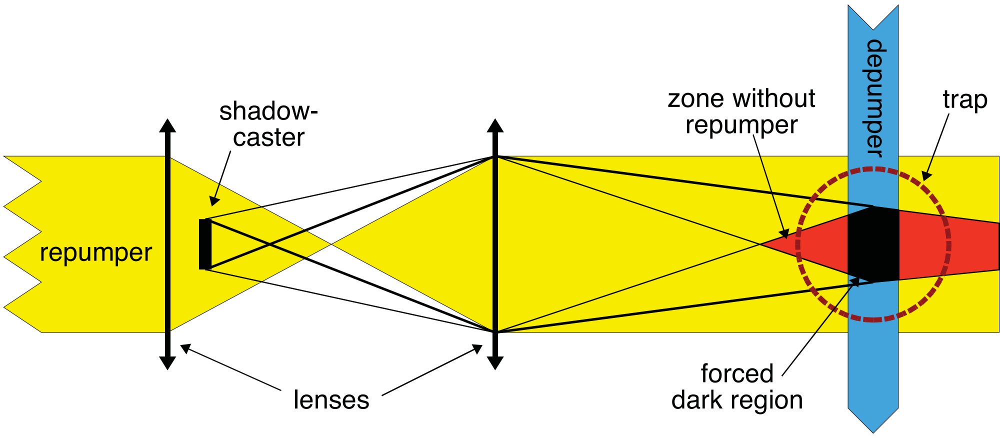

Figure 4.9: Schematic of the forced dark-spot MOT. An object in the repumping beam is imaged to the center of the trap, creating a shadowed region. A depumping beam enters the chamber perpendicular to this, creating a volume where the atoms are actively pumped to the $F = 1$ ground state. They then remain in this state due to the absence of the repumper.

- The interpretation of the photoassociation experiments presented here is greatly simplified if all atoms can be assumed to have been in the same state initially.

The effectiveness of a dark-spot MOT was first demonstrated for sodium, where the branching ratio to the dark ground state is higher than in rubidium. To help the atoms in the volume shaded from the repumper enter the dark state quickly, an additional weak depumping beam on the $F = 2$ to $F' = 2$ transition is used, increasing the population that can decay to the $F = 1$ state. This configuration is known as a forced dark-spot MOT (Anderson et al., 1994).

In this experiment, the depumper enters the vacuum chamber through one of the axial windows, perpendicular to the repumping beam. When positioned properly, the presence of the depumper reduces the trap fluorescence by 82% compared to the plain dark-spot MOT. Combined with the effect of the plain dark-spot MOT, it is safe to assume that $> 95\%$ of all atoms are in the dark state. The trapped atom number is nearly identical between bright and forced dark-spot MOT as the reduced collisional losses cancel out the additional losses through atoms drifting out of the trap in the dark state. It is also likely that the peak rubidium density in the dark-spot configuration is considerably increased.

4.3 Imaging and Trap Superposition

Several cameras continuously provide images of the MOTs. The main camera in these experiments is a UK1117 camera from ABS GmbH in Jena, connected via USB to a computer that optionally stores the images for later evaluation. The camera has an effective resolution of 764×512 pixels and supports exposure times down to $100\,\mu$s. It also offers a hardware trigger which starts exposure after a fixed delay with a jitter of less than $10\,\mu$s.

This camera images the trap from straight above such that the atoms will not fall out of the picture in time-of-flight measurements. The imaging optics consist of two achromatic lenses with focal lengths of $f_1 = 250\,\mathrm{mm}$ and $f_2 = 100\,\mathrm{mm}$ for a magnification of $a = 0.4$, resulting in a resolution of close to $20\,\mu\mathrm{m/pixel}$.

A second computer controlled camera (Meade Deep Sky Imager pro, 508 × 244 pixels) provides images of the traps on the horizontal axis. Since the signal-to-noise ratio and timing jitter of this camera is worse than that of the primary camera, the pictures are not generally used for numerical evaluation. They provide a good qualitative sense for the trapped atom number, however, and are therefore used as the main indicator when adjusting the alignment of the trapping beams, particularly when the fluorescence of the ytterbium trap is measured with the photomultiplier tube and the optical path to the main camera is therefore blocked.

Chromatic aberrations in these two imaging systems where found to be insignificant, so the camera pictures also provide information about the relative position of the traps. Theoretically, both traps should be centered on the zero of the magnetic field, but asymmetric light forces due to misalignment, imbalance or unwanted structure on the MOT beams can push the traps to other positions. The rubidium trap normally loads so many atoms that it is impossible to pinpoint an exact location due to saturation of the cameras and possibly due to density limiting effects near the trap center. Here it has proven useful to block the flow of atoms from the slower and look at the much smaller MOT loaded from the background gas. Figure 4.10 shows some example images.

A standard video camera and several webcams also supply diagnostic images from other directions. A resonant imaging beam can also be directed to the two main cameras to take absorption images.

4.4 Photoassociation Laser System

4.4.1 Laser

The experiments described in this thesis explore photoassociation of ytterbium-rubidium molecules near the rubidium line at 795 nm. Light at the intensities required to reach measurable molecule formation rates is provided by a titanium-sapphire laser (Tekhnoscan TIS-SF-07, shown in figure 4.11). This can supply a power of up to 1.5 W at wavelengths between 750 nm and 850 nm when pumped by 10 W from a DPSS laser.

Although the pumping laser allows for this amount of power, it is shared with the dye laser of the ytterbium trap, which uses between 1 W and 3.5 W depending on the age of the laser dye. This limits the available power of the Ti:Sapph to around 800 mW. After beam shaping and stabilization, 300 mW to 400 mW are available at the position of the traps.

A piezoelectric element in the resonator allows for automatic scanning over 3 GHz. An electronically controlled etalon ensures single-mode operation over this entire range.

4.4.2 Optical Setup

The optical setup used with the photoassociation laser is shown in figure 4.12. Most of the light is guided to the main chamber in a free-space beam, but at several points small

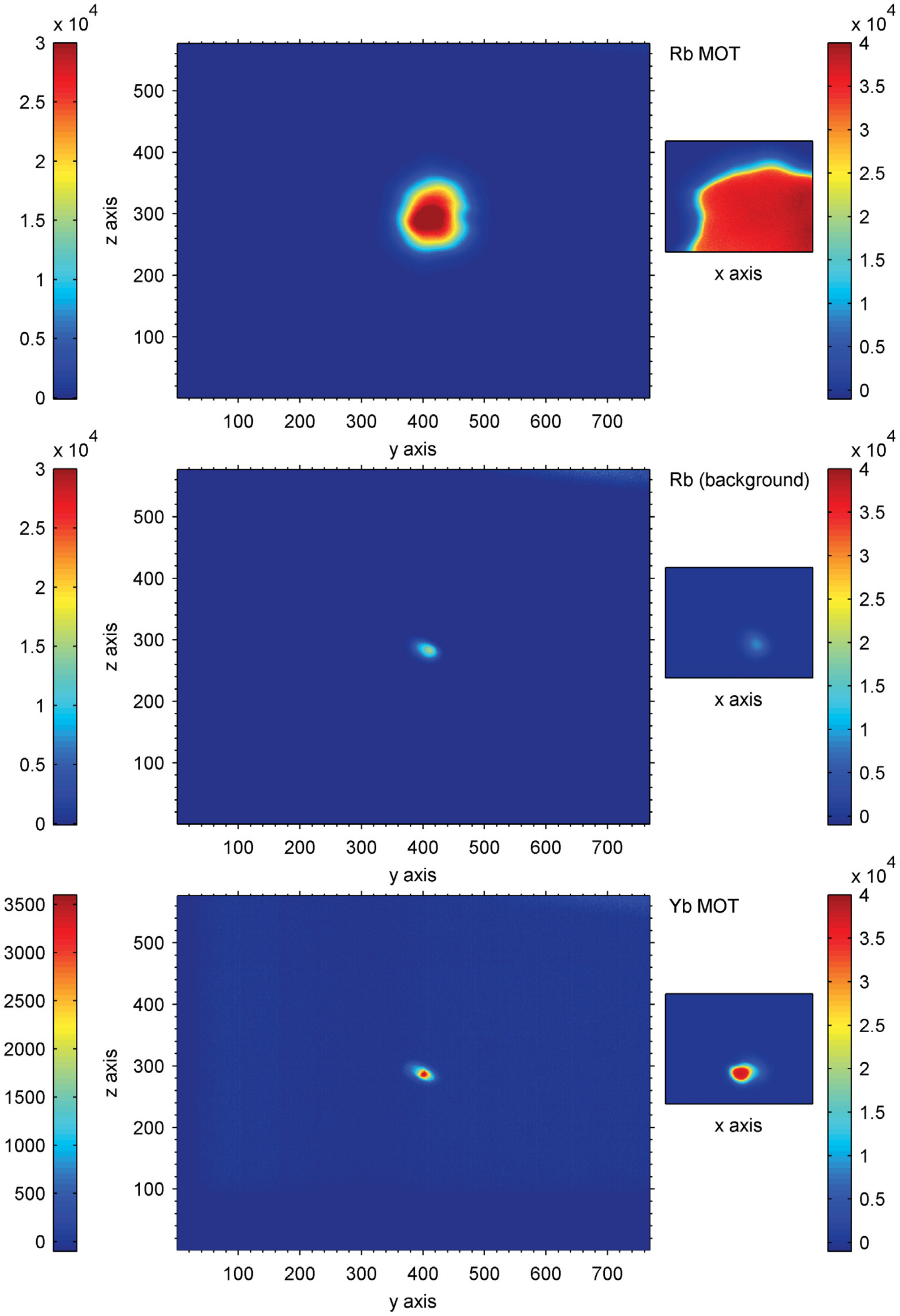

Figure 4.10: Camera pictures used to check the relative positions of the traps. Sizes have been adjusted to show identical scales after taking the imaging systems into account. Images from ABS UK1117 on the left, from Meade Deep Sky Imager on the right. The shared z axis corresponds to the chamber axis.

top: Normal rubidium MOT. Camera saturation even at short exposure time makes it difficult to find the exact location of the trap center.

center: Rubidium MOT loaded from background gas.

bottom: Ytterbium MOT.

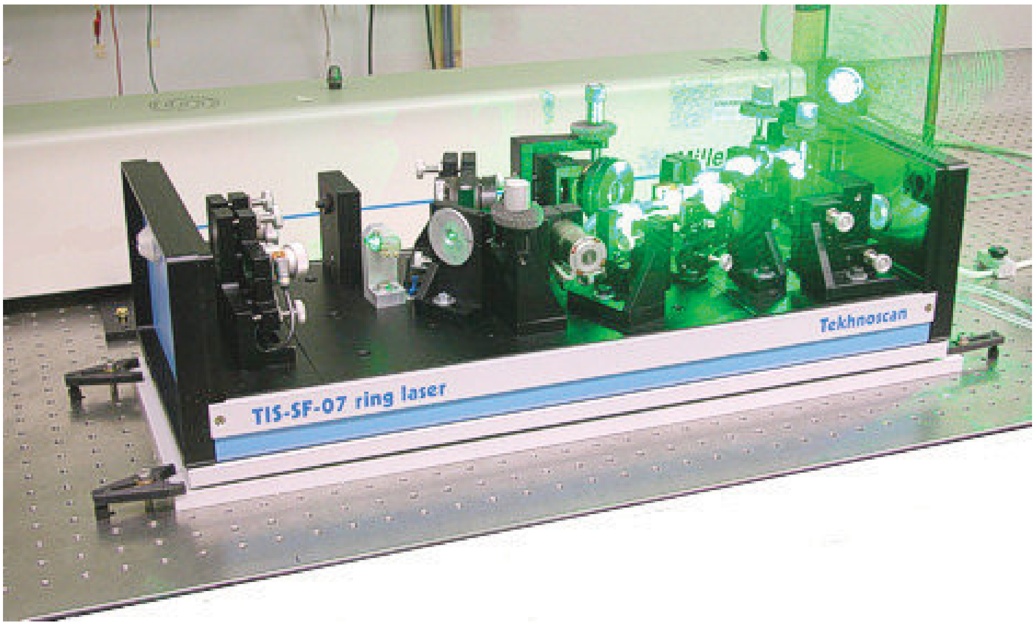

Figure 4.11: Tekhnoscan TIS-SF-07 Titanium-Sapphire laser of the same type as that used as photoassociation laser. (Picture from the company website at http://www.tekhnoscan.ru/english/)

fractions are branched off for diagnostic purposes. Two polarizing beamsplitter cubes provide adjustable intensities at a cavity used to improve the short-term of the laser and a fiber connection to a wavemeter. The first mirror after the laser was chosen to transmit a weak beam that is coupled into a longer resonator with a free spectral range of 67 MHz. This provides a comb of resonances when the laser frequency is changed and was used to characterize the scan. It is also designed to act as an actively stabilized reference during later stages of the experiment when the laser will need to be kept resonant with one of the photoassociation lines.

The main beam passes through an AOM before it reaches the vacuum chamber. This is used for switching and intensity stabilization. A photodiode measures the light leaked through one of the mirrors after the AOM. A PI-loop then provides a correction signal to the mixer in the AOM's microwave generation such that the power in the first refracted order is kept constant. This is necessary since the transmission of the manually controlled frequency selective elements in the laser will vary when the laser wavelength changes during a scan, causing a considerable variation in output power. To avoid having to re-optimize the resonator alignment of the Ti:Sapph laser several times during the day, the output power is normally set to values near 300 mW which ensures stability over the entire scanning range even after several hours.

An adjustable telescope near the vacuum chamber changes the beam size to 320 μm FWHM at the trap position, chosen to approximate the size of the ytterbium cloud. Figure 4.13 shows this result and also confirms the near-Gaussian profile of the beam.

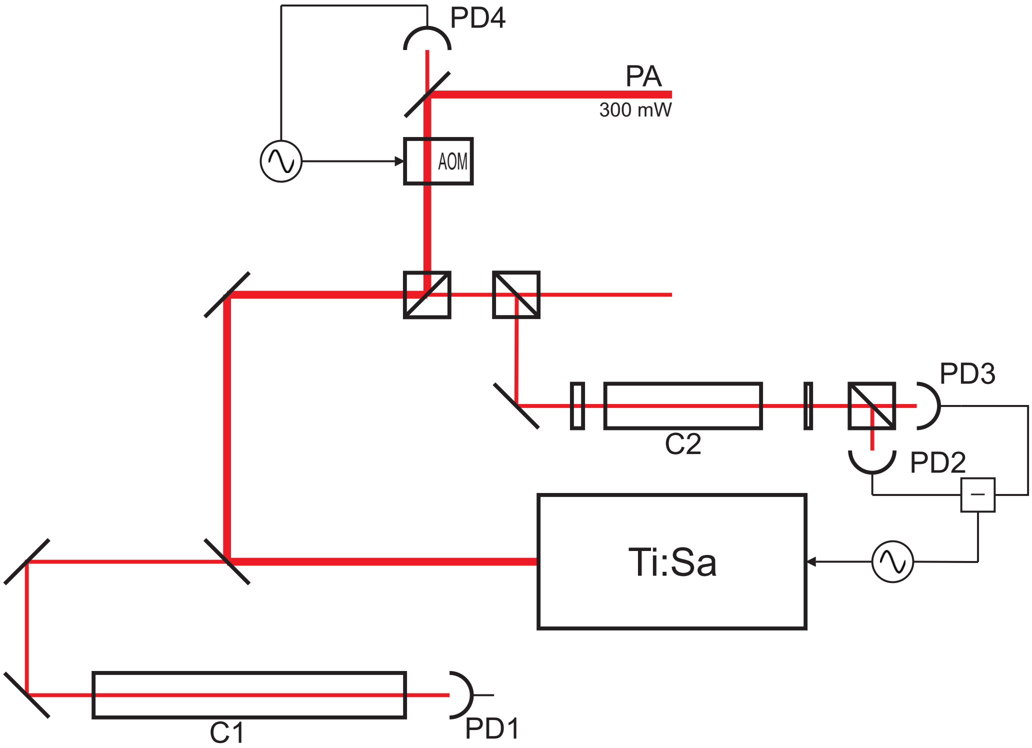

Figure 4.12: Optical system of the photoassociation laser. The beam passing straight through the second beam splitter cube is coupled into a single-mode fiber to the wavemeter.

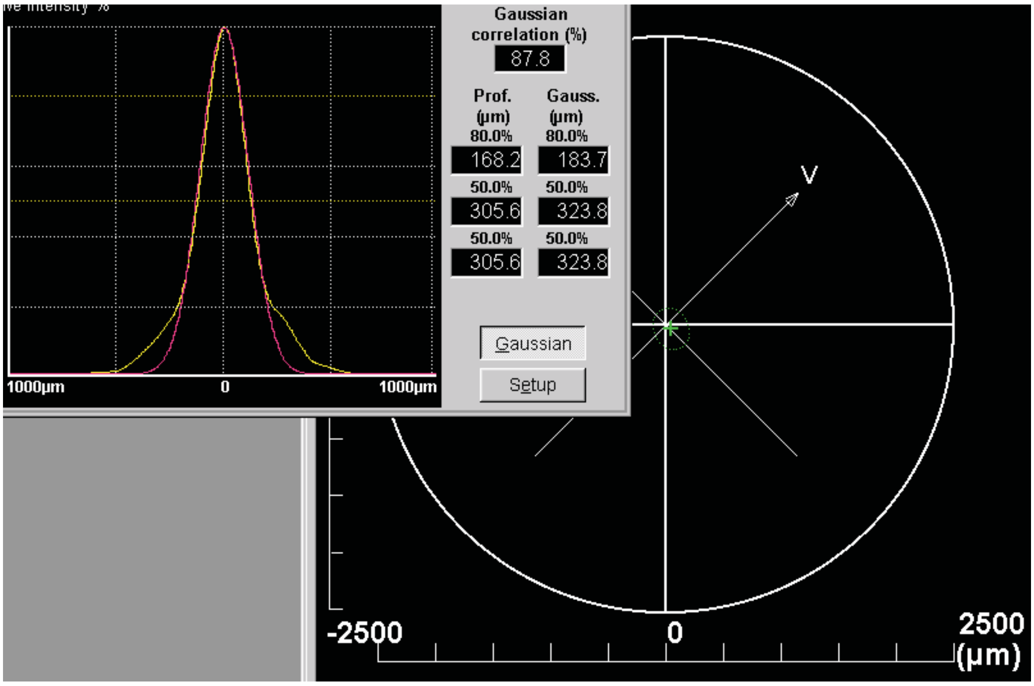
Gaussian correlation (%) 87.8

Prof. (µm) 80.0% 168.2
Gauss. (µm) 80.0% 183.7
50.0% 305.6
50.0% 323.8
50.0% 305.6
50.0% 323.8

Figure 4.13: Beam profile at a distance equivalent to the trap position, measured with a Coherent BeamMaster.

4.4.3 Short-Term Stabilization

When the the laser is scanned over a resonance of the long resonator, the transmission spectrum shows the characteristic signs of strong frequency noise as seen in figure 4.14. The linewidth of the unstabilized laser is estimated to be approximately 10 MHz.

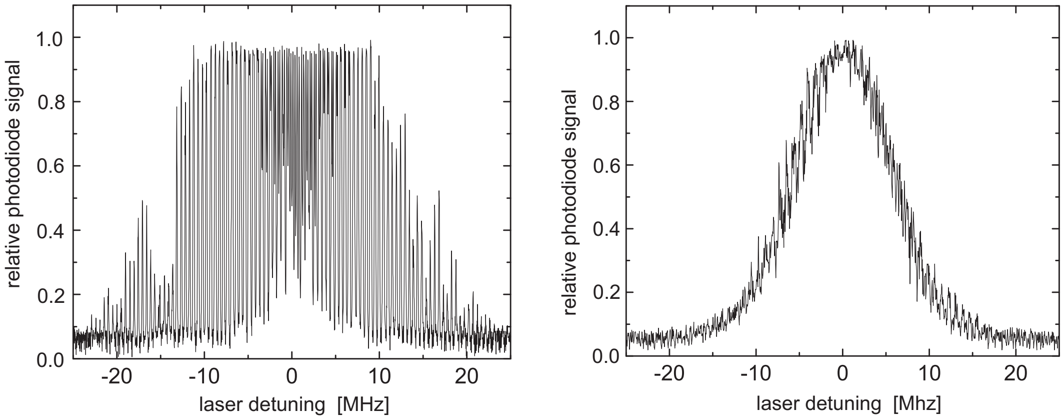

Figure 4.14: Light intensity transmitted through the long cavity over detuning from resonance for the Ti:Sapph photoassociation laser.
(left) The unstabilized laser shows strong frequency noise with a linewidth of approximately 10 MHz.
(right) The lock to the stabilization cavity reduces this to about 2 MHz.

An external resonator is used to reduce this. It contains a glass plate set to Brewster's angle for the wavelengths in question. A quarter-wave plate, a polarizing beamsplitter cube and two photodiodes provide an error signal in a transmission Hänsch-Couillaud setup (Nemitz, 2004; Münchow, 2008) very similar to the one used for the dye laser. A PI-loop then creates an adjustment signal for the Ti:Sapph's electronics for accurate but slow control, while the remaining difference signal is amplified through a high-voltage operational amplifier circuit and fed directly to a fast piezoelectric element in the laser resonator.

As evident from the second diagram in in figure 4.14, this reduces the short-term linewidth of the laser to an estimated value of 2 MHz. The long-term stability is limited by slow drifts of the resonator length, mostly caused by temperature changes.

In order to scan the laser in this mode of operation, the resonator length is varied using a piezoelectric tube between its body and one of the mirrors. This introduces nonlinearities and hysteresis effects to the scan, shown in figure 4.15. These were investigated in Münchow (2008) by using the fixed long resonator as a frequency reference.

It was found that the actual curve can be approximated by applying a gamma correction to the scanning signal in the form:

$$\Delta\nu_{\mathrm{PA}} = \Delta\nu_{\max}\left(\frac{U_{\mathrm{control}}}{U_{\max}}\right)^{\gamma} \tag{4.2}$$

The latest investigations determined an averaged optimum value of $\gamma = 1.124$. An earlier value of $\gamma = 1.15$ was used throughout the measurements presented here, resulting

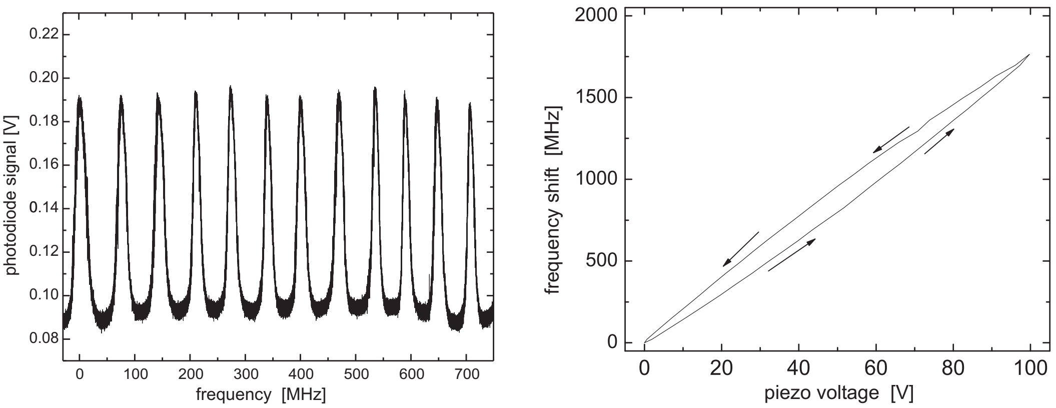

Figure 4.15: **(left)** Frequency reference provided by the long resonator. The photodiode signal is plotted over the frequency change of the incident light.
(right) Measured hysteresis curve (frequency shift over piezo voltage) for a typical scan of 100 V peak-to-peak amplitude as used to investigate the structure of photoassociation lines. (Both taken from Münchow (2008).)

in a somewhat higher uncertainty in the relative position of spectroscopic features observed within a single scan.

4.4.4 Overlaying the Beam on the Double Trap

By strongly attenuating the beam, the camera mounted axially on the other side of the chamber allows the preliminary alignment with the trap as seen in figure 4.16. By focussing the imaging system on the plane of the trap, this can actually provide information on the position of the laser in the same plane, in principle allowing for a direct check of overlap.

However, this requires simultaneous imaging of the weak scattered light from the trap and the strong light of the photoassociation beam pointed directly at the camera. To achieve this, a dichroic mirror was used to provide strong attenuation at 795 nm, while most of the 556 nm light from the trap was transmitted.

However, this was found to introduce chromatic aberrations that were strong enough to show the two spots entirely separated even when the beam was in fact overlapped with the trap, as shown in figure 4.16. After the first photoassociation lines had been found, the following alignment routine was used to avoid this effect:

- A strong photoassociation line is found by scanning over the approximate wavelength range.
- The laser wavelength is optimized to maximize trap loss and then kept at this value.
- The beam position is varied to further optimize trap loss.
- Now the beam should be aligned with the ytterbium trap. The laser frequency is changed to be resonant with one of the hyperfine lines of the rubidium D1 transition and the power transmitted through the rubidium cloud is observed on a photodiode.

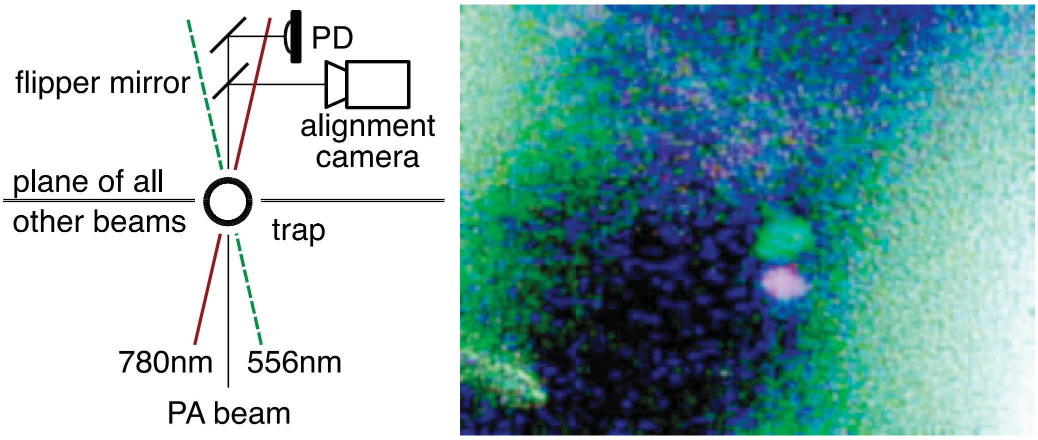

Figure 4.16: **(left)** Top view schematic of the trap, showing the angular separation of the trapping and photoassociation beams. The first of the two mirrors shown in the PA beam can be flipped down. The photoassociation beam then goes to a photodiode that is used to measure the absorption by the trapped rubidium atoms. When flipped up, a webcam provides information on the beam position relative to the ytterbium trap. A filter strongly attenuates the near-infrared wavelengths to create a comparable signal levels between both.
(right) Chromatic aberration causes a shift between the images of the photoassociation beam and the trap. In the picture shown here, the beam is in fact properly superimposed on the trap.

- The alignment of the beams and dark spot in the rubidium trap is optimized to increase absorption. This maximizes the rubidium density at the position of the ytterbium cloud.

- The laser is returned to the wavelength of the chosen photoassociation line and the process is repeated if necessary.

This guaranteed good overlap with relatively consistent loss rates for the photoassociation lines as long as the initial alignment of the two traps was sufficiently good.

4.5 Wavemeter

To measure the frequencies of the various laser systems, a wavemeter was set up and gradually refined over the course of this thesis. A photo with one set of beam paths overlaid is shown in figure 4.17.

The system is based on a Michelson interferometer with one moving end mirror. This is mounted on a sled that rides on an air track. Two electromagnets triggered by a photoelectric sensor provide a push to compensate frictional losses. A cat's eye reflector is used on the sled to reduce the sensitivity to angular alignment. The test beam is sent to the reflector approximately 5 mm above the center of the reflector, such that the beam returns 10 mm lower down. The same is done at the end of the fixed arm.

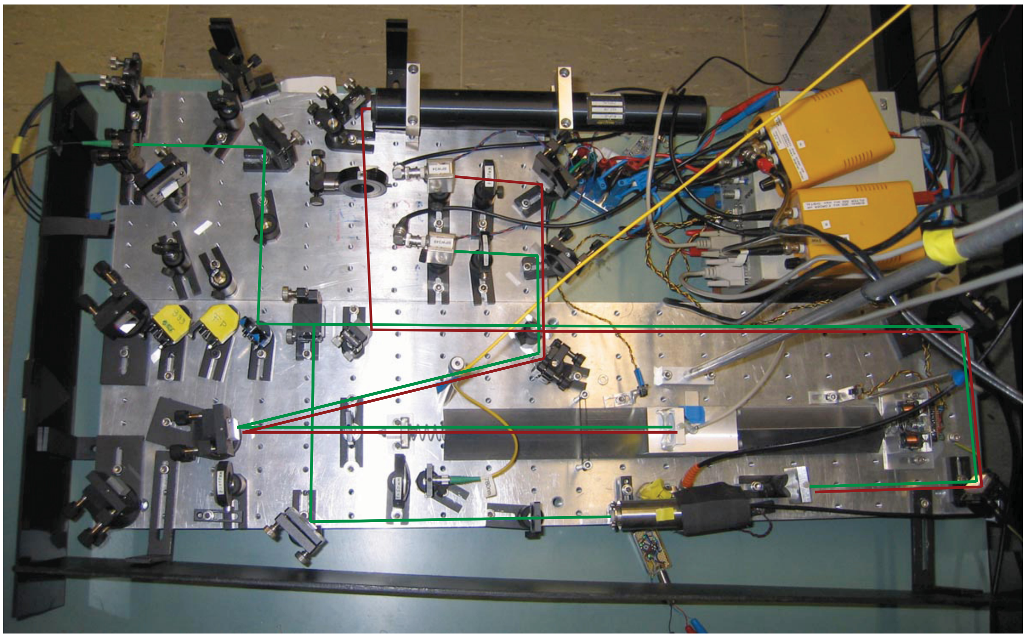

Figure 4.17: The self-built wavemeter described in the text. Red lines mark the beam path of the reference laser while green lines show the path of the photoassociation laser when it is selected for measurement.

A helium-neon laser is used to provide a stable reference. Since it is not temperature stabilized, it causes the absolute wavelength reading to vary by $\pm 1 \cdot 10^{-3}$ nm with temperature. To eliminate these drifts, a pair of flipper mirrors can be used to couple the spectroscopy-stabilized rubidium master laser into the reference beam path of the wavemeter. This requires a correction factor to be applied to the output of the wavemeter that was determined experimentally by repeatedly measuring the wavelength of a known hyperfine transition of rubidium.

The wavemeter readings also have a shot-to-shot fluctuation of around $\pm 0.5 \cdot 10^{-3}$ nm that mostly depends on the position of the sled on the track and quickly averages out with an increasing number of measurements. To reach this level of accuracy on the short available distance, a vernier counting method is used that takes advantage of random coincidences of the zero crossings in both interference signals.

A system of flipper- and magnetically mounted mirrors makes it possible to select any of the laser sources for measurement without realignment. Furthermore, a small part of the selected beam is coupled into a resonator that is continuously scanned to provide a diagnostic on the longitudinal mode of the laser. Silver coated mirrors provide a sufficient finesse for this purpose over the entire visible spectrum.

The entire logic and evaluation required for the wavelength measurement is done by a microcontroller that provides an ASCII-encoded wavelength reading over a standard serial bus. This is used to drive displays in different locations in the lab. It is also connected to the data-logging computer which recovers the actual wavelength values from the string. This computer also applies the required wavelength correction when the rubidium master laser is used as reference.

4.6 Datalogger

The computer that logs the measured wavelengths also contains a National Instruments PCI-6220 analog input board with 16 channels digitized at 16 bit precision. A data logging program written in LabView (Münchow, 2008), shown in figure 4.18, displays and records the scan control signal acting on the external resonator of the photoassociation laser, the fluorescence signals of the ytterbium and rubidium traps along with several other signals. It also displays the frequency of the laser currently selected at the wavemeter in units of wavelength, raw wavenumbers and wavenumbers relative to the rubidium line at 12578.862 cm^{-1}.

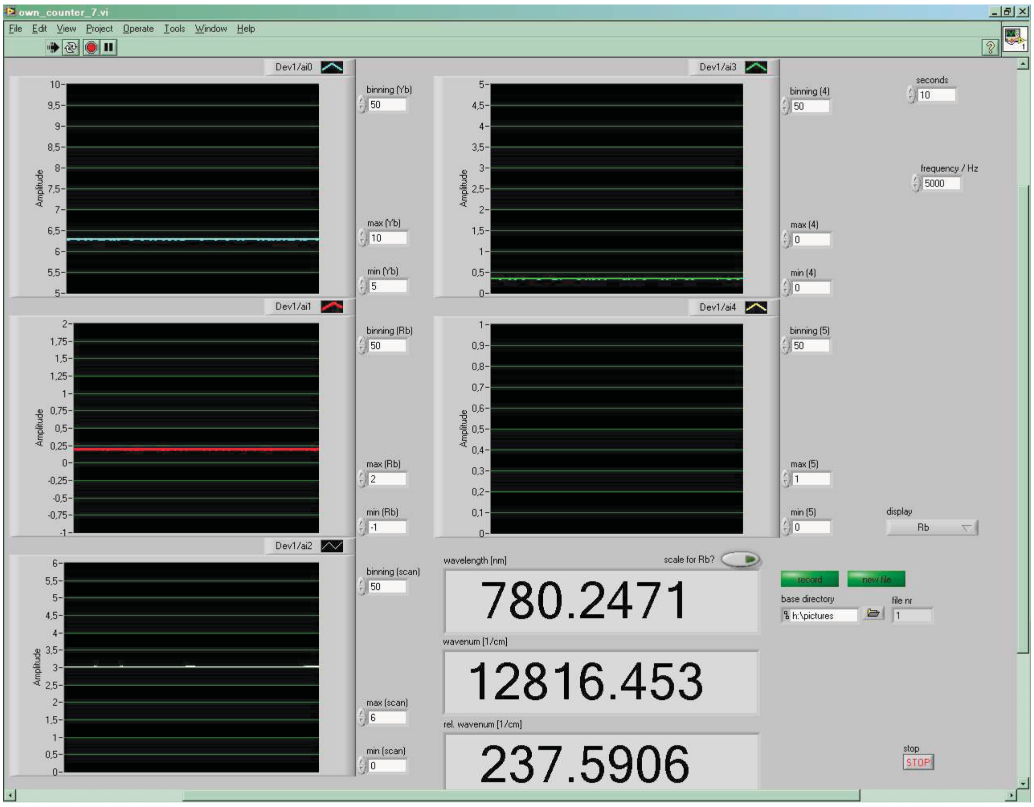

binning (Yb) 50
max (Yb) 10
min (Yb) 5
binning (Rb) 50
max (Rb) 2
min (Rb) -1
binning (scan) 50
max (scan) 6
min (scan) 0
binning (4) 50
max (4) 0
min (4) 0
binning (5) 50
max (5) 1
min (5) 0
seconds 10
frequency / Hz 5000
display Rb
wavelength [nm] 780.2471
wavenum [1/cm] 12816.453
rel. wavenum [1/cm] 237.5906
base directory h:\pictures
file nr 1

Figure 4.18: Main window of the data-logging program.

To reduce the volume of the stored data, it is averaged over a number of samples (individually selectable for each channel) before it is written to disk.

Chapter 5

Trap Characterization

This chapter describes measurements of the trap properties that are required for the analysis of the spectroscopic signals.

5.1 Atom Counting

In order to calculate accurate trap loss rates, it is necessary to know the numbers of atoms in the trap. This kind of measurement is often done through absorption images, comparing the intensity of resonant light reaching the camera with and without atoms in the path of the beam. The advantage is that as long as the camera has a good enough linearity, it is only necessary to know some atomic properties and the resolution of the pictures to find the atom number.

However, actual measurements were always found to show strong fluctuations that made the atom numbers measured in this way unreliable. The problems were later traced to a mechanical beam shutter disturbing the laser lock just when the absorption image was taken and they have only recently been eliminated. In the meantime, an alternative fluorescence method was used instead.

5.1.1 Scattering Rates

According to Metcalf and van der Straten (1999, chapter 2.4), the total scattering rate of atoms excited by near-resonant light is given by

$$\gamma_{\mathrm{sat}} = \frac{s_0\ \gamma/2}{1 + s_0 + (2\delta/\gamma)} \tag{5.1}$$

where γ is the natural linewidth of the transition. This is related to the lifetime τ of the excited state by the equation $\gamma = 1/\tau$. The saturation parameter $s_0 = I/I_{\mathrm{sat}}$ measures the intensity I relative to the saturation intensity I_{sat}. This equation can be changed to the form

$$\gamma_{\mathrm{sat}} = \frac{1}{1 + \frac{I_{\mathrm{eff}}}{I}}\,\frac{\gamma}{2} \qquad \text{with} \qquad I_{\mathrm{eff}} = (1 + 2\delta/\gamma) I_{\mathrm{sat}}. \tag{5.2}$$

If the incident intensity is high compared to the saturation intensity, the scattering rate will saturate at a maximum of $\gamma_{\mathrm{max}} = \gamma/2 = 1/(2\tau)$. Any detuning from resonance δ simply increases the effective saturation intensity I_{eff}, while leaving the characteristic shape of the saturation curve intact.

While this assumes an identical laser intensity for all atoms, it is also a good approximation for a real, more or less Gaussian laser beam under most circumstances, as will be shown in the following. A spherically symmetrical, Gaussian cloud of radius w centered on the origin has a density distribution

$$\rho(x,y,z) = \frac{N}{w^3(2\pi)^{3/2}}\; e^{-\frac{x^2}{2w^2}}\; e^{-\frac{y^2}{2w^2}}\; e^{-\frac{z^2}{2w^2}} \tag{5.3}$$

$$\text{or}\quad \rho(r,z) = \frac{N}{w^3(2\pi)^{3/2}}\; e^{-\frac{r^2}{2w^2}}\; e^{-\frac{z^2}{2w^2}} \tag{5.4}$$

in cartesian (5.3) or cylindrical (5.4) coordinates. The atom number in the cloud is given by N.

By integrating over the z-coordinate, a density equivalent $\rho'(r)$ can be obtained that describes the total atom number in an infinitesimal volume around the cylindrical shell with radius r:

$$\rho'(r) = \int_{-\infty}^{\infty} \rho(r,z)\; 2\pi r\; dz \tag{5.5}$$

$$= \frac{N\; 2\pi r}{w^2\; 2\pi}\; e^{-\frac{r^2}{2w^2}} \int_{-\infty}^{\infty} \frac{1}{w\sqrt{2\pi}}\; e^{-\frac{z^2}{2w^2}}\; dz \tag{5.6}$$

$$= \frac{Nr}{w^2}\; e^{-\frac{r^2}{2w^2}} \tag{5.7}$$

Next we will look at the intensity distribution in a Gaussian beam of radius u crossing the center of the cloud along the z-axis, assuming negligible absorption. While this is not generally justified, it becomes a reasonable approximation if the cloud is given enough time to expand before the beam is turned on. The relative absorption is also reduced if the detection light intensity is sufficient to saturate the transition.

The equation describing the intensity distribution can now be reversed to give the radius where a specific intensity occurs:

$$I(r) = I_{\max}\; e^{-\frac{r^2}{2u^2}} \tag{5.8}$$

$$\frac{I}{I_{\max}} = e^{-\frac{r^2}{2u^2}} \tag{5.9}$$

$$-\ln\frac{I}{I_{\max}} = \frac{r^2}{2u^2} \tag{5.10}$$

$$r(I) = u\sqrt{-2\ln\frac{I}{I_{\max}}} \tag{5.11}$$

Combining this with equation 5.7 gives the following formula for the “density” of atoms at a specific laser intensity ρ'':

$$\rho''(I) = \rho'(\ r(I)\ ) \cdot \frac{dr(I)}{dI} \qquad \left(\text{such that } N = \int_{I_\text{max}}^{0} \rho'' dI\right) \tag{5.12}$$

$$= \frac{N}{I} \frac{u^2}{w^2} \left(\frac{I}{I_\text{max}}\right)^{\frac{u^2}{w^2}} \tag{5.13}$$

With this, a histogram-type distribution of atoms over various intensities can be found, like those shown in the top of figure 5.1 for ratios of beam size to cloud size $u/w = 5$ and $u/w = 2$.

The actual scattering rate for an inhomogeneous intensity distribution of this form can be calculated as

$$\gamma_\text{inh} = \int_{I_\text{max}}^{0} \frac{\gamma}{2} \frac{\rho''(I)}{N} \frac{1}{1 + \frac{I_\text{eff}}{I}} dI \tag{5.14}$$

$$\approx \frac{\gamma}{2} \frac{1}{1 + \frac{I_\text{eff}}{I_\text{avg}}} \qquad \text{where} \qquad I_\text{avg} = \int_{I_\text{max}}^{0} \frac{\rho''(I)}{N} I\ dI \tag{5.15}$$

$$= \frac{\gamma}{2} \frac{1}{1 + \frac{I'_\text{eff}}{I_\text{meas}}} \tag{5.16}$$

The quality of this approximation can also be seen in the lower diagrams of figure 5.1. Even if the beam is only twice the size of the atom cloud, the maximum of the relative deviation $|\gamma_\text{inh} - \gamma_\text{sat}|/\gamma_\text{sat}$ is only 1.2%. Instead of replacing $I \to I_\text{avg}$, it is also possible to absorb the effect of the inhomogeneity into a new effective saturation intensity I'_eff. This can also be chosen to include the Clebsch-Gordan coefficient for the specific transition and any proportionality constants needed to account for absorption and changes in beam size, such that the intensity I_meas in the last equation can actually be measured at any convenient point.

The total number of photons scattered over a time t is

$$N_\text{ph} = N \frac{\gamma}{2} t \frac{1}{1 + \frac{I'_\text{eff}}{I_\text{meas}}} \tag{5.17}$$

and the atom number N can be obtained from a non-linear fit with N and I'_eff as parameters. The error in the atom number determined this way will be largely determined by the fluctuations in shot-to-shot atom numbers and calibration inaccuracies.

5.1.2 Calibration

Since the incident light needs to be integrated over an exactly known period, imaging is done with the ABS camera. The light is provided by the normal MOT beams with the detuning set to zero. To prevent Zeeman shifts from the trapping fields disturbing the result, the MOT beams and coils are switched off for a time of 2.5 ms (6 ms in rubidium) until the fields have fallen off far enough, then the beams are switched back on for a time of 500μs (100μs in rubidium). The camera is triggered to take a picture with an exposure that

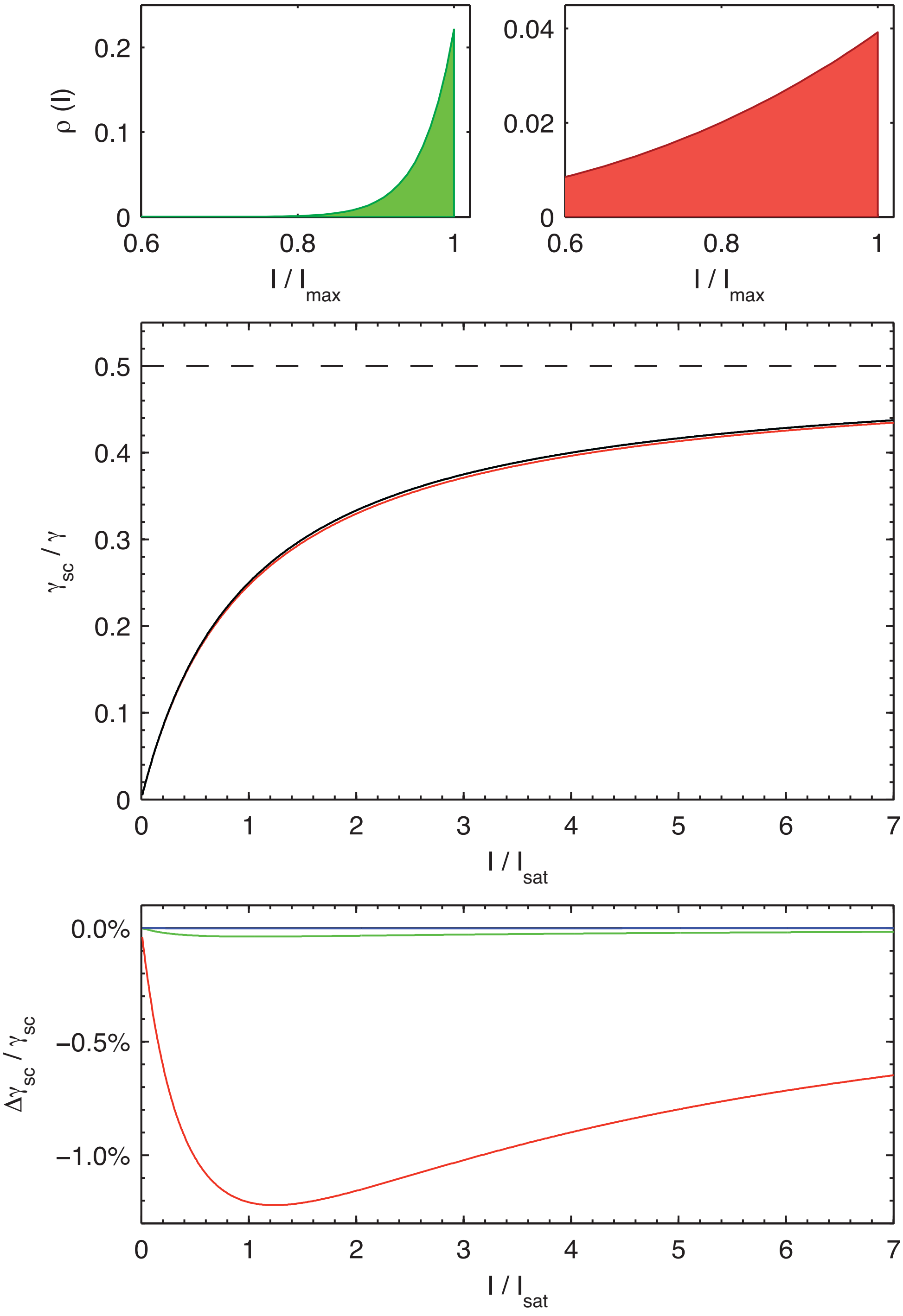

Figure 5.1: Effect of beam size on saturation curve shape. **top:** The green curve in the top left shows the relative atom number affected by a relative intensity $I/I_{\max}$ if the beam size u is five times larger than the size w of the atomic cloud. The red curve in the top right shows the same for the case of a beam that is only twice as wide as the cloud.
middle: After the changed average intensity has been absorbed into I_{eff}, the saturation curves for both beam sizes deviate very little from the curve for a homogenous intensity distribution (plotted in black)
bottom: Deviation of the scattering rate from the homogeneous case for several inhomogeneous distributions. red: $u = 2w$, green: $u = 5w$ and blue: $u = 10w$. It is worth noting that even for the red curve the maximum deviation is only 1.2%.

		Yb, $\lambda = 556\,\text{nm}$	Rb, $\lambda = 780\,\text{nm}$
angular collection efficiency	a_{ang}	$(2.03 \pm 0.09) \cdot 10^{-3}$	
window transmission	a_{wdw}	0.79 ± 0.01	0.91 ± 0.01
camera conversion factor	a_{cam}	0.066 ± 0.006	0.112 ± 0.012
total counts per photon	a_{tot}	$(1.06 \pm 0.16) \cdot 10^{-4}$	$(2.08 \pm 0.34) \cdot 10^{-4}$
natural linewidth	γ	$1.137\,\text{MHz}$	$38.11\,\text{MHz}$
exposure time	t	$500\,\mu\text{s}$	$100\,\mu\text{s}$
pixel count	$N_{\text{cam}}^{\text{max}}$	$(1.29 \pm 0.10) \cdot 10^{6}$	$(4.28 \pm 0.27) \cdot 10^{8}$
atom number	N_a	$(4.29 \pm 0.65) \cdot 10^{7}$	$(1.08 \pm 0.18) \cdot 10^{9}$

Table 5.1: Calibration factors and results for fluorescence-based atom counting in ytterbium and rubidium.

covers this time span. In rubidium it is necessary to switch on both the normal repumper and an extra beam that also repumps the atoms in the dark region.

All this is coordinated by the computer-based control program described in more detail in the appendix.

Without a magnetic field, the scattered photons should be evenly distributed over all spatial directions. Only a small fraction enters the imaging system and is detected by the camera. An additional fraction of this is absorbed or reflected by the chamber window and the lenses. The camera then creates a digital signal from the incident photons, depending on the CCD's quantum efficiency at the relevant wavelength and the settings and quality of the internal A/D-converters:

$$N_{\text{cam}} = \underbrace{a_{\text{CCD}} \cdot a_{\text{img}}}_{=a_{\text{cam}}} \cdot a_{\text{wdw}} \cdot a_{\text{ang}} \cdot N_{\text{ph}} = a_{\text{tot}} \cdot N_{\text{ph}} \tag{5.18}$$

The various factors have been measured for 556 nm and 780 nm and are given in table 5.1.

Now a complete equation for calculating the atom number from the pixel counts of the camera pictures can be found:

$$N_{\text{cam}}^{\text{max}} = a_{\text{tot}} \cdot N_{\text{ph}} = a_{\text{tot}} \cdot N \cdot \frac{\gamma}{2} t \tag{5.19}$$

$$N = \frac{2\, N_{\text{cam}}^{\text{max}}}{\gamma \cdot a_{\text{tot}} \cdot t} \tag{5.20}$$

$N_{\text{cam}}^{\text{max}}$ is the pixel count extrapolated to very large intensities according to equation 5.16.

5.1.3 Results

Figure 5.2 shows examples of the measurements in ytterbium and rubidium. Due to the much narrower linewidth in ytterbium, the MOT beams can provide roughly six times the saturation intensity. The pixel counts reach values close to the extrapolated maximum, which corresponds to an atom number of $N_{\text{Yb}} = (4.29 \pm 0.65) \cdot 10^{7}$.

In rubidium the effective saturation intensity is only reached near maximum laser power. This makes the extrapolation more critical. The final atom number of $N_{\text{Rb}} = (1.08 \pm 0.18) \cdot 10^{9}$ is comparable to the estimate for the single rubidium MOT in Batär (2005), which

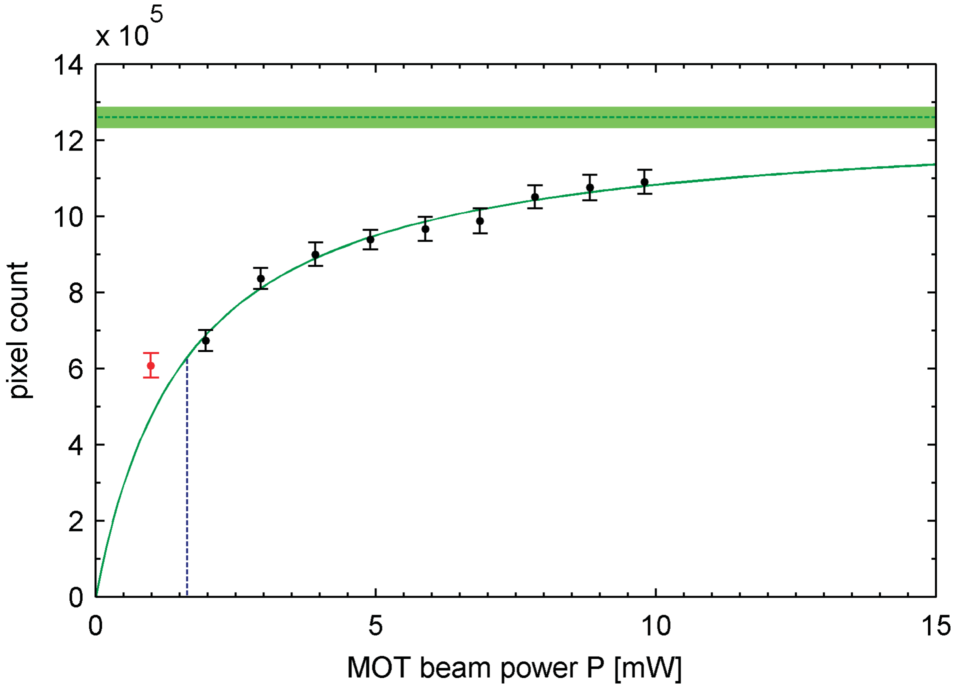

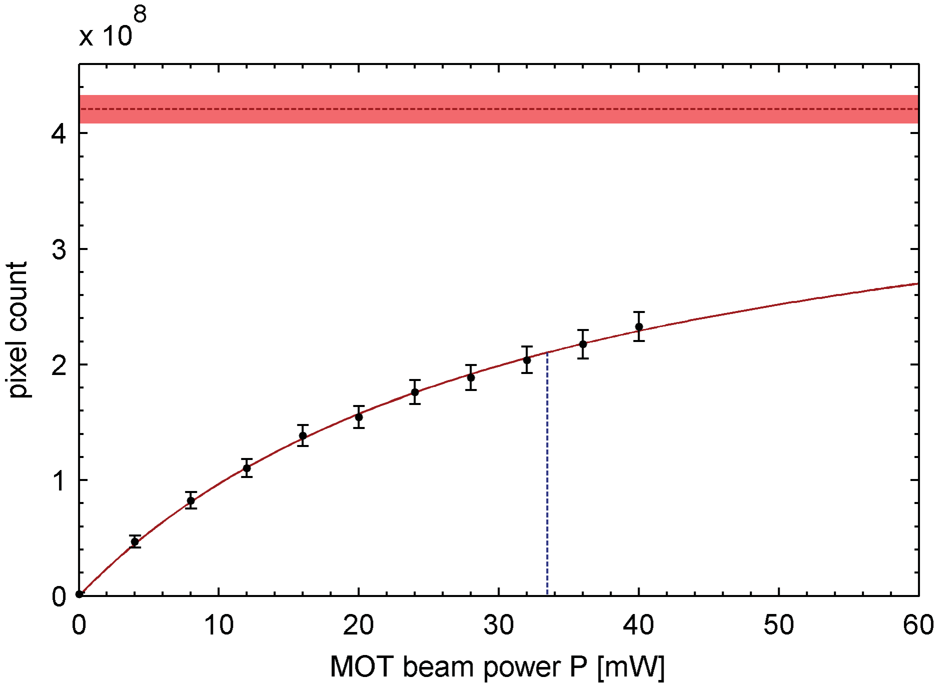

Figure 5.2: Saturation curves used for counting trapped Yb (top) and Rb (bottom) atoms. Pixel count near the trap region is plotted over total laser power at the MOT. Due to the narrow linewidth in ytterbium, the maximum intensity is high compared to the saturation intensity. In rubidium, the saturation intensity is only reached just below full power. In both cases the laser is resonant with the transition. The power corresponding to saturation intensity (as obtained from the fits) is marked by the vertical dashed line in both cases. The horizontal dashed lines indicates the extrapolated pixel count for high intensities with the green/red area indicating the range of uncertainty.
The red datapoint in the ytterbium curve was removed as an outlier.

shows that the chosen compromise in magnetic field gradient in the combined MOT does not dramatically affect the number of trapped rubidium atoms.

During the photoassociation experiments, the relative atom numbers are also monitored through the fluorescence from the trap. For increased sensitivity in ytterbium, the entire light from the imaging system is redirected to a photomultiplier tube. Scattered light from the rubidium MOT is focussed on a simple photodiode by a 1” lens.

5.2 Size and Temperature Measurements

Reliable imaging of the trapped atoms is difficult due to the effect of the magnetic fields. These create a Zeeman splitting that increases towards the outer regions of the trap. It is generally difficult to find the local proportionality between signal and atom density with enough precision to give definite values for the size of the trapped cloud.

Instead, the magnetic field currents and trapping beams are switched off and the cloud is allowed to expand ballistically until the fields have fallen off to insignificant values. The time required for this depends mostly on the ring-down circuits for the field coils. Details are given in Batär (2005, chapter 3.4.3). The measured decay times for the current in the MOT coils of $\tau_{\text{decay}} = 420\,\mu$s indicate that the field strenghts should be close to zero after a few milliseconds.

During this time the cloud size w increases from its initial value w_0 according to the equation (Ghezali et al., 1996; Kunze et al., 1997)

$$w_i(t) = \sqrt{w_{0,i}^2 + \frac{k_B\,T}{m}t^2} \qquad \text{with} \qquad i = [x, y, z] \tag{5.21}$$

After the desired expansion time has passed, the MOT lasers are set to resonance and the light is again turned on for a limited time to take a fluorescence picture. By varying the time between release from the trap and the picture, both the initial size and the temperature can be extracted from a fit, as shown in figures 5.3 and 5.4.

The temperatures obtained in this way differ noticeably between the radial and the axial directions of the trap, because the interaction of the atoms with the trap is somewhat stronger than the atom-atom interactions and the collision rate is not sufficient to reach a true thermal equilibrium. For the later calculations it is assumed that the deviations from a true thermal ensemble have less influence than the uncertainty in measurement and a single, averaged temperature is used. Since the experimental x-axis (in the radial plane of the chamber, see figure 4.1) points directly towards the camera, no measurements are possible here. Temperature and trap size for this axis are assumed to be identical to the other, visible radial axis z. This is therefore given twice the weight in the temperature average:

$$T^{\text{avg}} = \frac{1}{3}(T^x + T^y + T^z) \tag{5.22}$$

$$= \frac{1}{3}(2\,T^r + T^a) \tag{5.23}$$

The resulting temperatures are $T_{\text{Yb}}^{\text{avg}} = 513 \pm 81 \mu\text{K}$ for ytterbium and $T_{\text{Rb}}^{\text{avg}} = 341 \pm 28 \mu\text{K}$ for rubidium. Detailed numerical results are gathered in table 5.2. Due to the compromises

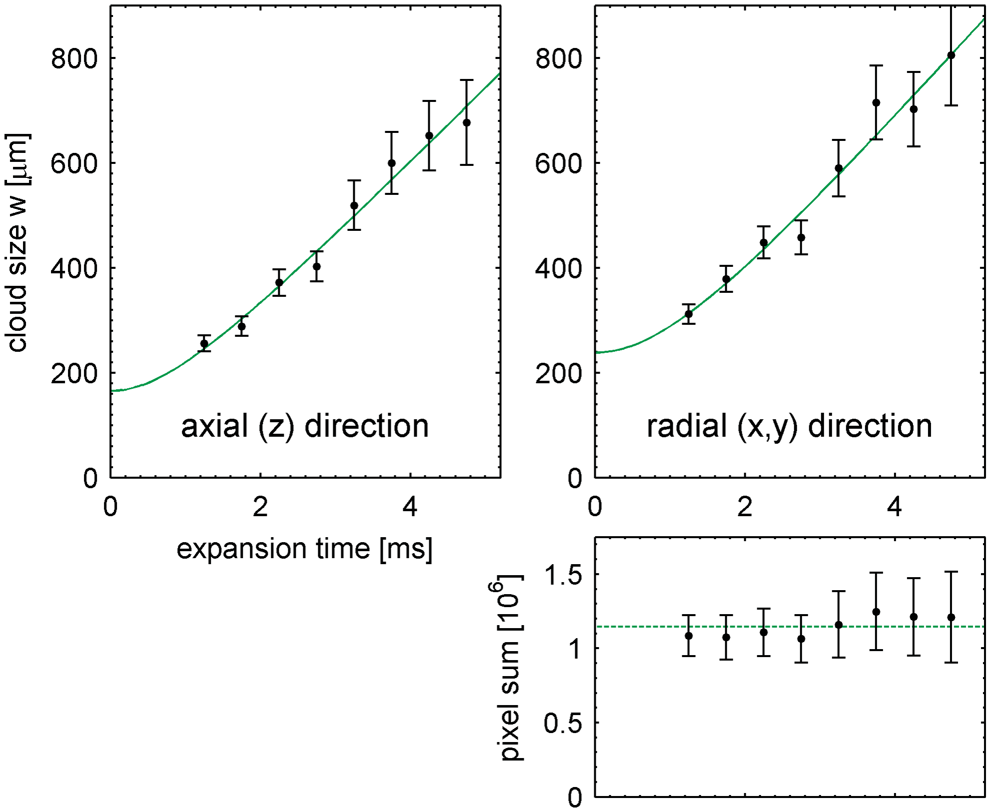

Figure 5.3: Time-of-flight temperature measurement in ytterbium. The temperatures found for the axial (top left) and radial (top right) expansion are consistently different: Axially, the temperature obtained from the fit is $T^a_{\mathrm{Yb}} = 439\,\mu$K and the initial cloud size is $w^a_{0,\mathrm{Yb}} = 165\,\mu$m. Radial values are $T^r_{\mathrm{Yb}} = 550\,\mu$K and $w^r_{0,\mathrm{Yb}} = 165\,\mu$m. Due to the high relative illumination intensity, the total pixel count becomes stable after about 1 ms, as the broadened line width is larger than the remaining Zeeman shifts.

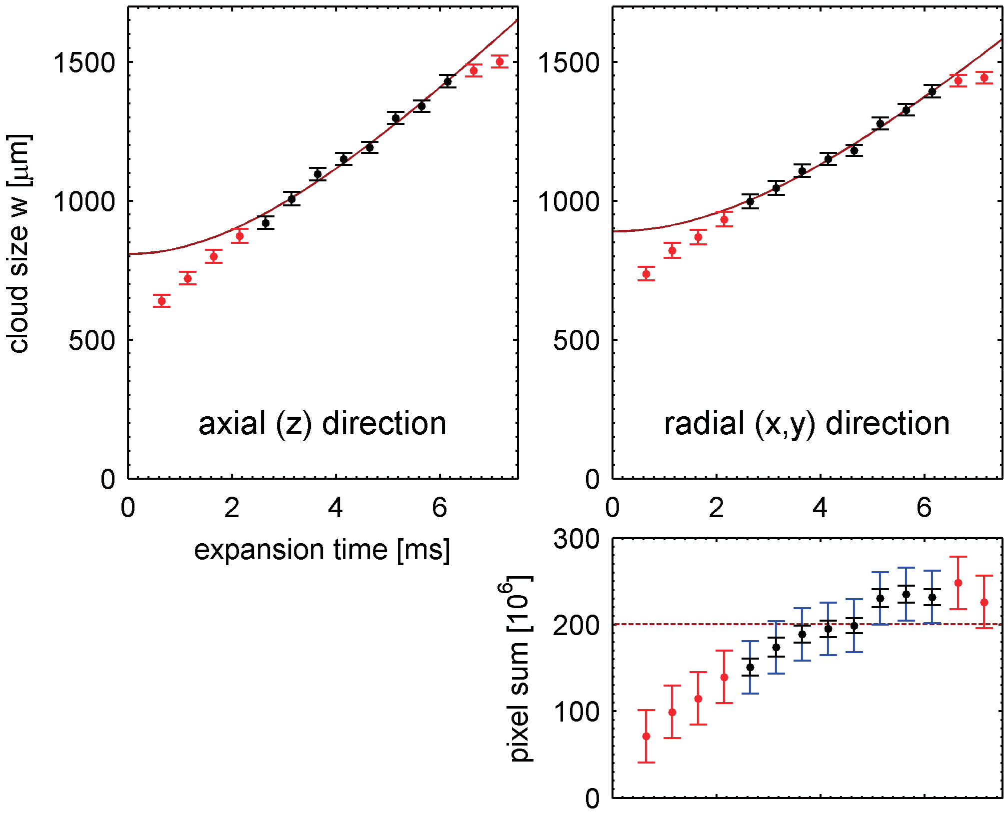

Figure 5.4: Time-of-flight temperature measurement in rubidium. At expansion times less than 3 ms the drop in total pixel count (bottom right) indicates reduced fluorescence due to remaining magnetic fields. Due the lower saturation broadening of the rubidium transition, the fields require more time to decay to a negligible level than for ytterbium. Since the Zeeman shift particularly affects the outer regions of the cloud, the data points marked in red have been excluded from the cloud size fits. At expansion times longer than 6 ms, the outer atoms begin to move into weakly illuminated regions. This leads to a stagnation of the perceived cloud size. The last two pictures have also been excluded from the fit for this reason. In the diagram showing the total pixel count (bottom right) the black error bars indicate the per-image counting uncertainty, while the extended blue bars include the shot-to-shot fluctuations. The latter are consistent with the relative uncertainty given for the pixel count in table 5.1. Results obtained from the fits are $T^a_{\mathrm{Rb}} = 386\ \mu$K, $w^a_{0,\mathrm{Rb}} = 809\ \mu$m axially (top left diagram) and $T^r_{\mathrm{Rb}} = 318\ \mu$K, $w^r_{0,\mathrm{Rb}} = 890\ \mu$m radially (top right).

		radial (x,y)	axial (z)	averaged
pixel size (incl. optics)	[μm]	(y:) 20.28 ± 0.08	20.532 ± 0.08	
ytterbium				
temperature	[μK]	550 ± 53	439 ± 31	513 ± 81
trap size (w)	[μm]	238 ± 33.6	165 ± 27	211 ± 20
trap size (FWHM)	[mm]	0.56 ± 0.08	0.39 ± 0.07	0.50 ± 0.05
atom number				$(4.29 \pm 0.65) \cdot 10^7$
peak density	[m^{-3}]			$(2.91 \pm 0.44) \cdot 10^{17}$
rubidium				
temperature	[μK]	318 ± 14	386 ± 20	341 ± 28
trap size (w)	[μm]	890 ± 18	809 ± 28	862 ± 21
trap size (FWHM)	[mm]	2.10 ± 0.04	1.90 ± 0.07	2.03 ± 0.05
atom number				$(1.08 \pm 0.18) \cdot 10^9$
peak density	[m^{-3}]			$(1.07 \pm 0.18) \cdot 10^{17}$
ytterbium w. Rb				
atom number				$(1.81 \pm 0.38) \cdot 10^6$
peak density	[m^{-3}]			$(1.23 \pm 0.27) \cdot 10^{16}$

Table 5.2: Results of temperature and trap size measurements. Numbers for ytterbium are for the isoptope ^{176}Yb. The FWHM-diameter is $2.355\,w$.

required in the combined trap and the main goals of reaching high densities and atom numbers, the temperatures are relatively high compared to the Doppler temperatures

$$T^d = \frac{\hbar\,\gamma}{2k_B} \tag{5.24}$$

of $T^d_{\mathrm{Yb}} = 4.3\,\mu$K and $T^d_{\mathrm{Rb}} = 146\,\mu$K.

An important value is the peak density of the rubidium cloud as this determines how often an ytterbium atom gets close to a rubidium atom. Only then can a molecule be formed by photoassociation. The density in the trap is found to be described well by the Gaussian distribution presented earlier:

$$\rho(r,z) = \frac{N}{(w_0^r)^2\,(w_0^a)\,(2\pi)^{3/2}}\; e^{-\frac{x^2}{2(w_0^r)^2}}\; e^{-\frac{y^2}{2(w_0^r)^2}}\; e^{-\frac{z^2}{2(w_0^a)^2}} \tag{5.25}$$

w_0^r and w_0^a are the radial and axial cloud sizes. The peak density at the center of the trap is then

$$\rho^{\max} = \frac{N}{(w_0^r)^2\,(w_0^a)\,(2\pi)^{3/2}} \tag{5.26}$$

and an effective cloud size w^{avg} can be found that yields the same peak density for a rotationally symmetrical cloud:

$$w^{\mathrm{avg}} = \sqrt[3]{(w^r)^2\,(w^a)} \tag{5.27}$$

For rubidium, $N_{\mathrm{Rb}} = 1.08 \cdot 10^9$ atoms are trapped in a cloud with an effective FWHM diameter of $d_{\mathrm{Rb}} = 2.03$ mm, resulting in a peak density of $\rho^{\max}_{\mathrm{Rb}} = 1.07 \cdot 10^{17}$ m^{-3}. In ytterbium $N_{\mathrm{Yb}} = 4.29 \cdot 10^7$ atoms in a trapped cloud of $d_{\mathrm{Yb}} = 0.50\,\mathrm{mm}$ give a similar peak density of $\rho_{\mathrm{Yb}}^{\max} = 2.91 \cdot 10^{16}\,\mathrm{m}^{-3}$.

5.3 Trap Interactions

For ytterbium, the numbers given are valid only in the absence of the rubidium trap. As soon as both traps are loaded simultaneously, the number of ytterbium atoms is reduced by a factor of more than 20. This suppression of the ytterbium trap as the rubidium trap loads is shown in figure 5.5.

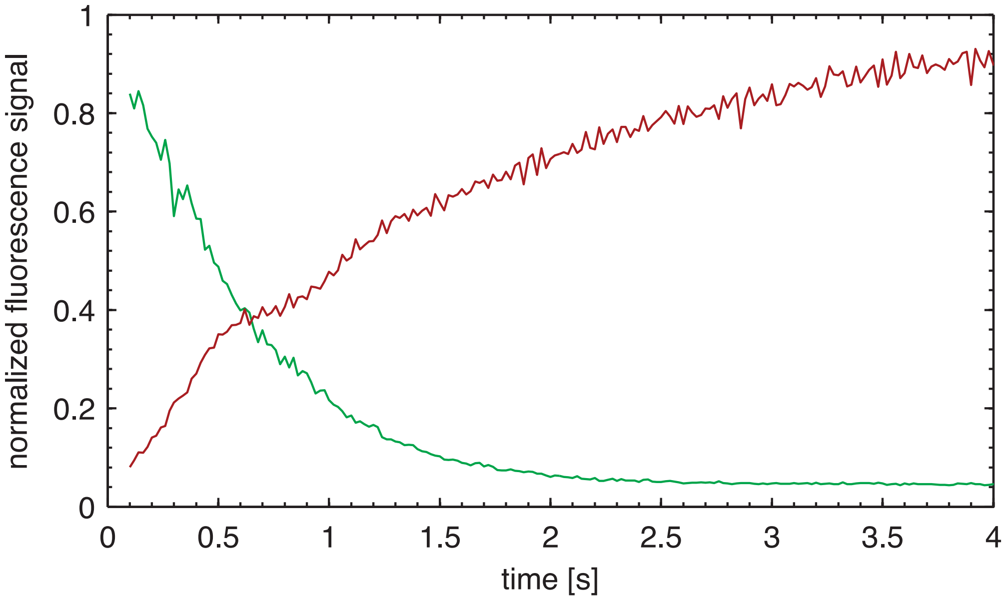

Figure 5.5: Gradual suppression of the ytterbium trap (green) as the rubidium trap (red) loads. The graph shows fluorescence values taken during an interaction measurement corrected for signal background and normalized.

The experiments described in Tassy (2007) did not see significant losses during thermalization measurements of several seconds duration at similar or higher densities of $\rho_{\mathrm{Rb}}^{\max} \approx 5 \cdot 10^{17}\,\mathrm{m}^{-3}$. Since these experiments were performed with the rubidium atoms in a magnetic trap and ytterbium in an optical dipole trap however, all interactions occurred between atoms in the electronic ground state.

Switching between a bright rubidium MOT and the forced dark-spot MOT, it was found that the losses do not depend on the electronic state of the rubidium atoms. Otherwise, the $> 90\%$ reduction of the excited state population in the dark-spot MOT would have greatly reduced the losses, as seen in other experiments.

This leaves the electronic state of ytterbium. Presumably there exists a fairly efficient mechanism converting at least part of the excitation energy of ytterbium into kinetic energy. Since the available energy corresponding to $17992\,\mathrm{cm}^{-1}$ is much higher than the trap depth (see chapter 4.2.1), both atoms will be lost from the trap. Any further collisions with the resulting fast atoms most likely also lead to atom loss. In this way, the majority of the energy is carried away by the escaping atoms and no heating of the rubidium cloud is detected.

The reduced atom number in ytterbium makes it impossible to measure reliable atom numbers and temperatures with the current imaging system. However, since any given atom -rubidium or ytterbium- has a similar chance of being hit by one of the fast atoms and there is no discernible effect on the rubidium cloud, it can be assumed that temperature and cloud size of ytterbium also remain unchanged. The ytterbium density then simply drops by the same fraction as the atom number, while its relative distribution is preserved.

5.3.1 Automated Measurement

The photoassociation process is influenced by many factors. To make it easier to track intentional and unintentional changes, a system was developed to measure certain properties with good repeatability. This consists of a specific "pattern" (`MOT_interaction_red_green`) in the control program, describing a sequence of different states for the trap and an analysis program in Matlab (`interact_06.m`) that interprets the resulting fluorescence data. The recorded data consists of the rubidium photodiode voltage U_{Rb} and the ytterbium photomultiplier signal U_{Yb} captured by the data-logging program.

Step by step the experiment is put through the following phases:

phase	period	function
-1	2 s	*init:* Sets experiment to normal operating conditions for a reproducible starting point. The rubidium MOT is loaded during this time. No measurements performed.
0	1 s	*all off:* All lasers are turned off. The rapid drop in rubidium fluorescence is used by the analysis program to mark the start of the main sequence. No measurements performed.
1	20 s	*load Rb MOT:* Ytterbium atom beam and all lasers are blocked by their mechanical shutters. The rubidium lasers are turned on and the trap loads. It is kept loaded for the phases 2-6. Measurements: Loading time τ_{Rb} from fitted exponential function. Final value $U^{1}_{\mathrm{Rb}} = U^{\mathrm{cloud}}_{\mathrm{Rb}} + U^{\mathrm{bg:bright}}_{\mathrm{Rb}}$ from average of data for $t > 3\,\tau_{\mathrm{Rb}}$. Average value $U^{1}_{\mathrm{Yb}} = U^{\mathrm{bg:Rb\text{-}trap}}_{\mathrm{Yb}} + U^{\mathrm{bg:dark}}_{\mathrm{Yb}}$. It is found that the number of atoms in the Rb trap has no effect on the signal.
2	10 s	*Yb atoms on:* The unslowed Yb atom beam is turned on and is found to cause a slight loss of Rb atoms. No measurements performed.

continued on next page

phase	period	function
3	10 s	*Yb slower laser on:* The Yb atom beam is turned off and the 399 nm slowing laser is turned on. No data from this phase was used because it is unclear when exactly the slow mechanical shutter stops the flow of atoms. No measurements performed.
4	10 s	*Yb MOT lasers on:* The 556 nm trapping lasers are turned on to measure their contribution to the background signals. Measurements: The Rb signal is found to be unaffected: $U^4_{\mathrm{Rb}} \approx U^1_{\mathrm{Rb}}$. Average value $U^4_{\mathrm{Yb}} = U^{\text{bg:Yb-trap}}_{\mathrm{Yb}} + U^{\text{bg:Rb-trap}}_{\mathrm{Yb}} + U^{\text{bg:dark}}_{\mathrm{Yb}}$
5	10 s	*Yb atoms and slower on:* Yb atom beam and 399 nm slower laser are turned on to measure their contribution to the Yb background signal. The Rb losses are similar to those caused by the unslowed beam. Measurements: Average value $U^5_{\mathrm{Yb}} = U^{\text{bg:Yb-beam}}_{\mathrm{Yb}} + U^{\text{bg:Rb-trap}}_{\mathrm{Yb}} + U^{\text{bg:dark}}_{\mathrm{Yb}}$ The Yb slower laser is assumed not to contribute to the Rb background signal.
6	20 s	*all on:* All elements of the Yb trap are turned on and the trap loads, although the final atom number is strongly reduced by the presence of Rb. Measurements: Loading time with suppression $\tau^{\text{supp}}_{\mathrm{Yb}}$ from fitted “exponential + linear” function, accounting for slow changes of the ytterbium equilibrium atom number. These are most likely caused by changes in trap overlap as the various AOMs thermalize. Final values from fit (Yb) / from average for $t > 3\,\tau^{\text{supp}}_{\mathrm{Yb}}$ (Rb): $U^6_{\mathrm{Rb}} = U^{\text{cloud}}_{\mathrm{Rb}} + U^{\text{bg:Yb-trap}}_{\mathrm{Rb}} + U^{\text{bg:bright}}_{\mathrm{Rb}}$ $U^6_{\mathrm{Yb}} = U^{\text{cloud}}_{\mathrm{Yb}} + U^{\text{bg:Rb-trap}}_{\mathrm{Yb}} + U^{\text{bg:bright}}_{\mathrm{Yb}}$
7	4 s	*all off:* All lasers and both atom beams are turned off to measure the dark background signals. Measurements: $U^7_{\mathrm{Rb}} = U^{\text{bg:dark}}_{\mathrm{Rb}}$ $U^7_{\mathrm{Yb}} = U^{\text{bg:dark}}_{\mathrm{Yb}}$

continued on next page

phase	period	function
8	20 s	*load Yb:* The Yb trap is loaded with the Rb beam and trap turned off. Measurements: Average $U^8_{\mathrm{Rb}} = U^{\mathrm{bg:Yb\text{-}trap}}_{\mathrm{Rb}} + U^{\mathrm{bg:dark}}_{\mathrm{Rb}}$ from average of data. It is found that the number of atoms in the Yb trap does not affect the Rb signal. Loading time τ_{Yb} and final $U^8_{\mathrm{Yb}} = U^{\mathrm{cloud}}_{\mathrm{Yb}} + U^{\mathrm{bg:bright}}_{\mathrm{Yb}}$ from fitted exponential function.
9	6 s	*Rb atoms on:* The unslowed Rb atom beam is turned on and is found to cause a slight loss of Yb atoms. No measurements performed.
10	6 s	*Rb slower laser on:* Due to the slow shutters for the atomic beams, data during this phase is again unreliable. No measurements performed.
11	6 s	*Rb MOT and repumping lasers on:* The effect of the various trapping lasers for Rb on the Yb fluorescence signal is found to be negligible in the absence of the Rb atom beam. Measurements: Average $U^{11}_{\mathrm{Rb}} = U^{\mathrm{bg:Rb\text{-}trap}}_{\mathrm{Rb}} + U^{\mathrm{bg:Yb\text{-}trap}}_{\mathrm{Rb}} + U^{\mathrm{bg:dark}}_{\mathrm{Rb}}$.
12	6 s	*Rb atoms and slower on:* The slowed beam of Rb atoms appears to have a slightly smaller effect on the Yb trap than the unslowed one, most likely due to its larger dispersion and the resulting drop in flux at the trap position. Measurements: Average $U^{12}_{\mathrm{Rb}} = U^{\mathrm{bg:Rb\text{-}beam}}_{\mathrm{Rb}} + U^{\mathrm{bg:Yb\text{-}trap}}_{\mathrm{Rb}} + U^{\mathrm{bg:dark}}_{\mathrm{Rb}}$.
13	20 s	*all on:* A final phase with both traps turned on again serves to confirm the suppressed fluorescence values and shows the reduction of the number of Yb atoms as the Rb trap gradually loads. Measurements: Loading time with suppression $\tau^{\mathrm{supp}}_{\mathrm{Rb}}$ from fitted exponential function. Final values from averaged data for $t > 3\,\tau^{\mathrm{supp}}_{\mathrm{Rb}}$: $U^{13}_{\mathrm{Rb}} = U^{\mathrm{cloud}}_{\mathrm{Rb}} + U^{\mathrm{bg:Yb\text{-}trap}}_{\mathrm{Rb}} + U^{\mathrm{bg:bright}}_{\mathrm{Rb}}$ $U^{13}_{\mathrm{Yb}} = U^{\mathrm{cloud}}_{\mathrm{Yb}} + U^{\mathrm{bg:Rb\text{-}trap}}_{\mathrm{Yb}} + U^{\mathrm{bg:bright}}_{\mathrm{Yb}}$

The entire sequence yields fluorescence signals as shown in figure 5.6. Analyzing the signals over the various phases makes it possible to identify the various components that contribute to the total measured signal but are not caused by the fluorescence of the trapped atoms. The signal voltages will be proportional to the atom number in the trap only after the reconstructed signal backgrounds have been subtracted. The individual contributions

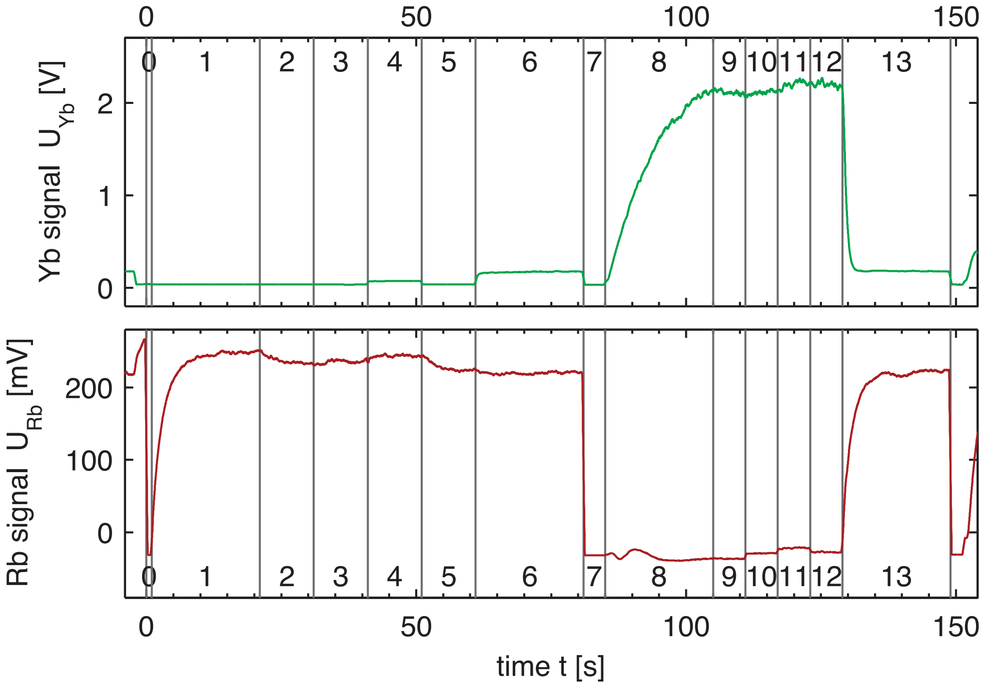

Figure 5.6: Fluorescence signals $U_{\mathrm{Yb}}(t)$ (green, top) and $U_{\mathrm{Rb}}(t)$ (red, bottom) taken in an automatic interaction sequence. Numbers mark the phases as described in the text.

can be found as follows:

$$U_{\mathrm{Rb}}^{\mathrm{bg:dark}} = U_{\mathrm{Rb}}^{7} \tag{5.28}$$

$$U_{\mathrm{Rb}}^{\mathrm{bg:Yb\text{-}trap}} = U_{\mathrm{Rb}}^{8} - U_{\mathrm{Rb}}^{7} \tag{5.29}$$

$$U_{\mathrm{Rb}}^{\mathrm{bg:Rb\text{-}trap}} = U_{\mathrm{Rb}}^{11} - U_{\mathrm{Rb}}^{7} \tag{5.30}$$

$$U_{\mathrm{Rb}}^{\mathrm{bg:Rb\text{-}beam}} = U_{\mathrm{Rb}}^{12} - U_{\mathrm{Rb}}^{7} \tag{5.31}$$

$$U_{\mathrm{Yb}}^{\mathrm{bg:dark}} = U_{\mathrm{Yb}}^{7} \tag{5.32}$$

$$U_{\mathrm{Yb}}^{\mathrm{bg:Rb\text{-}trap}} = U_{\mathrm{Yb}}^{1} - U_{\mathrm{Yb}}^{7} \tag{5.33}$$

$$U_{\mathrm{Yb}}^{\mathrm{bg:Yb\text{-}beam}} = U_{\mathrm{Yb}}^{4} - U_{\mathrm{Yb}}^{7} \tag{5.34}$$

$$U_{\mathrm{Yb}}^{\mathrm{bg:Yb\text{-}trap}} = U_{\mathrm{Yb}}^{5} - U_{\mathrm{Yb}}^{7} \tag{5.35}$$

When only one trap is operated, the relevant trapped-atom contributions to the total signals U_{Rb} and U_{Yb} are

$$U_{\mathrm{Rb}}^{\mathrm{cloud}} = U_{\mathrm{Rb}} - U_{\mathrm{Rb}}^{\mathrm{bg:bright}} = U_{\mathrm{Rb}} - (U_{\mathrm{Rb}}^{\mathrm{bg:dark}} + U_{\mathrm{Rb}}^{\mathrm{bg:Rb\text{-}trap}} + U_{\mathrm{Rb}}^{\mathrm{bg:Rb\text{-}beam}}) \tag{5.36}$$

$$U_{\mathrm{Yb}}^{\mathrm{cloud}} = U_{\mathrm{Yb}} - U_{\mathrm{Yb}}^{\mathrm{bg:bright}} = U_{\mathrm{Yb}} - (U_{\mathrm{Yb}}^{\mathrm{bg:dark}} + U_{\mathrm{Yb}}^{\mathrm{bg:Yb\text{-}trap}} + U_{\mathrm{Yb}}^{\mathrm{bg:Yb\text{-}beam}}) \tag{5.37}$$

	^{176}Yb + ^{87}Rb		^{174}Yb + ^{87}Rb	
parameter	ytterbium	rubidium	ytterbium	rubidium
background levels				
$U^{\text{bg:zero}}$ [mV]	88±12	-9.8±5.5	88±16	-6.2±7.8
$U^{\text{bg:both}}$ [mV]	90±11	-11.2±5.5	89±17	-4.2±7.7
maximum levels				
U^{full} [mV]	2269±97	162±65	3680±360	147±65
U^{supp} [mV]	96±14	152±56	143±24	137±57
$r_{\text{supp}} = U^{\text{supp}}/U^{\text{full}}$	0.042±0.006	0.94±0.04	0.039±0.007	0.94±0.02
loading times				
τ^{full} [s]	6.52±1.98	1.26±0.42	5.77±0.87	1.33±0.48
τ^{supp} [s]	0.26±0.07	1.04±0.34	0.21±0.05	1.26±0.38
$r'_{\text{supp}} = \tau^{\text{supp}}/\tau^{\text{full}}$	0.042±0.011	0.84±0.11	0.037±0.011	0.97±0.09
derived properties				
$N^{\text{full}}[10^6]$	42.9±6.5	1080±180	70±13	1080±180
$N^{\text{supp}}[10^6]$	1.81±0.38	1020±170	2.72±0.72	1020±170
$R^{\text{load}}[10^6/s]$	6.7±1.6	920±240	12.6±2.8	808±212
$L^{\text{YbRb}}[10^6/s]$	6.5±1.6	52±36	12.1±2.7	48±23
estimates				
loss rate $L_0[10^6/s]$	6.4		10.9	
loss propagation a_{amp}	1.01	8.0	1.11	4.4

Table 5.4: Averaged background and signal voltages from the automated interaction measurements taken over the course of the experiments. For directly measured values the uncertainties given are the standard deviations of the set of datapoints. Atom numbers for ^{176}Yb and ^{87}Rb were taken from the calculations in chapter 5.1, the atom number for ^{174}Yb was estimated by comparing the fluorescence signal for the unsuppressed trap U^{full} to that in ^{176}Yb. Uncertainties for the derived values for the suppressed atom numbers N^{supp}, the loading rate R^{load} and the extra loss rate due to ytterbium-rubidium collisions L^{YbRb} were found using error propagation.

For the photoassociation experiments described in the following, the additional background caused by the operation of the other trap needs to be taken into account. Fortunately its dependence on the number of atoms in that trap is found to be negligible:

$$U^{\text{cloud}}_{\text{Rb}} = U_{\text{Rb}} - U^{\text{bg:both}}_{\text{Rb}} = U_{\text{Rb}} - (U^{\text{bg:bright}}_{\text{Rb}} + U^{\text{bg:Yb-trap}}_{\text{Rb}}) \tag{5.38}$$

$$U^{\text{cloud}}_{\text{Yb}} = U_{\text{Yb}} - U^{\text{bg:both}}_{\text{Yb}} = U_{\text{Yb}} - (U^{\text{bg:bright}}_{\text{Yb}} + U^{\text{bg:Rb-trap}}_{\text{Yb}}) \tag{5.39}$$

Table 5.4 lists averages for the background and signal levels (both for the single traps: U^{full} and for the combined trap: U^{supp}) found from measurements taken over the course of the experiments. The trap loss spectra in chapter 6.3 were constructed using the results from the closest interaction measurement. However, it was repeatedly found that the values changed considerably over a time of only an hour. The uncertainty values found from the fluctuations of the measurements and given in the table should therefore be assumed to apply to the trap loss results as well.

5.4 Interpretation of Loading and Loss Rates

The suppression of the ytterbium trap by the presence of rubidium shows that a combination of different loss mechanisms limits the atom number in the traps. Photoassociation will also manifest itself as an additional atom loss. In order to separate the various effects and obtain a value for the photoassociation rate, a simple rate equation model for the equilibrium atom numbers is derived in this chapter.

5.4.1 Simple Rate Equation Model

The description of the loading and decay of the traps can be done in the form of rate equations:

$$\dot{N}_{\mathrm{Yb}}(t) = R_{\mathrm{Yb}}^{\mathrm{load}} - R_{\mathrm{Yb}}^{\mathrm{loss}}\left(\rho_{\mathrm{Yb}}\left(\vec{x},t\right),\rho_{\mathrm{Rb}}\left(\vec{x},t\right)\right) \tag{5.40}$$

$$\dot{N}_{\mathrm{Rb}}(t) = R_{\mathrm{Rb}}^{\mathrm{load}} - R_{\mathrm{Rb}}^{\mathrm{loss}}\left(\rho_{\mathrm{Yb}}\left(\vec{x},t\right),\rho_{\mathrm{Rb}}\left(\vec{x},t\right)\right) \tag{5.41}$$

where R^{load} is the loading rate for the respective element, assumed to be constant over time and R^{loss} is the loss rate which at each time t depends on the spatial density distributions $\rho_{\mathrm{Yb}}\left(\vec{x},t\right)$ and $\rho_{\mathrm{Rb}}\left(\vec{x},t\right)$ in a nontrivial way. A full theory would need to take into account the various collisions between two and more atoms of identical or different elements in both ground and electronically excited states. This would result in a system of complex differential equations even if the various collisional parameters could be determined with sufficient confidence and is beyond the scope of this thesis.

Certain simplifications nevertheless make it possible to gain an understanding of the behavior of the rubidium-ytterbium mixture. The most important of these is to neglect any interaction of trapped atoms of the same species. The atom number in a single-species trap is then limited by the balance between the loading rate and the losses through collisions with the hot background gas, atoms randomly moving out of the trapping region or being transferred to untrapped electronic states. A secondary effect is that the shape of the cloud then does not depend on the atom number and the density distribution becomes

$$\rho(\vec{x},t) = N(t)\cdot\tilde{\rho}(\vec{x}). \tag{5.42}$$

The dominant contribution from rubidium-ytterbium interactions will be collisions between one atom of each species. The resulting rate equations then have the form

$$\dot{N}_{\mathrm{Yb}}(t) = R_{\mathrm{Yb}}^{\mathrm{load}} - c_{\mathrm{Yb}}\left(\int \rho_{\mathrm{Yb}}(\vec{x},t)\,d\vec{x}\right) - c_{\mathrm{Yb\,Rb}}\left(\int \rho_{\mathrm{Yb}}(\vec{x},t)\cdot\rho_{\mathrm{Rb}}(\vec{x},t)\,d\vec{x}\right) \tag{5.43}$$

$$\begin{aligned} &= R_{\mathrm{Yb}}^{\mathrm{load}} - c_{\mathrm{Yb}}\cdot N_{\mathrm{Yb}}(t)\overbrace{\int \tilde{\rho}_{\mathrm{Yb}}(\vec{x})\,d\vec{x}}^{=1} \\ &\quad - c_{\mathrm{Yb\,Rb}}\cdot N_{\mathrm{Yb}}(t)\cdot N_{\mathrm{Rb}}(t)\int \tilde{\rho}_{\mathrm{Yb}}(\vec{x})\cdot\tilde{\rho}_{\mathrm{Rb}}(\vec{x})\,d\vec{x} \qquad . \end{aligned} \tag{5.44}$$

(similar for rubidium) and can be simplified further by absorbing the constant overlap integrals for the rubidium and ytterbium densities into a new loss coefficient $\tilde{c}$:

$$\dot{N}_{\mathrm{Yb}}(t) = R_{\mathrm{Yb}}^{\mathrm{load}} - c_{\mathrm{Yb}} \cdot N_{\mathrm{Yb}}(t) - \tilde{c}_{\mathrm{Yb\,Rb}} \cdot N_{\mathrm{Yb}}(t) \cdot N_{\mathrm{Rb}}(t) \tag{5.45}$$

$$\dot{N}_{\mathrm{Rb}}(t) = R_{\mathrm{Rb}}^{\mathrm{load}} - c_{\mathrm{Rb}} \cdot N_{\mathrm{Rb}}(t) - \tilde{c}_{\mathrm{Rb\,Yb}} \cdot N_{\mathrm{Rb}}(t) \cdot N_{\mathrm{Yb}}(t) \tag{5.46}$$

These are still coupled differential equations, but the strong imbalance in atom numbers makes it possible to separate them without sacrificing too much accuracy. After turning on the ytterbium trap, the rubidium atom number drops by only around 6% and can therefore be treated as constant in equation 5.45. Since this removes the circular effect of the rubidium numbers influencing the ytterbium numbers which in turn affect the rubidium numbers, the whole system will quickly settle to an equilibrium state. Using the equilibrium ytterbium atom number $N_{\mathrm{eq:Yb}}$ as a constant value for $N_{\mathrm{Yb}}(t)$ in equation 5.46 is not quite as good an approximation, but it will still yield good results as long as the rubidium trap is not depleted far enough for the ytterbium atom number to recover to near undisturbed levels. The final set of equations is then (in slightly reorganized form)

$$\dot{N}_{\mathrm{Yb}}(t) = R_{\mathrm{Yb}}^{\mathrm{load}} - (c_{\mathrm{Yb}} + \tilde{c}_{\mathrm{Yb\,Rb}} \cdot N_{\mathrm{eq:Rb}}) \cdot N_{\mathrm{Yb}}(t) \tag{5.47}$$

$$\dot{N}_{\mathrm{Rb}}(t) = R_{\mathrm{Rb}}^{\mathrm{load}} - (c_{\mathrm{Rb}} + \tilde{c}_{\mathrm{Rb\,Yb}} \cdot N_{\mathrm{eq:Yb}}) \cdot N_{\mathrm{Rb}}(t) \tag{5.48}$$

The exponential function fitted to the loading curves during the interaction measurements constitutes a solution to this:

$$N(t) = N_{\max} \cdot \left(1 - e^{-t/\tau}\right) \tag{5.49}$$

$$\Longrightarrow \dot{N}(t) = \frac{N_{\max}}{\tau} \cdot e^{-t/\tau} \tag{5.50}$$

Inserting into equations 5.47 and 5.48 shows the following relationships (given for ytterbium, but equivalent for rubidium):

$$\tau_{\mathrm{Yb}} = \frac{1}{c_{\mathrm{Yb}} + \tilde{c}_{\mathrm{Yb\,Rb}} \cdot N_{\mathrm{eq:Rb}}} \tag{5.51}$$

$$N_{\max} = R_{\mathrm{Yb}}^{\mathrm{load}} \cdot \tau_{\mathrm{Yb}} \tag{5.52}$$

$$\Longrightarrow R_{\mathrm{Yb}}^{\mathrm{load}} = \frac{N_{\max}}{\tau_{\mathrm{Yb}}} \tag{5.53}$$

This makes it possible to calculate loading rates from the atom number measurements described earlier. These are found to be on the order of $9 \cdot 10^8$ atoms per second for ^{87}Rb, $7 \cdot 10^6$ atoms per second for ^{176}Yb and $12 \cdot 10^6$ atoms per second for ^{174}Yb. Detailed values are given in table 5.4. The different rubidium loading rates found during the experimental series with ^{176}Yb and with ^{174}Yb are consistent to within the stated accuracy. The same is true for the loading rates of the ytterbium isotopes if the relative abundances of 12.8% for ^{176}Yb and 31.8% for ^{174}Yb are taken into account, although changes in alignment, oven temperatures or trap efficiency can easily cause additional changes of the loading rate.

Another indication for the validity of the simple model presented here is that it predicts a constant ratio between the loading-time τ and the maximum atom number N_{max} reached. In other words, any suppression of the atom number by interspecies collisions is expected to be accompanied by a loading time reduction by the same factor. This is shown in the table in the form of suppression factors $r_{\mathrm{supp}} = U^{\mathrm{supp}}/U^{\mathrm{full}}$ and $r'_{\mathrm{supp}} = \tau^{\mathrm{supp}}/\tau^{\mathrm{full}}$ that are well in agreement for all explored combinations.

Finally, figure 5.7 shows some measured loading curves along with the fits according to the model. The only noticeable deviations occur for very low loading states of the rubidium trap. This is most likely caused by neglecting the additional losses caused by rubidium-rubidium collisions. These will introduce additional losses at high densities and limit the achievable atom number. The resulting change in the loading curve causes the fitted curve to give a somewhat low initial loading rate. However, it still describes the near-equilibrium regime well if the calculated loading rates are understood to be effective values that include the extra losses.

5.4.2 Loss Rate from Interspecies Collisions

After equilibrium has been reached, the total loss rate L is equal to the loading rate. For ytterbium in the absence of trapped rubidium this can be written as

$$R_{\mathrm{Yb}}^{\mathrm{load}} = L_{\mathrm{Yb}} = c_{\mathrm{Yb}} \cdot N_{\mathrm{Yb}}^{\mathrm{full}} \tag{5.54}$$

In the presence of rubidium this becomes

$$\begin{aligned}
R_{\mathrm{Yb}}^{\mathrm{load}} &= L_{\mathrm{Yb}} + L_{\mathrm{Yb\,Rb}} && (5.55)\\
&= c_{\mathrm{Yb}} \cdot N_{\mathrm{Yb}}^{\mathrm{supp}} + L_{\mathrm{Yb\,Rb}} && (5.56)\\
&= c_{\mathrm{Yb}} \cdot N_{\mathrm{Yb}}^{\mathrm{full}} \cdot \frac{N_{\mathrm{Yb}}^{\mathrm{supp}}}{N_{\mathrm{Yb}}^{\mathrm{full}}} + L_{\mathrm{Yb\,Rb}} && (5.57)\\
&= R_{\mathrm{Yb}}^{\mathrm{load}} \cdot r_{\mathrm{supp}} + L_{\mathrm{Yb\,Rb}} \qquad \text{(with equation 5.54)} && (5.58)\\
\Longrightarrow L_{\mathrm{Yb\,Rb}} &= R_{\mathrm{Yb}}^{\mathrm{load}} \cdot (1 - r_{\mathrm{supp}}) && (5.59)
\end{aligned}$$

showing that the loss rate due to rubidium-ytterbium collisions can simply be found from the loading rate and the suppression rate $r_{\mathrm{supp}} = N^{\mathrm{supp}}/N^{\mathrm{full}}$. Table 5.4 once again gives the calculated numbers. Even considering the measurement uncertainties, the loss rate for rubidium atoms is found to be higher than that for ytterbium atoms. This can be explained by the removal of atoms through secondary collisions.

As mentioned earlier, the high observed loss rate is most likely due to collisions involving excited ytterbium atoms. The electronic excitation energy is very high compared to the thermal energies of the trapped atoms:

$$\frac{E_{\mathrm{el}}}{E_{\mathrm{th}}} = \frac{hc/\lambda}{k_B T} = 2.6 \cdot 10^8 \qquad \text{at } 100\,\mu\text{K and } 556\,\text{nm} \tag{5.60}$$

If even part of it is released as kinetic energy by the initial collision, the hot atoms produced will carry enough energy to remove other atoms from the trap before they escape. These

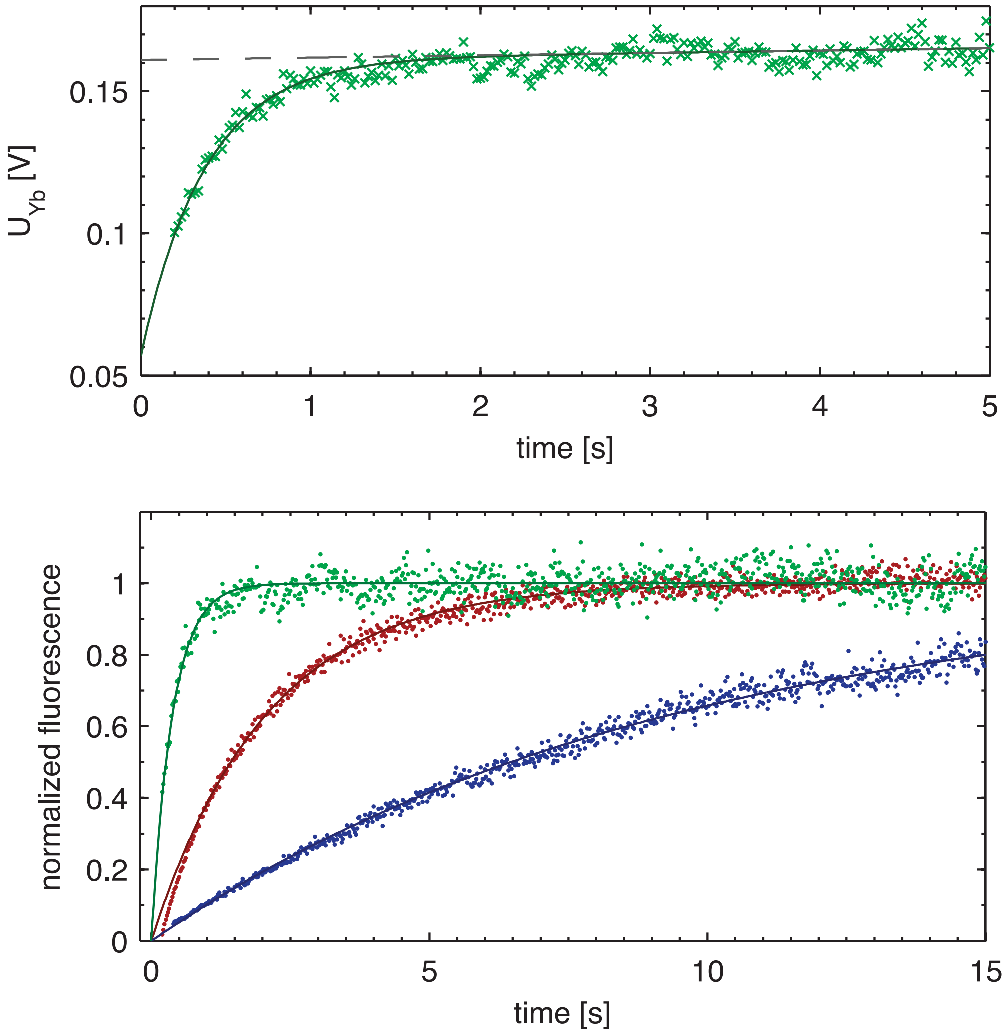

Figure 5.7: **(top)** Raw fluorescence signal for loading the suppressed ytterbium trap. The solid line shows the fitted curve while the grey dashed line indicates the linear component added to account for fluctuations in the fully loaded state. **(bottom)** Comparison of loading times for the suppressed (green) and undisturbed (blue) ytterbium trap to that of the rubidium trap (red). Solid lines indicate fits. All data was taken from the same interaction sequence and then normalized. Data for suppressed ytterbium was also corrected for fluctuations of the maximum value by removing the linear component shown in the top diagram.
The deviation of the rubidium fit from the measured fluorescence signal is due to rubidium-rubidium losses neglected in the model.

secondary collisions are much more likely to involve rubidium atoms due to their much larger number.

Ignoring the different collisional cross-sections and assuming that for equal numbers of rubidium and ytterbium atoms a secondary collision has the same probability for both provides a simple model that helps estimate the magnitude of the effect. In this model the observed loss rate is described by the rate of primary collisions L_0 between a cold ytterbium and a cold rubidium atom and the secondary collision coefficient $r_{2\mathrm{nd}}$:

$$\text{in Yb:} \qquad L^{\mathrm{Yb\,Rb}} = L_0 \cdot (1 + r_{2\mathrm{nd}} \cdot N_{\mathrm{Yb}}) \tag{5.61}$$

$$\text{in Rb:} \qquad L^{\mathrm{Rb\,Yb}} = L_0 \cdot (1 + r_{2\mathrm{nd}} \cdot N_{\mathrm{Rb}}) \tag{5.62}$$

This is trivial to solve for L_0.

$$L_0 = \frac{N_{\mathrm{Yb}} \cdot L_{\mathrm{Rb\,Yb}} - N_{\mathrm{Rb}} \cdot L_{\mathrm{Yb\,Rb}}}{N_{\mathrm{Yb}} - N_{\mathrm{Rb}}} \tag{5.63}$$

and the results are listed in the table together with the amplification factors $a_{\mathrm{amp}} = L^{\mathrm{Yb\,Rb}}/L_0$ caused by the secondary collisions. Since the factors found for ytterbium are very close to one and considering the uncertainty of the estimate, no attempt will be made to correct for this effect.

5.4.3 Photoassociation Rates

When the photoassociation laser is turned on and set to a suitable wavelength, it will cause the formation of excited YbRb* molecules. The lifetime of the excited state is expected to be similar to that of the rubidium atoms, which is not long enough to leave the trap volume. A small fraction will enter a bound molecular ground state after spontaneous emission of a photon. These molecules are not trapped because the excitation energies differ from the atomic case and the complex system of ro-vibrational states prevents the existence of a closed cycling transition. The majority of YbRb* atoms will decay into an ytterbium atom and a rubidium atom that are not bound anymore. As shown in figure 5.8, this is likely to convert part of the molecular binding energy into kinetic energy of the atoms. Since the depth of the YbRb* molecular potential is estimated to be around $5000\,\mathrm{cm}^{-1} \mathrel{\hat{=}} 7200\,\mathrm{K}$, even a small fraction will be sufficient to propel the atoms out of the trap. It is likely that the effect of secondary collisions once again amplifies the signal somewhat but there is no indication that this contribution has a larger effect than discussed in the previous section. For this reason, the additional losses of trapped ytterbium caused by the photoassociation laser will be attributed entirely to the initial molecule formation process.

In the rate equation model for ytterbium this adds another interspecies loss-term depending on the wavenumber $\tilde{\nu}$ and power P of the photoassociation laser:

$$\dot{N}_{\mathrm{Yb}}(t) = R_{\mathrm{Yb}}^{\mathrm{load}} - (c_{\mathrm{Yb}} + [\ \tilde{c}_{\mathrm{Yb\,Rb}} + \tilde{c}_{\mathrm{PA}}(\tilde{\nu}, P)\ ] N_{\mathrm{eq:Rb}}) N_{\mathrm{Yb}}(t) \tag{5.64}$$

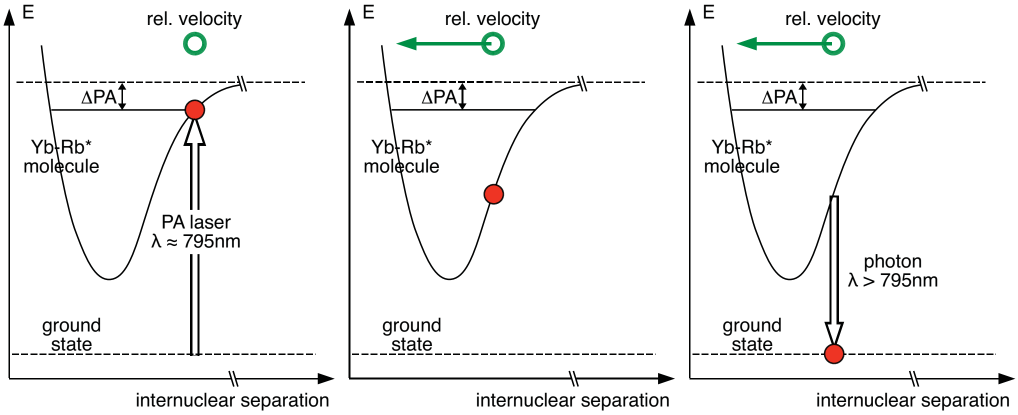

Figure 5.8: Classical interpretation of the photoassociation-induced trap loss. From left to right:
(1) Excited YbRb* molecules are formed through absorption of a photon with suitable energy. Due to the Franck-Condon principle, this preferably happens when the internuclear distance is near the outer turning point. At this point, the vibrational energy is purely in the form of potential energy.
(2) During the excited state lifetime the nuclei move in the molecular potential, converting potential to kinetic energy and back.
(3) Most of the molecules decay back to unbound ground state atoms. This process preserves the current velocities, leading to a considerable increase in kinetic energy. The energy gained by the atoms during this process corresponds to the difference between the absorbed and reemitted photon.

This equation is solved by the same exponential function as before, with

$$\tau_{\mathrm{Yb}} = \frac{1}{c_{\mathrm{Yb}} + [\ \tilde{c}_{\mathrm{Yb\,Rb}} + c_{\mathrm{PA}}(P,\tilde{\nu})\ ]N_{\mathrm{eq:Rb}}} \qquad \text{and} \tag{5.65}$$

$$N_{\max} = R^{\mathrm{load}}_{\mathrm{Yb}} \cdot \tau_{\mathrm{Yb}} = \frac{R^{\mathrm{load}}_{\mathrm{Yb}}}{c_{\mathrm{Yb}} + [\ \tilde{c}_{\mathrm{Yb\,Rb}} + \tilde{c}_{\mathrm{PA}}(P,\tilde{\nu})\ ]N_{\mathrm{eq:Rb}}} \qquad . \tag{5.66}$$

This shows that the fixed ratio of maximum atom number and time constant is maintained in this case. In the presence of additional photoassociation losses the atom number will therefore reach the reduced equilibrium value faster than indicated by the time constant without photoassociation (τ^{supp}).

However, the existence of three competing loss mechanisms complicates finding the photoassociation rate from the trap loss signal. Since the density distributions of the two clouds are only approximately known and no reasonably precise value for the original overlap integral can be calculated, the first useful quantity to extract is the molecule formation rate per ytterbium atom r_{PA} for a given wavenumber, power and rubidium distribution from the reduced atom number N_{PA}:

$$r_{\mathrm{PA}}(P,\tilde{\nu},\rho_{\mathrm{Rb}}) = \tilde{c}_{\mathrm{PA}} \cdot N_{\mathrm{eq:Rb}} \tag{5.67}$$

without PA:

$$N_{\max} \longrightarrow N^{\mathrm{supp}}_{\mathrm{Yb}} = \frac{R^{\mathrm{load}}_{\mathrm{Yb}}}{c_{\mathrm{Yb}} + \tilde{c}_{\mathrm{Yb\,Rb}} \cdot N_{\mathrm{eq:Rb}}} \tag{5.68}$$

with PA:

$$N_{\max} \longrightarrow N^{\mathrm{PA}}_{\mathrm{Yb}} = \frac{R^{\mathrm{load}}_{\mathrm{Yb}}}{c_{\mathrm{Yb}} + \tilde{c}_{\mathrm{Yb\,Rb}} \cdot N_{\mathrm{eq:Rb}} + r_{\mathrm{PA}}} \tag{5.69}$$

$$\Leftrightarrow N^{\mathrm{PA}}_{\mathrm{Yb}} \cdot (c_{\mathrm{Yb}} + \tilde{c}_{\mathrm{Yb\,Rb}} \cdot N_{\mathrm{eq:Rb}} + r_{\mathrm{PA}}) = R^{\mathrm{load}}_{\mathrm{Yb}} \tag{5.70}$$

$$\Leftrightarrow N^{\mathrm{PA}}_{\mathrm{Yb}} \cdot r_{\mathrm{PA}} = R^{\mathrm{load}}_{\mathrm{Yb}} - N^{\mathrm{PA}}_{\mathrm{Yb}} \cdot (c_{\mathrm{Yb}} + \tilde{c}_{\mathrm{Yb\,Rb}} \cdot N_{\mathrm{eq:Rb}}) \tag{5.71}$$

$$\Leftrightarrow r_{\mathrm{PA}} = \frac{R^{\mathrm{load}}_{\mathrm{Yb}}}{N^{\mathrm{PA}}_{\mathrm{Yb}}} - (c_{\mathrm{Yb}} + \tilde{c}_{\mathrm{Yb\,Rb}} \cdot N_{\mathrm{eq:Rb}}) \tag{5.72}$$

$$\Leftrightarrow r_{\mathrm{PA}} = \frac{R^{\mathrm{load}}_{\mathrm{Yb}}}{N^{\mathrm{PA}}_{\mathrm{Yb}}} - \frac{R^{\mathrm{load}}_{\mathrm{Yb}}}{N^{\mathrm{supp}}_{\mathrm{Yb}}} \qquad \text{(with equation 5.68)} \tag{5.73}$$

The absolute molecule formation rate is then once again

$$R_{\mathrm{PA}} = r_{\mathrm{PA}} \cdot N^{\mathrm{PA}}_{\mathrm{Yb}} = R^{\mathrm{load}}_{\mathrm{Yb}} - \frac{N^{\mathrm{PA}}_{\mathrm{Yb}}}{N^{\mathrm{supp}}_{\mathrm{Yb}}} R^{\mathrm{load}}_{\mathrm{Yb}} \tag{5.74}$$

$$= (1-X) R^{\mathrm{load}}_{\mathrm{Yb}} \tag{5.75}$$

where $X = N^{\mathrm{PA}}_{\mathrm{Yb}} / N^{\mathrm{supp}}_{\mathrm{Yb}}$ is the reduction in trapped atom number caused by the photoassociation laser. Figure 5.9 shows the resulting curves for typical trap parameters in ^{176}Yb and ^{174}Yb.

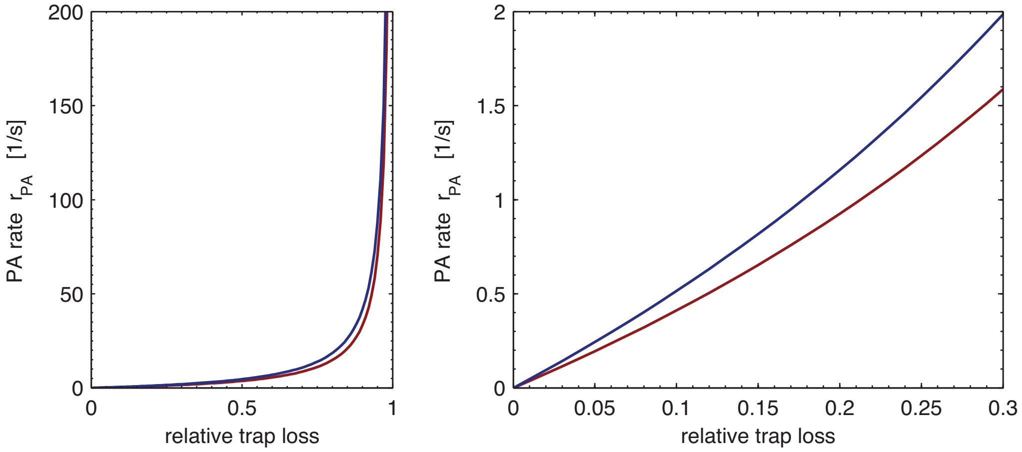

Figure 5.9: Photoassociation rate per ytterbium atom per second over observed trap loss according to the model presented in this chapter. The upper, blue curve corresponds to the trap parameters for ^{174}Yb, while the lower, red curve corresponds to ^{176}Yb. The left diagram covers the entire range from 0% to 100% loss while the right one provides details over the range of trap loss typically encountered in the experiments.

A very important consequence of this equation is that the various suppression factors do not limit the maximum achievable molecule formation rate. If the photoassociation process depletes the trap entirely, i.e. if the remaining atom number $N_{\mathrm{Yb}}^{\mathrm{PA}} = 0$, then the loss rate is equal to the trap loading rate, which is not affected by any of the loss mechanisms. Similarly, an additional reduction to 50% of the original suppressed atom number due to photoassociation indicates a loss rate equal to half the loading rate. In other words, even though finding a way to reduce the non-photoassociative suppression effects will increase the molecule formation rate, this increase is not necessarily proportional to the gain in suppressed atom number. The suppression of ytterbium by the presence of the rubidium cloud does not provide a hard limit to the maximum possible photoassociation rate.

Further insight into the relation of photoassociation rate to trapped atom number including photoassociation losses may be gained by reordering equation 5.73 to find $N_{\mathrm{Yb}}^{\mathrm{PA}}$ from r_{PA}:

$$N_{\mathrm{Yb}}^{\mathrm{PA}} = \frac{R_{\mathrm{Yb}}^{\mathrm{load}}}{r_{\mathrm{PA}} + \frac{R_{\mathrm{Yb}}^{\mathrm{load}}}{N_{\mathrm{Yb}}^{\mathrm{supp}}}} = \frac{R_{\mathrm{Yb}}^{\mathrm{load}}}{r_{\mathrm{PA}} + 1/\tau_{\mathrm{Yb}}^{\mathrm{supp}}} \tag{5.76}$$

For high photoassociation rates, this clearly shows a $1/r_{\mathrm{PA}}$ behavior. For $r_{\mathrm{PA}} = 1/\tau_{\mathrm{Yb}}^{\mathrm{supp}}$ the trapped atom number is reduced to half of the initial value and it asymptotically approaches zero with rising r_{PA}.

Chapter 6

Photoassociation Spectroscopy in a Cold Atomic Mixture

This chapter deals with the results of photoassociation spectroscopy in the double trap previously described. After an explanation of the data collection process, spectra for both ^{176}Yb^{87}Rb* *and* ^{174}Yb^{87}Rb* *are presented and analyzed.*

6.1 Definition of Relative Wavenumber

For a given electronic state, the lines found in photoassociation spectroscopy correspond to various vibrational levels of the molecule formed and to their rotational states. Due to the shallow upper region of the interatomic potential, higher vibrational lines will lie closer and closer together, converging on a state corresponding to two individual atoms. This will be called the "dissociation limit" in the following. In the wavelength range near 795 nm investigated here, this state consists of a ground state $6^1\mathrm{S}_0$ ytterbium atom and an excited $5^2\mathrm{P}_{1/2}$ rubidium atom. The photon energy required to reach a molecular state is therefore the excitation energy of the $5^2\mathrm{S}_{1/2}$,$(F = 1)$ to $5^2\mathrm{P}_{1/2}$ transition minus the molecular binding energy as shown in figure 6.1. Since the binding energy is a very important quantity for the characterization of a given rovibrational state, the wavelength of the photoassociation laser will be given

- in wavenumbers $\widetilde{\nu} = \frac{1}{\lambda} = \frac{\nu}{c} = \frac{E}{h\,c}$ (given in units of cm^{-1}), as this is essentially a unit of energy.
- relative to the rubidium D1, $5^2\mathrm{S}_{1/2}$,$(F = 1)$ to $5^2\mathrm{P}_{1/2}$,$(F' = 2)$ transition. The $F' = 2$ state was chosen as reference simply because it was found to provide higher photoassociation rates and is therefore the more likely candidate for further investigation.

This quantity will be called the "relative wavenumber" Δ_{PA}:

$$\begin{aligned}
\Delta_{\mathrm{PA}} &= \widetilde{\nu} - \widetilde{\nu}_{\mathrm{D1}(1\rightarrow 2)} && (6.1)\\
&= \widetilde{\nu} - 12578.862\,\mathrm{cm}^{-1} && (6.2)
\end{aligned}$$

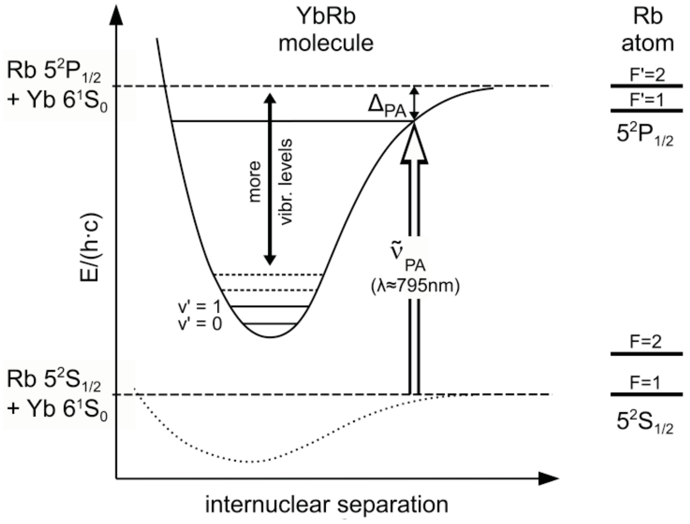

Figure 6.1: Definition of Δ_{PA} and review of relevant energy levels in the YbRb* molecule compared to those of a single rubidium atom.

6.2 Measurement of Spectra and Wavelength Assignment

The photoassociation laser can cover a wide wavelength range in the interesting region, with the highest accessible wavelength of 850 nm corresponding to a maximum relative wavenumber $\Delta_{\mathrm{PA}}^{\max} = 870\mathrm{cm}^{-1}$. Unfortunately only a very small part of this, approximately 4 GHz or $0.13\,\mathrm{cm}^{-1}$, can be covered in a continuous scan. Any larger changes necessitate manual adjustment of the selective elements in the laser resonator. Creating a continuous spectrum therefore requires combining data taken in separate measurements.

In each of these, the center wavelength of the photoassociation laser is manually set and the wavelength is then varied by changing the piezo voltage of the external reference cavity. The applied voltage follows a triangular waveform supplied by a function generator. The standard sequence used provides four full sweeps over the frequency range in one direction and three full sweeps in the other, with each taking a time of 50 s. During the entire time the datalogger records the scanning signal from the function generator, the wavelength measured by the wavemeter and the fluorescence signal for each atom cloud, as shown in figure 6.2. The spectrum for ^{176}Yb is based on 147 of such data blocks, while the spectrum for ^{174}Yb consists of 81.

After each measurement, the resulting file is opened in an analysis program written in Matlab. This first identifies the individual sweeps based on the maxima and minima of the scan control voltage. It then splits the measured data into blocks accordingly. The values provided by the wavemeter are delayed by the evaluation of the interference signals and the transfer to the datalogger. They also give a wavelength value averaged over a period of nearly a second. Timestamps that are corrected for this are assigned to the measurements. To avoid using measurements near the turning points that integrate over both up- and down-sweeps, any wavelength data in the upper or lower 5% is discarded. This also reduces the effect of the piezo hysteresis on data measured near the center of the sweep at the cost of larger errors of the wavelength measurements near the turning points.

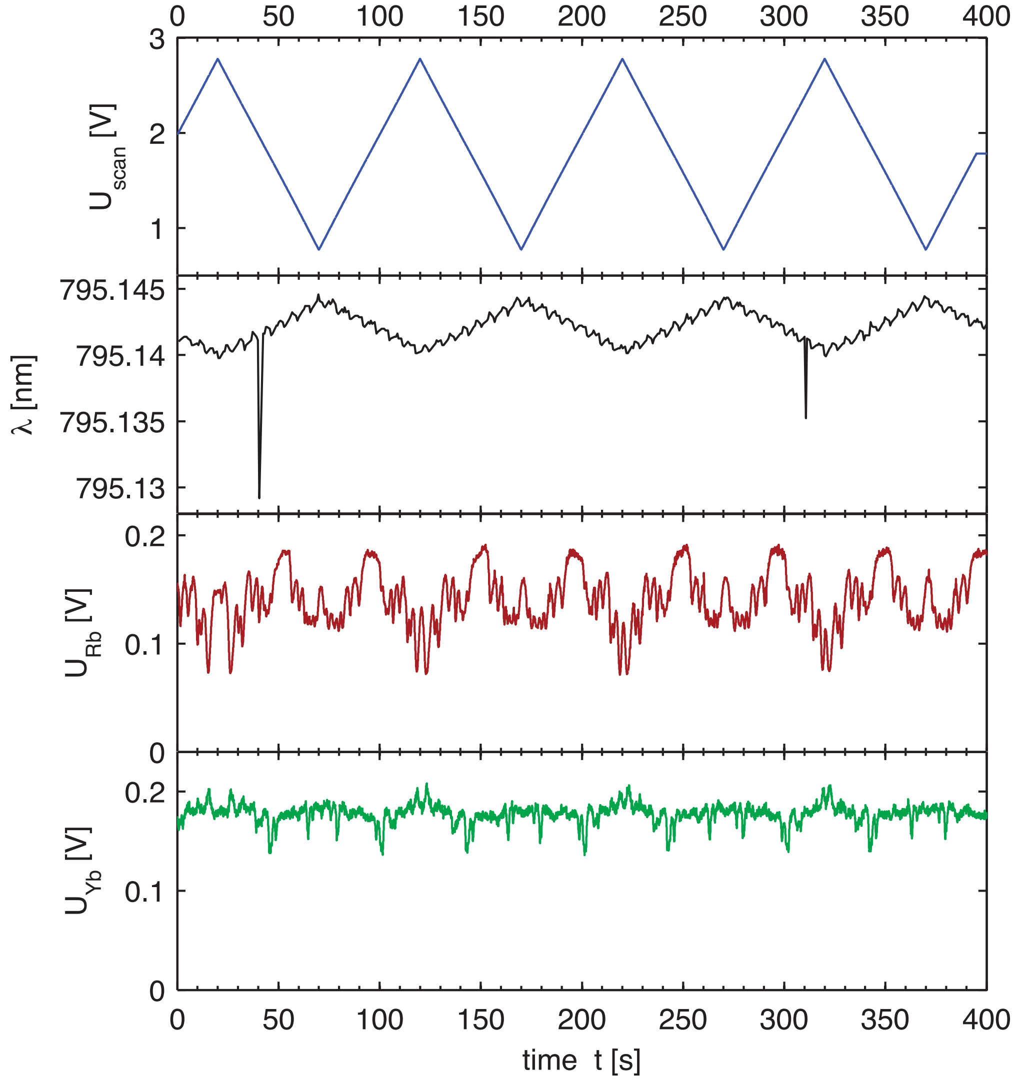

Figure 6.2: Example of the data recorded by the datalogger. The first, blue curve shows the control voltage applied to the piezo amplifier, the second, black curve the measured wavelength. Four full sweeps with increasing wavelength and and three full sweeps with decreasing wavelength were taken during this measurement. The graph also clearly shows the cyclical variation of the wavelength measurement as well as the occasional outlier caused by a miscount in the wavemeter electronics.
Shown below are the fluorescence signals for the rubidium (red) and ytterbium (green) cloud. Losses in fluorescence are caused by photoassociation (Rb-Rb and Yb-Rb, respectively).

Occasionally, electronic noise or fluctuations of the laser power coupled into the wavemeter causes a miscount of the interference fringes. This leads to errors in the wavelength data. Fortunately even a miscount by one fringe will change the reported value enough to be easily discarded as an outlier. Finally, a gamma-correction function as explained in chapter 4.4.3 is applied to the relative timing information of the various signals to linearize the scan. Now the wavemeter data can be fitted with a straight line, providing smooth, interpolated wavelength information for all the measurements. The entire process is illustrated in figures 6.2 to 6.5.

To make it possible to combine sweeps easily, the data from each is stored according to a new, binned scale, where each datapoint corresponds to $5 \cdot 10^{-5}\,\mathrm{cm}^{-1}$. This is done by linear interpolation, adding the value of each sample to the two nearest bins with a weight given by the wavelength difference. The size of the bins corresponds to a frequency difference of approximately 1.5 MHz and was chosen slightly smaller than the linewidth of the photoassociation laser to avoid limiting the resolution while still reducing the memory required by the spectra.

At the same time, the evaluation program also filters the fluorescence data, finds a maximum fluorescence value for each sweep and calculates the relative trap loss using this and the known background signal from the nearest characterization measurement (see chapter 5.3.1).

Occasionally Rb-Rb photoassociation depletes the rubidium trap far enough to reduce the ytterbium suppression. Fortunately this only has a significant effect for the strongest Rb-Rb lines, as can be seen in figure 6.4. To minimize the effect on the Yb-Rb photoassociation spectrum, an empirical function is used to predict the resulting increase in ytterbium fluorescence, which is then subtracted from the measured signal. The result is seen in figure 6.5.

6.2.1 Accuracy Estimate

Since the linearity correction is not perfect and the wavemeter fluctuations can also be on the order of 5 to 10 MHz when averaged over one sweep, the data from each sweep is not immediately combined straight away. Instead it is added to a database from which individual, groups of, or all sweeps can be plotted. This is then manually inspected and sweeps affected by problems such as drop-outs in the trapping lasers or mode-hops in the photoassociation laser can be removed entirely or limited to useful sections.

Each individual sweep is also manually assigned a shift value to improve the overlap and recover the maximum possible resolution, as shown in figures 6.4 and 6.5. Care was taken to balance the shifts such that the overall position of observed lines was affected as little as possible.

Global Wavelength Uncertainty

Larger shifts were required to align measurements of the same photoassociation lines taken at different times due to drifts of the wavemeter that occurred even when using the rubidium master laser as reference. Since the atomic rubidium resonances were used to optimize the optical alignment as described in chapter 4.4.4, spectra of them were taken during almost

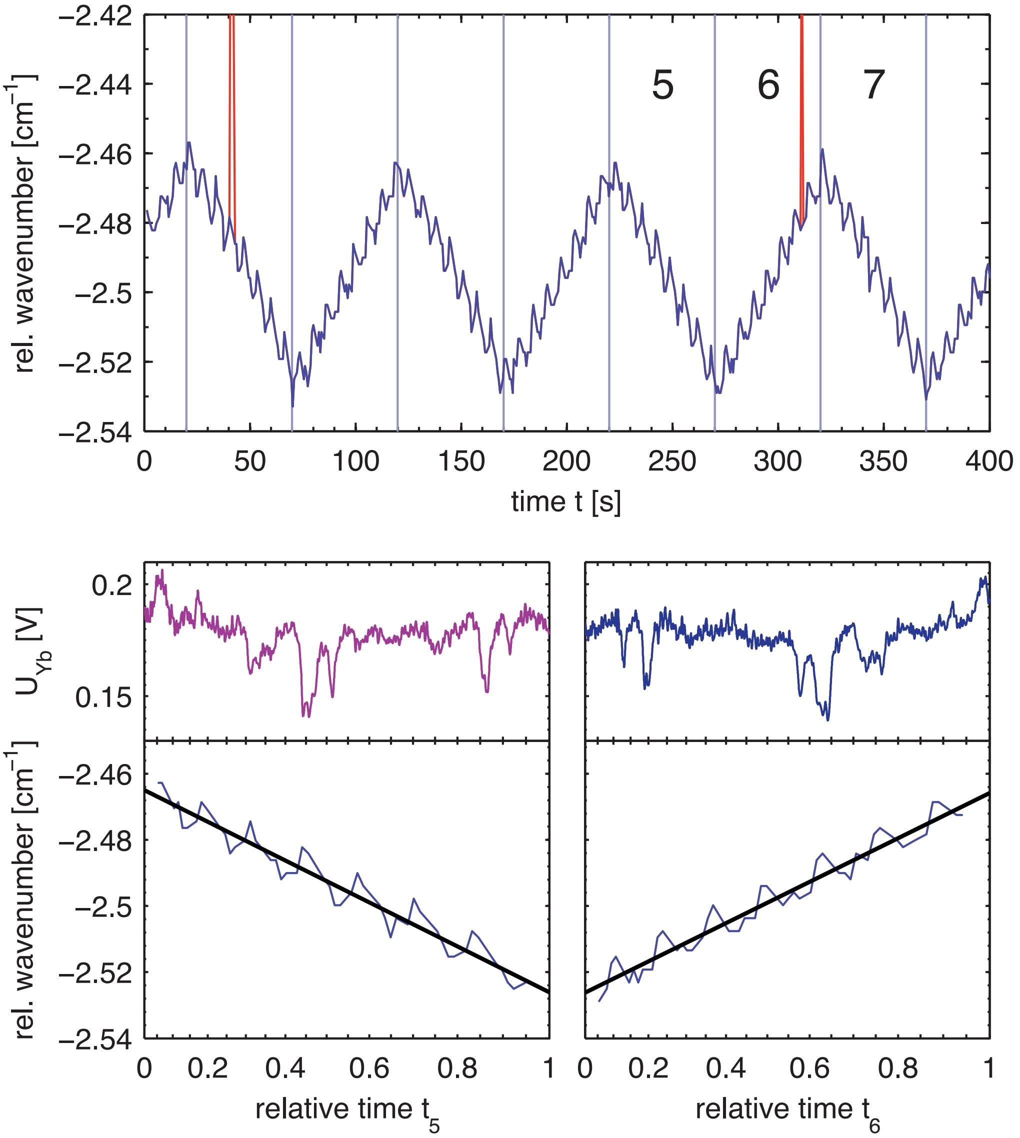

Figure 6.3: Assigning wavelengths to spectroscopic data.
(top) Outliers in the wavemeter data are found and removed, then all data is split into blocks according to the scan control voltage. The numbers 5 to 7 mark the sweeps that will be shown in the following examples.
(bottom) The wavelength measurements (shown for blocks 5 and 6) are linearized by applying a gamma correction function to the relative time values (note the non-linearity of the horizontal axis). A linear fit then provides wavelength data that can be applied to the fluorescence data shown at the top of each graph.

all measurement sessions. This has been used to find an uncertainty value of $\pm 0.005\,\mathrm{cm}^{-1}$ (or 150 MHz) for the wavemeter. The observed shifts were then corrected for, but not enough data is available to characterize the drifts or jumps in the wavemeter precisely. Therefore the uncertainty of the wavelength measurements will be assumed to be equal to the full measured standard deviation of the control measurements. The actual error is expected to be somewhat less, especially for lines that have been investigated repeatedly over several sessions. These were manually shifted in the spectrum shown to match the averaged value of the individual wavelength measurements.

After the manual clean-up procedure, 919 sweeps were left to contribute to the ^{176}Yb spectrum and 500 for the ^{174}Yb spectrum. About half of these cover the maximum scanning range of 4 GHz used to find interesting features of the spectrum and half were taken at a reduced range of around 1.75 GHz or $0.058\,\mathrm{cm}^{-1}$ to investigate the line shapes in detail.

Line Widths

The width of the photoassociation lines is determined by contributions from the natural linewidth, expected to be approximately twice (Comparat, 2008) that of the single rubidium atom ($\approx 2 \cdot 5.75$ MHz), the Doppler shift caused by the center of mass motion (negligible at $\approx$ 0.35 MHz) and the $E_{\mathrm{th}} = k_B T$ thermal energy contributions from rubidium and ytterbium atoms (Rb: $\approx$ 11 MHz, Yb: $\approx$ 7 MHz). Adding these in quadrature yields a rough estimate of 17.4 MHz.

The lines found in the spectrum have a full width at half maximum of approximately $0.001\,\mathrm{cm}^{-1}$ or 30 MHz. It is unclear what causes the additional broadening. At a sweep rate of 1.75 GHz/50 s = 35 MHz/s, the photoassociation laser needs 0.86 s to cover this frequency range. Since the loading rate of the suppressed ^{176}Yb trap is $\tau^{\mathrm{supp}} = 0.26$ s, this is sufficient for the system to approach the equilibrium state. When the laser is manually kept at the center of a photoassociation line during the optimization procedure described in chapter 4.4.4, it is found that the trap depletion is increased only by factor of 1.1 to 1.15 compared to the maximum depletion found in the spectra. Slower scanning thus does not lead to a worthwhile increase in the achieved resolution, as the lines are increasingly broadened by the medium term thermal drifts of the reference cavity of the photoassociation laser. Averaging over more sweeps taken in the same time was found to give better results.

Local Uncertainty

The accuracy of relative wavenumbers within a single scan is not limited by the drifts of the wavemeter and therefore considerably better. To provide an estimate of the uncertainty, the relative position of two easily identified lines (^{176}Yb, $\Delta\,\mathrm{v}' = -11$: $F' = 2$, $R' = 0$ at $\Delta_{\mathrm{PA}} = -4.897\,\mathrm{cm}^{-1}$ and $F' = 1$, $R' = 1$, $m'_{R'=1} = 0$ at $\Delta_{\mathrm{PA}} = -4.919\,\mathrm{cm}^{-1}$) was compared for the 34 sweeps that showed both with good signal-to-noise ratio. A standard deviation of

$$\sigma_{\mathrm{swp}}(0.022\,\mathrm{cm}^{-1}) = 2.68 \cdot 10^{-4}\,\mathrm{cm}^{-1} \tag{6.3}$$

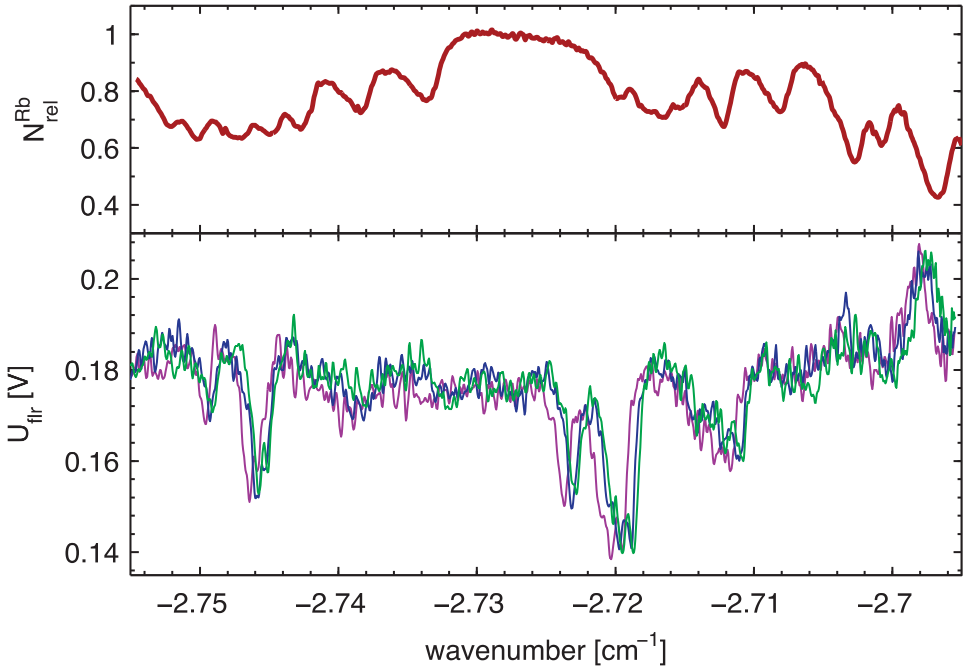

Figure 6.4: Partially evaluated fluorescence data after initial wavelength assignment. The remaining shifts between the individual sweeps are clearly visible in the ytterbium fluorescence data shown in the bottom chart. The top chart shows the combined rubidium data with Rb-Rb photoassociation lines. When the rubidium depletion is particularly strong, like it is near $\Delta_{\mathrm{PA}} = -2.7\,\mathrm{cm}^{-1}$, the suppression of the ytterbium trap is reduced, resulting in an increase in atom number.

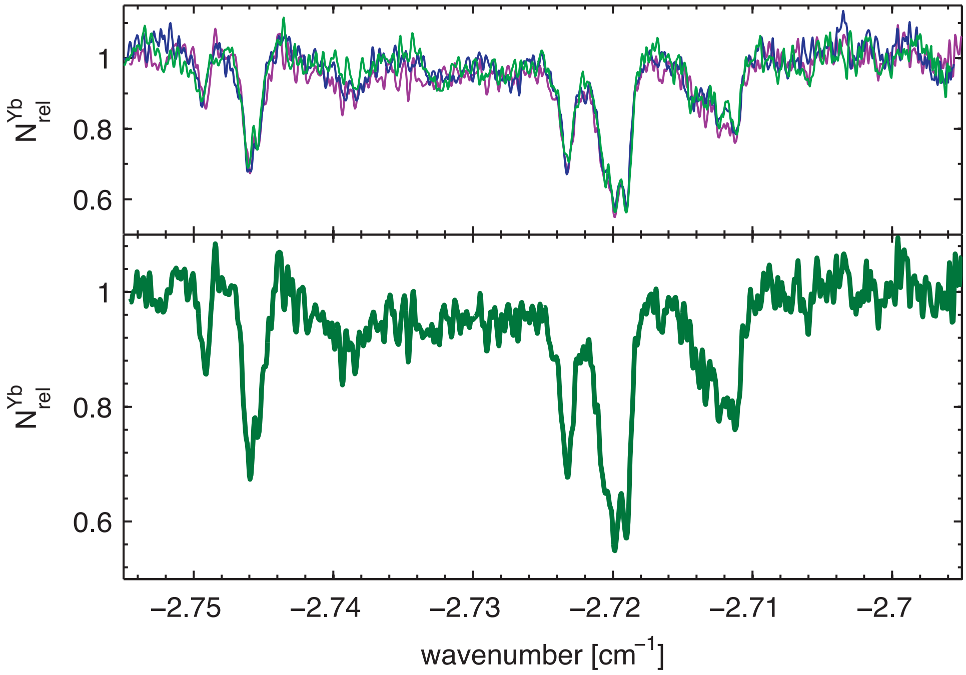

Figure 6.5: Fluorescence data after manual shifts, before and after averaging into a single spectrum. The increase in ytterbium atom number near $\Delta_{\mathrm{PA}} = -2.7\ \mathrm{cm}^{-1}$ has been partially compensated.

was measured. The largest rotational spacings were observed to be $0.0066\,\mathrm{cm}^{-1}$. Extrapolating the uncertainty values to smaller values requires some kind of model. A conservative estimate is to assume a random-walk of the wavelength error over time, resulting in a proportionality to the square root of the wavenumber difference:

$$\sigma_{\mathrm{swp}}(0.0066\,\mathrm{cm}^{-1}) = \sqrt{\frac{0.0066}{0.022}}\,\sigma_{\mathrm{swp}}(0.022\,\mathrm{cm}^{-1}) \tag{6.4}$$

$$= 1.47 \cdot 10^{-4}\,\mathrm{cm}^{-1} \tag{6.5}$$

This is already less than 5 MHz, or 1/6 of the observed linewidth. It can be assumed that the wavelength errors will not improve much more than this due to the limited signal-to-noise ratio.

It is worth noting that the uncertainty has only been investigated in terms of shot-to-shot fluctuations of the measurements. Since the gamma correction to the non-linearity of the scan is not perfect, especially near the turning points, the remaining non-linearity will translate into a wavelength error in these regions. Near the center of the scan this effect should be small. In this region an uncertainty of $\sigma_{\widetilde{\nu}}^{\mathrm{center}} = 1.5 \cdot 10^{-4}\,\mathrm{cm}^{-1}$ will be assumed, while the uncertainty over the full range is likely $\sigma_{\widetilde{\nu}}^{\mathrm{full}} = 3 \cdot 10^{-4}\,\mathrm{cm}^{-1}$ or better.

Another limitation that needs to be investigated is the correction to the calibration of the wavemeter. This was done after the data was separated into bins and had to be realized as a simple shift to avoid additional errors from a second interpolation process. An average shift of $0.247\ \mathrm{cm}^{-1}$ towards lower wavenumbers was required to match the measured values of the rubidium absorption lines used in the alignment procedure to the reference data. The most likely error in the wavemeter is an inaccurate wavelength value for the reference laser, resulting in an error in the proportionality constant. Correcting for this by applying a simple shift introduces an error $\delta\nu$ which grows linearly with the distance to the calibration point and therefore Δ_{PA}. At the largest detuning from the reference point of $\Delta_{\mathrm{PA}} = -33\,\mathrm{cm}^{-1}$ it is

$$\delta\widetilde{\nu}(-33\,\mathrm{cm}^{-1}) \approx \frac{33\ \mathrm{cm}^{-1}}{12579\ \mathrm{cm}^{-1}}\ 0.247\,\mathrm{cm}^{-1} = 6.5 \cdot 10^{-4}\,\mathrm{cm}^{-1} \tag{6.6}$$

and therefore small compared to the wavemeter uncertainty of $\sigma_{\mathrm{wm}} = 5 \cdot 10^{-3}\,\mathrm{cm}^{-1}$. Within a single sweep the contribution to the overall error is even smaller at

$$\delta\widetilde{\nu}(-0.027\,\mathrm{cm}^{-1}) \approx \frac{0.027\ \mathrm{cm}^{-1}}{12579\ \mathrm{cm}^{-1}}\ 0.247\,\mathrm{cm}^{-1} = 5.3 \cdot 10^{-7}\,\mathrm{cm}^{-1} \quad . \tag{6.7}$$

6.3 Spectra...

After alignment, the data from all sweeps is combined into a single spectrum. Data from the shorter scans of 1.75 GHz is assigned twice the weight compared to the scans covering 4 GHz to take advantage of the higher detail present.

The useful ytterbium spectrum starts a relative wavenumber $\Delta_{\mathrm{PA}}^{\mathrm{start}} = -0.38\,\mathrm{cm}^{-1}$. For shorter wavelengths the strong photoassociation laser is too close to the rubidium $5^2\mathrm{S}_{1/2}$, $F = 1$ to $5^2\mathrm{P}_{1/2}$, $F' = 1$ or $F' = 2$ transitions at $-0.228\,\mathrm{cm}^{-1}$, causing sufficient heating and depletion of the rubidium trap to obscure the photoassociation lines.

6.3.1 ...in ^{176}Yb

Figure 6.6 shows the spectrum created for ^{176}Yb in this way. The curve indicates the relative fluorescence of the ytterbium cloud for a given wavelength of the photoassociation laser. Since the lowest energy level accessible from the ground state is at a much higher energy corresponding to $17986\,\mathrm{cm}^{-1}$, no Yb-Yb photoassociation lines or other light-mediated loss processes are expected in this wavelength range. Any drop in fluorescence caused by the photoassociation laser is therefore attributed to the formation of YbRb* molecules. This was directly confirmed for some of the lines by removing the rubidium cloud and testing that this also eliminates the trap loss at this laser wavelength. It is indirectly confirmed for most of the remaining lines through the interpretation of the rovibrational states and the assignment to one of two vibrational series.

Green vertical lines mark the positions of observed vibrational lines identified as belonging to one of the main vibrational series, Red vertical lines indicate photoassociation lines that could not be assigned. The gray dashed line marked '(-4)' shows the position of a predicted vibrational line that is not observed due to the loss of rubidium near the atomic resonance. The other dashed line marked '(-19)' shows a vibrational line that is too weak to be investigated at the current noise level. A total of 32 vibrational lines were found. Basically all lines show a characteristic rotational structure that will be the subject of a detailed discussion in chapter 6.4.2.

The red curve shows the trap loss spectrum in rubidium. The losses caused by Yb-Rb photoassociation are too small to be noticeable, but due to Rb-Rb photoassociation there is still a complex pattern of trap loss lines. Assigning these lines to rovibrational states is outside the scope of this thesis, but it is obvious that the spacing of the lines is much closer than in YbRb*, as expected due to the flatter, longer range outer part of the potential for the homonuclear molecule. Some of the lines are also quite deep, reaching up to 50% trap depletion. At these wavelengths, the ytterbium spectrum generally shows an increase in fluorescence as the trap suppression by the presence of rubidium is reduced and more ytterbium atoms are loaded.

At the relative wavelengths of $\Delta_{\mathrm{PA}} = -0.228\ \mathrm{cm}^{-1}$ and $\Delta_{\mathrm{PA}} = -0.2553\ \mathrm{cm}^{-1}$ the rubidium $5^2\mathrm{S}_{1/2}$,$(F = 2)$ to $5^2\mathrm{P}_{1/2}$,$(F' = 2)$ and $(F' = 1)$ transitions used to optimize the optical alignment and the wavelength assignment are visible through increased trap loss.

6.3.2 ...in ^{174}Yb

The spectrum for ^{174}Yb^{87}Rb* is shown in figure 6.7. Since the spectrum shows no fundamental difference compared to the spectrum found when using ^{176}Yb and the photoassociation lines are generally weaker, only a reduced wavelength range was investigated in detail. A total of 17 vibrational lines were found, each with rotational structure.

Four of these lines, marked by red vertical lines and the letters A-D in the diagram could immediately be identified as "echoes" of the lines marked "-6" and "-8". Each of these shows the same rotational structure as a line at a wavenumber higher by $0.255\mathrm{cm}^{-1}$, the hyperfine splitting of the rubidium ground state. Photoassociation at these wavelengths simply creates the same molecular states starting from the $F = 2$ instead of the $F = 1$ ground state. Since the dark spot MOT concentrates the rubidium atoms in the lower

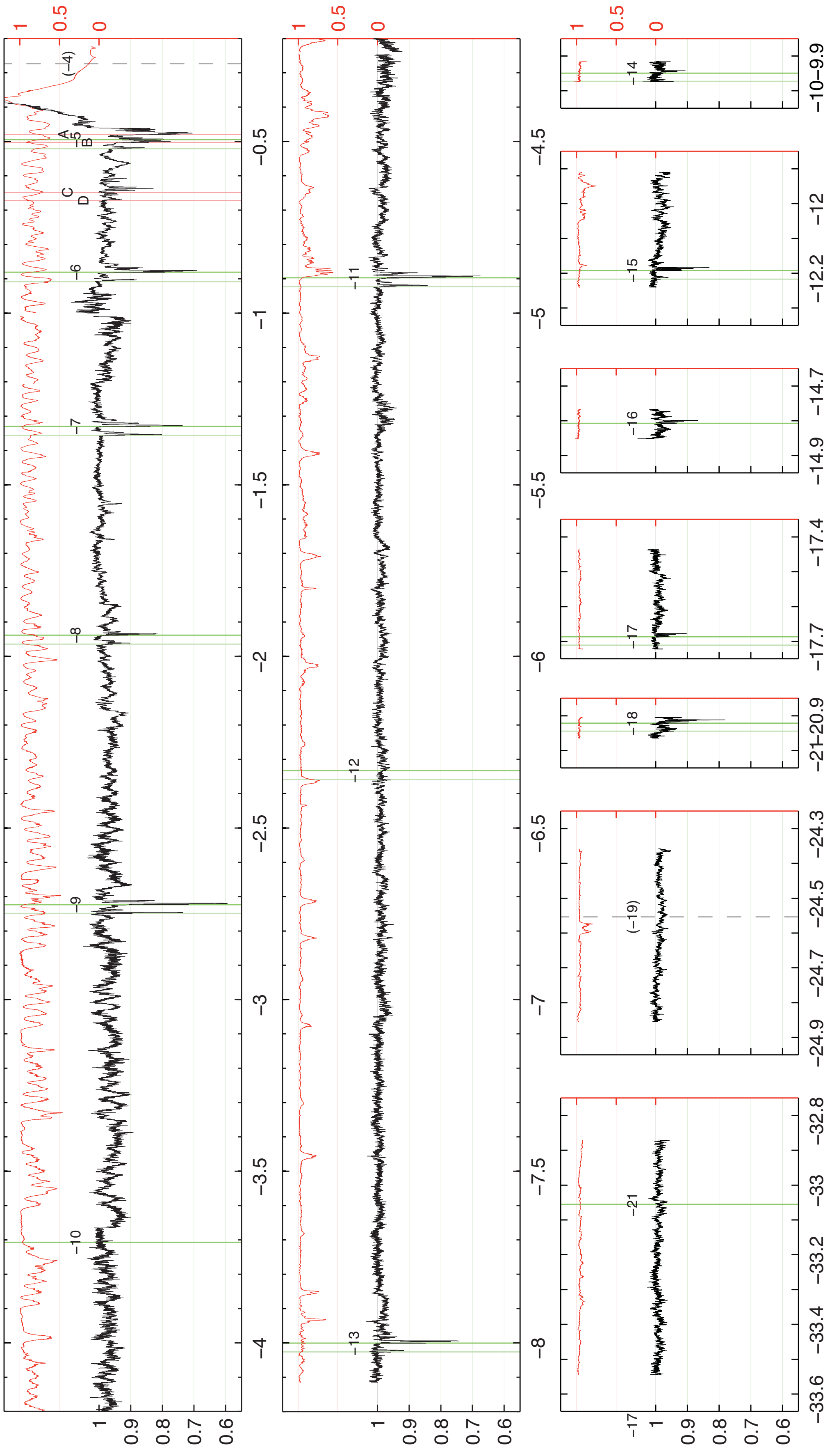

Figure 6.6: Combined spectrum taken for ^{176}Yb (black) and ^{87}Rb (red), shown as relative trap fluorescence over relative wavenumber Δ_{PA} of the photoassociation laser. Green lines mark observed lines in the 2 main vibrational series, red lines mark unassigned photoassociation lines and dashed gray lines mark predicted but unobserved/weak lines.

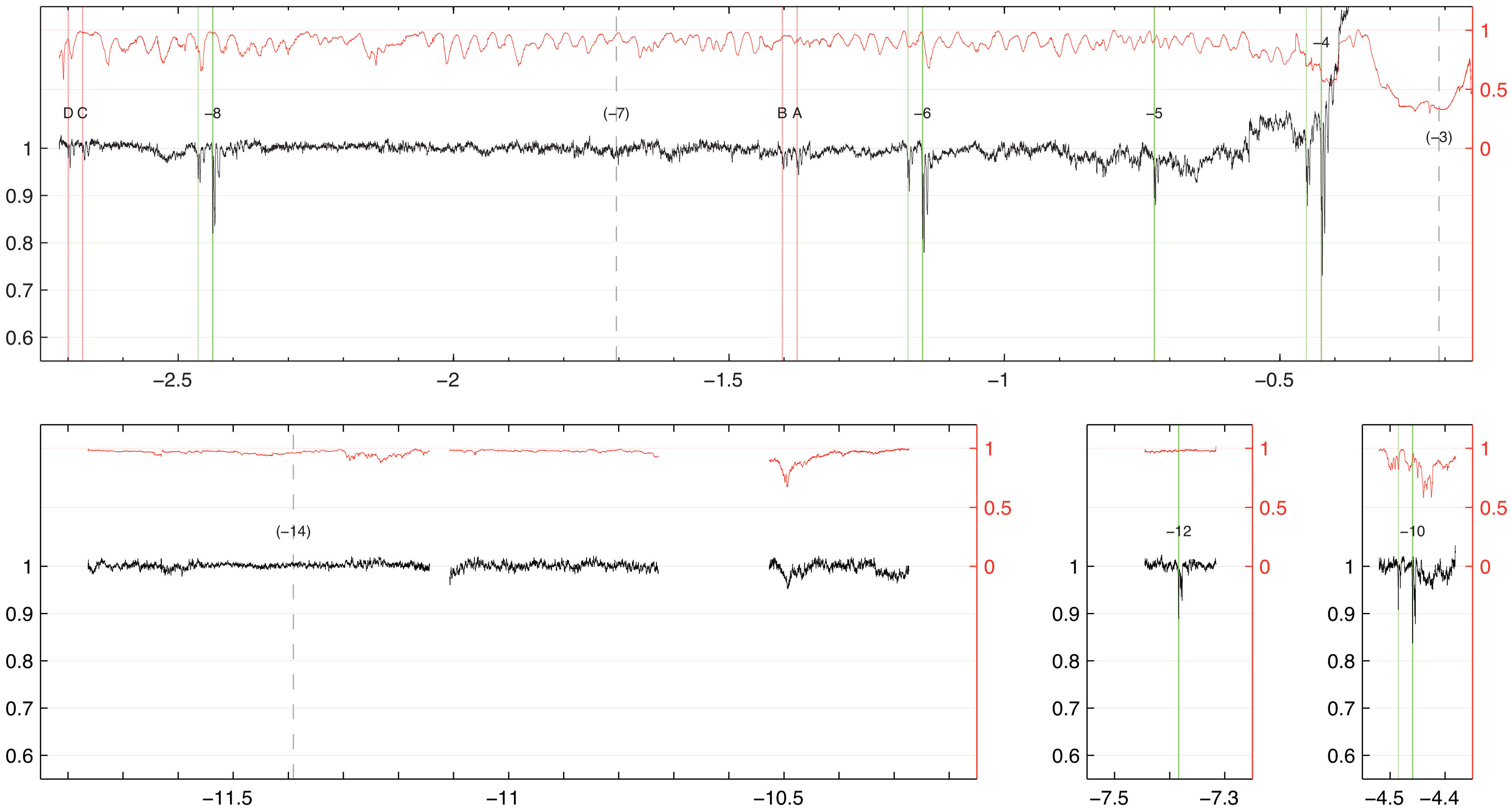

Figure 6.7: Combined spectrum taken for ^{174}Yb (black) and ^{87}Rb (red), shown as relative trap fluorescence over relative wavenumber Δ_{PA} of the photoassociation laser. Green lines mark observed lines, red vertical lines mark the “echo” lines discussed in the text and dashed gray lines mark predicted but unobserved lines.

$F = 1$ ground state, the echos are much weaker than the original lines. Since they do not immediately offer any additional insight into the physics of the YbRb* molecule, they were not examined in further detail. It is unclear why they appear at considerable strength here, but are not found in the ^{176}Yb^{87}Rb* spectrum. One possibility is an imperfect alignment of the dark-spot and depumper system in the experiments with ^{174}Yb although considerable effort was invested into re-optimizing this.

6.4 Line Assignment

Figures 6.8 and 6.9 show enlarged sections of the total spectrum for all the vibrational lines found in ^{176}Yb^{87}Rb*. Figure 6.10 does the same for ^{174}Yb^{87}Rb*. All of them show a similar structure based on the quantized rotational energies and a splitting of the rotational components.

6.4.1 Hyperfine Splitting

It is obvious from the spectra that the photoassociation lines generally appear in pairs split by approximately 0.027 cm^{-1}. This is the molecular equivalent of the hyperfine splitting of the excited $5^2\text{P}_{1/2}$ state in rubidium, measured here directly as $(2.735 \pm 0.015) \cdot 10^{-2}\,\text{cm}^{-1}$. This is in reasonable agreement with the literature value of $2.717 \cdot 10^{-2}\,\text{cm}^{-1}$, Steck (2008). Since the ytterbium atom in its ground state does not contribute any angular momentum, the nuclear spin of the rubidium atom remains coupled to the electronic (spin and orbit) angular momentum. For the long-range, weakly bound molecules explored by photoassociation spectroscopy, the electronic configuration of each atom will be changed only slightly from the atomic state as described by Hund's case (e).

The difference in transition strengths is also retained from the properties of the rubidium atoms: As explained in Steck (2008), the strength of the $F = 1$ to $F' = 1$ hyperfine transition is only 1/6 that of the $F = 1$ to $F' = 2$ transition. The spectra find the $F' = 1$ lines at around one third the trap loss of the $F' = 2$ lines, quite consistent with this number due to the less than linear increase of trap loss with the photoassociation rate and to the saturation effects examined later. However, since the two states connect to diabatic potentials that are expected to behave quite differently at short internuclear distances, the Franck-Condon factors can vary independently. This means that the ratio of the photoassociation rates for the $F' = 1$ series and the $F' = 2$ series can be quite different even between adjacent vibrational lines.

At lower vibrational levels the binding energy increases and the electronic configuration will gradually change until the electronic and nuclear angular momentum finally reach a state of strong coupling to the internuclear axis. The observations are compatible with this. As shown in figure 6.11, the splitting starts out near the value directly observed between the $5^2\text{S}_{1/2},(F = 1)$ to $5^2\text{P}_{1/2},(F' = 2)$ and $5^2\text{S}_{1/2},(F = 1)$ to $5^2\text{P}_{1/2},(F' = 1)$ transitions visible in the rubidium spectra near $-0.24\,\text{cm}^{-1}$. As the binding energy increases at lower Δ_{PA}, the splitting gradually decreases from initially $0.027\,\text{cm}^{-1}$ to less than $0.023\,\text{cm}^{-1}$ at

$\Delta_{\mathrm{PA}} = -21\,\mathrm{cm}^{-1}$. A linear fit yields the relation

$$\Delta\widetilde{\nu}_{\mathrm{hfs}} = 0.02678\,\mathrm{cm}^{-1} + 1.93 \cdot 10^{-4} \frac{\Delta_{\mathrm{PA}}}{\mathrm{cm}^{-1}} \quad . \tag{6.8}$$

Over the energy range investigated here, the sequence of lines is well described as two hyperfine states of a single vibration series. However, in the picture of diabatic potential curves the lines attributed to each of the two states couple to potentials that will be quite distinct at lower internuclear distances. In the following, the lines converging on the rubidium $F' = 1$ and $F' = 2$ atomic states will be treated as two separate series and the nomenclature of hyperfine splitting will simply be used to label the two.

6.4.2 Rotational Structure

The rotational energy of the molecule is described by

$$E_{\mathrm{rot}} = B'_{\mathrm{rot}}\ R'(R'+1)\ , \tag{6.9}$$

where B'_{rot} is called the rotational constant. and R' is the rotational quantum number for the nuclear motion.

Generally only components with $R' \leq 3$ are visible due to ground state centrifugal barrier discussed in chapter 3.4.3. For $R = 3$ this has a maximum at $114\,a_0$ equivalent to a temperature of $916\mu\mathrm{K}$ and prevents the majority of atoms from reaching the distance where photoassociation is likely to happen. And since the population of rotational molecular states is mostly a selection process, with the photon adding (or taking away) at most one unit of angular momentum, this is reflected directly in the resulting spectrum. The rotational series at $\Delta_{\mathrm{PA}} = -0.425\,\mathrm{cm}^{-1}$ (shown in figure 6.10) in ^{174}Yb is an exception in that it shows a clear $R' = 4$ component. This only appears because the wavelength of the photoassociation laser is close enough to the rubidium resonance to cause increased scattering which heats the rubidium cloud and allows more atoms to cross the centrifugal barrier.

Fitting a rotational progression as described above to this line clearly shows integer quantum numbers from 0 to 4, confirming the weak coupling of molecular rotation to electronic angular momentum and nuclear spin discussed in chapter 3.1.3.

In the fixed rotor approximation, the rotational constant is

$$B'_{\mathrm{rot}} = \hbar^2/(2\,\mu\,r^2)\ , \tag{6.10}$$

where μ is the reduced mass and r is the distance of the nuclei. For the low rotational quantum numbers in our experiment, centrifugal stretching effects can be neglected and an effective fixed-rotor radius

$$r'_{\mathrm{eff}} = \hbar/\sqrt{2\,\mu\,B'_{\mathrm{rot}}} \tag{6.11}$$

may be defined for the excited YbRb* molecules. For vibrational states near the dissociation limit this is expected to be close to the classical outer turning point, as the wavefunction has a large amplitude in this shallow region of the potential. The long range

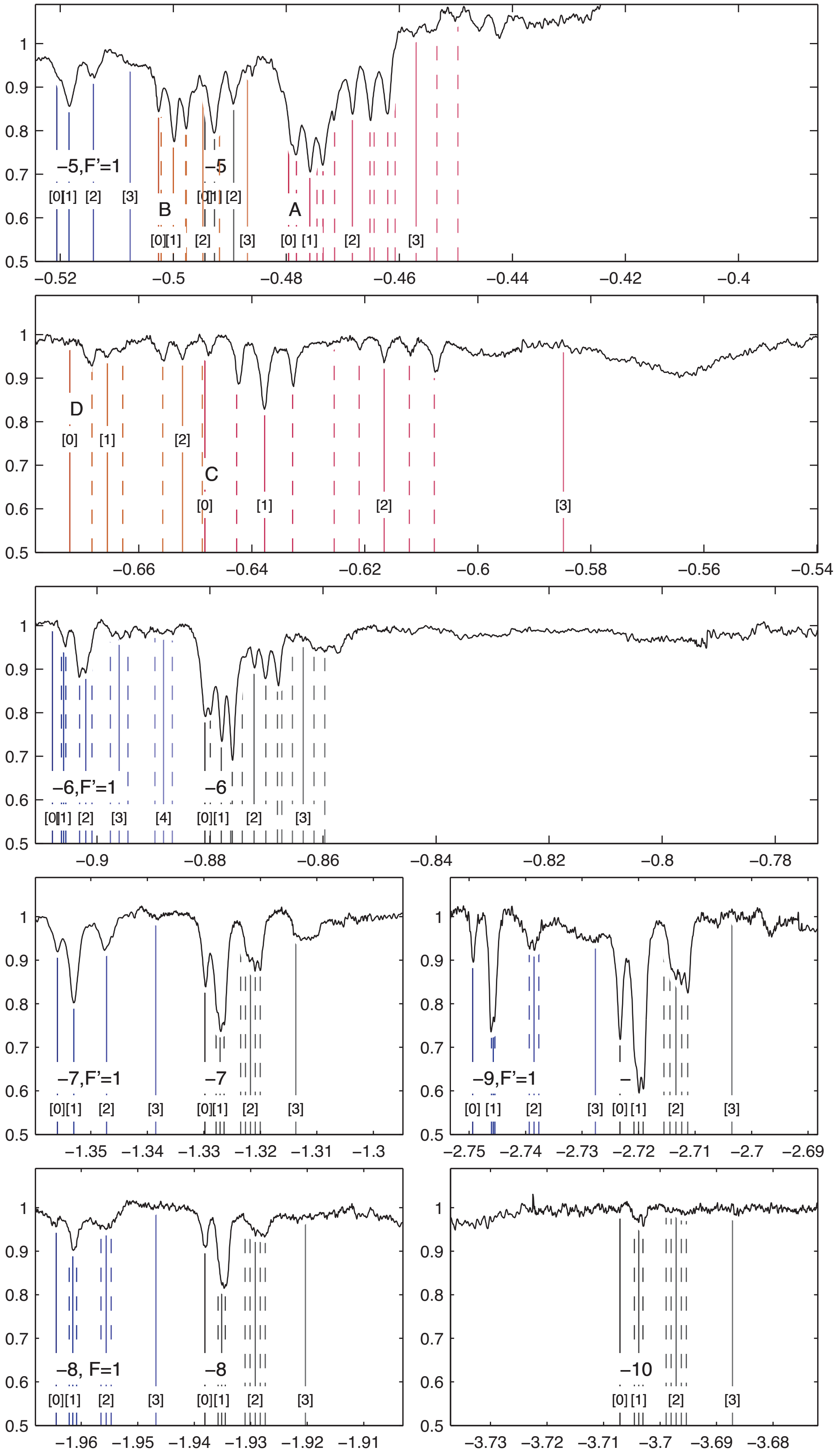

Figure 6.8: Close-up of photoassociation lines in $^{176}\mathbf{Yb}^{87}\mathbf{Rb}^*$ shown as relative trap fluorescence over Δ_{PA}. Solid lines mark rotational components (identified by $[R']$) with $m' = 0$, dashed lines mark $m' \neq 0$ components. Vibrational series are identified by relative vibrational quantum number $\Delta\,\mathrm{v}'$ and hyperfine state F' where required.

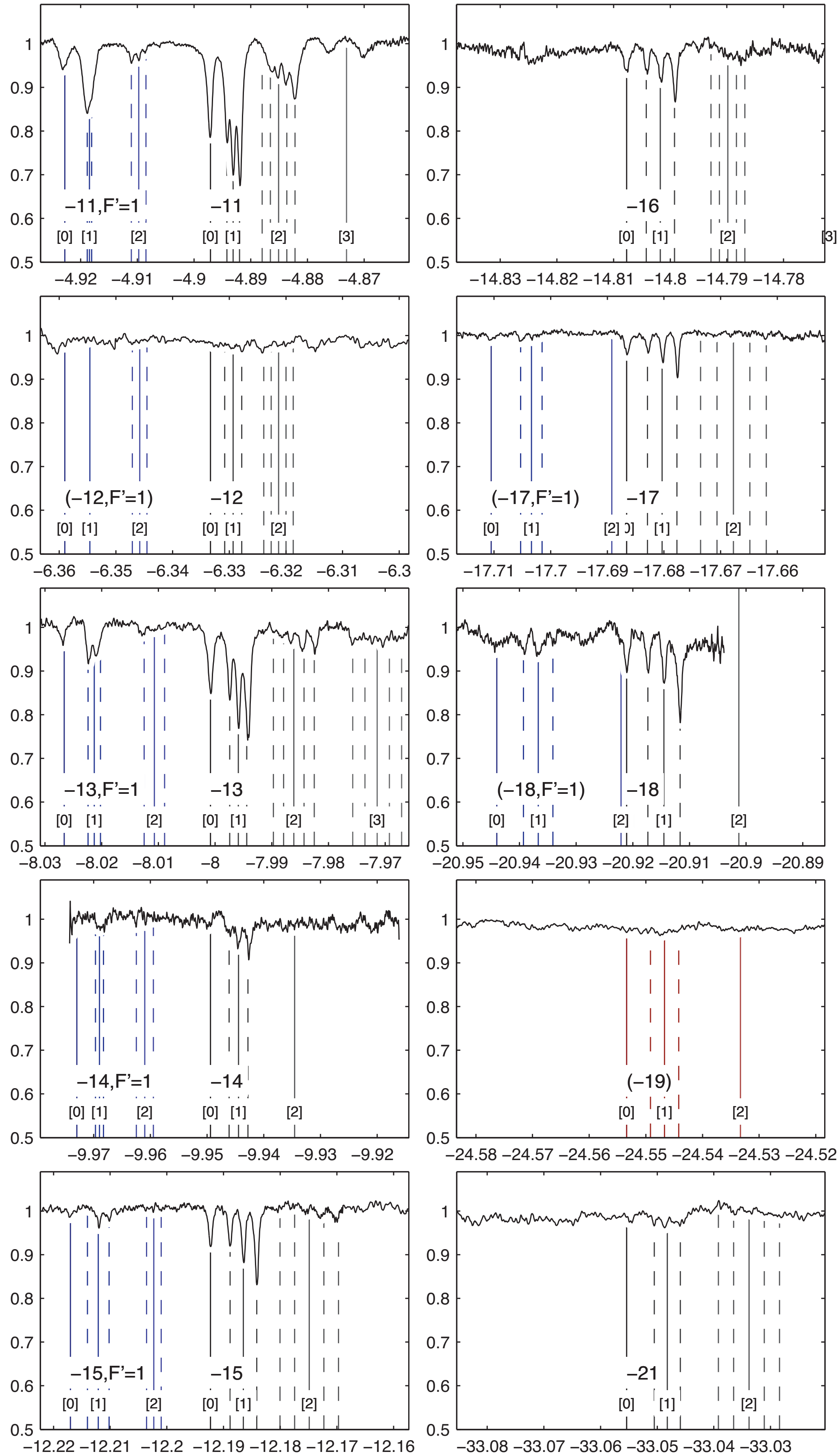

Figure 6.9: Close-up of further photoassociation lines in $^{176}\mathbf{Yb}^{87}\mathbf{Rb}^*$ shown as rel. trap fluorescence over Δ_{PA}. Solid lines mark rotational components (identified by $[R']$) with $m' = 0$, dashed lines mark $m' \neq 0$ components. Vibrational series are identified by rel. vibrational quantum number Δ v' and hyperfine state F' where required and in brackets for weak lines.

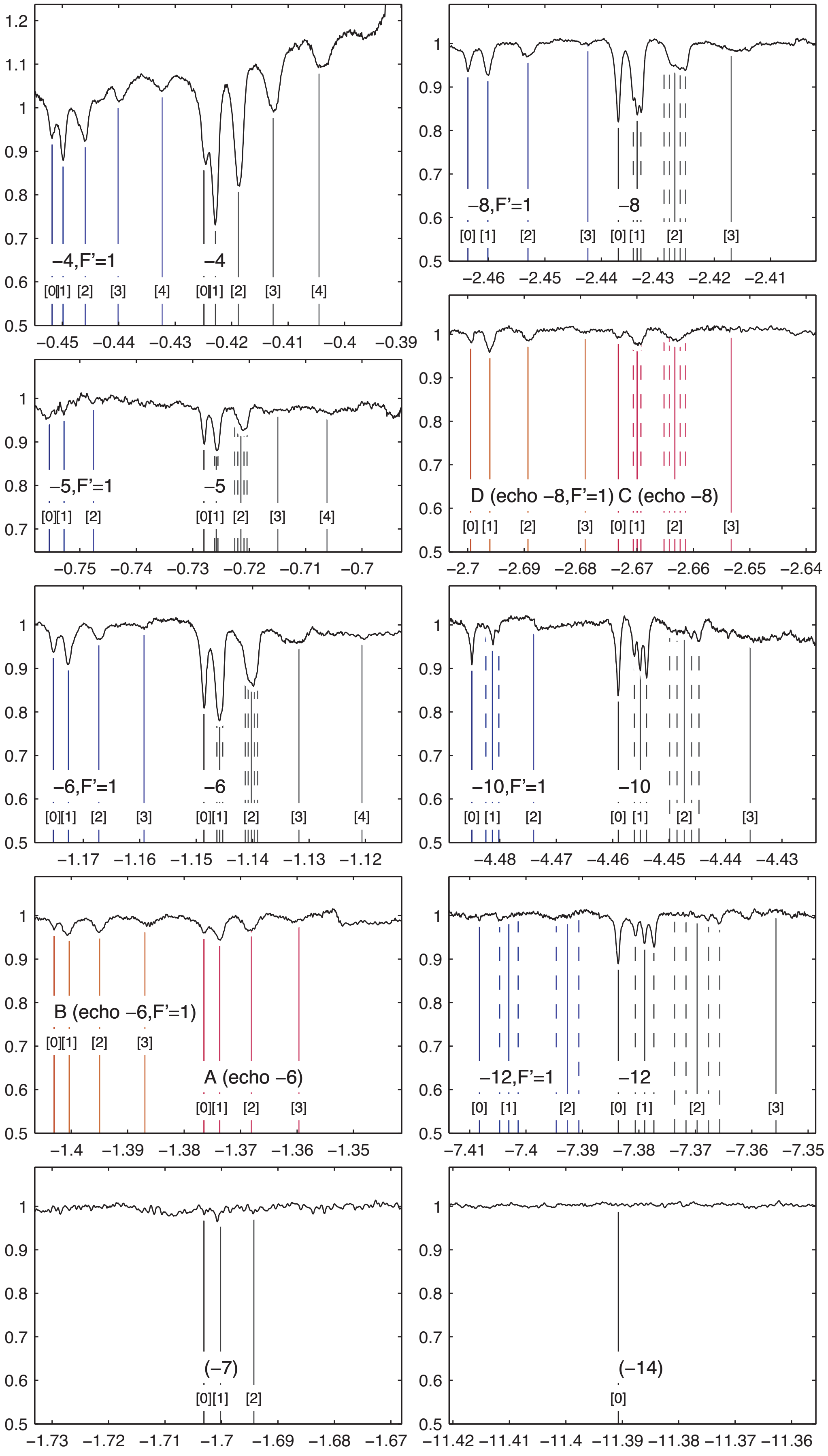

Figure 6.10: Close-up of photoassociation lines in ^{174}**Yb**^{87}**Rb** shown as rel. trap fluorescence over Δ_{PA}. Solid lines mark rotational $m' = 0$ components (identified $[R]$), dashed lines mark $m' \neq 0$ components. Lines are identified by relative vibrational quantum number $\Delta\,\mathrm{v}'$ and hyperfine state F' where required and in brackets for weak/unobserved lines.

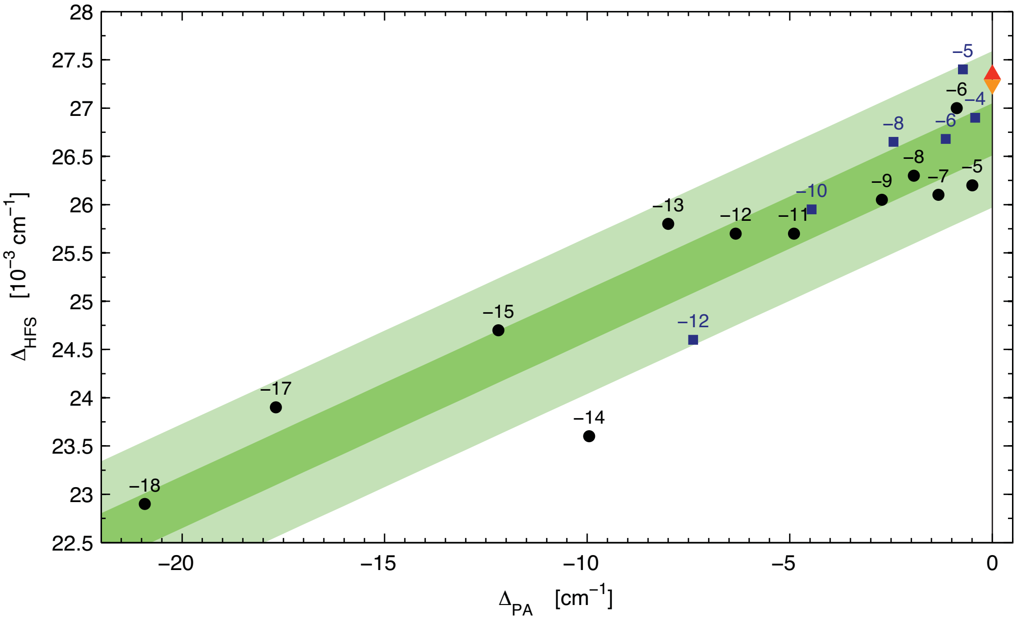

Figure 6.11: Separation (in cm^{-1}) between equivalent vibrational states in the $F' = 2$ and the $F' = 1$ series as found in the experiments. Black circles indicate values for ^{176}Yb^{87}Rb*, blue squares values for ^{174}Yb^{87}Rb*. The atomic hyperfine splitting in rubidium has been added at $\Delta_{\text{PA}} = 0\,\text{cm}^{-1}$: The orange, down-pointing triangle shows the literature value of $0.027241\,\text{cm}^{-1}$, while the red, upwards-pointing triangle gives the value of $0.02735\,\text{cm}^{-1}$ measured in the rubidium spectrum. The green zone corresponds to the linear fit described in the text, broadened to include the uncertainty estimate for the relative wavenumber. The dark green center zone shows the range for $\pm\sigma$ and the lighter outer zone shows $\pm 3\ \sigma$.

potential in a heteronuclear molecule has a $E \sim -1/r^6$ dependence and the rotational energies are therefore expected to approximately follow the relation

$$r \sim \frac{1}{-\Delta_{\mathrm{PA}}^{1/6}} \tag{6.12}$$

$$\Longrightarrow B_{\mathrm{rot}} \sim (-\Delta_{\mathrm{PA}})^{1/3} . \tag{6.13}$$

As figure 6.12 shows, this is indeed the case for most lines. The rotational constants marked as belonging to the $F' = 1$ series generally show a larger deviation from the fit. This is most likely due to the imperfect nonlinearity correction of the scan and the resulting wavelength error near the turning points. To provide as much information as possible, the close-up scans of the observed hyperfine pairs of lines were always set up to cover a wavelength range as those shown in figures 6.8 to 6.10. This puts the clearest ($R' = 0$ and $R' = 1$) lines of the $F' = 2$ rotational sequence near the center, while the same lines of the $F' = 1$ sequence are close to the edge of the scan, where the distortions are more pronounced.

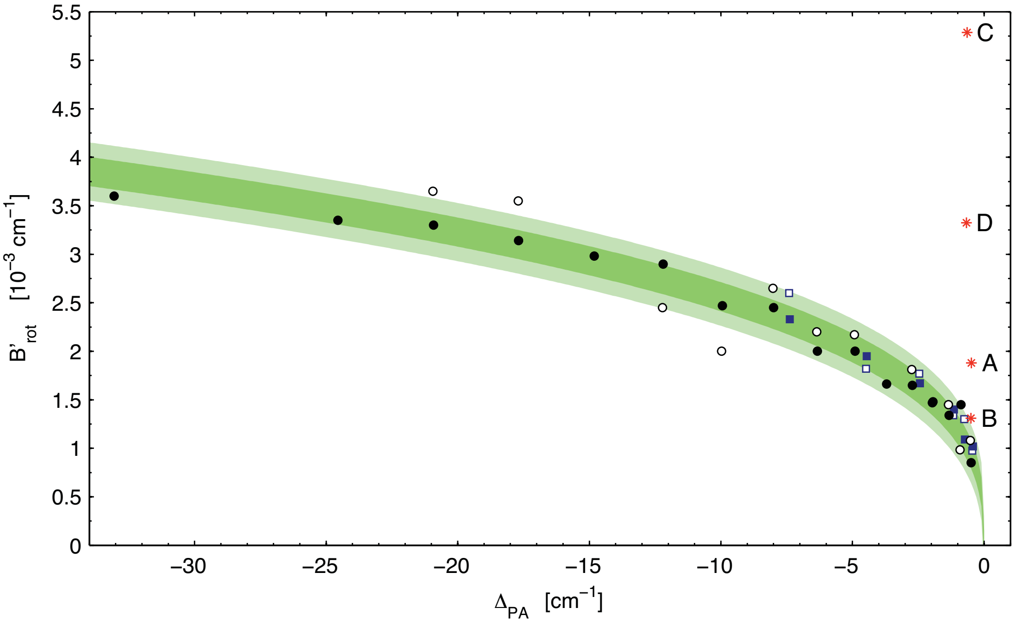

Figure 6.12: Rotational constants B'_{rot} over relative wavenumber Δ_{PA}. The green region shows a fit according to $B_{\mathrm{rot}} \sim \Delta_{\mathrm{PA}}^{1/3}$. The dark green center area indicates a deviation of up to $\sigma_{\tilde{\nu}}^{\mathrm{center}} = 0.15 \cdot 10^{-3}\,\mathrm{cm}^{-1}$ and the lighter area corresponds to the larger uncertainty $\sigma_{\tilde{\nu}}^{\mathrm{center}} = 0.3 \cdot 10^{-3}\,\mathrm{cm}^{-1}$ for measurements near the edge of the scan.
Red stars indicate lines not part of the main vibrational series which were excluded from the fit. Solid black circles indicate data for ^{176}Yb,($F' = 2$), while solid blue squares show data for ^{174}Yb,($F' = 2$). Open symbols give datapoints for lines of the weaker $F' = 1$ series.

For the lines near $\Delta_{\mathrm{PA}} = -10\,\mathrm{cm}^{-1}$ and $\Delta_{\mathrm{PA}} = -12\,\mathrm{cm}^{-1}$, the $F' = 1$ rotational sequence is weak and already partially obscured by the background noise as seen in figure 6.9. The rather large discrepancy is therefore most likely caused by the difficulties in precisely locating the rotational components.

This is different for the lines marked ‘A’ to ‘D’. Both pairs (A-B and C-D) show clearly defined rotational components, but the values found for B_{rot} are quite different from those for other lines in this wavelength range. The splittings between ‘A’ and ‘B’ ($0.0230\,\mathrm{cm}^{-1}$) as well as between ‘C’ and ‘D’ ($0.0239\,\mathrm{cm}^{-1}$) have the correct order of magnitude to be interpreted as derived from the hyperfine splitting of the rubidium $5^2\mathrm{P}_{1/2}$ state, but it is noticeably less than that of the neighboring lines in the main vibrational series. Finally, the analysis of the vibrational structure presented in the following chapter confirms that these lines are not part of the $F' = 1$ or $F' = 2$ vibrational series. Their depth seems to imply that they occur in the outer, shallow part of the molecular potential, making it unlikely that they belong to a vibrational series converging on a higher electronic state of the rubidium atom.

It is possible that they represent rovibrational states of a doubly-excited Yb*Rb* molecule. Excited ytterbium atoms are present in the MOT. Photoassociation near the rubidium resonance would create an additional vibrational series converging on $\Delta_{\mathrm{PA}} = 0\mathrm{cm}^{-1}$, but with a potentially quite different coupling type and strength due to the changed electronic configuration of the ytterbium atom.

A test for the electronic state of the ytterbium atom in the photoassociated atom pair is presented in chapter 6.4.7 and confirms the ytterbium atom in the ground state for the lines in the more common $F' = 1$ and $F' = 2$ series. The same test should be applied to the ‘A’ to ‘D’ lines at the next opportunity.

6.4.3 Splitting of Rotational Lines

The finest pattern in the line structure is a splitting of the rotational components. The observations agree with a Hund’s case (e) angular momentum coupling. Since there is no angular momentum contribution from internal degrees of freedom in the ytterbium atom, the total angular momentum of the rubidium atom described by F' is left to couple directly to the rotational angular momentum R' of the newly formed molecule.

This results in a number of projection states $m'_{R'}$ with integer quantum numbers running from $-R'$ to R', or $-F'$ to F' when R' is larger than F'. These follow a 1,3,3… pattern of sub-components for $F' = 1$ and a 1,3,5,5… pattern for $F' = 2$. The sub-components have an equidistant splitting $\Delta_{R'}$ corresponding to the alignment of the magnetic dipolar moment of the rubidium “atom” with regard to the field created by the relative motion of the ytterbium atom. Since this atom does not carry a charge, the actual field is most likely created through the deformation of the electronic clouds, but no model is available at this time.

Figure 6.13 shows the splittings found for $R' = 1$ and $R' = 2$ over the binding energy as given by Δ_{PA} as well as over the effective internuclear distance r'_{eff} found from the rotational constant. The lines already found to differ strongly in rotational constant again show a very distinct behavior.

For the $F' = 2$ series, where the stronger lines are resolved with more accuracy, the

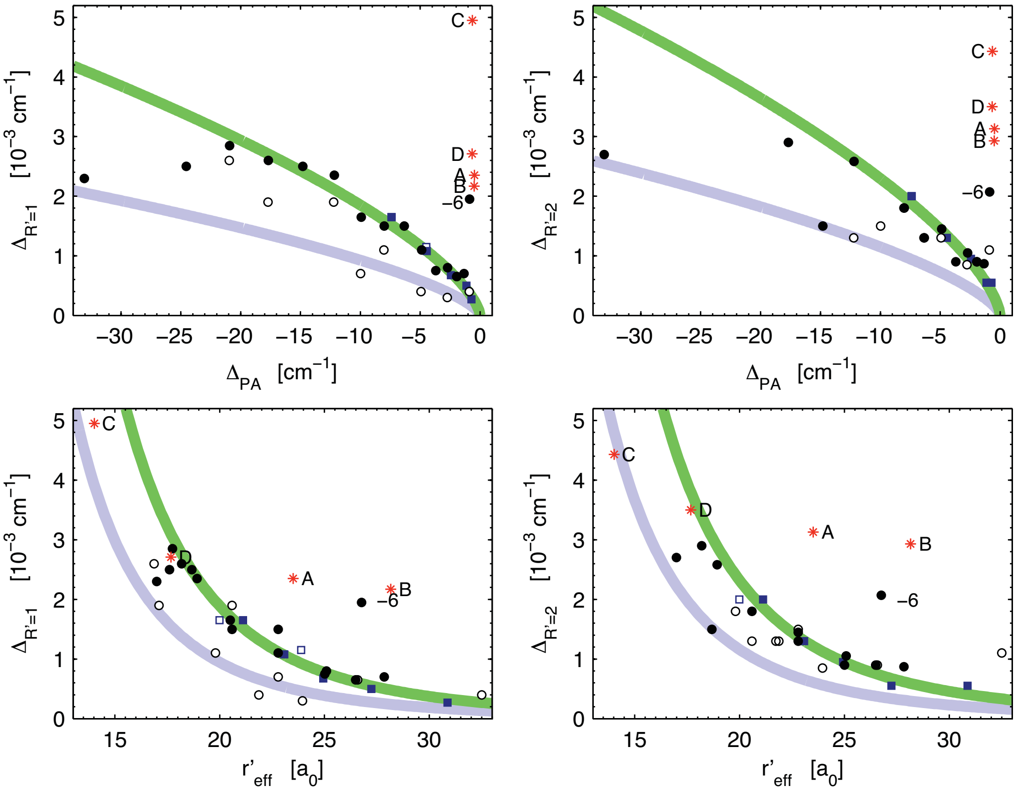

Figure 6.13: Splitting of the rotational lines for $R' = 1$ (left diagrams) and $R' = 2$ (right diagrams) over the binding energy given by Δ_{PA} (top) and over effective internuclear distance r'_{eff} found from B'_{rot}. Full symbols represent lines assigned to the $F' = 2$ series, open symbols belong to $F' = 1$. Black circles show data of ^{176}Yb, while blue squares show ^{174}Yb. Green lines are fits with the functions $\Delta_{R'} = -a\,\Delta_{\mathrm{PA}}^{2/3}$ (top) and $\Delta_{R'} = b\,\Delta_{\mathrm{PA}}^{-4}$ (bottom). The strongly deviating points near $-1\,\mathrm{cm}^{-1}$ (marked '-6') and near $-33\,\mathrm{cm}^{-1}$ were excluded from the fits, along with the lines found not to be part of the main vibrational series shown as red stars. The blue lines are drawn at half the value of the fitted function to show the expectations for the $F' = 1$ components.

splitting can be described well by the formulas

$$\Delta_{R'=1} = (302 \pm 47)\,\mathrm{cm}^{-1} \;\cdot\; (r'_{\mathrm{eff}}/a_0)^{-4} \tag{6.14}$$

$$\Delta_{R'=2} = (371 \pm 82)\,\mathrm{cm}^{-1} \;\cdot\; (r'_{\mathrm{eff}}/a_0)^{-4} \tag{6.15}$$

showing how the splitting increases at closer distance between the nuclei. The data also indicate an increase of the splitting for larger R', but this is not conclusive and might again be due to the imperfect non-linearity correction. The larger magnetic moment resulting from the higher angular momentum for $R' = 2$ manifests itself as the presence of additional components at $m'_{R'} = \pm 2$.

Due to the connection of r'_{eff} and Δ_{PA}, similar equations can be found for Δ_{PA}:

$$\Delta_{R'=1} = (-3.99 \pm 0.63) \cdot 10^{-4}\,\mathrm{cm}^{-1} \;\cdot\; (\Delta_{\mathrm{PA}}/\mathrm{cm}^{-1})^{2/3} \tag{6.16}$$

$$\Delta_{R'=2} = (-4.95 \pm 0.49) \cdot 10^{-4}\,\mathrm{cm}^{-1} \;\cdot\; (\Delta_{\mathrm{PA}}/\mathrm{cm}^{-1})^{2/3} \tag{6.17}$$

In nearly all cases, the splittings of the $F' = 1$ series is found to be less than that of the $F' = 2$ series. This is expected, since the magnetic dipolar moment in the rubidium atom

$$\mu'_F = g_{F'}\,\mu_b\,F' \qquad \text{with} \qquad g_{F'=1} = -1/6 \tag{6.18}$$

$$g_{F'=2} = +1/6 \tag{6.19}$$

is twice as large in magnitude for $F' = 2$ as it is for $F' = 1$. It is then expected that the splitting $\Delta_{R'}$ is half as big in $F' = 1$. Guiding lines for these values are shown in the diagrams, but the large inaccuracies in determining the spacings for the weaker lines do not allow for a judgement on the quality of this model.

The different signs in the g-factors for the excited hyperfine states of the rubidium atom is the most likely cause of another interesting effect: The rotational sub-components of the $F' = 1$ series increase in strength towards lower energies, while those of the $F' = 2$ series increase towards higher energies. This is particularly noticeable in the spectrum of the rotational structures near $\Delta_{\mathrm{PA}} = -4.9\,\mathrm{cm}^{-1}$ displayed in figure 6.14, but it is present in the other lines as well.

Since the difference in the depths of the lines is quite considerable given the small energy differences, this cannot reasonably be caused by the differences of the excited state potentials. A more likely model is based on the relative alignment of the $F = 1$ ground state rubidium atom with regard to the rotational momentum vector of the two-body system formed with an approaching ytterbium atom. For a direct head-on collision, the initial angular momentum will be zero and a molecule formed by photoassociation will in essentially all cases have the quantum number $R' = 0$. If the collision occurs with a high angular momentum (a larger distance of closest approach in the classical picture), the centrifugal barrier prevents an approach that is close enough for photoassociation. At low rotational quantum numbers the centrifugal barrier can be crossed, resulting in the creation of the $R' = [0, 1, 2, 3]$ molecules observed.

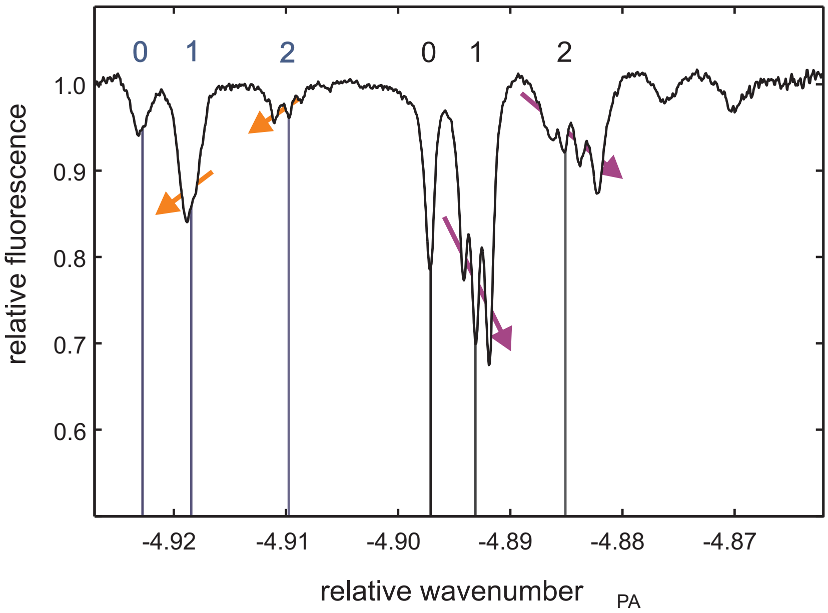

Figure 6.14: Splitting of the rotational components into subcomponents due to the coupling of atomic angular momentum F' to the molecular rotation R'. The photoassociation line at $\Delta_{\mathrm{PA}} = -4.9\,\mathrm{cm}^{-1}$ in $^{176}\mathrm{Yb}^{87}\mathrm{Rb}^*$ shows this well due to its high strength. The increase in trap loss towards the lower energy subcomponents in $F' = 1$ and towards the higher energy subcomponents in $F' = 2$ is particularly visible here.

The presence of the ytterbium atom will create an additional energy term based on the relative alignment of the nuclear rotational axis and the magnetic dipolar moment of the -now ground state- rubidium atom

$$\mu_F = g_F\,\mu_b\,F \qquad \text{with} \qquad g_{F=1} = -1/2\ . \tag{6.20}$$

This is 1.5 times larger for the $F = 1$ ground state than for the excited $F' = 2$ state. If the effective field caused by the molecular rotation is similar in the ground state, the resulting splitting should be of similar magnitude even at slightly larger distances. An energy difference of only $0.1 \cdot 10^{-3}\,\mathrm{cm}^{-1}$ already corresponds to a quite significant temperature of $T = E/k_B = 144\,\mu\mathrm{K}$. Since the splitting was found to fall off slower than the $1/r^6$ behavior of the heteronuclear molecular potential, this leads to a change of the centrifugal barrier, as shown schematically in figure 6.15. To illustrate the resulting differences from the unmodified potential, the assumed energy splitting used for the ground state was chosen to be 25 times stronger than that found for the excited state. However, this exaggerated splitting is not necessary to explain the comparably small differences in the strengths of the subcomponents.

Atom pairs that start in the rotational alignment of the energetically higher state are more likely to be prevented from approaching to the Condon point and therefore from photoassociation, while pairs aligned to form a lower energy state are more likely to be photoassociated.

The photoassociation photon will not usually affect the rotational quantum number of the nuclei directly and it can only change the rotation of the rubidium atom such that

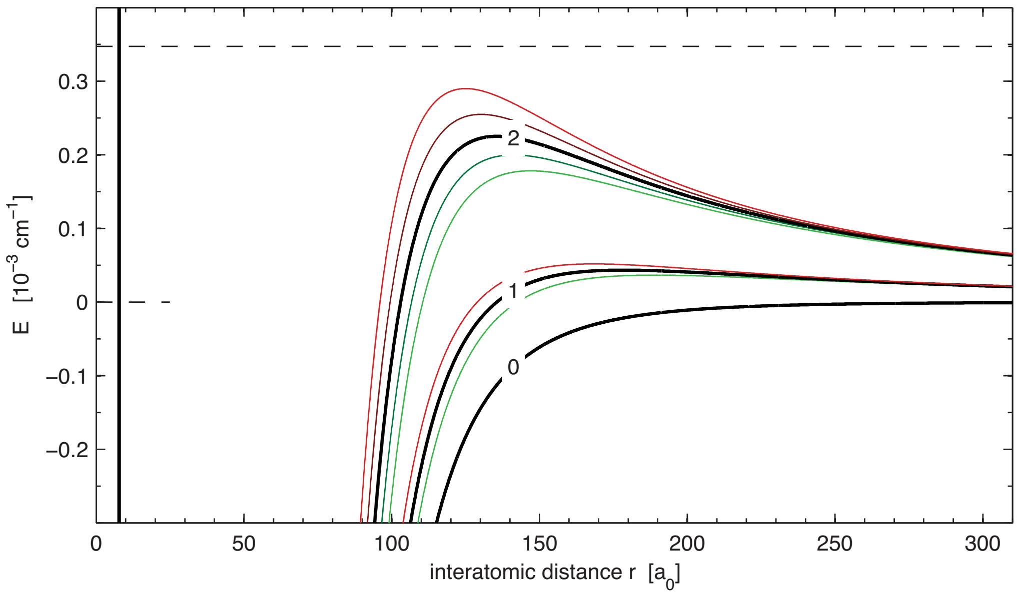

Figure 6.15: Modification of the ground state potentials by the spin-rotation coupling in the region of the centrifugal barrier. For clarity, the strength of the splitting assumed for the ground state was chosen to be 25 times larger than the values predicted from the excited state data. Black curves show the unchanged $m_R = 0$ potentials for $R = 0$, $R = 1$ and $R = 2$ as identified by the numbers. The latter two split into three and five subcomponents depending on the alignment of molecular rotation and atomic angular momentum of the rubidium atom. This is shown by the colored lines.

$m_{F'} = m_F + [0, \pm 1]$. A sign change (e.g. $m_F = -1$ to $m_{F'} = +1$) of the projected quantum number is therefore not possible. If the atomic g-factor was equal in all states, an atom-pair starting in an attractive, low-energy substate would be transformed into a molecule in a low energy substate or the unshifted $m_{F'=0}$ state at most. Atom pairs in a high potential energy substate would be less likely to form molecules due to the higher barrier. The sub-components would then decrease in depth towards higher energies.

This is true for the $F' = 1$ series. In the $F' = 2$ series, however, the excited state g-factor has the opposite sign and the magnetic dipole moment is reversed. Therefore, atom pairs in a low-energy substate become molecules in a high-energy substate and the formation rate should fall off at lower energies instead. This is exactly what is observed.

This factor is probably larger than needed to explain the differences in strength, as it leads to a change in the height of the centrifugal barrier by a factor of two between the $m_R = -2$ and $m_R = 2$ component of the $R = 2$ potential. But even this high value is not entirely unreasonable considering the quick decrease of the splitting with distance. Since there is currently no physical model for the splitting, the predictive capabilities of the fitted curve out to the location of the centrifugal barrier at $100\,a_0$ are unclear. It is also possible that the splitting simply is stronger in the ground state molecule.

Further theoretical work on the interplay of the thermal variation of collisional energies in the trap and the effect of small potential changes on the resulting wavefunction amplitude beyond the barrier is needed. Future experiments might then be devised to explore this phenomenon in more detail. For example, the different barrier heights for different initial substates will change the distribution of collisional energies contributing to molecule formation, such that the subcomponents are no longer equidistant. With sufficient improvement of the relative wavelength measurement, this might be detected directly.

6.4.4 Vibrational Levels

The most basic way to describe the vibrational states of a molecule starts with the nearly harmonic potential in the area of the equilibrium distance. This gives an equidistant series of vibrational states that is then corrected to account for the anharmonicity.

A full description of all vibrational states can in principle be obtained by solving the Schrödinger equation to find the nuclear wavefunctions in the diabatic potential given by the current electronic state. For many molecular systems the required potentials are available from ab-initio calculations. In the case of the YbRb* molecule, the potential curves are not yet known to a precision that allows useful predictions for molecules with energies near the dissociation limit such as those created by photoassociation.

Since the vibrational states are determined by the molecular potential, it is theoretically possible to reverse the calculation and find information about the potential shape from the energies and rotational constants of the observed vibrational levels. However, the most common ways to do this based on the Rydberg-Klein-Rees (RKR) or similar methods, construct the potential from the bottom up, requiring information that is simply not available from photoassociation spectroscopy.

Fortunately, the semiclassical formula presented by LeRoy and Bernstein (1970) describes the relation of the highest vibrational energy levels to the long range asymptotic potential coefficients. This was used here extensively to find vibrational lines further away from the rubidium resonance, where the distances between them become too large to cover entirely with the limited scanning range of the photoassociation laser system.

In a heteronuclear molecule the long-range part of the potential can usually be described as

$$V(r) \approx E_D + \frac{C_6}{r^6} + \frac{C_8}{r^8} + \dots \tag{6.21}$$

since there is no resonant component that will give rise to a longer range part in the potential. E_D is the dissociation energy, corresponding to an atom pair at infinite distance. For a full discussion of the long-range potentials of heteronuclear molecules, see Derevianko et al. (2001).

Leroy and Jones then find the relation for the energy of the vibrational level v

$$E(\mathrm{v}) \approx E_D - \left((\mathrm{v}_D - \mathrm{v}) \cdot \sqrt{\frac{\pi}{2\,\mu}} \cdot \frac{\Gamma(1+1/n)}{\Gamma(1/2+1/n)} \cdot \frac{\hbar\,(n-2)}{(-C_n)^{1/n}} \right)^{\frac{2n}{n-2}} \quad . \tag{6.22}$$

Here Γ indicates the gamma function, n is the order of the leading long range coefficient C_n and μ is once again the reduced mass of the diatomic system. v_D is the non-integer dissociation quantum number. Its integer part gives the maximum vibrational quantum number: $\mathrm{v}_{\mathrm{max}} = \lfloor \mathrm{v}_D \rfloor$ and the remaining (positive) fractional part

$$\mathrm{v}_{\mathrm{frac}} = \mathrm{v}_D - \mathrm{v}_{\mathrm{max}} \tag{6.23}$$

is an indication of the difference between the energy of the last vibrational level and the dissociation threshold. If it is close to zero, then the last vibrational level is positioned just below the threshold. If it is near one, then the last level is so far away from the threshold that an additional vibrational level would appear if the potential was just slightly deeper.

Since the measurements only cover the highest vibrational states, the total number of bound states $\mathrm{v}_{\mathrm{max}}+1$ remains unknown. To allow meaningful identification of states, a vibrational label is defined as

$$\Delta\,\mathrm{v} = \mathrm{v} - \mathrm{v}_{\mathrm{max}} \tag{6.24}$$

$$\Longrightarrow \mathrm{v} = \Delta\,\mathrm{v} + \mathrm{v}_{\mathrm{max}} = \Delta\,\mathrm{v} + \mathrm{v}_D - \mathrm{v}_{\mathrm{frac}} \tag{6.25}$$

such that the highest existing (although unobserved) state is identified by $\Delta\,\mathrm{v} = 0$ and lower vibrational levels by negative numbers. This sign convention was chosen to emphasize the difference to the original, absolute quantum number v.

With the relative wavenumber Δ_{PA}, which can be written as

$$\Delta_{\mathrm{PA}}(\mathrm{v}) = \frac{E(\mathrm{v}) - E_D}{h\,c^*} \qquad \text{(for the } F' = 2 \text{ vibrational series)} \tag{6.26}$$

the Leroy-Bernstein equation for $n = 6$ now takes the form

$$\Delta_{\mathrm{PA}}(\Delta\,\mathrm{v}) \approx -\left((-\Delta\,\mathrm{v} + \mathrm{v}_{\mathrm{frac}}) \cdot \sqrt{\frac{\pi}{2\,\mu}} \cdot \frac{\Gamma(7/6)}{\Gamma(4/6)} \cdot \frac{4\hbar}{(-C_6)^{1/6}}\right)^{\frac{12}{4}} \cdot \frac{1}{h\,c^*} \tag{6.27}$$

$$\approx -\frac{4}{\sqrt{2}} \cdot \left(\frac{1}{\sqrt{\pi}} \cdot \frac{\Gamma(7/6)}{\Gamma(4/6)}\right)^3 \cdot \frac{h^2}{c^*} \cdot \frac{1}{\sqrt{-C_6}} \cdot \left(\frac{-\Delta\,\mathrm{v} + \mathrm{v}_{\mathrm{frac}}}{\sqrt{\mu}}\right)^3 \tag{6.28}$$

$$\approx 0.1633\,\frac{h^2}{c^*} \cdot \frac{1}{\sqrt{-C_6}} \cdot \left(\frac{\Delta\,\mathrm{v} - \mathrm{v}_{\mathrm{frac}}}{\sqrt{\mu}}\right)^3 \tag{6.29}$$

The speed of light is written as c^* here as a reminder that it needs to be expressed in $\frac{\mathrm{cm}}{\mathrm{s}}$ to find the wavenumber in cm^{-1}.

The equation shows that the relative wavenumbers of the vibrational lines follow a simple cubic procession when plotted over the vibrational quantum number. Its slope is controlled by the C_6 coefficient and the reduced mass of the system. Some experimentation is required to assign vibrational quantum numbers to the individual lines. The line positions are found to be in very good agreement with the prediction if the lines marked ‘A’ to ‘D’ in the figures 6.6 to 6.10 are ignored and the remaining lines are assigned relative quantum numbers $\Delta\,\mathrm{v}$ as shown.

The predictions provided by the Leroy-Bernstein equation were used to great success in locating lines of lower vibrational energy without covering the full wavelength range.

6.4.5 Improved Leroy-Bernstein Equation

An improved version of the Leroy-Bernstein equation was presented recently in Comparat (2004) that takes into account some additional terms that were neglected previously and aims to achieve a 1% accuracy. The same paper also introduces a method to obtain information about the next long range coefficient, in this case C_8.

However, preliminary investigations showed that the influence of the C_8 coefficient on the observed vibrational series is low compared to the inaccuracies of the measurements. For this reason, only the basic improved equation will be used:

$$E(\mathrm{v}) \approx E_D - \left((\mathrm{v}_D - \mathrm{v}) \cdot \frac{1}{H_n^{-1}}\right)^{\frac{2n}{n-2}} \cdot \left(1 - \frac{2n}{n-2}\,\gamma \left(\frac{\mathrm{v}_D - \mathrm{v}}{H_n^{-1}}\right)^{\frac{2n}{n-2}-1}\right) \tag{6.30}$$

$$\Longrightarrow \Delta_{\mathrm{PA}}(\Delta\,\mathrm{v}) \approx -\left(\frac{-\Delta\,\mathrm{v} + \mathrm{v}_{\mathrm{frac}}}{H_n^{-1}}\right)^{\frac{2n}{n-2}}$$

$$\cdot \left(1 - \frac{2n}{n-2}\,\gamma \left(\frac{-\Delta\,\mathrm{v} - \mathrm{v}_{\mathrm{frac}}}{H_n^{-1}}\right)^{\frac{2n}{n-2}-1}\right) \cdot \frac{1}{h\,c^*} \tag{6.31}$$

$$\text{with} \qquad H_n^{-1} = \sqrt{\frac{2\,\mu}{\pi}} \cdot \frac{(-C_n)^{1/n}}{\hbar\,(n-2)} \cdot \frac{\Gamma\left(\frac{n+2}{2\,n}\right)}{\Gamma\left(\frac{n+1}{n}\right)} \tag{6.32}$$

$$\Longrightarrow \Delta_{\mathrm{PA}}(\Delta\,\mathrm{v}) \approx -\left(\frac{-\Delta\,\mathrm{v} + \mathrm{v}_{\mathrm{frac}}}{H_6^{-1}}\right)^3 \cdot \left(1 - 3\,\gamma \left(\frac{-\Delta\,\mathrm{v} - \mathrm{v}_{\mathrm{frac}}}{H_6^{-1}}\right)^2\right) \cdot \frac{1}{h\,c^*} \tag{6.33}$$

The term H_n^{-1} contains the constants of equation 6.22. The new parameter γ contains information about the modeling of the inner part of the potential. If it is set to zero, the equation becomes identical to the original Leroy-Bernstein equation.

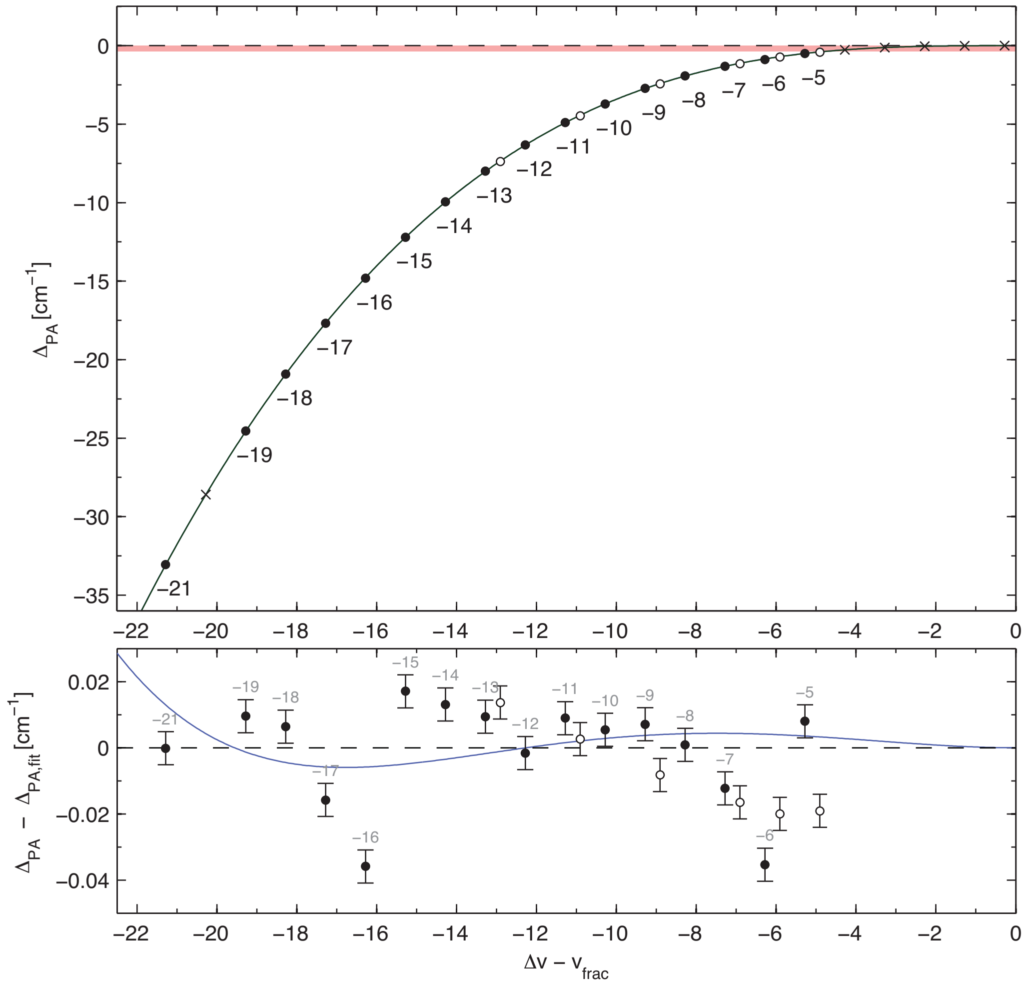

Figure 6.16: **(top)** Positions Δ_{PA} of vibrational lines over vibrational level relative to the non-integer dissociation level ($\mathrm{v} - \mathrm{v}_D = \Delta\,\mathrm{v} - \mathrm{v}_{\mathrm{frac}}$) for $^{176}\mathrm{Yb}^{87}\mathrm{Rb}^*$ (solid circles) and $^{174}\mathrm{Yb}^{87}\mathrm{Rb}^*$ (open circles). Levels for $^{176}\mathrm{Yb}$ are labeled with the relative vibrational quantum number $\Delta\,\mathrm{v} = \mathrm{v} - \mathrm{v}_{\mathrm{max}}$. Predicted but unobserved levels in $^{176}\mathrm{Yb}$ are marked 'x', the red zone between $-0.38\,\mathrm{cm}^{-1}$ and $0\,\mathrm{cm}^{-1}$ indicates the range obscured by the near-resonant rubidium loss.
(bottom) Difference between observed values and fit. The blue line gives the value of the simple Leroy-Bernstein fit compared to the improved version.

This equation is now fitted to the experimental values of $\Delta_{\mathrm{PA}}(\Delta\,\mathrm{v})$ in $^{176}\mathrm{Yb}^{87}\mathrm{Rb}^*$. The results are shown in figure 6.16. Due to the increase of Δ_{PA} with $\Delta\,\mathrm{v}^3$, lower vibrational states contribute more strongly to the value found for the C_6 coefficient. Since it is strongly expected that the choice of the (bosonic) ytterbium isotope has no influence on the electronic structure, the only expected difference in the vibrational spectrum can come from the different reduced mass of the system. As a test of the fitted values, equation 6.33 was also applied to the vibrational spectrum of $^{174}\mathrm{Yb}^{87}\mathrm{Rb}^{*}$ with γ and C_6 held fixed and the fractional dissociation quantum number $\mathrm{v}_{\mathrm{frac}}$ as the only free parameter. As can be seen in the diagram, this also results in very good agreement between theory and experiment.

The diagrams are plotted with the relative vibrational quantum number $\mathrm{v} - \mathrm{v}_D = \Delta\,\mathrm{v} - \mathrm{v}_{\mathrm{frac}}$ as the horizontal axis to better show the shape of the (nearly) cubic procession, with the saddle of the parabola at the origin. The changes introduced by the improved equation are too small to be noticeable at this scale.

The bottom diagram shows the difference between the actual measured values and the fit in more detail. The blue line corresponds to a fit with the original Leroy-Bernstein equation. It is obvious that both equations describe the data well, with the improved version agreeing slightly better for most of the vibrational lines. But even for this, the agreement is not as good as expected from the accuracy estimate of the wavelength determination. Further investigation is required to determine whether this is due to underestimated or unknown experimental errors or due to some perturbation of the actual vibrational energies. This can be caused by the interaction of different electronic states of similar energies as shown in Kokoouline et al. (2002). The regular structure of the deviations, consisting of a sharp dip and a gradual return to the expected value near $\Delta\,\mathrm{v} = -6$ and $\Delta\,\mathrm{v} = -16$ might be an indication of this, particularly since the rotational spectrum of $\Delta\,\mathrm{v} = -6$ also shows signs of distortion.

SI units: C_6	(-5.442	± 0.094)	$10^{-76}\,\mathrm{J\,m}^6$
atomic units: C_6	(-5684	± 98)	$E_h\,a_0^6$
$\mathrm{v}_{\mathrm{frac}}$ (^{176}Yb)	0.278	± 0.031	
$\mathrm{v}_{\mathrm{frac}}$ (^{174}Yb)	0.906	± 0.007	
γ	(2.03	± 2.06)	$\cdot 10^{11}$

Table 6.1: Results of the improved Leroy-Bernstein fit of the vibrational data

Table 6.1 lists the values that were extracted from the fit. The calculated C_6 coefficient of $-5684 \pm 98\,E_h\,a_0^6$ is similar to the values predicted for other heteronuclear atom pairs (Marinescu and Sadeghpour, 1999). It also agrees well with the value of $C_6^{\mathrm{simple}} = -5597\,E_h\,a_0^6$ found from a fit of the data with the original Leroy-Bernstein equation. The listed uncertainties are purely based on the fit and do not include systematic errors or the limits of the fitted model itself. However, some simple investigations using the basic Leroy-Bernstein equation and varying the wavenumber of the most deeply bound vibrational state seem to indicate that at least the effect of the wavemeter uncertainty is well below the limits given.

6.4.6 Overview of Assignment Results

With the definitions introduced throughout this chapter, the wavenumbers of the various components of the observed lines are given by

$$\widetilde{\nu}(\Delta\,\mathrm{v}, R', m'_{R'}) = \widetilde{\nu}_{\mathrm{D1}(1\rightarrow 2)} + \Delta_{\mathrm{PA}}(\Delta\,\mathrm{v}) + B_{\mathrm{rot}}(\Delta\,\mathrm{v})\,R'(R'+1) + m'_{R'}\Delta_{R'}(\Delta\,\mathrm{v}, R')$$

(6.34)

where $\widetilde{\nu}_{\mathrm{D1}(1\to 2)} = 12578.862\,\mathrm{cm}^{-1}$ is again the wavenumber of the hyperfine component of the D1 line that was chosen as reference.

All vibrational lines, rotational constants and splittings between subcomponents that were found in the analysis of the spectra are listed in tables 6.2 and 6.4. Many lines, particularly in the $F' = 1$ series, were too weak to find values for all expected components. In other lines near the dissociation threshold, the splitting of the rotational lines is small and the subcomponents are not clearly separated. In these cases no values are given.

In some other cases the most likely interpretation of an unclear spectrum is listed. This is mentioned in the comments. For vibrational lines that are so weak that they were not observed at all, positions for the $R' = 0$ component of the $F' = 2$ series were calculated from the fit. These are marked “prediction”.

6.4.7 Electronic State

As mentioned earlier, molecules might be formed with ytterbium atoms in either the ground or the excited state. Since the population in the excited state is created by the MOT lasers, it can be reduced by temporarily interrupting the trap. As long as it is turned back on before the atoms leave the trap, the atom number is not significantly reduced. It was found that a duty cycle of 75%, with a bright phase of 144 μs follow by a dark phase of 48 μs works reasonably well, with the small resulting loss of fluorescence almost entirely due to the reduced illumination.

This supports the theory that the ytterbium suppression is caused by collisions involving excited ytterbium atoms, since a constant loss rate at zero loading rate during a dark cycle should lead to a dramatic reduction in the number of atoms available for recapture during the next bright cycle. This is not observed.

As the dark phase is considerably longer than the lifetime $\tau = 5.5\,\mu$s of the ytterbium $^3\mathrm{P}_1$ state, the atoms will spend most of it in the ground state. By applying the photoassociation laser either during the dark or during the bright phase, the electronic state of the photoassociated molecules can now be investigated. If molecules are formed from excited ytterbium atoms at a given wavelength of the photoassociation laser, then the loss rate should decrease dramatically when the laser is applied during the dark phase.

The required switching of trap and photoassociation laser is done with the AOMs already in place for power stabilization. The results are presented in figure 6.17. It is found that the trap loss actually increases from 7% to 11% for a pulse during the dark phase. This corresponds to a doubling of the molecule formation rate per atom from $r_{\mathrm{dark}} \approx 0.3\,\mathrm{s}^{-1}$ to $r_{\mathrm{bright}} \approx 0.6\,\mathrm{s}^{-1}$. This is directly proportional to the increase in the ground state atom number expected when the fraction of atoms normally kept in the excited state by the trap lasers return there: Since the laser supplies considerably more than the saturation intensity, this fraction is expected to be close to 50%, even when taking the detuning into account.

This result is clear evidence that at least for the investigated line at $\Delta_{\mathrm{PA}} \approx -2.44\,\mathrm{cm}^{-1}$ in $^{174}\mathrm{Yb}^{87}\mathrm{Rb}^*$ the molecules are formed from the ytterbium ground state. Because the line examined is clearly part of the main vibrational series this should also apply to the other

		Δ_{PA}	depth	r_{eff}	B_{rot}	$\Delta_{R'=1}$	$\Delta_{R'=2}$	$\Delta_{R'=3}$	
Δv'	F'	[cm^{-1}]	of R'=0	[a_0]	all in units of 10^{-3} cm^{-1}				comment
0	2	−0.00007	−−						prediction
-1	2	−0.00713	−−						prediction
-2	2	−0.04039	−−						prediction
-3	2	−0.1204	−−						prediction
-4	2	−0.2675	−−						prediction
-5	2	−0.49440	3%	34.89	**0.85**	–	–	–	
	1	−0.52060	3%	30.95	*1.08*	–	–	–	
-6	2	−0.88090	10%	26.71	**1.45**	1.95	2.07	1.90	
	1	−0.90787	4%	32.44	*0.98*	0.40	1.10	1.55	unclear
-7	2	−1.32980	15%	27.79	**1.34**	0.70	0.87	–	
	1	−1.35590	8%	26.71	*1.45*	–	–	–	
-8	2	−1.93810	9%	26.44	**1.48**	0.65	0.90	–	
	1	−1.96440	4%	26.53	*1.47*	0.65	0.90	–	
-9	2	−2.72330	27%	25.04	**1.65**	0.80	1.05	–	
	1	−2.74935	10%	23.91	*1.81*	0.30	0.85	–	
-10	2	−3.70710	2%	24.97	**1.66**	0.75	0.90	–	
-11	2	−4.89710	20%	22.75	**2.00**	1.10	1.45	–	
	1	−4.92280	5%	21.84	*2.17*	0.40	1.30	–	
-12	2	−6.33330	2%	22.75	**2.00**	1.50	1.30	–	weak line,
	1	−6.35900	2%	21.69	*2.20*	–	1.30	–	unclear
-13	2	−8.00080	16%	20.55	**2.45**	1.50	1.80	2.15	
	1	−8.02660	3%	19.76	*2.65*	1.10	1.80	–	
-14	2	−9.94940	2%	20.47	**2.47**	1.65	–	–	
	1	−9.97300	2%	22.75	*2.00*	0.70	1.50	–	weak line
-15	2	−12.19230	8%	18.89	**2.90**	2.35	2.58	–	
	1	−12.21700	2%	20.55	*2.45*	1.90	1.30	–	
-16	2	−14.80770	6%	18.63	**2.98**	2.50	1.50	–	
-17	2	−17.68660	5%	18.15	**3.14**	2.60	2.90	–	
	1	−17.71050	2%	17.07	*3.55*	1.90	–	–	
-18	2	−20.92110	10%	17.71	**3.30**	2.85	–	–	
	1	−20.94400	3%	16.84	*3.65*	2.60	–	–	
-19	2	−24.5534	1%	17.58	*3.35*	2.50	–	–	weak line
-20	2	−28.598	−−						prediction
-21	2	−33.0554	2%	16.95	*3.60*	2.30	2.70	–	weak line
-22	2	−37.955	−−						prediction
-23	2	−43.319	−−						prediction
-24	2	−49.168	−−						prediction
-25	2	−55.525	−−						prediction
uncertainty:					**±0.15**				
		±0.005	±2%		*±0.30*	±0.2	±0.2	±0.2	

Table 6.2: Properties of photoassociation lines in ^{176}Yb^{87}Rb*

Δv'	F'	Δ_{PA} [cm^{-1}]	depth of R'=0	r_{eff} [a_0]	B_{rot} all in units of 10^{-3} cm^{-1}	$\Delta_{R'=1}$	$\Delta_{R'=2}$	$\Delta_{R'=3}$	comment
A	2?	-0.47960	4%	23.46	**1.88**	2.35	3.13	3.70	
B	1?	-0.50260	15%	28.11	*1.31*	2.17	2.93	–	
C	2?	-0.64829	4%	13.99	**5.29**	4.95	4.43	–	
D	1?	-0.67220	2%	17.64	*3.33*	2.71	3.50	–	

Table 6.3: Properties of unassigned photoassociation lines in $^{176}\mathrm{Yb}^{87}\mathrm{Rb}^{*}$

Δv'	F'	Δ_{PA} [cm^{-1}]	depth of R'=0	r_{eff} [a_0]	B_{rot} all in units of 10^{-3} cm^{-1}	$\Delta_{R'=1}$	$\Delta_{R'=2}$	comment
0	2	-0.00256	– –					prediction
-1	2	-0.02380	– –					prediction
-2	2	-0.08434	– –					prediction
-3	2	-0.2048	– –					prediction
-4	2	-0.42490	9%	31.91	**1.02**	–	–	
	1	-0.45180	9%	32.64	*0.98*	–	–	
-5	2	-0.72800	10%	30.87	**1.09**	0.27	0.55	
	1	-0.75540	4%	28.27	*1.30*	–	–	
-6	2	-1.14860	18%	27.24	**1.40**	0.50	0.55	
	1	-1.17528	6%	27.84	*1.34*	–	–	
A		(-1.37648)	4%	27.24	**1.40**	–	–	echo of -6, F'=2
B		(-1.40303)	3%	27.84	*1.34*	–	–	echo of -6, F'=1
-7	2	-1.70310	2%	26.58	**1.47**	–	–	
	1		– –					unobserved
-8	2	-2.43700	17%	24.94	**1.67**	0.68	0.95	
	1	-2.46365	6%	24.23	*1.77*	–	–	
C		(-2.67330)	2%	24.94	**1.67**	0.68	0.95	echo of -8, F'=2
D		(-2.69945)	3%	24.79	*1.69*	–	–	echo of -8, F'=1
-9	2	-3.0761	– –					prediction,
	1		– –					unobserved
-10	2	-4.45900	15%	23.08	**1.95**	1.08	1.30	
	1	-4.48495	8%	23.89	*1.82*	1.15	–	
-11	2	-5.8062	– –					prediction,
	1		– –					unobserved
-12	2	-7.38365	11%	21.11	**2.33**	1.65	2.00	
	1	-7.40825	2%	19.99	*2.60*	1.65	2.00	weak line
-13	2	-9.2560	– –					prediction
-14	2	-11.4031	– –					prediction
-15	2	-13.8597	– –					prediction
uncertainty:					**±0.15**			
		±0.005	±2%		*±0.30*	±0.2	±0.2	

Table 6.4: Properties of photoassociation lines in $^{174}\mathrm{Yb}^{87}\mathrm{Rb}^{*}$

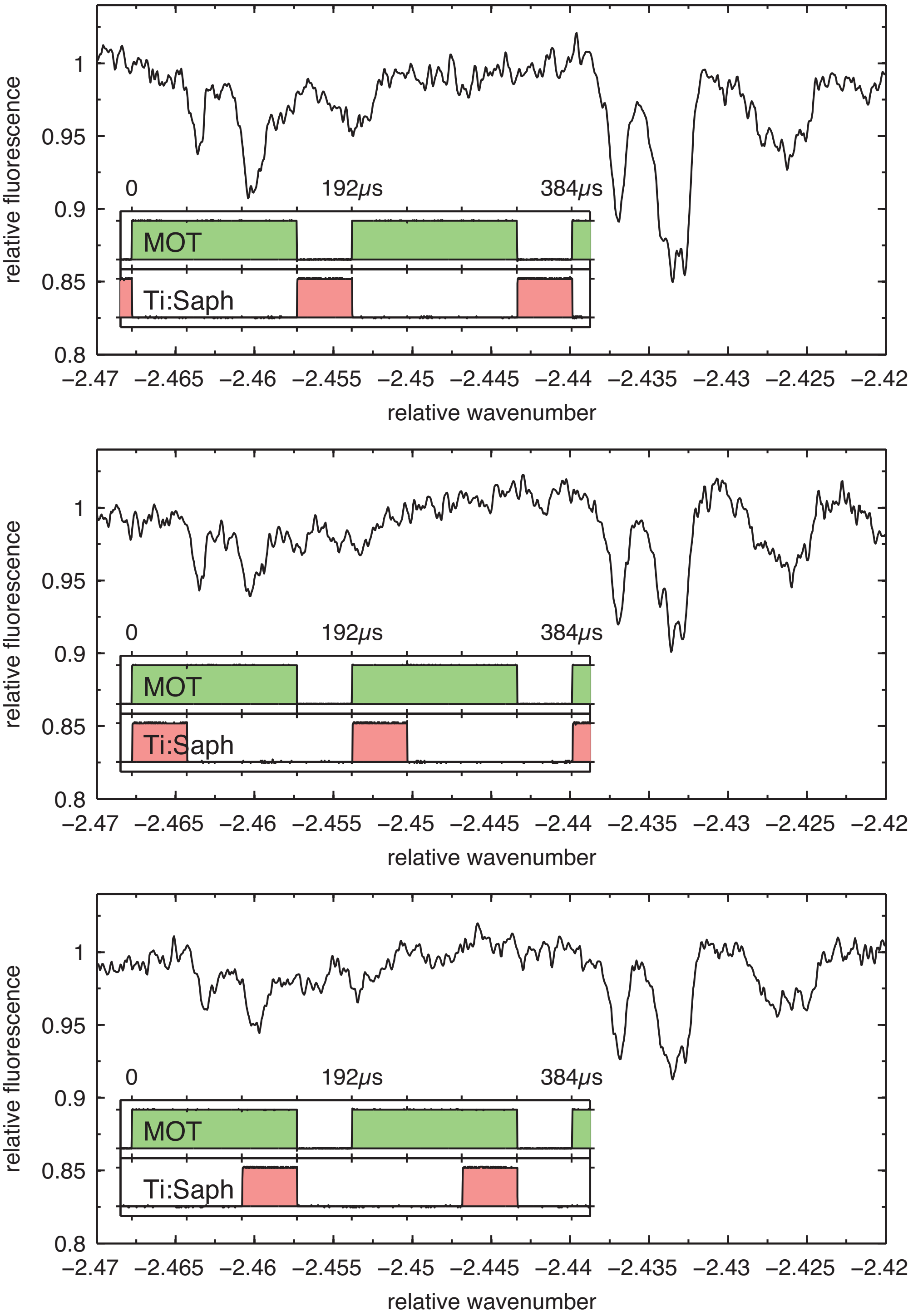

Figure 6.17: Spectra with periodically interrupted ytterbium MOT. Applying the PA laser during the dark phase **(top)** results in an increase in the photoassociation rate by a factor of two compared to what is found with photoassociation pulses during the bright phase **(middle, bottom)**.

lines. And since the lines in the ^{176}Yb^{87}Rb* experiments follow a vibrational progression that matches an identical potential curve, they are obviously formed from ground state ytterbium atoms, too.

The unassigned lines found in the ^{176}Yb-^{87}Rb spectrum are prime candidates for investigation using this method, however, and might very well be found to belong to a doubly excited state.

6.5 Saturation of the Photoassociation Rate

It is obvious that the photoassociation rate depends on the intensity of the photoassociation light. But it is also clear that it cannot increase without limit at high intensities, because the photoassociation process depends on the presence of ytterbium-rubidium atom pairs in a configuration suitable for forming a bound state. After an initial increase with intensity, the photoassociation rate is therefore expected to saturate once a certain level is reached.

6.5.1 Theoretical Predictions

Models for this saturation have been presented in various sources, like Azizi et al. (2004) and Schlöder et al. (2002). This chapter follows the detailed theoretical description of Jones et al. (2006, section 3.C). For brevity only the central points will be repeated here with a focus on the assumptions and simplifications made to adapt the model to our experimental conditions.

The total event rate coefficient K_d is described by

$$K_d(E) = \frac{\pi v_{\mathrm{rel}}}{k^2} \sum_{\ell} (2\ell + 1) \cdot \frac{\hbar\Gamma_d \; \hbar\Gamma_b(E,\ell)}{[E + h\nu - h\nu_0 - S_b(E)]^2 + [\hbar\Gamma_{\mathrm{tot}}/2]^2} \tag{6.35}$$

Here E is the energy of the collision between two atoms with relative velocity $v_{\mathrm{rel}} = \hbar k/\mu$ and wave vector k.

The partial wave ℓ of the collision describes the angular momentum of the two atoms. Since the coupling between rotation and electronic state is weak in the molecular states examined here, it will be assumed that the photon causing the photoassociation process does not change the molecular rotation. The final rotation quantum number R' is then entirely given by ℓ, and the contributions from different values are well separated in the spectrum. In the following we will primarily look at the $R' = 0$ component and therefore at $\ell = 0$.

The first term in the denominator describes the position of the photoassociation line. Here ν is the laser frequency, ν_0 is the actual resonance frequency, which is then shifted due to the initial kinetic energy of the atoms E and the light shift $S_b(E)$. Due to the natural and laser linewidths, Doppler broadening and the smearing of the line by the laser scan, the observed line shapes do not show the distinct asymmetry described by the model. When the laser frequency is tuned to the center of the line, the frequency dependent term can be assumed to be small compared to the other term of the denominator for all collisional energy classes and can be treated as zero when looking at resonant photoassociation only.

The second term contains information about the resulting linewidth of the photoassociation process:

$$\Gamma_{\text{tot}} = \Gamma_{\text{nat}} + \Gamma_b(E,\ell) + \Gamma_0 \qquad , \tag{6.36}$$

where Γ_{nat} is the natural linewidth given by the lifetime of the excited state. For molecules in the near-dissociation regime, this will be close to the lifetime of the corresponding excited atomic state. Γ_0 is the rate of losses through channels such as predissociation that do not depend on the light field, assumed to be zero in this case, and the detection rate enters as $\Gamma_d = \Gamma_{\text{nat}} + \Gamma_0$ in the case of trap loss spectroscopy. Finally, Γ_b describes the rate of molecules returning to the initial ground state through stimulated emission:

$$\begin{aligned} \hbar\Gamma_b(E,\ell) &= 2\pi\,|V_b(E,\ell)|^2 && (6.37)\\ &= 2\pi\frac{2\pi\, I}{c}\left|\left\langle b\middle|\vec{d}\cdot\vec{e}\middle|E,\ell\right\rangle\right|^2 && (6.38)\\ &= \frac{4\,\pi^2}{c} I\, a_t^2 && (6.39)\end{aligned}$$

Here I is the intensity of the photoassociation beam and $a_t = |\langle b|\vec{d}\cdot\vec{e}|E,\ell\rangle|$ is the matrix element describing the coupling between the collisional state $|E,\ell\rangle$ and the bound state $|b\rangle$. In this notation $\vec{d}$ is the molecular dipole moment and $\vec{e}$ the polarization vector of the light field.

All of this can now be put into equation 6.35 yielding

$$\begin{aligned} r_{\text{PA}}^{\text{res}}(I) &= K_d^r(E_{\text{avg}})\,\rho_{\text{Rb}} && (6.40)\\ &= \frac{\pi\, v_{\text{rel}}}{k^2}\cdot\frac{\hbar\Gamma_d\;\hbar\Gamma_b(E_{\text{avg}},\ell)}{0+[(\hbar\Gamma_{\text{nat}}+\hbar\Gamma_b(E_{\text{avg}},\ell)+\hbar\Gamma_0)/2]^2}\,\rho_{\text{Rb}} && (6.41)\\ &= \frac{\pi\, v_{\text{rel}}}{k^2}\cdot\frac{4\hbar\Gamma_{\text{nat}}\;\frac{4\pi^2}{c}I\,a_t^2}{[\hbar\Gamma_{\text{nat}}+\frac{4\pi^2}{c}I\,a_t^2]^2}\,\rho_{\text{Rb}} && (6.42)\\ &= \frac{\pi\, v_{\text{rel}}}{k^2}\cdot 4\frac{\left(\frac{\hbar\Gamma_{\text{nat}}\,c}{4\pi^2 a_t^2}\right)\cdot I}{\left[\left(\frac{\hbar\Gamma_{\text{nat}}\,c}{4\pi^2 a_t^2}\right)+I\right]^2}\,\rho_{\text{Rb}} && (6.43)\\ &= \underbrace{\frac{\pi\, v_{\text{rel}}\,\rho_{\text{Rb}}}{k^2}}_{\text{amplitude}}\cdot\underbrace{4\frac{I_{\text{opt}}\cdot I}{[I_{\text{opt}}+I]^2}}_{\text{shape}} && (6.44)\end{aligned}$$

for the on-resonance event rate of the $\ell = 0$ collisions that contribute the main part of the $R' = 0$ photoassociation line. The contributions to the $R' = 0$ components from $\ell = 1$ collisions are likely to be suppressed due to the weak coupling of molecular rotation to the electronic angular momentum and the resulting low dipole matrix element for $\Delta m' = \pm 1$ transitions.

Most of the constants have been pulled into I_{opt} and the equation is clearly separated into two parts now, with the first describing the maximum value reached by the saturation curve and the second describing the shape. The maximum photoassociation rate is reached when $I = I_{\text{opt}}$. The second part of the equation takes on a value of 1 at this point. Afterwards it falls off as $4\, I_{\text{opt}}/I$ for $I \gg I_{\text{opt}}$. Due to the large relative size of the rubidium MOT, ρ_{Rb} can be assumed to be constant over the volume of the ytterbium cloud.

It needs to be pointed out that within the limits of this model, the maximum photoassociation rate is controlled entirely by the distribution and movement of the atoms. The transition matrix element a_t only appears in the second term, always in conjunction with the incident intensity I (see equation 6.42). This means that while the variation of the Franck-Condon factors causes some lines to be more easily accessible than others, this only affects the intensity of the photoassociation laser required to reach the same maximum rate as for other photoassociation lines.

The relative atomic velocity and the corresponding wave vector are given by

$$v_{\text{rel}} = \hbar k/\mu = \sqrt{2E/\mu} \tag{6.45}$$

$$k = \sqrt{2E\mu}/\hbar \tag{6.46}$$

and the maximum photoassociation rate as given by the amplitude term in equation 6.35 then becomes

$$r_{\text{PA}}^{\max} = \frac{\pi\, v_{\text{rel}}}{k^2}\rho_{\text{Rb}} \tag{6.47}$$

$$= \frac{\pi\,\sqrt{2E/\mu}}{(2\,E\,\mu)/\hbar^2}\,\rho_{\text{Rb}} \tag{6.48}$$

$$= \frac{\pi\,\hbar}{\sqrt{2\,E\,\mu^3}}\,\rho_{\text{Rb}} \tag{6.49}$$

$$= \frac{\pi\,\hbar}{\sqrt{k_B\,T_{\text{eff}}\,\mu^3}}\,\rho_{\text{Rb}} \tag{6.50}$$

With an effective temperature (Tassy, 2007) in the mixture of

$$T_{\text{eff}} = \frac{m_{\text{Yb}}\,T_{\text{Rb}} + m_{\text{Rb}}\,T_{\text{Yb}}}{m_{\text{Yb}} + m_{\text{Rb}}} \approx 398\,\mu\text{K} \tag{6.51}$$

and a peak rubidium density of $\rho_{\text{Rb}} = 1.07{\cdot}10^{11}\text{cm}^{-3}$ (see chapter 5.1) this gives a maximum photoassociation rate per ground state ytterbium atom of $r_{\text{PA}}^{\max} = 1.7\text{s}^{-1}$, common for both ytterbium isotopes. To compare this number to the observed loss rates, it is necessary to correct it for the fraction of ground state atoms to total atoms in the trap. Assuming full saturation of the transition, this is ratio is 1/2 and the expected rate becomes $r_{\text{PA}}^{\text{corr}} = 0.85\,\text{s}^{-1}$ per atom.

6.5.2 Size Effects of the Photoassociation Beam

A constant intensity of the photoassociation beam over the entire volume of the ytterbium cloud is assumed in the current model equation. This is not realistic given the near-Gaussian intensity distribution and limited laser power. In order to reach the maximum possible photoassociation rate, the beam needs to be focussed to a similar size as the atom cloud to increase the intensity at the dense center. But if the spot size is chosen too small, the intensity will be higher than optimal for a few atoms and unnecessary low for the majority of them. This leads to a reduced rate, just as choosing the beam size too large does. This chapter will discuss the choice of beam size that optimizes the molecule production.

In chapter 5.1.1, equation 5.13 was derived for the density-equivalent as a function of the local beam intensity:

$$\rho"(I) = \frac{N}{I}\frac{u^2}{w^2}\left(\frac{I}{I_{\max}}\right)^{\frac{u^2}{w^2}} \tag{6.52}$$

This describes how for a large ($u > w$) beam many atoms will see very similar (but low) intensities, while for a beam that is smaller than the atomic cloud ($u < w$) the intensity will be concentrated on a low number of atoms. Figure 6.18 illustrates this.

Equations 6.52, 6.47 and 6.35 can be combined to give a new model equation for the on-resonance photoassociation rate over beam power that includes the sizes of beam and cloud:

$$\widetilde{r}_{\text{PA}}(u, w, I_{\max}) = \frac{R_{\text{PA}}}{N_{\text{Yb}}} \tag{6.53}$$

$$= \int_{I_{\max}}^{0} \frac{\rho''(I)}{N_{\text{Yb}}} \cdot r_{\text{PA}}(I)\, \mathrm{d}I \tag{6.54}$$

$$= \int_{I_{\max}}^{0} \frac{1}{I}\frac{u^2}{w^2}\left(\frac{I}{I_{\max}}\right)^{\frac{u^2}{w^2}} r_{\text{PA}}^{\max} \cdot 4\frac{I_{\text{opt}} \cdot I}{(I_{\text{opt}} + I)^2}\, \mathrm{d}I \tag{6.55}$$

$$= 4\, r_{\text{PA}}^{\max}\frac{u^2}{w^2}\int_{I_{\max}}^{0}\left(\frac{I}{I_{\max}}\right)^{\frac{u^2}{w^2}} \frac{I_{\text{opt}}}{(I_{\text{opt}} + I)^2}\, \mathrm{d}I \tag{6.56}$$

The power dependence of $\widetilde{r}_{\text{PA}}$ for different ratios u/w was calculated numerically and is plotted in the second diagram of figure 6.18. The relation

$$I_{\max} = \frac{P_{\text{beam}}}{2\,\pi\,u^2} \tag{6.57}$$

was used to connect the maximum intensity $I_{\max}$ to the total power in the photoassociation beam. Several interesting points can be seen from the resulting graph:

The intensity distribution smears out the peak in the photoassociation rate, especially at small beam diameters. If the beam size is chosen to be half that of cloud, the maximum achievable photoassociation rate is only half of $r_{\max}$, while a beam of three times the size ($u/w = 1.5$) allows for a rate of $0.95\, r_{\max}$. This maximum occurs at a total beam power that is twice as high as that of the smaller beam, however.

While a large beam is therefore preferable in order to reach high molecule production rates, an increase of the beam radius beyond 1.5 times the cloud radius offers very little gain. On the other hand, a smaller beam can be advantageous for photoassociation lines with a low transition matrix element that require a high intensity to reach the maximum

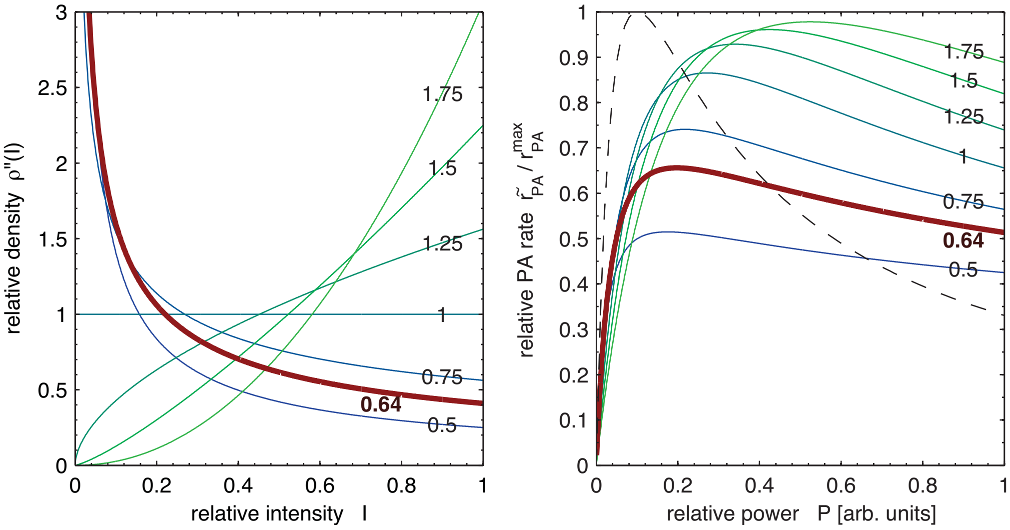

Figure 6.18: **(left)** Distribution of the equivalent atom density $\rho''(I)$ over the relative intensity $I/I_{\max}$ for relative beam sizes u/w between 0.5 and 1.75 (indicated by numbers), normalized to a total atom number of 1. The red curve corresponds to the relative size of 0.64 used in the experiments.
(right) photoassociation rate $\widetilde{r}_{\mathrm{PA}}$ relative to the maximum achievable rate over laser power. Colored graphs correspond to different beam sizes, with numbers indicating size relative to the cloud size (u/w). The red curve corresponds to the ratio used in the actual experiments. The dashed line shows the PA rate as given by the model for a large, constant intensity beam. It is included to highlight the change in the shape of the curve caused by the intensity variations and is not drawn to the same power scale.

rate. A smaller beam can increase the initial rise of the photoassociation rate, leading to higher actual rates achieved at photoassociation beam powers below a certain point.

Figure 6.19 explores this in more detail. It presents an enlarged version of the previous diagram for beam sizes smaller than the cloud. It is readily apparent that there seems to be a lower limit to the useful size, too: While moving from $u/w = 1$ to $u/w = 0.64$ -the ratio used in the experiments- still gives a noticeable increase in $\widetilde{r}_{\mathrm{PA}}$ for rates around $\widetilde{r}_{\mathrm{PA}} \approx 0.25\, r_{\mathrm{PA}}^{\max}$, any further decrease offers no noticeable gain for any beam power. The current size ratio therefore appears to be well chosen for photoassociation spectroscopy, focussing more on finding weak lines instead of maximizing molecule production from stronger ones.

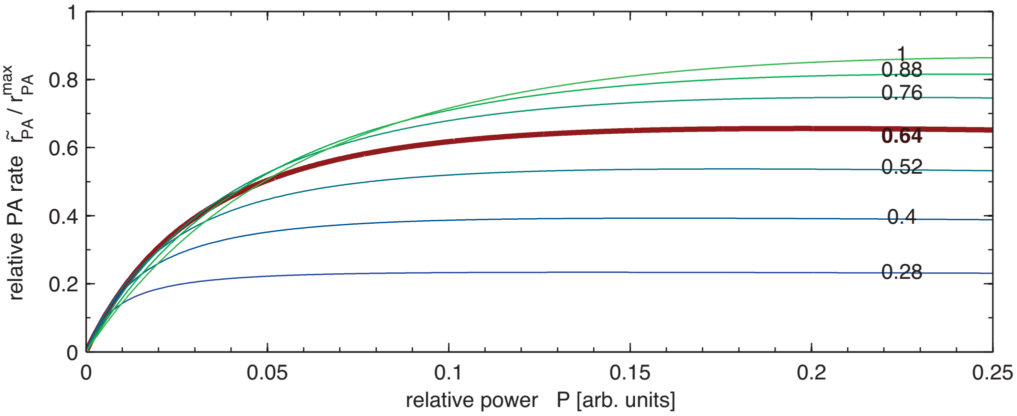

Figure 6.19: Relative photoassociation rate $\widetilde{r}_{\mathrm{PA}}/r_{\mathrm{PA}}^{\max}$ over power of the photoassociation beam for different relative beam sizes as indicated by the numbers.

6.5.3 Application to Experimental Data

During the course of the experiments, the intensity dependence of the trap loss has been investigated for several of the stronger photoassociation lines. This section will present a comparison of the results to the predictions of the theory developed so far.

Actual photoassociation rates have been extracted from the loss rates using equation 5.73 and the trap data from table 5.4. The results are presented in figure 6.20. At the full power of around 400 mW normally available in the photoassociation beam, none of the investigated lines have reached a maximum yet. The decrease of the photoassociation rate predicted by the model is therefore still unconfirmed. However, the nearly linear increase of the photoassociation rate in $^{174}\mathrm{Yb}, \Delta\,\mathrm{v} = -10$ over the entire observed range supports the interpretation that the "weaker" photoassociation lines simply require a higher intensity to reach a similar maximum rate as the stronger ones. If the parameters can be controlled sufficiently well, this might provide an instrument to directly measure the matrix element in equation 6.38.

The lines for $^{176}\mathrm{Yb}, \Delta\,\mathrm{v} = -11$ and $^{174}\mathrm{Yb}, \Delta\,\mathrm{v} = -8$ were fitted with the model presented in the previous section. This is shown by the red curves, which agree well with the data points throughout the accessible range. The results of the fits are listed in table 6.5.

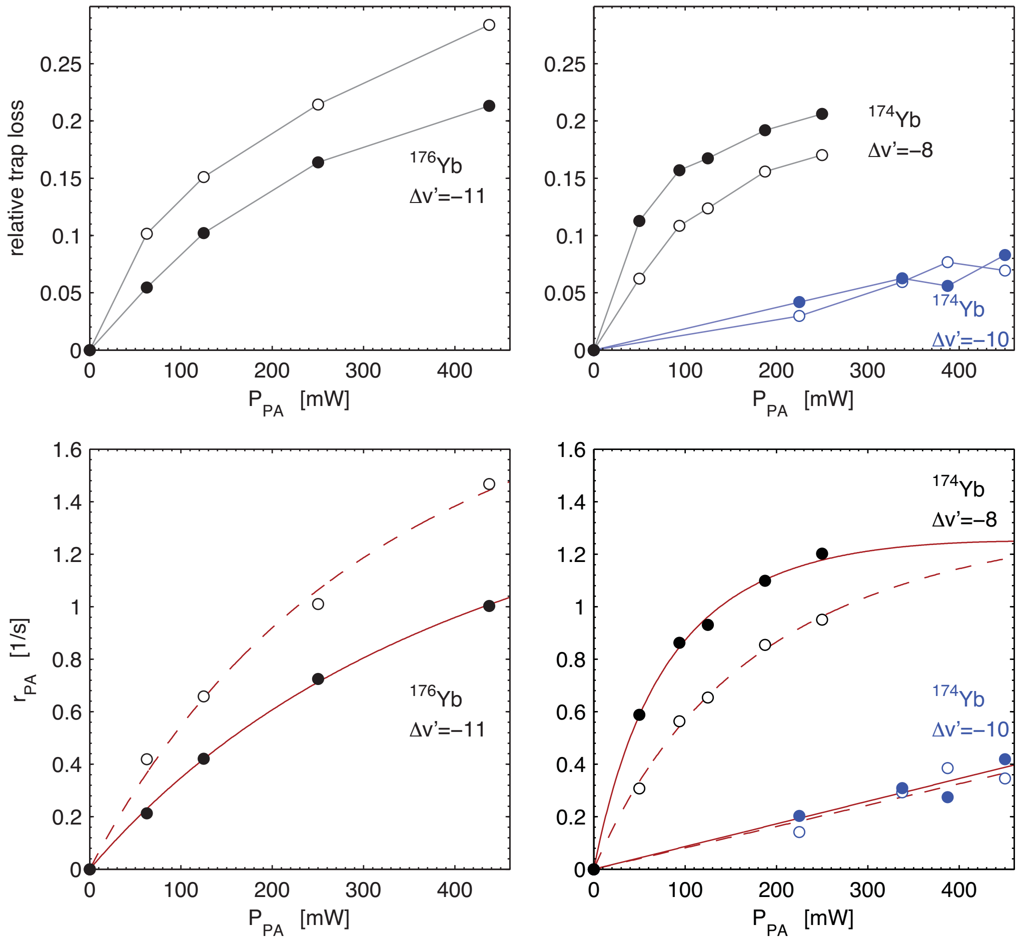

Figure 6.20: **(top)** Relative trap loss over power of PA laser for the $\Delta\,\mathrm{v} = -11$ line in ^{176}Yb (left) and for the $\Delta\,\mathrm{v} = -8$ and $\Delta\,\mathrm{v} = -10$ lines in ^{174}Yb (right). Solid markers correspond to the $R' = 0$ components, open circles to the center $R' = 1$ component. The data points for ^{174}Yb,$\Delta\,\mathrm{v} = -8$ were taken under slightly different conditions than those for the other points, most importantly with an undocumented beam size of the PA laser. **(bottom)** Photoassociation rates r_{PA} calculated from the trap losses shown in the top diagrams. The red curves show a fit according to the model presented in the text, including the influence of the finite size of the PA beam.

			projected		extracted	
mixture	$\Delta\,\mathrm{v}$	R'	P_{max}	$r_{\mathrm{PA}}(P_{\mathrm{max}})$	I_{opt}	$r_{\mathrm{PA,fit}}^{\mathrm{max}}$
$^{176}\mathrm{Yb}^{87}\mathrm{Rb}$	-11	0	2725 mW	$1.63\,\mathrm{s}^{-1}$	$5.97\,\mathrm{W/mm}^2$	$2.48\,\mathrm{s}^{-1}$
		1	2080 mW	$2.04\,\mathrm{s}^{-1}$	$4.56\,\mathrm{W/mm}^2$	$3.10\,\mathrm{s}^{-1}$
$^{174}\mathrm{Yb}^{87}\mathrm{Rb}$	-8	0	495 mW	$1.25\,\mathrm{s}^{-1}$	$1.08\,\mathrm{W/mm}^2$	$1.91\,\mathrm{s}^{-1}$
		1	1115 mW	$1.32\,\mathrm{s}^{-1}$	$2.45\,\mathrm{W/mm}^2$	$2.01\,\mathrm{s}^{-1}$

Table 6.5: Results from the fits of the saturation data

The columns marked “projected” lists results for the maximum at identical beam parameters obtained from a simple extrapolation of the fitted curve. For the $R' = 1$ data points, the height of the center $m_{R'}$ component was used in the evaluation and the theory suggests that this should allow for a similar maximum photoassociation rate as found for the $R' = 0$ rotational component. The data agrees well with this, especially considering that the trap loss at the wavelength of the $m_{R'} = 0$ component will also include contributions from the adjacent $m_{R'} = \pm 1$ components and is therefore somewhat overestimated. The columns marked “extracted” assume a beam size relation of $u/w = 0.64$ during the measurements and give an estimate of the expected photoassociation rate in a beam with a flat intensity distribution together with the optimal intensity required to reach it.

Unfortunately no true comparison between different lines is possible for the available data as the $\Delta\,\mathrm{v} = -8$ line for $^{174}\mathrm{Yb}$ was taken at an earlier time and most likely with a smaller beam diameter of the photoassociation laser, resulting in the observed earlier saturation.

The values found for the maximum photoassociation rate in a flat intensity distribution $r_{\mathrm{PA,fit}}^{\mathrm{max}}$ are higher than the prediction of $r_{\mathrm{PA,th}}^{\mathrm{corr}} = 0.85\ \mathrm{s}^{-1}$, but since the extrapolation depends heavily on the exact values found for the data points at high intensities and the theoretical prediction depends strongly on the exact cloud temperatures and densities at the time of the measurement, all of which carry large uncertainties, the agreement is still quite good. The main candiate for further examination is the temperature of the suppressed ytterbium cloud, which cannot be measured directly with the current experimental setup. A larger temperature would lead to more frequent collisions and therefore to a higher possible photoassociation rate.

6.5.4 Consequences for Future Experiments

The saturation of the photoassociation process has been directly observed. For a more quantitative investigation, the following points will be of importance:

- More laser power is necessary to confirm the shape of the intensity dependence, ideally in a larger Gaussian beam or with a tailored, flat intensity profile to reduce the wash-out.
- Exact values for cloud sizes, beam size, temperatures and atom numbers need to be measured for the time of the measurements.

- Investigations should concentrate on the strongest lines to reduce the required laser power.

The most valuable information gained for photoassociation experiments away from the saturation regime is about the importance of the beam size used. Figure 6.21 provides a summary: If enough laser power were available, a beam size of near 1.5 times the cloud size would be advantageous to reach the maximum photoassociation rates possible. But even at high power, there will always be weak lines where the available intensity is below optimal. In this case a beam size between 0.5 to 1.0 times the cloud size is vastly preferable as -for the same available power- this will result in photoassociation rates up to twice higher.

6.6 Line Strengths

The observed vibrational lines show strong variation in depth. This is well-explained by the Franck-Condon principle, the application of which to photo-association will be outlined in this chapter.

6.6.1 Franck-Condon Principle

When a photon is absorbed by a molecule, it basically changes one of its electrons to a different state. While this dramatically affects the potential experienced by the nuclei in the Born-Oppenheimer approximation, it will not alter their position or, quantum-mechanically, their wavefunction. Therefore a transition between states that have no overlap between their nuclear wavefunctions will be forbidden, even if the electronic selection rules allow it. If any overlap is present, then its degree will influence the strength of the transition (Condon, 1926).

In quantum-mechanical formulation the transition matrix element is

$$p = \langle \psi' | \mu | \psi \rangle \tag{6.58}$$

where ψ is the total wave function in the ground state, ψ' is the wavefunction in the excited state and μ is the electric dipole operator. If the Born-Oppenheimer approximation holds, the wavefunction can be separated into a nuclear and an electronic part:

$$|\psi\rangle = |\psi_n \cdot \psi_e\rangle \tag{6.59}$$

With the dipole operator also split into a nuclear and an electronic part $\mu = \mu_n + \mu_e$, equation 6.58 becomes

$$p = \langle \psi'_n \cdot \psi'_e | \mu_n + \mu_e | \psi_n \cdot \psi_e \rangle \tag{6.60}$$

$$= \langle \psi'_n | \mu_n | \psi_n \rangle \underbrace{\langle \psi'_e | \psi_e \rangle}_{=0} + \underbrace{\langle \psi'_e | \mu_e | \psi_e \rangle}_{a_e} \underbrace{\langle \psi'_n | \psi_n \rangle}_{a_{\mathrm{FC}}} \tag{6.61}$$

where the the marked term is 0 because different electronic states are always orthogonal. a_{el} is the electronic transition matrix element and finally, $F = |a_{\mathrm{FC}}|^2$ is the Franck-Condon factor. The square comes in because the actual transition probability is $P = p^2$.

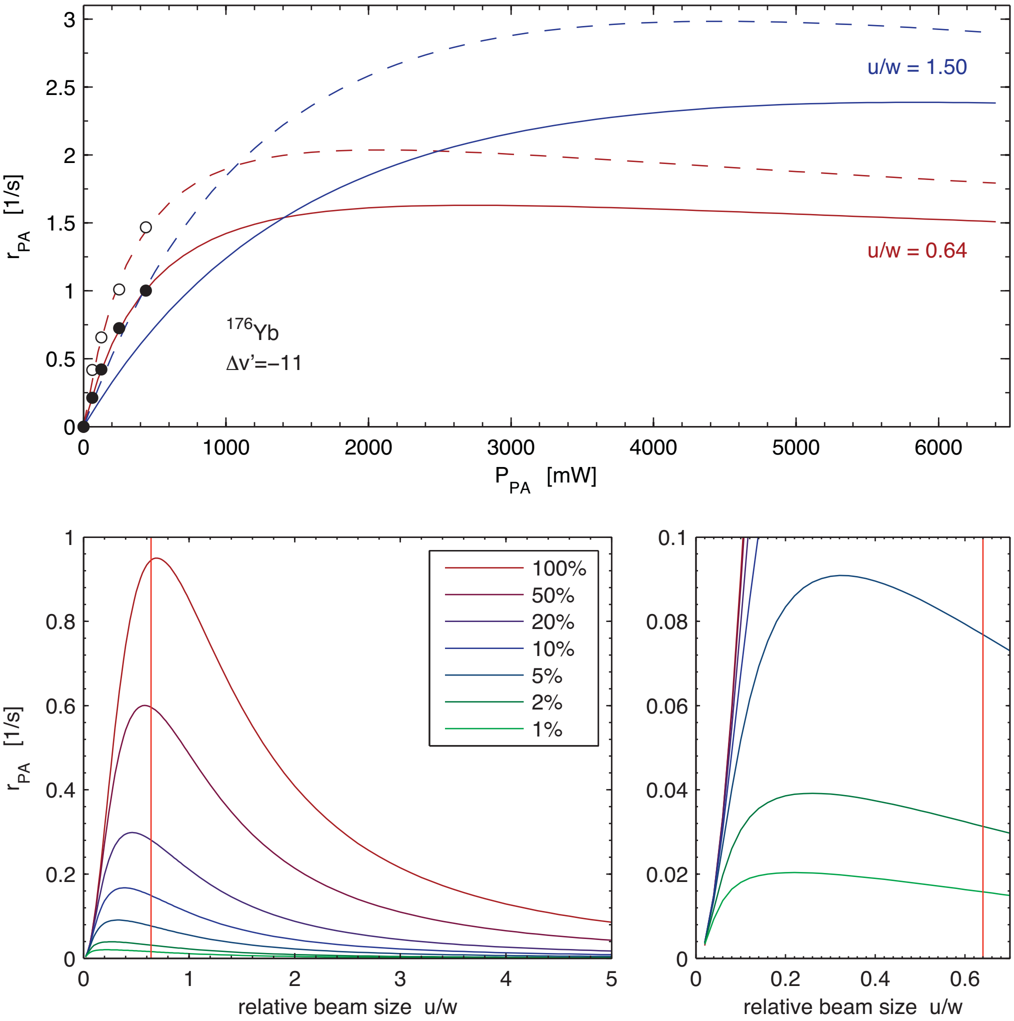

Figure 6.21: **(top)** Saturation of photoassociation rate over power of the PA beam. Circles show measured data for ^{176}Yb, $\Delta\,\mathrm{v}' = -11$ as before. Red curves are extrapolated from the fit. Using the resulting parameters to calculate a curve for a larger relative beam size of $u = 1.5\,w$ gives the blue curves. These clearly show that with a larger beam higher maximum rates can be reached, but that they occur at considerably higher powers. At the power levels of the measurements, the small beam results in higher photoassociation rates.
(bottom left) Photoassociation rates for lines of different strengths (1% to 100% as indicated) at a fixed beam power of 390 mW over the relative size u/w of the photoassociation beam. The red vertical line marks the ratio of 0.64 used in the experiments.
(bottom right) magnification of the lower left region of the previous diagram, showing how the maximum of the curve keeps shifting towards lower beam sizes for weaker lines. However, the width of the peak also becomes larger in this case, reducing the improvement in r_{PA} gained for $u/w < 0.5$.

6.6.2 Application to Photoassociation

In the photoassociation process, the absorbed photon changes the electronic configuration from the ground state to a bound excited state.

At long interatomic distances, there is no noticeable effect of the ground state potential yet and the oscillation of the wavefunction is given by the deBroglie wavelength with $\lambda_{dB} = h/p$. At an exemplary temperature of $500\,\mu$K, this corresponds to a value of $\lambda_{dB} \approx 18\,$nm. When the atoms move closer, the depth of the potential quickly becomes much deeper than the thermal energy. According to the Schrödinger equation, the curvature of the wavefunction is determined by the energy relative to the local potential

$$-\frac{\hbar^2}{2m}\frac{d^2\psi(r)}{dr^2} + V(r)\psi(r) = E\psi(r) \tag{6.62}$$

$$\Longrightarrow \frac{d^2\psi(r)}{dr^2} = -\frac{2m}{\hbar^2}\left(E - V(r)\right)\psi r \tag{6.63}$$

and the oscillations become faster and more shallow at closer range. This is exemplified in figure 6.22. Points of particular interest are the classical inner and outer turning points (r_i and r_o), where the potential curve intersects the energy level of a given bound state. The curvature of the wavefunction is near zero around these points, leading to comparably large scale features that often have significant impact on the overall physics of the system.

Exemplary wavefunctions have been calculated using Matlab and the free software package MATSLISE (Ledoux, 2006) designed for the computation and visualization of the eigenvalues and eigenfunctions of Sturm-Liouville and Schrödinger problems. In the units used by the program, the model potentials used are Lennard-Jones potentials of the form

$$\text{ground state:}\quad V_{\text{exc}}(r') = 7.90 \cdot 10^{12} \cdot r'^{12} - 1.70 \cdot 10^{8} \cdot r'^{6} \tag{6.64}$$

$$\text{excited state:}\quad V_{\text{exc}}(r') = 6.35 \cdot 10^{13} \cdot r'^{12} - 1.37 \cdot 10^{9} \cdot r'^{6} \tag{6.65}$$

chosen to be both as simple as possible while giving results that approximate the following properties of the Rb-Yb potential known either from observation or from the calculations of Fleig (2008):

- long range potential falls off with r^{-6}
- from observation: approximate energy levels of the observed vibrational levels
- from potentials: minimum inner turning point: $r_i = 6\,a_0$, such that $V(r_i) = 0$
- from potentials: potential depth $V'_{\text{min}} \approx -7500\,\text{cm}^{-1}$ for the excited state and $V_{\text{min}} \approx -900\,\text{cm}^{-1}$ for the ground state.

In this form, the excited state potential supports vibrational states up to $v_{\text{max}} = 136$. A small rescaling of $r = r'/1.05$ has been done to reach better agreement between measured and calculated effective internuclear distances. The figure demonstrates that wavefunctions of vibrational states near the dissociation limits have a large final lobe near the classical outer turning point due to the flat potential in this region.

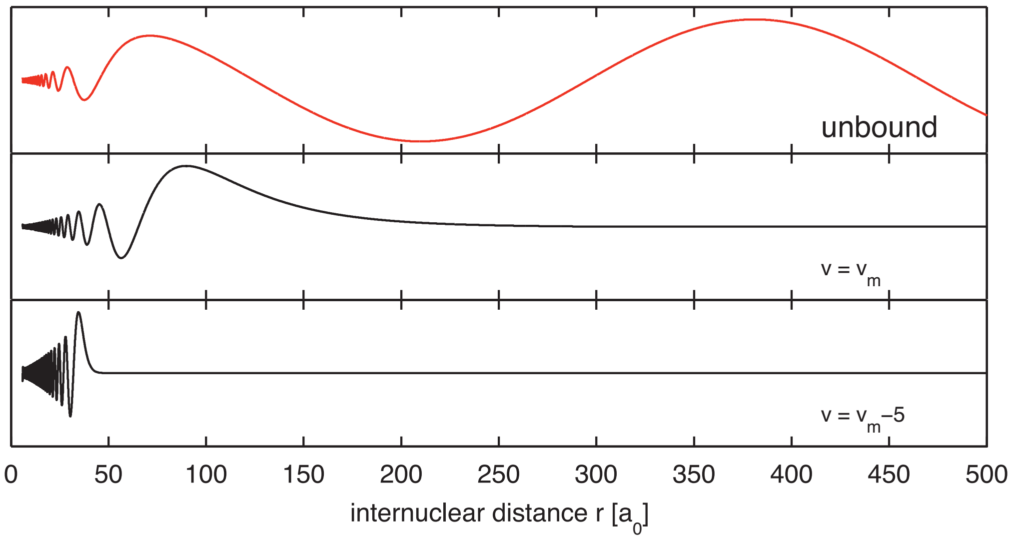

Figure 6.22: Example wavefunctions: **(top)** unbound wavefunction for $E = 500\,\mu$K for the ground state model potential, **(middle)** wavefunction for the highest bound (v $=$ $\mathrm{v_{max}}$) vibrational state in the excited model potential and **(bottom)** wavefunction for a lower vibrational state v $= \mathrm{v_{max}} - 5$. Note the slight increase in amplitude near the inner turning point.

In homonuclear molecules, this last lobe is even more pronounced and located at greater r in the excited state wavefunction due to the resonant Van-der-Waals C_3 coefficient. Since this resonant effect does not occur in the ground state, the continuum wavefunction extends at nearly full amplitude into the distance range covered by the bound excited states. For this reason, there is a strong overlap of the unbound wavefunction with many excited molecular states.

In a heteronuclear molecule the degeneracy between the atomic excitation energies is generally lifted and the resulting C_3 component is then 0. For the asymptote investigated here, corresponding to ytterbium in an S state and rubidium in an excited P state, the longest-range coefficient is C_6 with the next higher one being C_8 (Marinescu and Sadeghpour, 1999). In this case, the excited state wavefunction only extends into the nearly undisturbed region of the ground state wavefunction for the very highest v, with rapidly decreasing overlap for lower vibrational states as illustrated in figure 6.22.

Although the most obvious feature of the ground state wavefunction is the decreasing envelope of the oscillations for smaller r, another important point is the location of the nodes. Since much of the probability amplitude of the excited state wavefunction is concentrated in the last lobe, the Franck-Condon factor will be small whenever this coincides with a node in the ground state function.

6.6.3 Reconstructing "last lobe" Positions

Since knowledge of the ytterbium-rubidium potentials is still limited, a direct calculation of the actual wavefunctions is not possible. Instead, wavefunctions were calculated for the model potential and then examined for properties that might be transferred to the real ytterbium-rubidium system. The ones found most useful are the effective radius r_{eff} calculated from the wavefunctions as

$$\sqrt{\frac{\int_0^\infty r^2 \psi(r)^2 dr}{\int_0^\infty \psi(r)^2 dr}} \tag{6.66}$$

and the position r_L of the outermost lobe of the wavefunction. Figure 6.23 illustrates this and shows how these properties relate to the model potential, in particular the classical outer turning point r_o.

The relations of the three quantities r_{eff}, r_o and r_L are compiled in figure 6.24. For most vibrational levels, the position of the maximum in the last lobe r_L is located at 95% to 99% of the classical outer turning point r_o. At very high v the potential becomes so shallow that the width of the lobe extends, pushing its center inwards, away from the inflection point that occurs at r_o.

The factor r_L/r_o obtained in this way can be applied to the outer turning points calculated from the C_6 coefficient of the actual YbRb* potential to find an approximation of the positions of the outermost lobe for the observed vibrational states.

To check the validity of this model, the effective radius r_{eff} was also calculated from the numerical wavefunctions as

$$\sqrt{\frac{\int_0^\infty r^2 \psi(r)^2 dr}{\int_0^\infty \psi(r)^2 dr}} \tag{6.67}$$

and the ratio of the effective radius r_{eff}/r_o is also plotted in figure 6.24 as the blue dashed line. For low vibrational states, inner and outer turning points are very close together and the wavefunction is contained in a small range. The closer the eigen-energies get to the bottom of the potential, the closer together are r_i, r_{eff} and r_o. In the highest vibrational states, the last lobe moves very far out and becomes large in size as described before. The effect of the rest of the wavefunction can then be more and more ignored. This causes r_{eff} to converge on r_o again. For the range in between these points, where all of the spectroscopic data was taken, the calculations show a nearly constant factor of $r_{\text{eff}}/r_o = 0.88$.

This is very close to the factor of 0.89 found in the spectroscopic data for the ratio of measured r_{eff} to the outer turning point r_o (figure 6.25) obtained from the fitted dispersion coefficient C_6, thus showing that the method is not without merit.

6.6.4 Nodes of the Ground State Wavefunction

According to the Franck-Condon arguments given before, the photoassociation rates and therefore the line depths in the spectrum strongly depend on the wavefunction overlap between ground and excited state. Under favorable conditions, the reflection approximation (Boisseau et al., 2000) can be used to link photoassociation rates to ground state wavefunction amplitude. Unfortunately this has been found to be invalid for heteronuclear systems, where the density of vibrational states is generally low (Azizi et al., 2004). However, qualitative statements can still be made without full knowledge of the exact

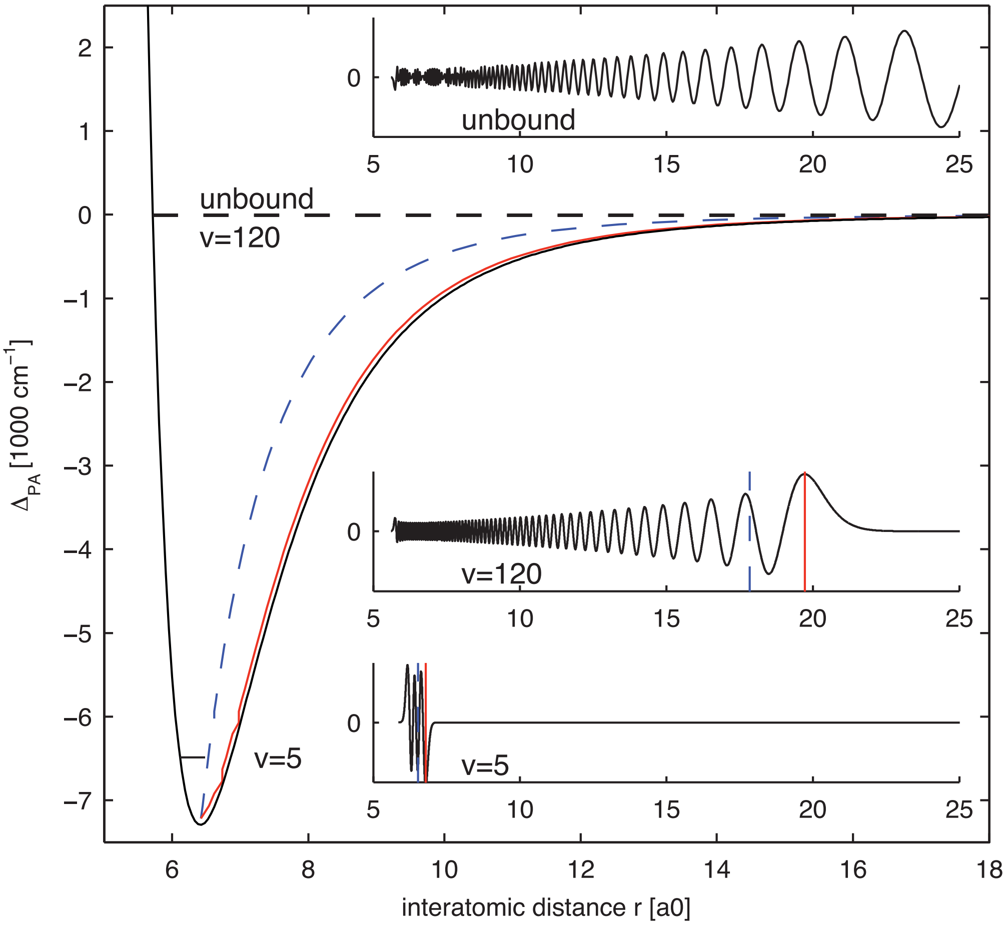

Figure 6.23: Model potential (black curve) and the effective radius r_{eff} (blue, dashed curve) extracted from the numerically calculated wavefunctions. The calculated position of the last lobe of the wavefunction is also shown (red curve).

The lower insets show examples of the calculated wavefunctions and the properties extracted from them (red line: last lobe, blue dashed line: effective radius). The upper inset shows the close range part of the unbound wavefunction. The distortions for low r are due to sampling artifacts.

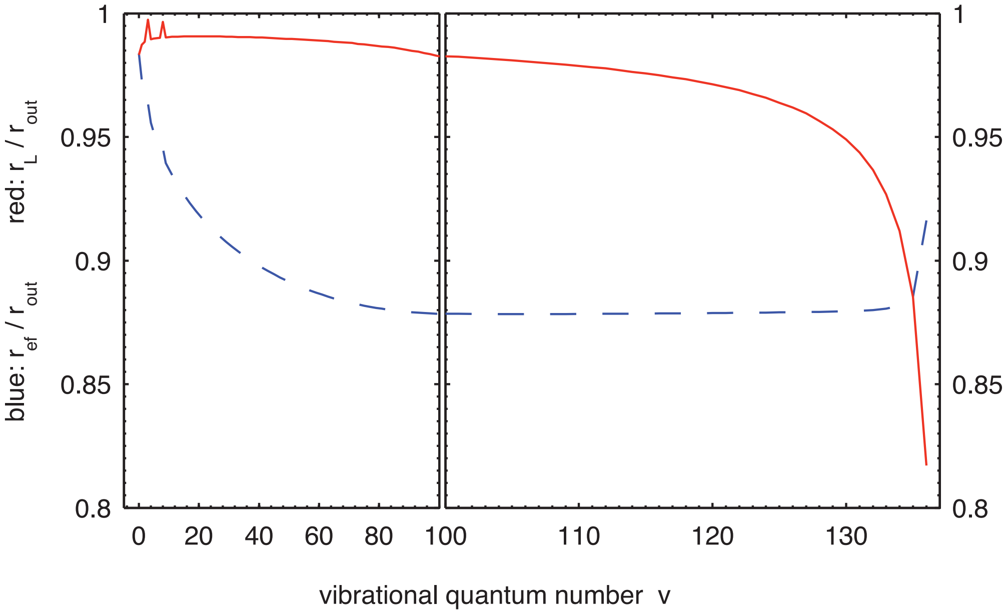

Figure 6.24: Ratio of last lobe position relative to outer turning point r_L/r_o over the vibrational states of the model potential (red solid line) and ratio of effective radius to outer turning point r_{eff}/r_o (dashed blue line).

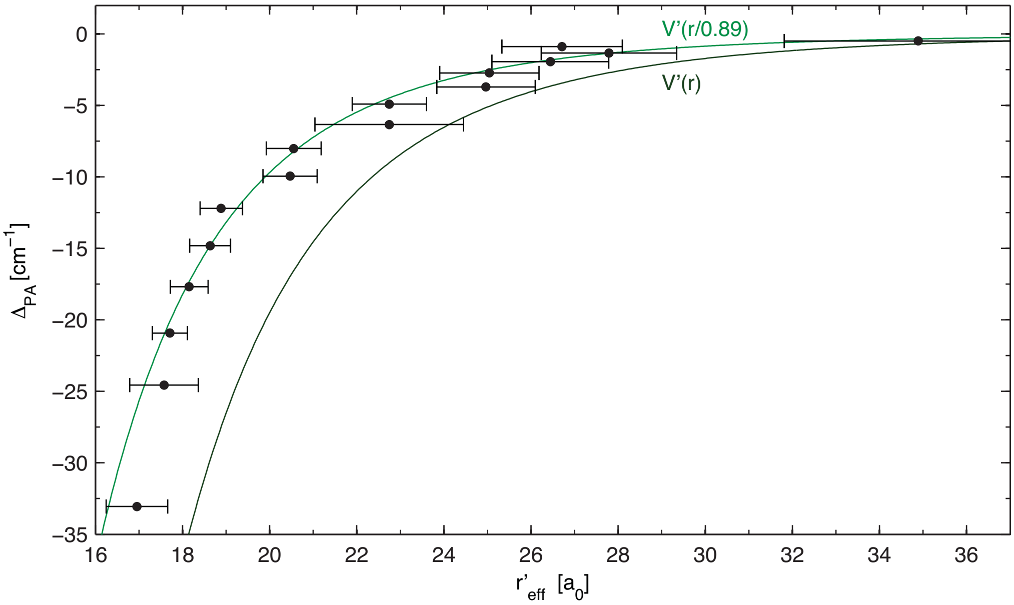

Figure 6.25: Comparison of the effective radius r_{eff} calculated from measured rotational constants (black points) to the potential obtained from the improved Leroy-Bernstein fit (black curve). The values for r_{eff} are consistently found slightly inwards of the outer turning point. Their positions can in fact be described as 89% of the classical outer turning points r_o to within the uncertainty given by the measurement of the rotational constants B_{rot}. This is illustrated by the green line, which is simply the black potential curve rescaled horizontally by 0.89.

wavefunctions by looking at the amplitude of the ground state function at the position of the last lobe in the excited state function.

According to normal scattering theory, the s-wave ground state wavefunction at large r is entirely described by the scattering length. If the outer part of the potential is known, then it is possible to work inward from here. A method for this is given in (Tiesenga et al., 1996), where the scattering length is found to be related to the position of a zero in the wavefunction by the equation

$$a_{sc} = \frac{\sqrt[4]{\tilde{C}_6}}{2} \cdot \frac{J_{-1/4}(\tilde{r}_0)}{J_{1/4}(\tilde{r}_0)} \cdot \frac{\Gamma(3/4)}{\Gamma(5/4)} \tag{6.68}$$

$$\text{with} \qquad \tilde{r}_0 = \frac{\sqrt{2\,\mu\,C_6}}{2\,\hbar\,r_0^2} \qquad \text{and} \qquad \tilde{C}_6 = \frac{2\,\mu\,C_6}{\hbar^2}. \tag{6.69}$$

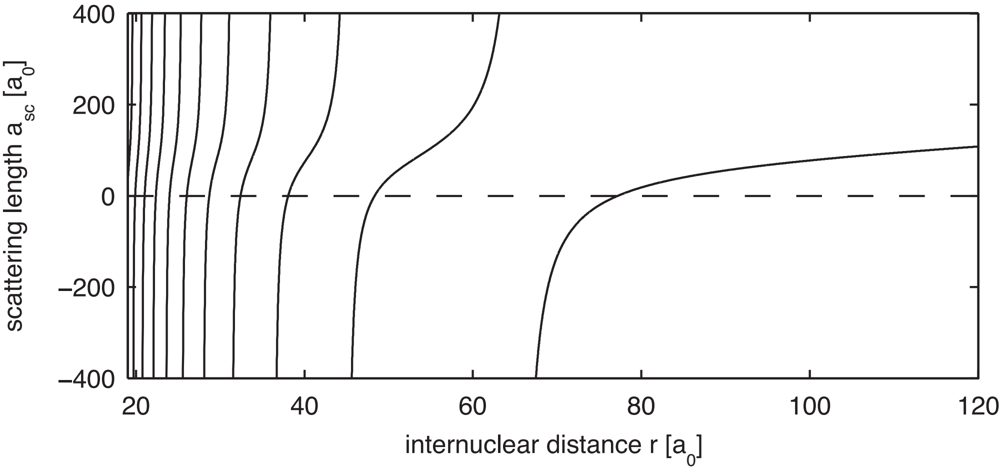

Figure 6.26: Relation of node positions in the ground state wavefunction to scattering length. If a horizontal line is plotted for a given scattering length, such as the dashed line for $a_{\rm sc} = 0\,a_0$, the r-values of the intersections with the graph mark the locations of nodes in the wavefunction. For example, the last three nodes for $a_{\rm sc} = 0$ would be at approximately $40\,a_0$, $50\,a_0$ and $80\,a_0$.

The shape of this function is shown in figure 6.26, using the estimated dispersion coefficient $C_6 = 3186$ a.u. for the ground state molecule from chapter 3.4.3. If the location of a node can be localized with enough precision, it can often be used to find the scattering length. The shallow slope of the function at large internuclear distances makes this method particularly accurate for long-range homonuclear molecules (Mickelson et al., 2005; Enomoto et al., 2007). At longer ranges the impact of deviations of the true potential from the assumed C_6 coefficient is also smaller.

Earlier experiments on sympathetic cooling of ytterbium with rubidium (Tassy, 2007) have already yielded values for the interspecies scattering lengths of different isotope combinations. The reported values were $|a_{\text{Rb-Yb176}}| = 127^{+245}_{-45} a_0$ and $|a_{\text{Rb-Yb174}}| = 83^{+89}_{-25} a_0$.

Only absolute values are given since the experiments did not yield any information on the signs of the scattering lengths.

6.6.5 Wavefunction Overlap and Observed Line Strengths

Combining the results of the last two section gives an explanation for the alternation of weak and strong photoassociation lines observed in the experiment. Figure 6.27 puts together the relation of scattering length to the position of nodes in the ground state wave function and the location of the last lobe in the excited wave function. The length of the vertical bars has been chosen to correspond to the expected range of the scattering length, their color and pattern differentiates between strong (green), weak (yellow) and unobserved (red) lines.

If the scattering length is assumed to be $a_{\text{Rb-Yb176}} = +150\,a_0$ in the top graph and $a_{\text{Rb-Yb174}} = -100\,a_0$ in the bottom graph, as marked by the gray horizontal line, it becomes apparent that the Franck-Condon principle can be used to explain the observed fluctuations. To reach this agreement, the value of the unknown ground state dispersion coefficient was manually varied. The graph shown corresponds to a value of $C_6 = 2700\,\text{a.u.}$, reasonably close to the value estimated earlier $C_6^{\text{est}} = 3186$ a.u.. It is possible that this indicates a real discrepancy, but due the strong dependence on both the measured rotational constants and the factors obtained from the model wavefunctions, this should no be considered a quantitative result.

Qualitatively however, each of the weaker photoassociation lines has a calculated last lobe position near the intersection of the node function with the scattering length prediction. For the strong lines, the last lobe is more or less centered between node positions, indicating a larger Franck-Condon overlap. This is true for the results both with ^{176}Yb and ^{174}Yb, using the same ground state C_6 coefficient.

For more deeply bound vibrational states, the model presented gradually loses accuracy, both because the error in accumulated phase of the wavefunctions caused by inaccurate potential curves becomes larger and because the last wavefunction lobe becomes less pronounced.

Too many assumptions and approximations were needed in the construction of the model to use it to improve the values of the scattering lengths over those found in Tassy (2007). However, when varying the ground state C_6 coefficient it is apparent that over a range from 2700 a.u. to 3500 a.u., near the predicted value of 3186 a.u., there was no value that would cause good agreement between predicted and observed line strengths for the opposite signs of the scattering length compared to that marked by the gray line in the diagram.

This might be taken as an indication that the ground state scattering length for ^{87}Rb and ^{176}Yb is positive and that for ^{87}Rb and ^{174}Yb is negative, which is compatible with theory. The best currently available estimates are then:

$$a_{\text{Yb174-Rb87}} = -83^{+89}_{-25}\,a_0 \tag{6.70}$$

$$a_{\text{Yb176-Rb87}} = 127^{+245}_{-45}\,a_0 \tag{6.71}$$

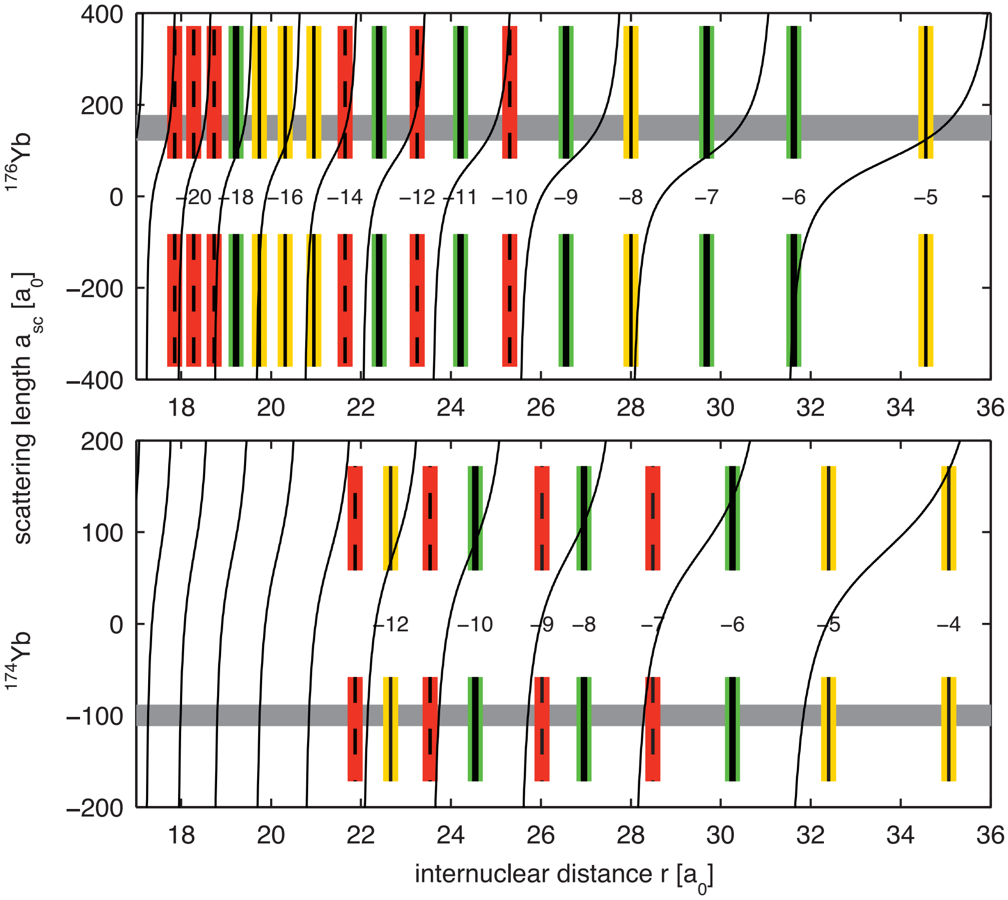

Figure 6.27: Schematic of wavefunction overlap. The black curve shows the relation of scattering length to nodes in the continuum wavefunction calculated for a ground state C_6 coefficient of 2700 a.u.. The thick gray lines point out the scattering length currently considered to be most likely for the mixture of ^{87}Rb and ^{176}Yb (top diagram) and for of ^{87}Rb and ^{174}Yb (bottom diagram). The intersections between the gray line and the black curve give the expected nodes of the ground state wavefunction.

Each set (top and bottom half) of vertical lines indicate the position of the last lobe in the wavefunction of the excited state for one of the vibrational states, extracted from the measured rotational constants B_{rot} with the help of the behavior of the model wavefunctions. Numbers indicate the relative quantum number Δ v. Color and thickness of the lines indicate line depth. Heavy lines with green background mark trap loss of at least 10%, lines with lower losses are thinner with yellow background and lines that were weaker than 2% (including predicted but unobserved lines) are dashed with red backing. The vertical length of the lines show the uncertainty of the interspecies scattering length found in previous experiments.

Any intersection of the black curve with a vertical line means that for a certain scattering length, the last lobe of the excited wavefunction will overlap a node in the ground state function. When this happens at or near the gray line, the Franck-Condon factor will be very low and the line is therefore expected to be weak.

If this is confirmed, it would mean that besides the choice of bosonic-bosonic and bosonic-fermionic combinations, experiments with ytterbium and rubidium also offer the possibility of exploring the effects of positive and negative interspecies scattering lengths of similar magnitude.

Chapter 7

Future experiments

The results presented so far are a first step towards a scheme for the efficient production of state molecules that are ultracold not only translationally, but also in terms of rotation and vibration. This chapter looks at the next steps that might be taken in this direction.

7.1 Formation of Ground States Molecules

The simplest way to create molecules in the ground state is to rely on spontaneous emission. The problem is that an excited state wavefunction that has good overlap with the continuum wavefunction generally does not give good Franck-Condon factors for the decay into lower, strongly localized, bound ground states. Most decay will then occur back to unbound states.

If enough laser power is available, it should be possible to create bound excited molecules in lower vibrational levels that have less overlap with the continuum states. A branching ratio of 7% to a specific vibrational (triplet) ground state has been reached in RbCs by using an excited state at a rather large detuning of $38\,\mathrm{cm}^{-1}$ from resonance (Sage et al., 2005).

In any scheme based on spontaneous emission, the only way to increase the production of molecules in a desired final state is to choose an excited state that has a good Franck-Condon overlap with it. This more or less rules out a one-step process to create molecules in the $\mathrm{v} = 0$ state.

A possible two-step approach would involve spontaneous emission from the initially photoassociated molecular state chosen for good overlap with a known bound ground state. A second laser then excites atoms from this state into a second excited state. The simplified Franck-Condon principle states that transitions between different electronic states are most likely to occur “vertically” (that is without directly changing interatomic distance and kinetic energy) at the turning points. Because of the different equilibrium distances of ground and excited state, it might then be possible to choose this to achieve a useable decay probability into the vibrational ground state. This scheme is illustrated in figure 7.1 with the two lasers driving the transitions marked [1] and [3]. For a certain fraction of atoms [2] and [4] then occur through spontaneous emission.

Optimizing this scheme would largely consist of picking the proper intermediate excited

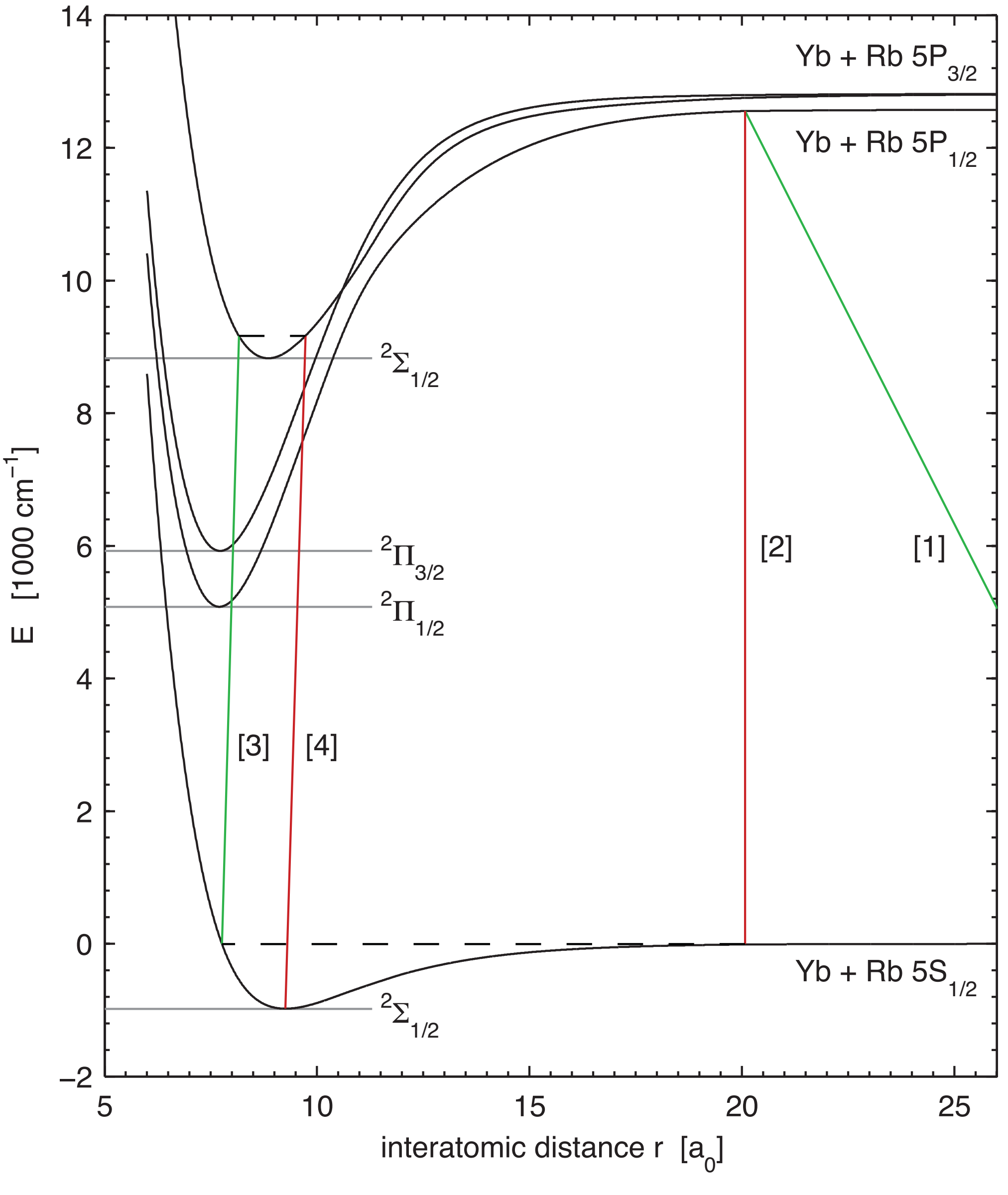

Figure 7.1: Potential curves and relevant transitions in a simple two-step scheme designed to reach the rovibrational ground state. Green lines mark transitions driven by lasers, while red lines show important channels of spontaneous emission. Molecules are formed through photoassociation in step [1]. Some of them are converted into stable but vibrating ground state molecules in step [2]. A second excitation [3] populates a new excited molecular state with a decay channel [4] to the absolute ground state.

states to reach good excitation rates and maximal branching ratios into the target states. Transition [3] is likely to offer the most opportunity to do so, since the wavefunction overlap is expected to be less important as bound-bound transitions generally have a lower saturation intensity than comparable free-bound transitions.

Trapping of both the intermediate and final products of this process is possible in an optical dipole trap. This will require a laser with a photon energy that is so low that is does not drive any transitions back to an excited state. A low estimate of the energy difference between the dissociation threshold of the ground state and the bottom of the potential well of the ${}^2\Pi_{1/2}$ excited state is $\Delta E \approx h\,c^{*}\,5000\,\mathrm{cm}^{-1}$ corresponding to a minimum wavelength of 2000 nm. A magnetic trap might also be used, as discussed in chapter 7.6.2.

The main disadvantage of this experimentally simple method is that there will always be Franck-Condon overlap with several vibrational states and after the spontaneous emission process a considerable fraction of molecules will be in states other then the desired one. These are not only lost to the process, but will also remain trapped and create obstacles to the experiments both due to collisions with the fraction of ground state molecules and due to the difficulties of knowing which initial population contributed to a given experiment.

An improvement on this scheme would be the introduction of a third laser that drives the transition from the secondary excited state down to the vibronic ground state. If both the additional lasers are operated in successive pulses and above the saturation intensity, the transfer efficiency from the high-v electronic ground state to the final vibronic ground state can reach 25%.

Assuming the 7% branching ratio into a known ground state vibrational level mentioned before, the total production rate for ground state molecules would then be $R_{\mathrm{v}=0} = 0.25 \cdot 0.07 R_{\mathrm{PA}}$ or less than 2% of the initial PA rate.

7.2 Autler-Townes spectroscopy

In the previous section, the two additional laser were assumed to operate sequentially, without interaction effects. The main source of these is the AC stark effect (also called “light shift”). Autler-Townes spectrocopy (Autler and Townes, 1955) takes advantage of these effects to spectroscopically probe a level that is not directly accessible from the initial state. It can be used in photoassociation experiments to obtain information on the vibrational levels of the ground state that will be vital in the development of efficient transfer methods. Theoretical potentials are of limited use here as the effect of their inaccuracies is strongly amplified for high vibrational levels.

In the photoassociation variant of Autler-Townes spectroscopy, the photoassociation laser is operated on resonance for a transition between the unbound ground state continuum and a bound excited state as before. An additional laser then connects this level to a bound ground state. This laser will be called the “Raman laser” in the following. If its intensity is high enough, the AC Stark effect will cause a significant splitting of the original energy levels into two components. Since the upper energy level is common to both the Raman and the photoassociation transition, the splitting will move the components out of resonance with the photoassociation laser, reducing the photoassociation rate. This loss can partially be recovered by varying the frequency of the photoassociation laser until the

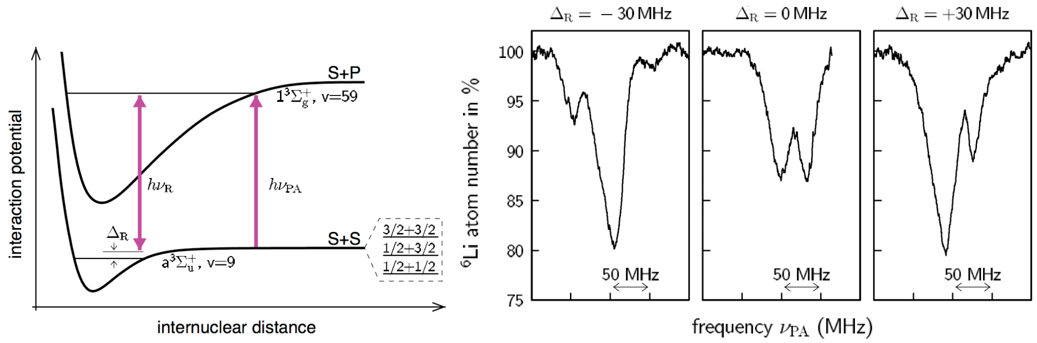

Figure 7.2: Autler-Townes spectroscopy in photoassociation experiments as reported in Schlöder et al. (2003) for Li_2.
(left) Molecular levels and frequencies of the photoassociation (ν_{PA}) and the Raman (ν_R) laser. The low vibrational level in the excited state was chosen to optimize overlap with the bound ground state wavefunction and lower the required intensity for the Raman laser. In a heteronuclear system this overlap should be better even for higher vibrational states due to the shorter range of the excited potential.
(right) Trap loss spectra taken by scanning the PA laser, while the Raman laser was held fixed at −30 MHz, 0 MHz or +30 MHz relative to resonance between the ground state v = 9 level and the excited state v = 59 level.

changed frequency matches one of the shifted components in the upper level. In this way a spectrum of the split line can be taken. If the Raman laser is resonant to the transition, the splitting between the components is identical to the Rabi frequency:

$$\Delta f_{\text{split}} = \frac{\Omega}{2\pi} = \sqrt{\frac{3\,c^2\,I_R\,\Gamma_{\text{bb}}}{16\,\pi^3\,h\,\nu_R^3}} \tag{7.1}$$

Here ν_R and I_R are frequency and intensity of the Raman laser and Γ_{bb} is the (undriven) transition rate between the two bound states. In Schlöder et al. (2003), this is investigated for a transition between high vibrational levels in Li_2. A transition rate of approximately $4 \cdot 10^5\,\text{s}^{-1}$ is calculated from a splitting of $\Delta f_{\text{split}} = 34.6\,\text{MHz}$ for an intensity of the Raman laser of $I_R = 30\,\text{W/cm}^2$. Figure 7.2 shows example spectra from Schlöder et al. (2003).

An advantage of the Autler-Townes method is that it does not require additional detection methods. The PA laser is held in resonance with the chosen vibrational line and the Raman laser is slowly scanned. When it is in resonance with a transition, the loss rate will decrease. Once the location of a ground state vibrational level has been identified this way, it can be examined closer by also varying frequency and intensity of the photoassociation laser.

By slightly changing the wavelength of the photoassociation laser to bring it back into resonance with the shifted excited level, the Raman laser also serves as a more efficient way to populate the target ground state. If the splitting is big enough to be fully resolved as in the pictures shown, then the Rabi frequency that determines the splitting is obviously larger than the natural linewidth. This also means that the bound-bound transition driven by the Raman laser is saturated and nearly 50% of the photoassociated molecules will be transferred to the bound ground state, which is a significant improvement over transfer by spontaneous emission. This method is known as stimulated emission pumping (Hamilton et al., 1986).

7.3 Stimulated Raman Adiabatic Passage

A further improvement is possible by the implementation of **STI**mulated **R**aman **A**diabatic **P**assage or STIRAP (Gaubatz et al., 1988). This uses essentially the same system of lasers and molecular levels as before, with the laser connecting the initial ($|1\rangle$) to the excited level ($|2\rangle$) called the pumping laser and the one connecting $|2\rangle$ to the final state ($|3\rangle$) called the Stokes laser. This is shown in figure 7.3.

These are used in counter-intuitive sequence: At first the the Stokes laser is turned on, coupling $|2\rangle$ and $|3\rangle$. This leaves the initial state dark and no molecules enter the excited state $|2\rangle$. Now the intensity of the pumping laser is increased while the Stokes laser is gradually turned off. In the end, $|3\rangle$ is dark while $|1\rangle$ and $|2\rangle$ are strongly coupled. By looking at the resulting eigenstates in more detail (see Bergmann et al. (1998)) it is found that the influence of both lasers forms a trapped state that converges on one of the two dark states when the entire intensity is in one of the beams. If the sequence is performed properly, the molecules will stay in the trapped state and be transferred adiabatically from state $|1\rangle$ to state $|3\rangle$.

Practically complete population transfer can be reached if the maximum laser intensities are chosen to give similar Rabi frequencies and if the pulse length is larger than ten Rabi periods. It should be noted that the time available for this is limited by the coherence of the laser sources and not by the lifetime of the excited state, because it is not populated at any time during the transfer. Although pulsed lasers with ns pulse times are most often used, this makes it possible to use CW laser systems, too. Because these generally offer better coherence, their lower available intensity can at least partially be compensated by using longer pulses. The proper sequence of pulses can be formed by using AOMs (Lindinger et al., 1997). For Gaussian pulse shapes, it has been shown that the optimum delay between the Stokes and the pump pulse is equal to the pulse width (Gaubatz et al., 1990) as illustrated in figure 7.3.

Another interesting point is that while the relative frequency of the two lasers needs to be closely matched to the energy difference between states $|1\rangle$ and $|3\rangle$, the resonance with state $|2\rangle$ is much less critical when the detunings are identical for both lasers. The process will be efficient as long as it happens adiabatically, with the Rabi frequencies being high compared to the time scale of the transfer cycle. At a larger detuning from the single-photon resonance, this simply requires higher intensities. A controlled detuning can actually circumvent problems arising from a Zeeman splitting of otherwise degenerate levels.

7.4 Application to the Experiment

As equation 7.1 shows, a weak transition with low transition rate Γ_{bb} requires high laser intensities to achieve useful Rabi frequencies. Therefore a good Franck-Condon overlap

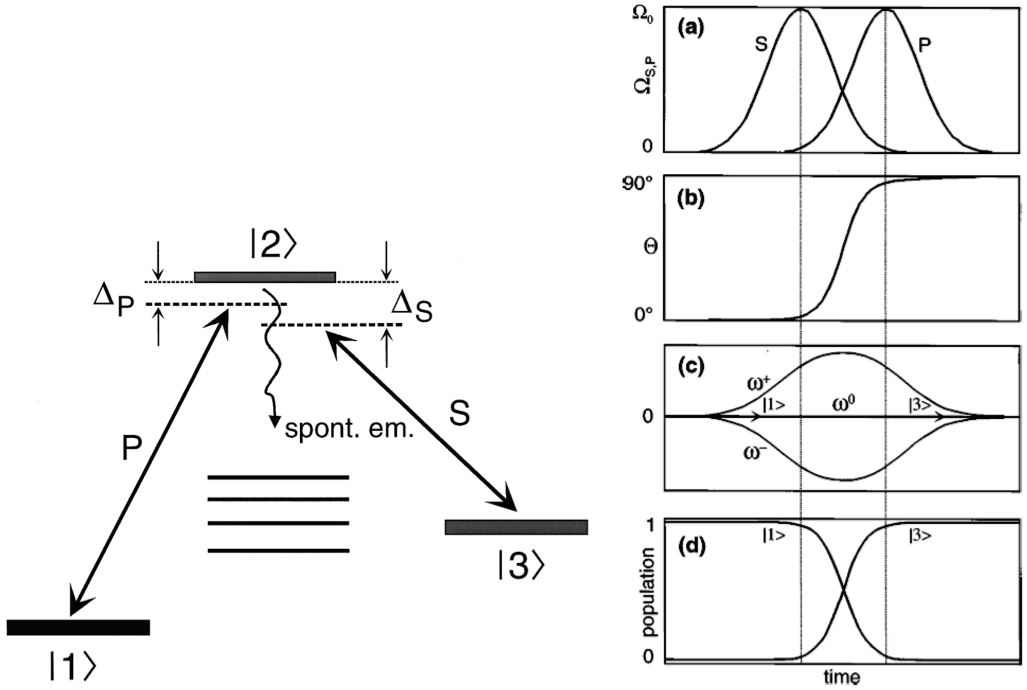

Figure 7.3: Stimulated Raman adiabatic passage. Figures from Bergmann et al. (1998). **(left)** Molecular levels and photon energies of the connecting laser fields. 'P' marks the pumping laser with a detuning of Δ_P from single-photon resonance, 'S' marks the Stokes laser. For efficient population transfer from $|1\rangle$ to $|3\rangle$, the two-photon transition needs to be resonant, i.e. $\Delta_P = \Delta_S$.

(right, a) counter-intuitive pulse sequence with the Stokes pulse before the pumping pulse. Laser intensities are given in terms of Rabi frequencies. **(b)** mixing angle indicating contributions of $|1\rangle$ at 0° and $|3\rangle$ at 90°. **(c)** Progression of eigenstates connecting $|1\rangle$ to $|3\rangle$ as the laser intensities are varied. **(d)** Relative state population over time showing smooth and complete transfer.

is still desirable. This makes it unlikely that a single-step process to the vibronic ground state is possible. In the following, the two-step scheme presented in an earlier section is adapted to work with the STIRAP process. Figure 7.4 illustrates this.

Since the current ab-initio calculations of the molecular potentials (Fleig, 2008) only include a limited number of states so far, the absolute energies found do not yet converge on the Rb atomic states. To partly compensate for this, the dispersion coefficients calculated previously were combined with the known energies of the atomic states to fill in the gap in the potential curves at large internuclear distances. The ab-initio energies were then scaled by a factor of approximately 1.15 to match the energy differences between the Rb $5S$ and $5P_{1/2}$ states. Scaling was chosen over a shift of the higher potentials as it simultaneously caused the difference between the $5P_{1/2}$ and $5P_{3/2}$ states to match expectations. However, all energies and wavelengths obtained from this model should be considered to be first estimates only.

The first step needs to happen at wavelengths that avoid losses from $\mathrm{Rb_2}^*$ photoassociation. Close to resonance this is unlikely as the vibrational lines in the long-range homonuclear potential of $\mathrm{Rb_2}^*$ are very closely spaced in this region. Figures 7.5 and 7.6 show the observed loss rates for both rubidium and ytterbium around the stronger lines of the YbRb* photoassociation spectrum. It should be noted that the photoassociation rate for $\mathrm{Rb_2}^*$ is strongly limited by the poor overlap of the Ti:Sapph laser with the larger rubidium cloud. Therefore losses might be considerably larger in a different trap geometry. Moving to a different trap will also make the formation ratio of YbRb* to $\mathrm{Rb_2}^*$ more important as continuous loading will generally not be possible in this case. If sufficient laser intensity is available for an efficient transfer, the formation of $\mathrm{Rb_2}^*$ is can be avoided by choosing a suitable photoassociation line. This is more likely to be found at greater detuning where both series have wider spacings and are less likely to overlap.

The figures show that there are several candidate lines where the Rb-Yb photoassociation is not hindered much by Rb-Rb losses even without going to very large detunings Δ_{PA}. The primary targets of further investigation using ^{176}Yb should be $\Delta\,\mathrm{v} = -9$ (at $-2.72\,\mathrm{cm}^{-1}$) and $\Delta\,\mathrm{v} = -11$ (at $-4.90\,\mathrm{cm}^{-1}$). It might also prove useful to look at the $F' = 1$ lines for $\Delta\,\mathrm{v} = -11$ (at $-4.92\,\mathrm{cm}^{-1}$) and $\Delta\,\mathrm{v} = -13$ (at $-8.03\,\mathrm{cm}^{-1}$) that are also relatively strong and unobscured by Rb-Rb losses. Unfortunately the unassigned line near $-0.65\,\mathrm{cm}^{-1}$, which is very interesting due to its very large rotational spacing, coincides with a strong $\mathrm{Rb_2}^*$ line.

When using ^{174}Yb, good candidates to explore might be the $\Delta\,\mathrm{v} = -6$ (at $-1.15\,\mathrm{cm}^{-1}$), $\Delta\,\mathrm{v} = -8$ (at $-2.44\,\mathrm{cm}^{-1}$) and $\Delta\,\mathrm{v} = -12$ (at $-7.38\,\mathrm{cm}^{-1}$) vibrational levels of the $F' = 2$ state. There is no obvious candidate for the $F' = 1$ state.

In any case the wavelengths λ_1 and λ_2 involved in the first step will be in the range of 795 nm to 798 nm. A laser system based on a tapered amplifier is currently under development and promises 500 mW of power output at 795 nm. This should be enough to reach useful photoassociation rates (see the saturation measurements in chapter 6.5.3) and free up the titanium-sapphire laser for Autler-Townes spectroscopy. Once a suitable transition has been found, a simple diode laser should provide enough power for the Stokes laser since this is a bound-bound transition that is nearly ‘vertical’ in the Franck-Condon picture.

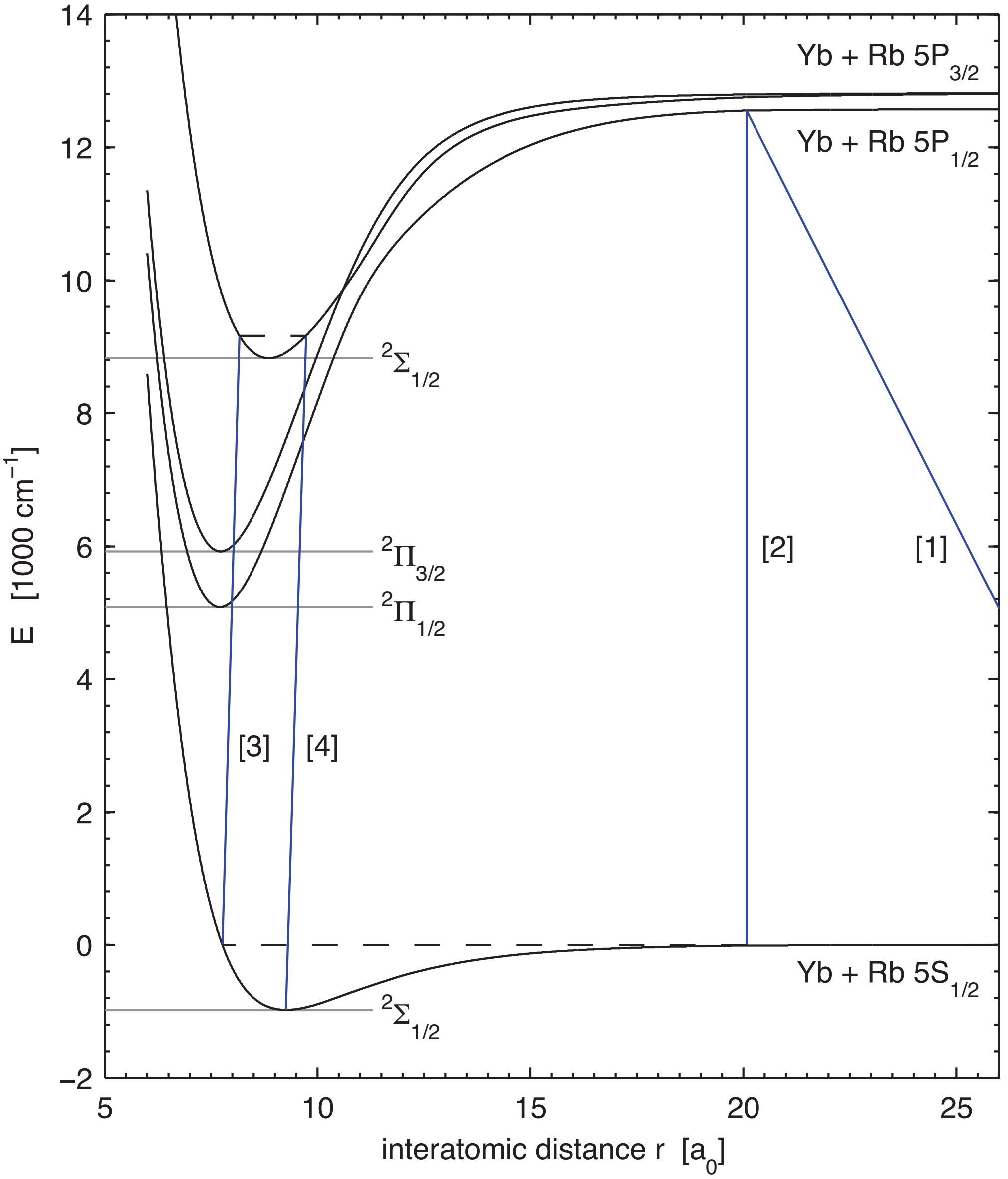

Figure 7.4: Potential curves and transitions driven in the proposed double STIRAP scheme. Energies are given in wavenumbers relative to the atomic ground states, interatomic distance in units of the Bohr radius a_0. The energies of the ab-initio potential curves from Fleig (2008) have been rescaled to converge on the rubidium atomic levels. Transitions [1] and [2] are part of the first STIRAP process. Both wavelengths are close to the Rb atomic transition, plotted here are $\lambda_1 = 796.6\,\mathrm{nm}$ and $\lambda_2 = 796.3\,\mathrm{nm}$. Transitions [3] and [4] are shown here with photon energies corresponding to $\lambda_3 = 1090\,\mathrm{nm}$ and $\lambda_4 = 986\,\mathrm{nm}$.

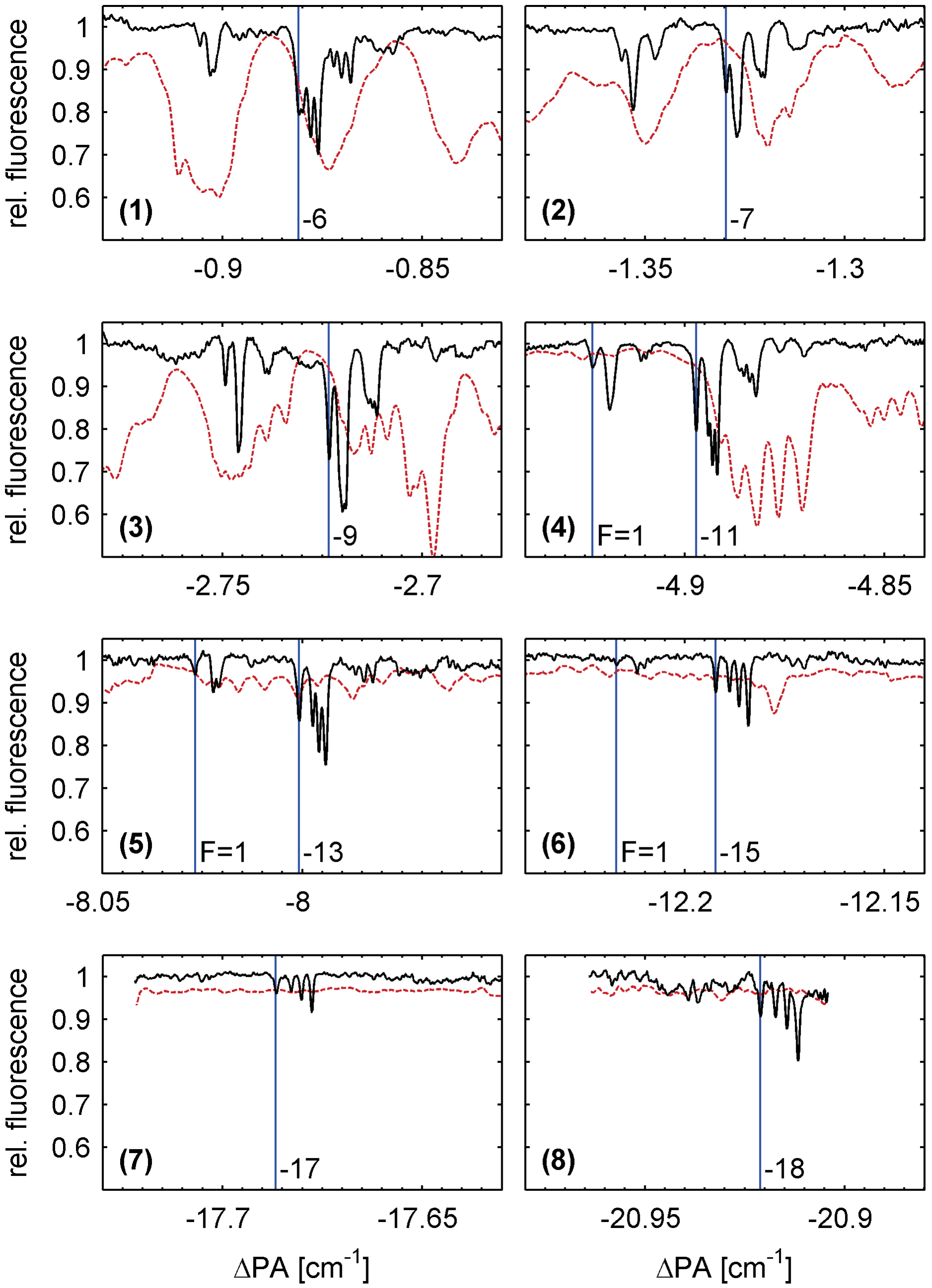

Figure 7.5: **(1-8)** Candidate lines for molecule production using ^{176}Yb. Trap loss spectra for both Yb (solid black line) and Rb (dashed red line) are shown for PA lines with useful $R = 0$ components. Loss in Rb fluorescence indicates formation of Rb$_2$* molecules. However, due to fluctuations, a relative fluorescence of 1 does not always correspond to a zero loss rate. Especially near resonance the Rb lines are so closely spaced that the loss rate does not necessarily return to zero between lines.
Efficient formation of YbRb* molecules requires a deep line in the Yb spectrum at a wavelength where the Rb losses are low. The best candidates to explore might be the $\Delta\,\mathrm{v} = -9$ **(3)** and $\Delta\,\mathrm{v} = -11$ **(4)** vibrational levels of the $F' = 2$ state. The $F' = 1$ state is both accessible and relatively strong for $\Delta\,\mathrm{v} = -11$ **(4)** and $\Delta\,\mathrm{v} = -13$ **(5)**.

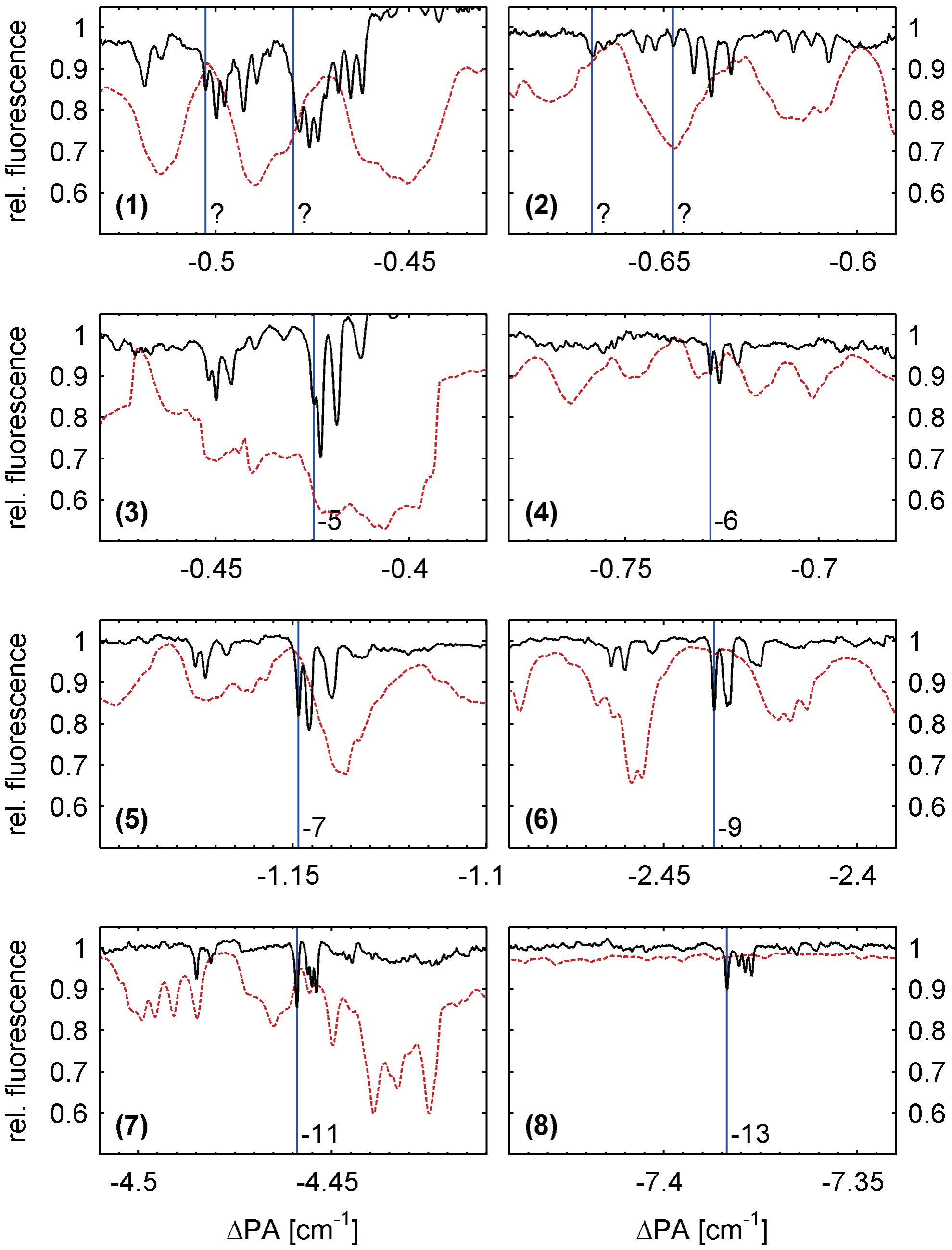

Figure 7.6: Candidate lines for YbRb* molecule production, continued.
(1-2) Unassigned lines in Rb-^{176}Yb photoassociation.
(3-8) Observed photoassociation lines for ^{174}Yb. The best candidates to explore might be the $\Delta\,\mathrm{v} = -7$ **(5)**, $\Delta\,\mathrm{v} = -9$ **(6)** and $\Delta\,\mathrm{v} = -13$ **(8)** vibrational levels of the $F' = 2$ state. There is no obvious candidate for the $F' = 1$ state.

The wavelengths for the second step can only be estimated at this point due to the uncertainty of the potential curves. If the applied scaling was found to yield correct results even deep inside the potential wells, then the most likely candidate for efficient transfer uses a pumping laser at $\lambda_3 = 1091\,\mathrm{nm}$ and a Stokes laser at $\lambda_4 = 986\,\mathrm{nm}$. This takes advantage of a pumping transition that is near-vertical when looking at the inner turning points of the ground and the $^2\Sigma_{1/2}$ excited states, while the Stokes transition is near-vertical when looking at the bottom of the ground state potential well and the outer turning point of the $^2\Sigma_{1/2}$ state. This should provide good Franck-Condon factors for both. High-power diode lasers are generally available in this wavelength range, although gaps in availability might require choosing a higher vibrational level of the excited state and moving both lasers to slightly lower wavelengths.

Hopefully, improved theoretical potentials will become available soon. If the current potentials are matched to the atomic states by shifting instead of scaling, the wavelengths for the second STIRAP process become $\lambda_3 = 1046$ nm and a $\lambda_4 = 949$ nm. This clearly shows that additional information is required before the final laser systems can be chosen.

7.5 Spectroscopy with Ion Detection

A problem in working with trapped molecules is the lack of closed transitions. The operation of a MOT requires the presence of such transitions where the atom will always return to the initial ground state at the end of a cycle, possibly with the help of a repumping laser. The same transition can then be used in imaging: A single atom can absorb many resonant photons or spontaneously emit them at a rate of $\Gamma_{\mathrm{atom}}/2$ if driven at saturation levels. A ground state molecule will absorb a first resonant photon, but when it returns to the ground state there is a high probability that it will end up in a different rovibrational state, no longer resonant with the imaging beam. For this reason state selective detection of molecules is generally done with an ion-detector and a selective ionization scheme.

One of these schemes is **R**esonance **E**nhanced **M**ulti**P**hoton **I**onization (Popescu et al., 1974; Haimberger et al., 2004) or REMPI. This normally uses a pulsed dye laser in a two-photon process. The energy from both photons together is high enough to cross the ionization threshold, but the expected ionization rate would normally be very low. However, if the first photon is resonant with a molecular transition, the probability is greatly enhanced. If the intermediate state is known, then the photon energies where enhancement occurs provide information about the energies of the populated ground states.

In the RbYb molecule, ionization might be reached via an intermediate state based on an excitation of either the ytterbium or the rubidium atom. Since the ionization threshold is lower in rubidium at $33691\ \mathrm{cm}^{-1}$, this might be easier to work with than ytterbium, where it is $50441\,\mathrm{cm}^{-1}$. All level energies in the following are taken from the NIST atomic spectra database at *http://physics.nist.gov/PhysRefData/ASD/*).

The wavelength required for a two-photon process with a near-resonant intermediate level in ytterbium would probably need to match the 346 nm ($28902\,\mathrm{cm}^{-1}$) transition as the stronger 399 nm ($25063\,\mathrm{cm}^{-1}$) transition is just below half the ionization energy.

The molecular state converging on the rubidium 6P state has an energy that is high enough to serve as an intermediate level and the transition from the ground state is electronically allowed. Its two fine-structure levels are located at $23793\,\mathrm{cm}^{-1}$ and $23715\,\mathrm{cm}^{-1}$, roughly 420 nm, from the ground state. Unfortunately the necessary photon energies are then high enough to reach the ionized continuum directly from the excited 5P state at $12578\,\mathrm{cm}^{-1}$ that is used for photoassociation. It would therefore be necessary to wait until all molecules have returned to the ground state before an ionization measurement to reduce the background signal.

A feasible way to create these wavelengths might be a frequency doubled pulsed titan-sapphire laser or a pulsed dye laser, possibly using a Anti-Stokes frequency shift in a Raman cell. Depositing the required energy in a short pulse instead of over time has the advantage that a large number of ions is formed at a known time. This information can then be used to identify the ions and measure temperatures by time-of-flight spectroscopy.

Unfortunately the necessary photon energies are already high enough to reach the ionized continuum directly from the excited 5P state at $12578\ \mathrm{cm}^{-1}$ that is used for photoassociation. It would therefore be necessary to wait until all molecules have returned to the ground state before an ionization measurement to reduce the background signal.

A technically simpler way might be the implementation of a scheme as described in Sage et al. (2005). This uses an ionization laser to connect the excited state populated by photoassociation to an ionized state. This takes a photon energy of $20874\ \mathrm{cm}^{-1}$ for a near-dissociation molecule in a state converging on the rubidium $J = 3/2$ state. For a low vibrational level of the upper $\Omega = 1/2$ state that is likely to be used as the intermediate state in the production of vibronic ground state molecules, the maximum expected ionization energy is $24100\,\mathrm{cm}^{-1}$ or 415 nm. The required energy might be less if the potential for the ionized state is of comparable depth.

Transfer to the ground state by a resonant laser can then be detected as a reduction in the ion signal and further analyzed by waiting until the excited state molecules have decayed back to the ground state and then selectively returning molecules from the targeted ground state to the excited state using the same transfer laser.

7.5.1 Detector Design

A proper ion detector consists of an electron multiplier (channeltron or microchannel plate) mounted somewhere near the trap to amplify the small electrical signals created by the ions attracted by a charged electrode. Without electron multiplication it is extremely unlikely that any ion signal can be detected, because even if $1 \cdot 10^6$ atoms are neutralized at the electrode over a time of 100 ms, the average current over this time is only $1.6 \cdot 10^{-12}\,\mathrm{A}$. The installation of a properly designed ion-detector will therefore be a valuable improvement to the current experimental setup.

Even a simple detection system as described in Sage et al. (2005) should provide the necessary resolution to distinguish Rb^+, Yb^+ and RbYb^+ ions.

The installation requires breaking the vacuum of the main chamber, however, making this upgrade quite time consuming if a new baking-out cycle is necessary afterwards. The possibility of mounting a simple detector after flooding the chamber with nitrogen to minimize contamination and skip the baking-out process needs further investigation. It might be preferable to develop a more sophisticated setup for the ion detector based on Wiley and McLaren (1955) or Kraft et al. (2007), which allows for higher mass resolution in time-of-flight spectroscopy and might be useful in future experiments.

7.6 Trapping Molecules

There is a point when the physics of ultracold molecules can only be explored further if the same sample can be investigated over time. This requires some form of trapping. While magneto-optical traps cannot be used due to the lack of closed transitions mentioned before, several other methods have been demonstrated successfully.

Polar molecules can be held in electrostatic traps (Bethlem et al., 2000; Kleinert et al., 2007) but this requires an experimental chamber built around the required structure of electrodes from the beginning. More relevant to this thesis is the demonstration of optical and magnetic trapping schemes since the required infrastructure is compatible with the existing setup.

7.6.1 Optical Trapping

Optical trapping has been shown for Cs_2 (Takekoshi et al., 1998) as well as RbCs molecules (Fioretti et al., 2004). In both cases CO_2 lasers at powers close to 100 W were used. This reduces off-resonance photon scattering due to the very long wavelengths near $10\,\mu$m.

The bichromatic optical dipole trap already in place uses components at 1064 nm and 532 nm with intensities chosen to balance the attractive and repulsive effects on rubidium. This is possible in the atomic case without excessive heating of the sample since absorption occurs only at the well defined energies corresponding to transitions between the relatively few electronic states. For molecules, each of these states has one or more potentials converging on it and the entire rovibrational structure needs to be taken into account. There is no reason to expect the potential wells to support significantly less vibrational states at higher levels of excitation and the more closely spaced atomic levels that the molecular states converge on in this region lead to heavily overlapping vibrational series for this reason.

At high vibrational levels within a given electronic state this is somewhat simplified as the Franck-Condon overlap will favor transitions to other high vibrational levels. Both energies will then be close to the atomic values the series converges on. Thus the 1064 nm trap will likely be effective for the ground state molecules produced by spontaneous emission after simple photoassociation or those created through the first step of the suggested STIRAP scheme. However, unless the $^2\Sigma_{1/2}$ potential is considerably shallower than currently assumed (as shown in figure 7.4) the overlap of wavefunctions near the inner turning point the laser will also excite atoms to this state. The same might be true for the 532 nm photons driving a transition to a low vibrational level of a state converging on an excited 6S Rb or 6P Yb state. Table 2.3 in chapter 2 lists the electronic states in the energy range that might be reached from either the ground state or the excited states converging on the 5P Rb state used in photoassociation. For comparison, photon energies in wavenumbers for some relevant wavelengths are also given. ODT1 and ODT2 are the lasers currently used.

7.6.2 Magnetic Trapping

The use of a magnetic traps to hold cold molecules has already been demonstrated quite a while ago (Weinstein et al., 1998). A case that is more similar to the experiments in this thesis is described in Vanhaecke et al. (2002). Cs atoms are held in a MOT, while molecules are created by photoassociation and detected with an ionization method. It is found that if the fields are set to be strong enough, molecules are detected for a span of several hundred milliseconds after the photoassociation laser has been turned off.

Similar results have been reported for the heteronuclear KRb molecule (Wang et al., 2004). Here lifetimes were found to be limited by the MOT lasers exciting molecules from the trapped triplet ground state into a higher state that allows decay to the singlet ground state, which has no significant magnetic moment and is not trapped. This particular effect will not be a problem for YbRb molecules since the ground state Yb atom does not contribute any electronic spin to compensate the unpaired electron in Rb.

The fact that magnetic trapping is possible at all is interesting in that it requires the magnetic moment of the trapped particle to adiabatically follow the orientation of the local field as the particle travels around in the trap. This is simple if the particle is an atom where the heavy nucleus is essentially point-like and has a very low moment of inertia resisting changes in alignment.

In a molecule, the rotational moment of inertia of the nuclear structure is obviously considerable. The only way the molecular magnetic momentum can follow the rapid changes of the field near the center of the trap is for it to become uncoupled from the frame of reference provided by the nuclei. In Cs_2 the trapping forces per atom were found to be the same as in a single Cs atom. This means that the electronic and nuclear spin of both atoms couple together without being affected by the molecular alignment in what is called Hund's case $b_{\beta S}$.

For YbRb*, our investigations clearly show the presence of a coupling between electronic and molecular angular momentum on the order of $\Delta \approx 10^{-3}\,\mathrm{cm}^{-1} \approx 30\,\mathrm{MHz}$ in the form of the splitting of the rotational lines for $R > 0$. This will likely prevent trapping of molecules in theses states, unless the bias field can be made strong enough that the field minimum at the trap center is still strong enough to overcome this coupling. In the language of RF-evaporation used to create Bose-Einstein-Condensates, the trap bottom needs to be higher than 30 MHz. It is likely that states without rotation can be trapped at lower minimum fields.

In the molecular ground state, both ytterbium and rubidium atoms are in S states and the rotational coupling will quite likely be even smaller. Autler-Townes spectroscopy should provide further insight, but it appears almost certain that ground state molecules can be magnetically trapped.

7.6.3 Balancing Gravity

Another factor that needs to be taken into account is the effect of the greater mass of a YbRb molecule compared to a single rubidium atom. If the trapping forces are equal in the atomic and molecular cases then the trap frequency will vary as

$$\omega_m = \sqrt{\frac{k}{m_m}} = \sqrt{\frac{k}{m_a} \cdot \frac{m_a}{m_m}} = \sqrt{\frac{m_a}{m_m}} \cdot \omega_a \tag{7.2}$$

where m_m and m_a are the molecular and atomic masses and ω_m and ω_a are the respective trap frequencies. Since the radial trap frequency for rubidium in the magnetic trap was previously measured as $\omega^r = 2\pi \cdot 176\,\mathrm{Hz}$ (Tassy, 2007, page 74), the molecular value will be $\omega_m^r = 2\pi \cdot 101\,\mathrm{Hz}$ for ^{176}Yb.

This has no effect on the size of the molecular cloud compared to the atomic case at identical temperatures, as the lower velocities of the molecules compensates for the reduced confinement. The $1/\sqrt{2}$-size of the cloud σ is given by

$$\sigma = \frac{1}{\omega_m}\sqrt{\frac{k_B T}{m_m}} \tag{7.3}$$

$$= \sqrt{\frac{m_m}{m_a}} \cdot \frac{1}{\omega_a}\sqrt{\frac{k_B T}{m_a} \cdot \frac{m_a}{m_m}} \tag{7.4}$$

$$= \frac{1}{\omega_a}\sqrt{\frac{k_B T}{m_a}} \approx 1.24 mm \quad \text{at } 500\ \mu K \tag{7.5}$$

However, gravity will pull the cloud further down before it is balanced by the trapping forces

$$F_{\mathrm{grav}} = -F_{\mathrm{trap}} \tag{7.6}$$

$$\Longleftrightarrow mg = k\,x \tag{7.7}$$

$$\Longleftrightarrow mg = m\,\omega^2\,x \tag{7.8}$$

$$\Longleftrightarrow x = \frac{g}{\omega^2} = 0.024\,\mathrm{mm} \tag{7.9}$$

This drop relative to the magnetic field minimum is small enough to leave the cloud in the area where the field still has the required properties for trapping and is therefore tolerable. The resulting separation might actually reduce losses through atom-molecule collisions.

Chapter 8

Summary

This chapter provides a review and summary of the results presented throughout the previous chapters. For convenience it is available in a German version as well.

8.1 English Version

In this thesis I have described the formation of electronically excited but translationally cold YbRb* molecules by means of photoassociation as well as the analysis of the resulting spectra.

The experiment itself was done in a combined magneto-optical trap loaded from two Zeeman slowers. The rubidium trap uses a forced dark spot scheme and holds a large cloud of approximately 10^9 atoms at a temperature of 340μK and a peak density of $10^{17}\,\mathrm{m}^{-3}$. Due to the shared magnetic field, the ytterbium trap is considerably smaller. It contains $4 \cdot 10^7$ atoms at a temperature of $510\,\mu$K when operated by itself. Collisions of excited ytterbium atoms with rubidium lead to a suppression of more than a factor of 20, resulting in an atom number of $1.8 \cdot 10^6$ when both traps are loaded. Rubidium losses are not significant due to the large reservoir of atoms in the outer regions of the trap.

The photoassociation process was driven with a titanium-sapphire laser providing around 300 mW of power in a $320\,\mu$m FWHM beam, chosen to be somewhat smaller than the ytterbium cloud which optimizes photoassociation rates at limited available power. The laser line width is approximately 2 MHz.

Spectra were taken by monitoring the reduction of trap fluorescence due to molecule formation and subsequent loss from the trap. Photoassociation lines were found over a range of $33\,\mathrm{cm}^{-1}$, or 2 nm, on the "red" side of the 795 nm D1 transition from the rubidium ground state to the $5^2\mathrm{P}_{1/2}$ state.

The majority of lines were identified as belonging to two series of vibrational levels of the excited YbRb* molecule, converging on a system of a single ground state ytterbium atom and a single $5^2\mathrm{P}_{1/2}$ excited rubidium atom. At longer wavelengths, the binding energy increases approximately with the third power of $\mathrm{v}_{\mathrm{max}} - \mathrm{v}$, the vibrational quantum number relative to that of the last bound state. This is predicted by the Leroy-Bernstein equation (LeRoy and Bernstein, 1970), which relates the energies of the vibrational levels to the long range coefficient of the molecular potential. Application of a recently improved version of this equation showed the leading coefficient to be $C_6 = (-5684 \pm 98)\,\mathrm{E_h}\ \mathrm{a}_0^6$, which agrees well with expectations (Marinescu and Sadeghpour, 1999). It also agrees with the value of $C_6^{\mathrm{LB}} = -5597\,\mathrm{E_h}\ \mathrm{a}_0^6$ found with the basic Leroy-Bernstein equation.

For all but the weakest of the observed lines a resolved rotational structure was found. This follows a progression $E_{\mathrm{rot}} = B_{\mathrm{rot}}\, R\,(R+1)$ expected from a basic quantum mechanical model. The series terminates with the third or forth rotational component where the thermal energy of the approaching atoms becomes insufficient to cross the centrifugal barrier. The rotational constant B_{rot} changes considerably and systematically over the investigated range. This was shown to be consistent with the nuclear wavefunctions for different energy levels in the molecular potentials.

An unexpected discovery was the splitting of the rotational components into subcomponents, based on the relative alignment of the angular momentum of the rubidium atom relative to the rotational axis of the molecule. This indicates a variant of Hund's case (e) coupling where all angular momenta of the rubidium atom combine to form F', which then couples to the nuclear rotation described by the quantum number R'. The ground state ytterbium atom does not have any internal angular momentum to contribute.

These subcomponents were found to vary in depth in a way that indicates a similar splitting in the ground state, with sub-states having higher or lower energies based on the alignment of the rubidium atom's magnetic dipole moment relative to the angular momentum carried by the approaching ytterbium atom. The resulting modification of the potential leads to a new barrier, similar to that created by centrifugal effects. This partially suppresses some of the subcomponents.

This is not a problem for the molecular states with $R' = 0$ that are most interesting as intermediate states on the way to truly ultracold molecules in the electronic, vibrational and rotational ground state. To extract the production rate of such intermediate states from the trap loss spectrum, a simple rate equation model was developed. For the available laser power a maximum rate of $1.4\,\mathrm{s}^{-1}$ per ytterbium atom was measured. Over the entire trap volume, this means $2.5 \cdot 10^6$ molecules formed per second. An analysis of the saturation of the loss rate at high photoassociation laser intensities showed that the maximum achievable rate per atom might be even higher at around $2\,\mathrm{s}^{-1}$ per ytterbium atom. Theory predicts that given enough laser power, this rate can be reached even for the weaker lines in the spectrum.

The relative strength of the photoassociation lines was found to vary strongly even between adjacent vibrational lines due to the Franck-Condon overlap between the unbound continuum wavefunction and that of the bound excited state. Examining the positions of the outermost lobe of the nuclear wavefunctions in the excited molecular state as found from numerical calculations and comparing them to the nodes in the ground state atomic wavefunctions was found to predict a similar variation in line strength for potentials based on the excited state C_6 coefficient and ground state scattering length calculated in previous work of the group.

With the various properties of cold molecules investigated throughout this thesis, it is possible to outline a path to molecules that are not only translationally ultracold, but also in the electronic and rovibrational ground state. The next step will be the development of an efficient transfer of the molecules to a non-rotating electronic ground state in a known vibrational level. A suitable level will be found through Autler-Townes spectroscopy to gain the required knowledge for implementing a stimulated Raman adiabatic passage scheme.

None of the current results hint at any major obstacles for this process and the subsequent transfer to the vibrational ground state, although more spectroscopic work will be required for the latter.

The new experimental control system implemented throughout this work and described in the appendix will help with the increasingly complex experimental sequences required for this.

8.2 Deutsche Version

Diese Arbeit beschreibt die Bildung von ultrakalten YbRb* Molekülen, die durch Photoassoziation in elektronisch angeregten Zuständen mit hohen Vibrationsquantenzahlen erzeugt werden. Sie präsentiert neben einer Beschreibung der durchgeführten Experimente auch die komplette Analyse der aufgenommenen Spektren.

Die Experimente wurden in einer kombinierten magneto-optischen Falle durchgeführt, die durch zwei Zeeman-Abbremser mit Atomen versorgt wird. Die Rubidiumfalle hat eine Konfiguration, die als “forced dark spot” bezeichnet wird und eine hohe Dichte von Atomen in einem definierten Hyperfeinzustand zulässt. Die Falle hält eine Wolke mit etwa 10^9 Atomen bei einer Temperatur von $340\,\mu$K und einer maximalen Dichte von 10^{17} m^{-3}. Aufgrund des gemeinsamen Magnetfelds fällt die Ytterbiumfalle deutlich kleiner aus. Sie enthält $4 \cdot 10^7$ Atome bei einer Temperatur von $510\,\mu$K solange sie einzeln betrieben wird. Sobald die Rubidiumfalle aktiviert wird, führen Stöße zwischen Rubidium und angeregten Ytterbiumatomen zu einer Reduktion der Ytterbiumatomzahl um einen Faktor von mehr als 20. Die resultierende Anzahl von Ytterbiumatomen ist dann etwa $1.8 \cdot 10^6$. Durch das große Reservoir von unbeeinflussten Atomen im äußeren Fallenbereich sind die Rubidiumverluste vernachlässigbar gering.

Zur Photoassoziation wird ein Titan-Saphir Laser mit etwa 300 mW nutzbarer Leistung verwendet, dessen Strahl eine volle Halbwertsbreite von $320\,\mu$m aufweist. Diese wurde etwas kleiner als die Ytterbiumfalle gewählt, um die Photoassoziationsrate bei begrenzter verfügbarer Leistung zu maximieren. Die Linienbreite des Lasers beträgt etwa 2 MHz.

Der Laser kann nun durch Photoassoziation zur Bildung von Molekülen in einem elektronisch angeregten Zustand führen. Da diese nicht in den Atomfallen gehalten werden, führt dieser Prozess zu einer Abnahme der Fallenfluoreszenz. Die Abnahme der Fluoreszenzsignale in Abhängigkeit von der Wellenlänge des Photoassoziationslasers wurde in Spektren für ^{87}Rb mit ^{174}Yb und mit ^{176}Yb zusammengestellt. Photoassoziationslinien wurden über einen Bereich von 33 cm^{-1} oder 2 nm in der Nähe des D1-Übergangs vom Rubidium-Grundzustand zum $5^2\mathrm{P}_{1/2}$ Zustand bei einer Wellenlänge von 795 nm gefunden.

Die Mehrzahl der Linien konnten einer von zwei Serien von Vibrationszuständen des YbRb*-Moleküls zugeordnet werden. Für höhere Energien konvergieren die Vibrationszustände gegen einen Zustand, der sich aus einem Grundzustands-Ytterbiumatom und einem Rubidiumatom im angeregten $5^2\mathrm{P}_{1/2}$ Zustand zusammensetzt. Bei größeren Wellenlängen nimmt die Bindungsenergie mit der dritten Potenz der relativen Vibrationsquantenzahl $\mathrm{v}_{\mathrm{max}} - \mathrm{v}$ zu. Dies entspricht den Erwartungen aufgrund der Leroy-Bernstein-

Gleichung, die den Zusammenhang der Energien hoher Vibrationszustände und der langreichweitigen Koeffizienten des molekularen Potentials beschreibt (LeRoy and Bernstein, 1970). Eine kürzlich publizierte Verbesserung der Leroy-Bernstein-Gleichung liefert einen Wert für den langreichweitigsten Koeffizienten von $C_6 = (-5684 \pm 98)\ \mathrm{E_h\ a_0^6}$, in guter Übereinstimmung mit Werten für andere heteronukleare Moleküle (Marinescu and Sadeghpour, 1999). Die Unsicherheit schließt auch den Wert $C_6^{\mathrm{LB}} = -5597\,\mathrm{E_h\ a_0^6}$ ein, der sich aus der Anwendung der ursprünglichen Leroy-Bernstein-Gleichung ergibt.

Außer den schwächsten beobachteten Linien zeigen alle eine aufgelöste Rotationsstruktur. Diese folgt dem aus der Quantenmechanik erwarteten Muster $E_{\mathrm{rot}} = B_{\mathrm{rot}}\,R\,(R+1)$. Die Serie bricht nach der dritten oder vierten Komponente ab, da die thermische Energie der freien Atome nicht ausreicht, um die Zentrifugalbarrieren der höheren Rotationszustände zu überwinden. Die Rotationskonstante B_{rot} zeigt eine deutliche, systematische Entwicklung über den untersuchten Wellenlängenbereich. Es konnte gezeigt werden, dass diese konsistent ist mit den Erwartungen aus den nuklearen Wellenfunktionen in einem Potential wie dem durch den C_6-Koeffizienten beschriebenen.

Eine unerwartete Entdeckung war die Aufspaltung der Rotationskomponenten in verschiedene Subkomponenten. Diese ergibt sich aus einer Drehimpulskopplung entsprechend einer Variante von Hunds Fall (e), in der der komplette Drehimpuls des Rubidiumatoms F' an die molekulare Rotation R' koppelt und so -je nach relativer Ausrichtung- die Aufspaltung bewirkt. Das Ytterbiumatom trägt dabei keinen Drehimpuls bei.

Die Subkomponenten zeigen Unterschiede in ihrer Stärke, die sich durch eine gleichartige Kopplung für die noch ungebundenen Atome im Grundzustand erklären lässt. Je nach Ausrichtung des magnetischen Dipolelements des Rubidiumatoms relative zum Drehimpuls des sich nähernden Ytterbiumatoms haben einige Zustände eine erhöhte, andere eine erniedrigte Energie. Dies resultiert in einer neuen Potentialbarriere, ähnlich der, die aus dem Zentrifugalpotential hervorgeht, und unterdrückt teilweise die energetisch ungünstigeren Zustände.

Um die Molekülproduktionsrate beurteilen zu können, wurde ein einfaches Ratengleichungsmodell entwickelt, mit dem sich diese aus den gemessenen Fallenverlusten berechnen lässt. Bei der gegenwärtig verfügbaren Leistung des Photoassoziationslasers wurde eine maximale Rate von 1.4 Molekülen pro Atom und Sekunde beobachtet. Für die gesamte Falle bedeutet das $2.5 \cdot 10^6$ gebildete Moleküle pro Sekunde. Eine Analyse der Sättigung der Photoassoziationsrate bei hoher Leistung zeigt, dass die maximal erreichbare Rate vermutlich bei etwa 2 Molekülen pro Atom und Sekunde liegt. Die Theorie sagt vorher, dass diese Rate auch für die schwächeren Linien erreichbar sein sollte, solange genug Laserleistung verfügbar ist.

Die Tiefen der beobachteten Linien variieren sehr stark, sogar zwischen benachbarten Linien. Die Ursache dafür ist der wechselnde Franck-Condon-Überlapp zwischen den ungebundenen Kontinuumswellenfunktionen der einzelnen Atome und den Wellenfunktionen der gebundenen angeregten Zustände. Eine Untersuchung der Position des letzten Wellenbauches des gebundenen Zustands im Vergleich zu den Knoten der Grundzustandswellenfunktion sagt eine Variation der Linienstärke voraus, die der beobachteten sehr nahe kommt. Die dabei verwendeten charakteristischen Eigenschaften basieren auf dem aus den Spektren bestimmten C_6-Koeffizienten sowie auf der Grundzustandsstreulänge, die in vorherigen Experimenten zur sympathetischen Kühlung bestimmt wurde.

Mit den hier untersuchten Eigenschaften ist es nun möglich, ein weiteres Vorgehen auf dem Weg zu ultrakalten Grundzustandsmolekülen zu planen. Der nächste Schritt wird die Entwicklung einer effizienten Transfermethode der gebildeten Moleküle in einen definierten elektronischen Grundzustand sein. Ein geeignetes Energieniveau sollte sich mittels Autler-Townes Spektroskopie finden und untersuchen lassen, so dass die Atome schließlich durch die Methode der "stimulated Raman adiabatic passage" (STIRAP) dorthin transferiert werden können.

Keines der gegenwärtigen Resultate deutet auf bedeutende Probleme für diesen Prozess sowie die anschließende Übertragung in the Vibrationsgrundzustand hin, obwohl der zweite Schritt natürlich weitere spektroskopische Arbeit erfordern wird.

Das neue Steuerungssystem, dass ebenfalls während dieser Arbeit entwickelt wurde und im Anhang beschrieben ist, sollte sich dabei als nützlich erweisen, um die zunehmend komplexen Steuersequenzen zu implementieren.

Appendix A

Control System

During the course of this thesis, a new control system was developed for the experiment. It allows for precise, repeatable control over the various subsystems at a rate of 50 kHz. *While the actual spectra shown herein were all taken with fixed parameters, the new system was already used in many of the supporting measurements, such as temperatures and loading times.*

Since it will become increasingly more important as the loading, cooling and population transfer scheme grows in complexity, this appendix aims to provide both a simple operations manual and an explanation of what happens in the actual program.

A.1 System Overview

The control system consists of a PC with three National Instruments I/O boards plus a 19” electronics rack with line drivers that the various experimental systems are connected to.

Two of the I/O boards are NI PCI-6229 M-series boards, each providing 32 digital output channels capable of the buffered, clocked output mode used by the system. Maximum output rate is 1 MHz. Eight additional digital lines can be updated manually. Each of the boards also provides 4 analog output channels capable of full 16-bit resolution. Since the analog values are generated by a single D/A converter, the maximum generation rate of 833 kS/s (kilo-samples per second) limits the analog output to a rate of approximately 200 kHz.

Since eight analog output channels are not sufficient to control the entire experiment, the third boards is a NI PCI-6723, providing 32 analog output channels capable of 13-bit resolution and a maximum update rate stated to be 204 kS/s when operating from the on-board buffer containing a maximum of 2048 samples.

National Instruments I/O boards were chosen for their easy integration with the LabView environment available from the same company. The complete support for the more advanced features directly from this high-level language avoids the need for a fast low-level layer to provide the necessary high-speed I/O. The NI-DAQmx drivers provide a mode that uses both the onboard buffers and direct memory access (DMA) to system RAM to effectively provide a larger buffer that can be refilled at more manageable intervals than the onboard buffer alone would provide.

It was found that although the analog board is only rated for 45 kS/s (all channels) in this mode, the advances of memory and CPU speeds allowed for continuous, unproblematic generation of output signals at 100 kHz if CPU workload was kept to a minimum otherwise. Since the computer only uses a AMD Sempron 3000+ CPU in an Abit NF7 mainboard with 512 MB of PC400 RAM, rather modest in performance even when it was bought, it can safely be assumed that operation at 100 kHz output rate would be feasible on a more modern, faster machine.

As it is, the output rate is set to 50 kHz with a virtual buffer of 50000 samples as this leaves enough CPU time remaining for the sample generation code to operate. The three boards are connected via an internal cable distributing signals called the "real time system interconnect" (RTSI). This is used to synchronize signal output, with the analog board generating the sample clock signal used by all three.

The output signals from the three boards are connected via cables to the electronics rack containing line drivers. Although the I/O boards themselves provide considerable capacity to source or sink current, these drivers have specifically been designed to avoid oscillations when connected to the long coaxial cables connected to AOMs and other devices distributed over all three optical tables. They will also protect the I/O boards and the computer from damage caused by broken or improperly connected equipment. The electronics rack is set up such that each board is connected to a 3U high subrack with a backplane distributing the signals to driver the modules.

Currently eight of the 32 main analog channels are connected to one module capable of handling devices with 50 Ω input impedance common in radio-frequency technology, the remaining ones are connected to three identical modules providing slightly lower maximum output currents. Similarly, the digital outputs are hooked up to output modules providing eight drivers along with output status LEDs for each channel. The same digital module can also be used in a slot that provides access to the eight unbuffered digital lines. In the same way the backplane provides a narrow slot for the four analog channels available on each of the digital boards that is compatible with the circuit boards used in the standard analog modules. Accessing these will simply require the construction of a narrower front panel equipped with only four instead of eight connectors.

All digital channels provide standard TTL level signals, generated by drivers of the 74HCT240 family. All analog channels are used in a mode that allows signals ranging from −10 V to 10 V and the driver modules are designed for this voltage range.

The electronics rack also contains a panel with inverters and basic logic gates.

A.2 Control Program

The control program serves as a frontend to the hardware described, aiming to give control of the various experimental subsystems as transparently as possible. This is simplified by the fact that the interface between high-level software and the hardware provided in LabView already contains the application of calibration curves set in the *Measurement and Automation eXplorer* (MAX) to the data. For example, this allows specifying the deflection efficiencies of the various AOMs directly instead of having to choose appropriate control voltages. This can be seen in the annotated screenshots of figures A.1 and A.2.

As mentioned earlier, the program is entirely written in LabView to make understanding it, and therefore maintenance and updates, as painless as possible. It also allows for debugging of the entire system using LabView's powerful tools and eliminates the need for maintaining a second development environment to compile intermediate libraries.

The program is generally operated either in *steady state* or *pattern* mode, both of which will be explained in the following.

A.3 Steady State Operation

In this mode only the screen area to the left of the run control buttons is relevant. Clicking the button labeled "jump to steady state" moves the view to a position where this is visible.

Digital channels can be turned on and off by using the green (for the first block of 32 channels) or yellow (for the second block) buttons in the left section. Analog channels can be controlled by entering numbers into the fields in the right section. Clicking the blue button on the bottom right of each channel block selects it. It is then shown with name, current value and unit in the channel settings section in the top left of the screen. The slider below these can now be used to control the analog value directly with the mouse. It is worth noting that the update rate of the output signal is the same as that for the value displayed in the value box (in the right hand section) for this channel, so moving the slider quickly will result in a staircase-like signal the the output.

It is also possible to change the settings for the selected channel. This always includes the channel name and a delay compensation value. For analog channels, it also includes the unit, the allowed limits (which affect both the slider and the manually entered values) and the virtual channel. Virtual channels need to be defined in the Measurement and Automation eXplorer, outside the control program. This includes the ability to set a calibration curve. There is no consistency check between the allowed range for the virtual channel and that set for a channel in the control program. If the program tries to generate a value outside the defined range of the virtual channel, there will be an error message and the signal output will be disabled until the error condition is fixed by the user and the big red "output disabled" switch over the run controls is deactivated manually. The delay compensation in analog channels assumes that the attached device will always lag behind the control voltage by the time given and compensates accordingly by making all output changes happen earlier than in the other channels.

When changing the settings for a digital channel, the compensation time will only affect the off-on transition. There is never any compensation for an on-off transition. This is intended to make it easier to work with the typical combination of AOM and mechanical shutter, where the latter needs to open before the AOM, but close after it. The buttons labeled "high", "none" and "low" set overrides for a digital channel. A channel set to "low" will ignore any activation requests in both steady state or pattern mode. Setting it to "high" will keep it active all the time instead. This can be useful in testing and debugging patterns. If any override is set, the red light next to the selection button in the steady state digital panel will light up for this channel.

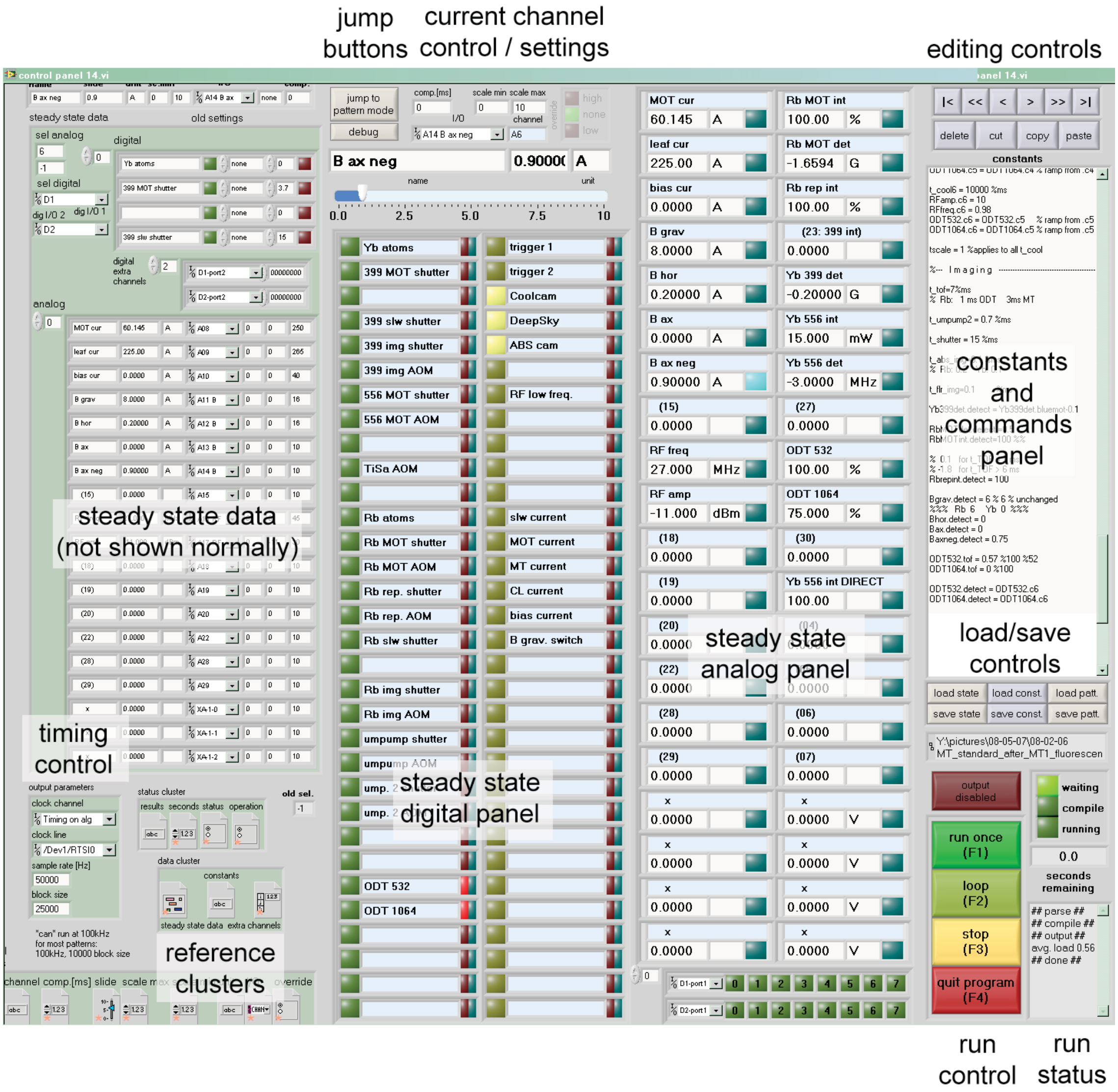

B ax neg 0.90000 A

MOT cur 60.145 A
Rb MOT int 100.00 %
leaf cur 225.00 A
Rb MOT det -1.6594 G
bias cur 0.0000 A
Rb rep int 100.00 %
B grav 8.0000 A
(23: 399 int) 0.0000
B hor 0.20000 A
Yb 399 det -0.20000 G
B ax 0.0000 A
Yb 556 int 15.000 mW
B ax neg 0.90000 A
Yb 556 det -3.0000 MHz
(15) 0.0000
(27) 0.0000
RF freq 27.000 MHz
ODT 532 100.00 %
RF amp -11.000 dBm
ODT 1064 75.000 %
(18) 0.0000
(30) 0.0000
(19) 0.0000
Yb 556 int DIRECT 100.00
(22) 0.0000
(28) 0.0000
(06) 0.0000
(29) 0.0000
(07) 0.0000
x 0.0000
x 0.0000 V

t_cool6 = 10000 %ms
RFamp.c6 = 10
RFfreq.c6 = 0.98
ODT532.c6 = ODT532.c5 % ramp from .c5
ODT1064.c6 = ODT1064.c5 % ramp from .c5
tscale = 1 %applies to all t_cool
t_tof=7%ms
t_umpump2 = 0.7 %ms
t_shutter = 15 %ms
Rbrepint.detect = 100
Bgrav.detect = 6 % 6 % unchanged
Bhor.detect = 0
Bax.detect = 0
Baxneg.detect = 0.75
ODT532.tof = 0.57 %100 %52
ODT1064.tof = 0 %100
ODT532.detect = ODT532.c6
ODT1064.detect = ODT1064.c6

Y:\pictures\08-05-07\08-02-06 MT_standard_after_MT1_fluorescen

parse
compile
output
avg. load 0.56
done

Figure A.1: Left half of control panel.
The very left part containing the cluster labeled **steady state data** is not usually on screen and will only be visible if the lower jump button **debug** is clicked. This area contains the representation of various internal pieces of data (such as the **reference clusters**). The block **timing control** controls the output rate and the number of samples prepared in each block of data.
A bit further to the right is the **steady state digital panel** that controls the state of the digital output lines outside of pattern mode via the buttons on the left. The red "lights" indicate whether any overrides are currently active for this channel. Clicking the blue button next to it selects this channel for the **current channel control / settings** panel above for changing configuration or overrides for digital channels and provides a slider control for analog channels.
Next to the right is the **steady state analog panel**. Values can be directly entered into the fields. Blue buttons once again select a channel for control or setup. Below this panel is a field that controls the extra digital lines not capable of buffered output.
The rightmost part contains the **editing controls** for the pattern section (seen on the opposite page) as well as buttons for moving around in the pattern. Below this is the **constants and commands panel**, followed by . . . (continued on opposite page)

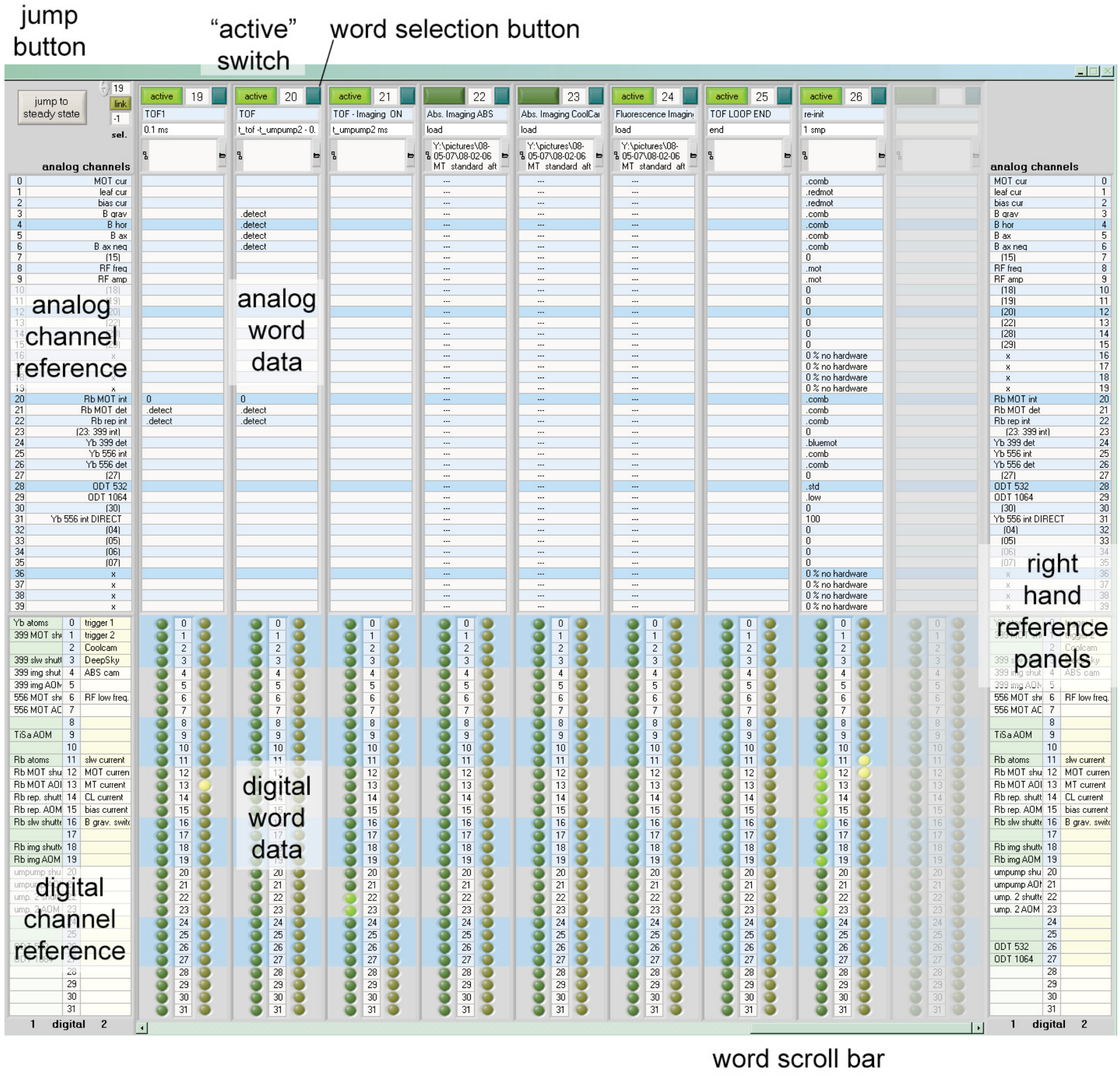

Figure A.2: Right half of control panel.

Starting from the left again, below the **jump button** that moves the screen to the steady state field-of-view, are the **analog and digital channel references**. These repeat the name of the channel this particular line of the word controls.

To the right of this is the actual pattern area. It consists of several "words" of identical layout, each consisting of a green **active switch**, number and blue selection button over a name field, a function field and a file field. Below these fields are the **analog and digital word data** blocks. On the very bottom of this area is the **word scroll bar** that allows moving within the pattern without using the controls on the left. If moved all the way to the right, one inactive word will be shown after the last used one.

On the very right is another set of **reference panels** to make it easier to find the line of a certain channel.

(continued) . . . the **load/save controls** for patterns, constants and steady state (including channel setup). The text field below displays the latest pattern filename used. Finally, the **run control** buttons initialize or cancel pattern mode operation while **run status** information is given just right of them.

A.4 Pattern Output Mode

A pattern is a set of instructions given in blocks (called words) of values describing the sequence of output signals to the control program. The words are shown on the right hand side of the screen. The screen area dedicated to them can be increased by clicking the “jump to pattern mode” button.

Output mode for the current pattern is entered by clicking the “run once” or “loop” button of the run controls or pressing the matching key. The control program will then evaluate the constants panel from top to bottom before using the values obtained in this way to substitute all the placeholders in the present pattern with numbers. During this time the run status field will show the message “`## parse ##`”. If this was successful, the message “`## compile ##`” will be shown. During this time the program translates the pattern information into a data format that is very fast and easy to translate into actual output values while taking comparably little space. Finally, the countdown timer will start counting down seconds, the message “`## output ##`” is shown and signal generation starts.

It is worth noting that in order to keep the code simple, the program will always output a full number of data blocks, and at least three of them. At this time, the block length is 0.5 s, meaning that a pattern is at least 1.5 s long. The time between the end of the output sequence given by the pattern and the end of the last block is filled by holding the last values. The last word will therefore in most cases be longer than requested and using ramps in it is not recommended.

After pattern generation has finished the load measured for this pattern is displayed. This is based on the time after the next output block has been prepared, but before it is requested for output. If the computer were fast enough to prepare the next block instantly, this would be 0. If the block becomes ready at exactly the same time it is requested, the load is 1. Since a block is only half the buffer size, it is possible that a short pattern can be output without error even at loads greater than one. If the buffer runs out during output, a “buffer underrun” message will **always** be generated.

If the loop button is active at the end of a run, then the pattern will immediately and without recompilation repeat from the beginning after the last block is completed. The output signals will not go back to the steady state values between repeats. It is possible to switch between “run once” and “loop” even during the output phase.

At any time during parsing, compilation or output it is possible to select cancel to return to steady state mode. However, if any of the attached devices depend on the signal history, such as the cameras in modes with flush or multiple exposures, they might be stuck in the middle of a cycle when this happens and will need manual resynchronization.

A.5 Writing Patterns

This section describes the instructions that can be used in a pattern. Table A.1 provides a short overview.

The simplest pattern possible consists of a single activated word with a length such as `100 ms` (the space between number and unit is mandatory) given in the function field, and values provided for all the fields of the analog channels. Since each of the digital channels is either on or off in a given word, there is no way to leave digital channels undefined. If all analog values are within the range allowed by the settings for their channel, the pattern can then be output by selecting “run once”.

A.5.1 Analog Field Instructions

The pattern can be made easier to adapt by using constants instead of numbers. A constant’s name is case sensitive and it has to start with an alphabetical character, but can contain numbers and the underscore character after that. It can then be defined in the constants panel above the run control buttons in the form of `const_a = 10`. The character ‘%’ serves as comment marker both here and in most other fields of the pattern. Anything after it will be ignored up to the end of the line.

To save space in the pattern section, a “.” character can be added before the constant name. This will internally prefix the constant name with a string generate from the channel name by removing all spaces. So if `.const_A` is entered into the line that corresponds to a channel called “channel A”, then the variable name that has to be used in the constants field will be `channelA.const_A`. If it is necessary to use a constant that has been defined this way in another channel, its full name including the channel prefix can be used.

Unfortunately, there is currently a bug causing the prefix to be added in front of the decimal point of a number. For this reason these will cause errors when entered into one of the analog fields. The recommended work-around is to define all numbers requiring decimals in the constants field.

It is also possible to enter basic mathematical commands in any place that will evaluate a constant to the extent that the built-in LabView function “Eval Formula String.vi” is able to handle.

By entering `ramp a to b` into one of the analog fields, the channel can be made to ramp from value a to value b over the time of the word. To keep entries into the analog fields short, it is also possible to give only the second value. The ramp will then start at the last value of the previous word. The `to` is optional in this case and `ramp` can always be written as `R` instead. Proper capitalization is important, though.

The command `smooth a to b`, shortened to `S` with the same option of giving only the final value, will give a smooth transition. This means that the rate of change is zero in the beginning, then gradually increases until the middle of the word and the decreases again back to zero. The shape of the curve is described by the polynomial $f(t) = -2t^3 + 3t^2$ for t=[0;1].

Direct access to the entire range of functions that the control program can generate within a single word is provided through the command `poly a b c d` (shorthand: `P a b c d`). The output value is then given by $f(t) = a + bt + ct^2 + dt^3$ where t runs from 0 to 1 over the time of the word. Very little bounds-checking is done for this command, however. Putting incorrect values will most likely lead to a run-time error when the hardware cannot generate the requested values.

function field

data word	example: `10.5 ms` syntax: `a ms` (`s`, `us`/`mus`, `samples`/`smp`)	defines values for the digital and analog channels (fixed or ramped) to be output for the duration given by `a`. For details on specifying analog values see table below.

loop	example:
	`for t_tof = 3 to 7`
	syntax:
	`for a = b to c`
	`for a = b to c step d`
	`for a = b, c, d`
		loops over the values from `b` to `c`, using the step size given in `d` or 1 if not specified. After the loop, `a` will keep the last assigned value. Alternatively a comma-separated list of values can be provided.
		The `for` word also reproduces the `define` functionality.

end loop	syntax: `end`	Every `for` command needs an `end` to mark the end of the loop.
re-define	syntax: `define`	Allows redefinition of "constants". In a define word, analog fields can contain assignments like `.valA = 2*.valA`.
debug	syntax: `display`	Any constant given in analog fields will be displayed in a message box during compilation.
load subpattern	syntax: `load`	will be replaced by the words in the subpattern specified in the file field.

analog fields

constant value	examples:
	`3*5`
	`constA`
	`4+ .valA`
		hold constant value for the time specified. Calculations in the analog field will be evaluated at compile-time. Constants beginning with '.' will be prefixed with the condensed channel name.

simple ramp	syntax:
	`ramp a to b`
	`ramp [to] b`
	`R a to b`
	`R [to] b`
		ramps analog output value from value `a` to `b` over the time specified for the word. If no starting value is specified, the final value of the previous data word is used. If only a single parameter is given, `to` is optional.

smooth ramp	syntax:
	`smooth a to b`
	`smooth [to] b`
	`S a to b`
	`S [to] b`
		syntax analog to `ramp`. Generates a smooth transition that starts and ends with zero rate-of-change.

polynomial	syntax:
	`poly a b c d`
	`P a b c d`
		analog output value is given by the function $f(x) = a + bt + ct^2 + dt^3$ with t ranging from 0 to 1 over the time of the word.

Table A.1: Pattern mode instruction reference

A.5.2 Function Field Commands

Coming back to the very beginning of this section, the function field of the basic word can simply contain the time the word is supposed to be held during output. This must be given as "*value* (space) *unit*" where *value* can of course be a constant. Valid units are `s` for seconds, `ms` for milliseconds, `us` or `mus` for microseconds and `samples` or `smp` to specify the length relative to the sampling rate. The compiler will try to round the length to the nearest possible value, but there will be an error message if the difference between requested and available length is too large. If the length of a word is zero after evaluation, it will be ignored by the compiler and not cause any output.

The function field can also take one of several commands. If one of these is found instead of a time value, then the word will again not cause any output and the state of the digital channels in particular is entirely without function.

The most important command takes the form `for a = b to c step d` and creates a loop. In the first iteration of the loop `a` has the value given by `b`. For each successive iteration `a` is increased by `d` until the next value would be larger than `b`. At this point the loop ends with `a` remaining at the last value that was still inside [b;c]. Negative step values are also possible. A loop can also be specified as `for a = b, c, d` (with as many items in the list as required). This will cause one iteration of the loop for each entry in the list, with `a` set to the respective value (in the same order as given). Entries in the analog fields can be used to redefine variables for the loop iteration (see `define`, below). These will be evaluated once for each loop iteration with the loop variable already set to the new value. The end of each loop is marked by the `end` command. Entries in the analog fields are without effect here. Due to the lack of intelligence of the fast output routine, all loops are completely unrolled at the compilation step. For this reason, it can be useful to split experimental runs that use loops to explore parameter ranges into several smaller parts as compilation times increase much faster than linearly with pattern length.

The `define` command makes it possible to change "constants" during the pattern. This is done by putting an assignment of the form `a = b + c` into one or several of the analog fields. Basic mathematical functions are available here as well, and channel prefixes work as expected.

If the command `display` is entered into the function field, the compiler will output a status message listing the value of any constants or formulas in the analog fields. This makes it possible to check the values of constants at any part of the pattern.

Finally, `load` loads a subpattern specified in the path field below. Only the actual words are included while constants specified in the subpattern are ignored. The inclusion happens before the compilation step so the overall effect is that of cutting the main pattern apart at the `load` word, pasting in the subpattern and then compiling the new pattern.

A.5.3 Directives

A directive is an instruction that can be given in the constants field to create special compiler behavior. Directives are prefixed by # and a space in the constants field. Currently the only directive implemented is `# flush_camera`. This detects the typical pattern of three camera trigger signals in an absorption image and automatically generates an additional trigger before those to flush the camera. This can be very helpful if no existing word starts at a suitable time or if the lengths of words before the camera trigger are changed often.

The syntax of this directive is `# flush_camera channelgroup channelnumber time` where channelgroup is the group of digital channels the required channel is in and channelnumber is the channel itself; time is the time in milliseconds that it will take the camera to become ready again after the flush. For the FLI coolcam, appropriate parameters are `# flush_camera 2 2 4000`.

A.5.4 Loading and Saving Patterns

Loading a pattern is simply done by clicking on the "load pattern" button under the constants field. Saving is the same way. There are some points of note, however.

- If the pattern name does not start with a date in the form YY-MM-DD, a date in this form will automatically be prefixed.
- Any subpattern included by `load` commands will by copied to a folder of the same name as selected for the pattern. The references in the load commands will be changed to point to these files instead of the originals.

A.6 How it Works

The full control program consists of many subroutines and the translation from the on-screen pattern to the final data structures optimized for fast output involves multiple steps. This section aims to give a broad overview what happens in the program to make it easier to understand when upgrades become necessary.

A.6.1 Steady State / Editing

control panel 14.vi

This VI contains the main loop of the program that reacts to button presses and updates the output signals in steady state mode.

When a subroutine is required to interact with a control or data structure on screen, this is generally done by passing references. Since the more complicated subroutines need to access many things, these references are bundled to form the status cluster (dealing with run status and controls) and the data cluster (containing steady state data and channel information). There is also the channel settings cluster that groups the controls of the same name. This is only done for geometrical reasons specific to the graphical programming methods in LabView: Had the controls been put into a cluster, it would have interfered with the placement of the top left jump buttons.

After the VI is started, it first initializes the various steady state panels from the hidden steady state data cluster by calling **set from steady state 5.vi**.

The actual main loop first checks the status of the jump buttons in **handle panel shifts 1.vi**, then updates the hidden steady state data with any changes made to the various control panels in **handle steady state 3.vi** (see below for details). First load/save, then editing and pattern scrolling operations are performed based on the state of the respective control fields.

run pattern 3.vi is called which will compile and run the current pattern if the control buttons are set to “run once” or “loop”. If they are not, execution will continue directly to **output state 3.vi** which will update the output signals if it is necessary to match changed state state data or if pattern output has changed the state.

The loop will the return to the beginning. The zero millisecond delay in the main loop serves as a form of cooperative multitasking, temporarily handing off execution privileges to other tasks.

pattern output 8.vi

The only complicated part in the steady state loop is the synchronization between the hidden steady state data, the analog state controls, and the channel settings area.

The routine first checks whether a new channel was selected for the channel settings panel. If it was, then the panel is updated to reflect the new channel. If the channel is the same as in the last iteration of the loop, then the VI transfers any settings changes to steady state data. It then checks whether the slider was moved. If it was, the analog state panel and steady state data is updated to show this change in data. If it was not, the selected channel’s value on the analog state panel is checked for change and the slider is updated if necessary.

Next the digital state panel is handled. In a loop over the left (green buttons), then the right (yellow buttons) block of the panel, name and override status are overwritten with their respective settings, so that they appear as read-only to the user. The on/off status is copied to steady state data. The same is done with the analog state panel that was synchronized with the slider before.

A.6.2 Pattern Output

Once “run” is selected, the normal loop will be interrupted until pattern generation has been finished or aborted.

run pattern 03.vi

This VI checks the state of the run control buttons and then initiates pattern parsing and compilation by calling **prepare pattern 1.vi**. This creates the necessary data structures for **pattern output 8.vi**.

pattern output 8.vi

Pattern output is built around a fast routine (**_render analog samples 4.vi**) that generates the required analog samples from a third degree polynomial. This takes very little time and provides data compression by only requiring a set of four 32-bit values per channel and word. To keep everything as simple as possible, this list of coefficients is used for all words, even when the output values are constant. This avoids the presence of different paths through the output routine thus simplifying development and testing. It also means that there is no difference between a word with all analog channels held constant and one with all of them performing smooth transfers. The only way a pattern can create increased load for the output routine is the use of many very short words.

Sending data to the I/O boards is done by so-called “tasks”. A task can address a list of either digital or analog channels on the same I/O board. Each of the boards can only support one buffered-output task for analog data and one task for digital data running at any given time. For this reason three analog tasks (one of the analog board and one each to control the four analog channels on the digital boards) and two digital tasks are created. A sixth task serves to create the clock signal on the RTSI bus used to synchronize output.

Because the differences between the two kinds of I/O boards are hidden by the commands used to access them from LabView, the only remaining distinction for the rest of the output sequence is between digital and analog tasks. Both are handled in loops and receive the next block of sample data from a rendering function as an array (for the tasks) of arrays (containing the samples). The rendering functions similarly expect their data in the form of an array (for the tasks) containing an array of blocks mostly corresponding to the words of the pattern. Each block gives a start and end sample as well as the data for this block: digital values take the form of one 32-bit number for each task and board, while for analog data the inner array is actually two-dimensional providing a set of blocks with start, end and coefficient information for each channel. This makes it possible to cut the pattern into different blocks for each analog channel, e.g. to introduce a delay compensation. It also allows for the creation of routines that sub-divide blocks to create functions more complicated than possible with the simple polynomial method. This is not implemented at this point and the number of analog blocks will be identical for all channels.

prepare pattern 1.vi

This VI calls the various subroutines required for pattern compilation. **_parse constants field 4.vi** provides constant values to the subroutine **parse pattern 7.vi** in the form of a substitution list. It also supplies a list of directives to **_directives to events 1.vi**. Since the only implemented directive at this time deals with digital triggers, the output of this is only sent to **_compile digital group 2.vi**, where they are added to the compiled digital blocks. Similarly **_compile analog group 2.vi** serves to create the final block data for the analog tasks. An additional loop creates one set of values per data block for each group of digital extra channels not capable of buffered output. The output routine uses this to update their status every time it sends new data to the I/O boards. Since there is no front end to control these values from the control panel, each set of values consists of all zeros at this point.

parse pattern 7.vi

The compilation routines can only handle a simple pre-parsed pattern without any loops or sub-patterns and filled entirely and exclusively with numerical values. This routine does the required simplification. It loops over all active words, first looking at the function field. In a data word, it converts the time given into samples and then calls **_parse lines of**

analog block 6.vi to handle the analog field entries (constants, formulas, ramps etc.). Handling digital data is easier and the only complication consists of the collection of values from the individual controls in the digital part into an array. This is done in **_word cluster to digital state data 3.vi**. The main case statement deals with the various functions. Most of these are fairly straightforward.

A short explanation of how for loops are handled might be helpful, though. Whenever the parser encounters a `for` command, it generates a list of *values* for the iterations of the loop. It then sets a *counter* to the first of them. All of these are bundled into a cluster with a pointer at the *word* the loop starts in and the name of the *variable* the values need to be applied to. This cluster is then added to an array that serves as a LIFO (last-in, first-out) stack and the function field of the current word is changed to "define". The pattern index counter is decremented by 1. This way the same word will be evaluated again, this time to handle any definitions given in the analog fields. After this, evaluation proceeds normally through the pattern, until an "end" command is encountered. When this happens, the last entry is read from the loop stack (corresponding to the innermost loop). The *variable* is set to the next value in the *values* list and the *counter* is incremented. The pattern index counter is then set back to the word that contained the original "for" command. Since this has been changed to a "define" function, this allows changing of other constants according to the new value of the variable, but it does not cause a new entry into the loop stack. If the variable was already set to the last value when "end" was encountered, the entry is removed from the loop stack and evaluation continues normally.

_compile analog group 2.vi

The only complication in assembling the final analog block data are the different compensation times. Based on the compensation for the current channel compared to the maximum compensation value in *max comp.* the start and end times for each block are set. Finally extra blocks are created to fill the time from sample 0 to to the beginning of the actual pattern and from the end of the pattern until the end of the actual output sequence. These simply hold the first (or last) value of the pattern.

_compile digital group 2.vi

Achieving the same effect for the digital channels is more complicated, as all the channels on one I/O board need to be updated at the same time. The blocks provided by the original words therefore need to be split up. This is done by converting the data into a list of "events" stored in a cluster containing the sample (*smp*) when the channel switches output, which *bit* contains the relevant channel and what logical level it switches *to*. After one event has been generated for each channel to indicate its initial state, the routine looks at each word in succession and generates events for each channel that changes state. Whenever the switch is off-to-on, the time of the event is moved back as many samples as required by the compensation value.

After this is done, the extra events generated by the flush_camera directive are added. Events are then sorted by the sample they happen in. A digital block is created for each distinct value in the list. All events that happen at this sample are combined into this block. High compensation values or short words can cause a (time-corrected) turn-on event to happen before a previous (not time-corrected) turn-off event. This is referred to as a “cross-over” and when it occurs, the redundant events are discarded and a warning message is generated.

Bibliography

M. H. Anderson, W. Petrich, J. R. Ensher, and E. A. Cornell. Reduction of light-assisted collisional loss rate from a low-pressure vapor-cell trap. *Physical Review A*, 50(5):R3597–R3600, Nov 1994.

S. H. Autler and C. H. Townes. Stark effect in rapidly varying fields. *Physical Review*, 100(2):703–722, Oct 1955.

M. Aymar and O. Dulieu. Calculations of transition and permanent dipole moments of heteronuclear alkali dimers NaK, NaRb and NaCs. *Molecular Physics*, 105(11-12):1733–1742, 2007.

S. Azizi, M. Aymar, and O. Dulieu. Prospects for the formation of ultracold ground state polar molecules from mixed alkali atom pairs. *European Physical Journal D*, 31(2):195–203, Nov 2004.

M. Baranov, L. Dobrek, K. Goral, L. Santos, and M. Lewenstein. Ultracold dipolar gases - a challenge for experiments and theory. *Physica Scripta*, T102:74–81, 2002.

A. Batär. *Erzeugung und Charakterisierung ultrakalter Rubidium- und Ytterbiumatome – auf dem Weg zu einem gemischten Quantengas*. PhD thesis, Universität Düsseldorf, 2005.

K. Bergmann, H. Theuer, and B. Shore. Coherent population transfer among quantum states of atoms and molecules. *Reviews of Modern Physics*, 70(3):1003–1025, Jul 1998.

H. L. Bethlem, G. Berden, F. M. H. Crompvoets, R. T. Jongma, A. J. A. van Roij, and G. Meijer. Electrostatic trapping of ammonia molecules. *Nature*, 406:491–494, 2000.

C. Boisseau, E. Audouard, J. Vigue, and P. S. Julienne. Reflection approximation in photoassociation spectroscopy. *Physical Review A*, 62(5):article 052705, Nov 2000.

J. Brown and A. Carrington. *Rotational spectroscopy of diatomic molecules*. Cambridge University Press, 2003.

S. Chu, L. Hollberg, J. E. Bjorkholm, A. Cable, and A. Ashkin. Three-dimensional viscous confinement and cooling of atoms by resonance radiation pressure. *Physical Review Letters*, 55(1):48–51, Jul 1985.

D. Comparat. Improved LeRoy-Bernstein near-dissociation expansion formula, and prospect for photoassociation spectroscopy. *Journal of Chemical Physics*, 120(3):1318–1329, 2004.

D. Comparat. Cold molecules. Lecture at INTERCAN and IFRAF PreDoc School on “Laser Cooling and Bose-Einstein Condensation”, Sep 2008.

E. Condon. A theory of intensity distribution in band systems. *Physical Review*, 28(6):1182–1201, Dec 1926.

J. G. Danzl, E. Haller, M. Gustavsson, M. J. Mark, R. Hart, N. Bouloufa, O. Dulieu, H. Ritsch, and H. C. Nägerl. Quantum gas of deeply bound ground state molecules. *arXiv:0806.2284v1*, 2008.

J. Deiglmayr, A. Grochola, M. Repp, K. Mortlbauer, C. Gluck, J. Lange, O. Dulieu, R. Wester, and M. Weidemüller. Formation of ultracold polar molecules in the rovibrational ground state. *Physical Review Letters*, 101(13):133004, 2008.

D. DeMille. Quantum computation with trapped polar molecules. *Physical Review Letters*, 88(6):067901, Feb 2002.

D. DeMille, S. B. Cahn, D. Murphree, D. A. Rahmlow, and M. G. Kozlov. Using molecules to measure nuclear spin-dependent parity violation. *Physical Review Letters*, 1(2):023003, Jan 2008.

A. Derevianko, J. F. Babb, and A. Dalgarno. High-precision calculations of van der Waals coefficients for heteronuclear alkali-metal dimers. *Physical Review A*, 63(5):052704, Apr 2001.

J. Doyle, B. Friedrich, R. V. Krems, and F. Masnou-Seeuws. Quo vadis, cold molecules? *European Physical Journal D*, 31(2):149–164, Nov 2004.

T. M. Dunn. 4: Modern research. In K. N. Rao and C. W. Mathews, editors, *Molecular Spectoscopy*. Academic Press, New York, 1972.

C. Eckart. Some studies concerning rotating axes and polyatomic molecules. *Physical Review*, 47(7): 552–558, Apr 1935.

K. Enomoto, M. Kitagawa, K. Kasa, S. Tojo, and Y. Takahashi. Determination of the s-wave scattering length and the C6 van der waals coefficient of Yb-174 via photoassociation spectroscopy. *Physical Review Letters*, 98(20):203201, May 2007.

A. Fioretti, J. Lozeille, C. A. Massa, M. Mazzoni, and C. Gabbanini. An optical trap for cold rubidium molecules. *Optics Communications*, 243(1-6):203–208, Dec 2004.

T. Fleig. Rb-Yb potentiale. private communication, Apr 2008.

T. Fukuhara, Y. Takasu, M. Kumakura, and Y. Takahashi. Degenerate fermi gases of ytterbium. *Physical Review Letters*, 98:030401, 2007.

U. Gaubatz, P. Rudecki, M. Becker, S. Schiemann, M. Kulz, and K. Bergmann. Population switching between vibrational levels in molecular-beams. *Chemical Physics Letters*, 149(5-6):463–468, SEP 2 1988.

U. Gaubatz, P. Rudecki, S. Schiemann, and K. Bergmann. Population transfer between molecular vibrational levels by stimulated raman scattering with partially overlapping laser fields. A new concept and experimental results. *Journal of Chemical Physics*, 92(9):5363–5376, 1990.

S. Ghezali, P. Laurent, S. N. Lea, and A. Clairon. An experimental study of the spin-exchange frequency shift in a laser-cooled cesium fountain frequency standard. *Europhysics Letters*, 36(1):25–30, oct 1996.

C. Haimberger, J. Kleinert, M. Bhattacharya, and N. P. Bigelow. Formation and detection of ultracold ground-state polar molecules. *Physical Review A*, 70(2):021402, Aug 2004.

H. Haken and H. C. Wolf. *Molekülphysik und Quantenchemie*. Springer Verlag, 3rd edition, 1998.

C. Hamilton, J. Kinsey, and R. Field. Stimulated-emission pumping - new methods in spectroscopy and molecular-dynamics. *Annual Review of Physical Chemistry*, 37:493–524, 1986.

T. W. Hänsch and B. Couillaud. Laser frequency stabilization by polarization spectroscopy of a reflecting reference cavity. *Optics Communications*, 35(3):441–444, 1980.

G. Herzberg. *Molecular Spectra and Molecular Structure*, volume I. Spectra of Diatomic Molecules. Van Nostrand Reinhold, 1950.

E. A. Hinds. Testing time reversal symmetry using molecules. *Physica Scripta*, T70:34, 1997.

E. R. Hudson, H. J. Lewandowski, B. C. Sawyer, and J. Ye. Cold molecule spectroscopy for constraining the evolution of the fine structure constant. *Physical Review Letters*, 96(14):143004, Apr. 2006.

F. Hund. Concerning the importance of some appearances in the molecular spectra. *Zeitschrift für Physik*, 36:658, 1926.

K. M. Jones, E. Tiesinga, P. D. Lett, and P. S. Julienne. Ultracold photoassociation spectroscopy: Long-range molecules and atomic scattering. *Reviews of Modern Physics*, 78(2):483–535, Apr-Jun 2006.

W. Ketterle, K. B. Davis, M. A. Joffe, A. Martin, and D. E. Pritchard. High densities of cold atoms in a dark spontaneous-force optical trap. *Physical Review Letters*, 70(15):2253–2256, Apr 1993.

J. Kleinert, C. Haimberger, P. J. Zabawa, and N. P. Bigelow. Trapping of ultracold polar molecules with a thin-wire electrostatic trap. *Physical Review Letters*, 99(14):143002, Oct 2007.

V. Kokoouline, C. Drag, P. Pillet, and F. Masnou-Seeuws. Lu-Fano plot for interpretation of the photoassociation spectra. *Physical Review A*, 65(6):062710, Jun 2002.

S. D. Kraft, J. Mikosch, P. Staanum, J. Deiglmayr, J. Lange, A. Fioretti, R. Wester, and M. Weidemuller. A high-resolution time-of-flight mass spectrometer for the detection of ultracold molecules. *Applied Physics B*, 89(4):453–457, Dec 2007.

S. Kroboth. Laserkühlung von Ytterbiumatomen. Diplomarbeit, Universität Stuttgart, 2002.

S. Kunze, S. Dürr, K. Dieckmann, M. Elbs, U. Ernst, A. Hardell, S. Wolf, and G. Rempe. Standing wave diffraction with a beam of slow atoms. *Journal of Modern Optics*, 44(10):1863–1881, 1997.

V. Ledoux. *Study of Special Algorithms for solving Sturm-Liouville and Schrödinger Equations*. PhD thesis, Universiteit Gent, 2006.

R. J. LeRoy and R. B. Bernstein. Dissociation energy and long-range potential of diatomic molecules from vibrational spacings of higher levels. *Journal of Chemical Physics*, 52(8):3869–3879, 1970.

A. Lindinger, M. Verbeek, and H. Rubahn. Adiabatic population transfer by acoustooptically modulated laser beams. *Zeitschrift für Physik D*, 39(2):93–100, FEB 1997.

T. H. Loftus. *Laser Cooling and Trapping of Atomic Ytterbium*. PhD thesis, University of Oregon, 2001.

M. Marinescu and H. R. Sadeghpour. Long-range potentials for two-species alkali-metal atoms. *Physical Review A*, 59(1):390–404, Jan 1999.

H. Metcalf and P. van der Straten. *Laser Cooling and Trapping*. Springer–Verlag, New York, 1999.

A. Micheli, G. K. Brennen, and P. Zoller. A toolbox for lattice-spin models with polar molecules. *Nat Phys*, 2(5):341–347, 2006.

P. G. Mickelson, Y. N. Martinez, A. D. Saenz, S. B. Nagel, Y. C. Chen, T. C. Killian, P. Pellegrini, and R. Cote. Spectroscopic determination of the s-wave scattering lengths of Sr-86 and Sr-88. *Physical Review Letters*, 95(22):223002, Nov 2005.

F. Münchow. Photoassoziationsspektroskopie an einem ultrakalten RbYb-gemisch. Master's thesis, Universität Düsseldorf, 2008.

N. Nemitz. Setup of a stable high-resolution laser system. Diplomarbeit, Universität Stuttgart, 2004.

K.-K. Ni, S. Ospelkaus, M. H. G. de Miranda, A. Pe'er, B. Neyenhuis, J. J. Zirbel, S. Kotochigova, P. S. Julienne, D. S. Jin, and J. Ye. A High Phase-Space-Density Gas of Polar Molecules. *Science*, 322(5899): 231–235, 2008.

D. Popescu, C. B. Collins, B. W. Johnson, and I. Popescu. Multiphoton excitation and ionization of atomic cesium with a tunable dye laser. *Physical Review A*, 9(3):1182–1187, Mar 1974.

G. Pupillo, A. Micheli, H. P. Büchler, and P. Zoller. Condensed matter physics with cold polar molecules. *arXiv:0805.1896v1*, 2008.

E. L. Raab, M. Prentiss, A. Cable, S. Chu, and D. E. Pritchard. Trapping of neutral sodium atoms with radiation pressure. *Phys. Rev. Lett.*, 59(23):2631–2634, Dec 1987.

J. M. Sage, S. Sainis, T. Bergeman, and D. DeMille. Optical production of ultracold polar molecules. *Physical Review Letters*, 94(20):203001, May 2005.

U. Schlöder, C. Silber, T. Deuschle, and C. Zimmermann. Saturation in heteronuclear photoassociation of (LiLi)-Li-6-Li-7. *Physical Review A*, 66(6):061403, Dec 2002.

U. Schlöder, T. Deuschle, C. Silber, and C. Zimmermann. Autler-Townes splitting in two-color photoassociation of li-6. *Physical Review A*, 68(5):051403, Nov 2003.

F. T. Smith. Diabatic and adiabatic representations for atomic collision problems. *Physical Review*, 179 (1):111–123, Mar 1969.

D. A. Steck. Alkali d line data. URL `http://steck.us/alkalidata/`.

D. A. Steck. Alkali d line data. URL `http://steck.us/alkalidata/`.

Y. Takasu, K. Maki, K. Komori, T. Takano, K. Honda, M. Kumakura, T. Yabuzaki, and Y. Takahashi. Spin-singlet bose-einstein condensation of two-electron atoms. *Physical Review Letters*, 91(4):040404, 2003.

T. Takekoshi, B. M. Patterson, and R. J. Knize. Observation of optically trapped cold cesium molecules. *Physical Review Letters*, 81(23):5105–5108, Dec 1998.

S. Tassy. *Sympathetische Kühlung von Ytterbium mit Rubidium*. PhD thesis, Institut für Experimentalphysik, Heinrich-Heine-Universität Düsseldorf, 2007.

H. R. Thorsheim, J. Weiner, and P. S. Julienne. Laser-induced photoassociation of ultracold sodium atoms. *Physical Review Letters*, 58(23):2420–2423, Jun 1987.

E. Tiesenga, C. J. Williams, P. S. Julienne, K. M. Jones, P. D. Lett, and W. D. Phillips. A spectroscopic determination of scattering lengths for sodium atom collisions. *Journal of Research of the National Institute of Standards and Technology*, 101(4):505, 1996.

N. Vanhaecke, W. D. Melo, B. L. Tolra, D. Comparat, and P. Pillet. Accumulation of cold cesium molecules via photoassociation in a mixed atomic and molecular trap. *Physical Review Letters*, 89(6):063001, Aug 2002.

D. Wang, J. Qi, M. F. Stone, O. Nikolayeva, B. Hattaway, S. D. Gensemer, H. Wang, W. T. Zemke, P. L. Gould, E. E. Eyler, and W. C. Stwalley. The photoassociative spectroscopy, photoassociative molecule formation, and trapping of ultracold (krb)-k-39-rb-85. *European Physical Journal D*, 31(2):165–177, Nov 2004.

J. D. Weinstein, R. deCarvalho, T. Guillet, B. Friedrich, and J. M. Doyle. Magnetic trapping of calcium monohydride molecules at millikelvin temperatures. *Nature*, 395(6698):148–150, 1998.

C. E. Wieman and L. Hollberg. Using diode lasers for atomic physics. *Review of Scientific Instruments*, 62 (1):1–20, 1991.

W. C. Wiley and I. H. McLaren. Time-of-flight mass spectrometer with improved resolution. *Review of Scientific Instruments*, 26(12):1150–1157, 1955.

Acknowledgements

First of all, I would like to thank Megumi and Kuno for tolerating a stressed and tired husband and father for much longer than they deserved. Thanks guys... I promise to take a bit of a break now.

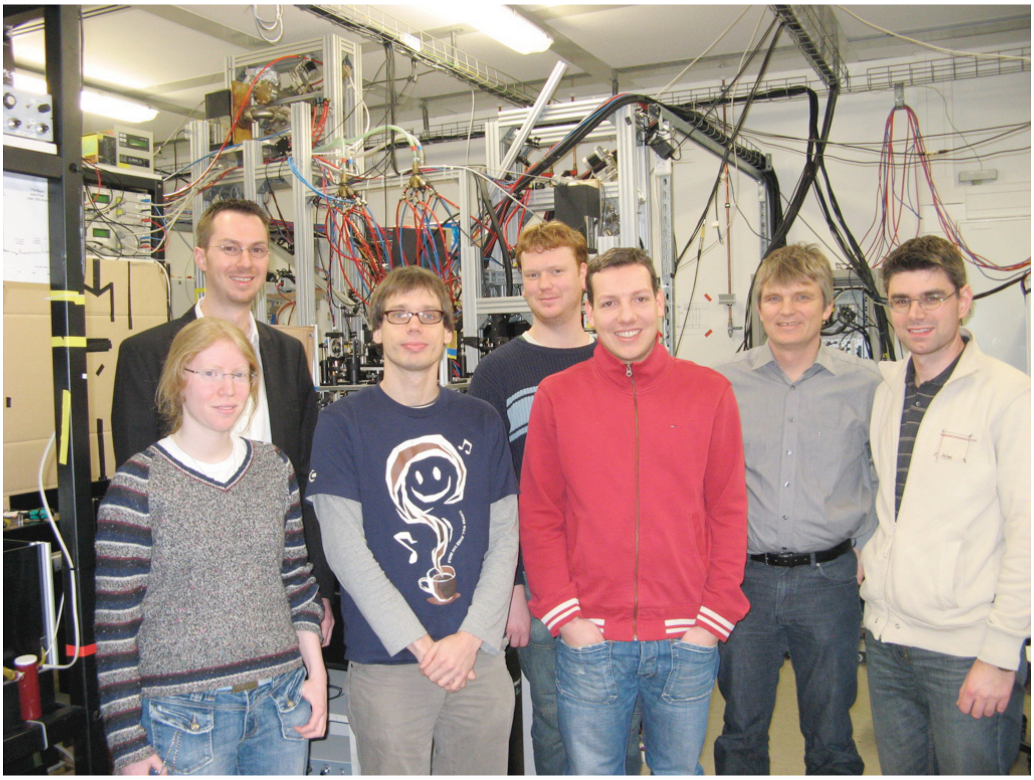

Figure A.3: The ytterbium-rubidium group in 2008:
(from left to right) Claudia Höhl, Sven Tassy, Nils Nemitz, Frank Münchow, Florian Baumer, professor Axel Görlitz and Ralf Stephan

There are more than a few other people who deserve credit. In more or less chronological order and with no claim to completeness, I would like to thank:

my family	For supporting me throughout the entire trip that took me to this place. Thank you... Even when I've been far away, you have always been there for me.
Thomas Biedermann	For pointing me in this direction and showing me the fun in making things, and then making them **work**.
Rudolf Gati	For getting me through uni when there was too much paper and not enough toys. Thank you for your help in organizing the year in Adelaide. Things would have been quite different for me without that.
Axel Görlitz	For taking me into his group and then to Düsseldorf. I had the great opportunity to see a complex experiment put together from bits in boxes, I have learned how to do science with sticky tape and epoxy and that it is sometimes the best way to do things... and sometimes it is not. It was fun.
Alexander Batär	For teaching me how to operate screwdrivers...
Sven Kroboth	For great patience with a complicated experiment and stubborn beam alignments. And for providing a sense that things were going somewhere, even when they did not want to.
Florian Baumer	For making work fun, while still being better with all these annoying screws and optical things than I will ever be. Good luck with the **really** cold ytterbium!
Ralf Stephan	For moving things past the "sticky tape and epoxy" phase where necessary and tolerating it where it wasn't. For getting things done before "sometime next year" and being able to make, setup and operate an impressive number of things.
Claudia Höhl	For being the first diploma student on a grown, massively complex experiment. I am sorry that it was harder than it was supposed to be.
Frank Münchow	For unexpected dedication in a diploma student and for taking the next watch in looking after the "machine". I hope I've drawn you a map here. Now it's your job to go and catch some molecules.

Thanks to all of you. And good luck for the future!